

UNIVERSITY OF BIRMINGHAM

PEMFC System Integration and Design Optimisation of a Hydrogen Fuel Cell Battery Hybrid Electric Propulsion System

by

Naseruddin Khan

July 2023

A thesis submitted to the University of Birmingham for the degree of

DOCTOR OF PHILOSOPHY

Centre for Fuel Cell and Hydrogen Research

School of Chemical Engineering

College of Engineering and Physical Sciences

University of Birmingham

UNIVERSITY OF
BIRMINGHAM

University of Birmingham Research Archive

e-theses repository

This unpublished thesis/dissertation is copyright of the author and/or third parties. The intellectual property rights of the author or third parties in respect of this work are as defined by The Copyright Designs and Patents Act 1988 or as modified by any successor legislation.

Any use made of information contained in this thesis/dissertation must be in accordance with that legislation and must be properly acknowledged. Further distribution or reproduction in any format is prohibited without the permission of the copyright holder.

Dedicated to my parents

Abstract

This thesis focuses on the topic of system integration of the polymer electrolyte membrane fuel cell (PEMFC) and design optimisation of a fuel cell hybrid electric vehicle (FCHEV) powertrain. Both of these aspects play a crucial role in the performance and sizing of components when integrated within an electric vehicle. At a system level, an optimised reactant gas management can reduce the fuel cell parasitic losses, thereby leading to an increased overall efficiency. The FCHEV powertrain design, incorporating the energy management system, involves fuel cell and battery sizing. Thus, the aim of optimising these can lead to reduced fuel consumption, system size and costs.

A 5 kW PEMFC system running on dry hydrogen with appropriately sized balance of plant was built to conduct experimental studies and analysis of the gas supply systems. A particular scrutiny in our work was on the development of a novel hydrogen purging strategy in the anode compartment of the fuel cell, based on a parameter independent of operational time. Through experimental validation, an ideal range of purging with recirculation of hydrogen was proposed. Furthermore, a model-based design strategy, employing dynamic programming methodology, was devised with the objective of optimal component sizing that can be applicable to specific powertrain configurations.

Acknowledgements

First and foremost, I would like to unreservedly thank my supervisors Prof. Robert Steinberger-wilckens and Dr. Yousif Al-sagheer for their valuable academic support and guidance. It was through their continued efforts, I had managed to reach the milestones of my research even with unprecedented challenges. It is only fair to suggest, with my deepest gratitude, that my supervisors stood as true mentors to me. I must also thank other important personalities within the department for helping me at every step, John Hooper, Chyntol Kanhimbe and Jacqueline Deans.

My unconditional gratitude is also due towards my entire family, in particular, my parents who have always been the biggest motivation in my life. Their hard work, moral support and Godly prayers have always been the backbone of everything I have achieved in this worldly life.

My research colleagues, who have become good friends, Abdul Hye, Marcus Taylor, Liam Cooper, Ali Alwani, Bhargav Pandayan, Ahmed Ibrahim and Recep Akdeniz deserve nothing but appreciation from me for their valuable friendship and good times.

Table of Contents

Abstract II
Acknowledgements III
Table of Contents IV
List of Figures 1
List of Tables 7
1 Introduction 8
1.1 Background and Motivation 9
1.1.1 The Need for Electric Vehicles 9
1.1.2 GHG Emissions 11
1.1.3 Energy Security 13
1.1.4 Challenges for Fuel Cell Vehicles 15
1.2 System and Design Optimisation 18
1.3 Research Aims and Objectives 20
1.4 Thesis Structure 21
2 Electrification via Hydrogen 25
2.1 Hydrogen Fuel Cells 26
2.1.1 Fuel Cell Operation 27
2.1.2 PEMFC Components 28
2.1.3 Hydrogen Production 30
2.1.4 On-board Hydrogen Storage 33
2.2 Electric Vehicles Classification 36
2.2.1 Commercial FCEVs 37
2.2.2 Powertrain Architectures 39
2.3 Energy Storage Systems 41
2.3.1 Batteries 41
2.3.2 Supercapacitors 44
3 Experimental Setup 46

3.1 Fuel Cell System 47
3.2 Anode Subsystem 51
3.3 Cathode System 55
3.4 Thermal Management 59
3.5 Electrical System 61
3.5.1 Sensors 63
3.5.2 Electrical Load Banks 68
3.6 Hydrogen Supply and Storage 70
3.7 FC Controller 71
3.8 System Process 74
4 PEMFC System Design 76
4.1 Introduction 76
4.2 Literature on PEMFC System 79
4.3 Hydrogen Fuel Feed Loop 81
4.4 Oxidant Feed Loop 85
4.5 Temperature Management 86
4.6 Results, Comparisons and Discussion 87
4.6.1 Experiments 87
4.6.2 Cathode Blower Experimental Modelling 89
4.6.3 Hydrogen Purging Strategy 95
4.6.4 Comparative Analysis 98
4.6.5 System Control 105
4.7 Conclusions 107
5 FCHEV Modelling and Simulation 110
5.1 Model Based Design 111
5.2 Literature Capture 112
5.3 Vehicle Performance Considerations 117
5.3.1 Powertrain Configuration 117
5.3.2 Drive Cycle Analysis 118

5.3.3 Regenerative Braking 120
5.4 Model Architecture 122
5.4.1 Vehicle model 124
5.4.2 Fuel Cell 125
5.4.3 Battery 128
5.4.4 DC-DC Converter 130
5.4.5 Electric Motor 131
5.5 Heuristic Controller 133
5.6 Toyota Mirai Case Study 137
5.7 Simulation Results 141
5.7.1 Controller Functional Behaviour 141
5.7.2 System Operation 145
5.7.3 Usage Envelopes 149
5.8 Summary 153
6 Design Optimisation Part I: Strategy 154
6.1 Introduction 154
6.2 Literature Review 156
6.3 Energy Management System (EMS) and Its Strategy 162
6.3.1 Optimisation Theory 162
6.3.2 Dynamic and Quadratic Programming 163
6.3.3 Fuel Cell System 164
6.3.4 Battery Model 166
6.3.5 Problem Formulation 167
6.3.6 Assumptions 169
6.3.7 Charge Depletion Mode 170
6.3.8 Charge Sustaining Mode 172
6.3.9 Sizing Strategy 174
7 Design Optimisation Part II: Implementation and Analysis 178
7.1 CD Control Mode Results 178

7.1.1 Energy Consumption 179
7.1.2 Component Sizing 187
7.1.3 Power Split Curves 190
7.1.4 System Mass and Volume 194
7.1.5 System Cost 196
7.2 CS Control Mode Results 201
7.2.1 Energy and Fuel Consumption 203
7.2.2 System Sizing and Cost 211
7.3 Summary 215
8 Conclusions 218
8.1 Summary and conclusions 218
8.2 Future Recommended Work 221
References 223
Appendices 237

List of Figures

Figure 1: Global GHG emissions by fossil fuels from 2000 to 2022 [8] 12
Figure 2: Graphically displays the historical top five emitters of CO_2 globally from 1990 onwards [10] 12
Figure 3: Invention flow as a result of R&D activity in the realm of hydrogen and its technologies between 2010 and 2020 [12] 14
Figure 4: Research work visual compartmentalisation between fuel cell system and powertrain design optimisation. 20
Figure 5: Hydrogen fuel cell components, a: graphical representation of the cell within a stack, b: block diagram representation of FC components. PEM: polymer electrolyte membrane, CL: catalyst layer, GDL: gas diffusion layer, BPP: bipolar plate and MEA: membrane electrode assembly. 30
Figure 6: Different shades of hydrogen based on the source and process of production [20]. 32
Figure 7: Carbon emissions for different shades of hydrogen, highlighting the low carbon hydrogen threshold [23]. 33
Figure 8: Different types of compressed hydrogen storage tanks and their manufacturing procedures [24]. 35
Figure 9: Electric vehicles classification. 36
Figure 10: FC technology adoption in passenger car and long haul truck industries. a: Toyota Mirai, b: Hyundai Nexo, c: Nikola TRE FCEV truck d: Toyota FC logistic truck. 39
Figure 11: Different topologies applicable in an FCEV, a: standalone FCEV, b: fuel cell hybrid electric vehicle with passive control over ESS, c: fuel cell hybrid with active control over ESS and d: fuel cell tri-hybrid with active control over both ESSs. 40
Figure 12: Gravimetric and volumetric energy densities evolution of Lithium-ion battery chemistry since 1990 to 2016 [31]. 42
Figure 13: OEM integrated in Audi A6 PHEV high voltage battery discharge and charge power as a function of SoC and temperature [33]. 44

Figure 14: Comparison of automotive energy storage technologies, a: Ragone plot depicting specific power vs specific energy, b: techno-economic comparison between Lithium-ion and EDLC energy storage systems [35]. 45
Figure 15: Fuel Cell stack with BoP rear CAD view 51
Figure 16: Experimental fuel cell stack with BoP frontal CAD view 51
Figure 17: Diaphragm based pressure regulator [36]. 52
Figure 18: Internals of the medium to low pressure regulator [36]. 52
Figure 19: Calibrated H2 MFM [37]. 53
Figure 20: Hydrogen sensor [38]. 53
Figure 21: BLDC H_2 recirculation pump [39]. 54
Figure 22: Recirculation process highlighting the suction and discharge ports of the recirculation pump [39]. 54
Figure 23: Blower calibration using experimental set up employing high flow rate meter. 56
Figure 24: Cathode blower performance behaviour with step changes via analogue control signal 57
Figure 25: Cathode blower calibration based on the stack power and flow rate at different ASR values. 58
Figure 26: Passive humidifier incorporated in the cathode sub-system: (a): principle operation description, (b): humidifier by Perma Pure brand used in the experimental test rig. 59
Figure 27: Heat exchanger details integrated within the FC system. a: Aspen Plus design model, b: procured heat exchanger used in Ford Fiesta commercial vehicle 61
Figure 28: DC-DC boost converter, a: CAD side-view, b: CAD top-view with annotation, c: wiring diagram with load, battery and FC 62
Figure 29: Operational behaviour of the DC-DC boost converter. 63
Figure 30: hall-effect sensor with input and outputs shown. 64
Figure 31: Voltage sensor with measurement signals illustrated 65
Figure 32: a: Mini pressure switch to shut monitor the anode pressure, b: pressure sensor to monitor pressure build up inside the stack. 66
Figure 33 Devices used within the thermal management sub-system[42]. a: RTD temperature sensor, b: high accuracy temperature transmitter [43]. 67

Figure 34: RH sensing within the FC BoP. a: RH sensor by Measurement Specialties, b: RH level against output voltage signal [44] 68
Figure 35: Electrical load banks, a: current vs voltage characteristics, b: parallel connection in the lab set up illustration [45]. 69
Figure 36: Pressure regulation from the storage tank to stack inlet with multiple stages illustrated. 70
Figure 37: NI cRIO series embedded controller. 71
Figure 38: Additional modules for digital, analogue input and outputs for cRIO. 71
Figure 39: FC embedded controller interface with hardware devices in the lab test set up ... 73
Figure 40: System process diagram depicting all the sub-system and the auxiliary components with each system distinctly segregated. 75
Figure 41: Illustrative classification of hydrogen purging process. 84
Figure 42: (a) Anode subsystem experimental setup and (b) cathode sub-system design. 86
Figure 43: Step change experiment on the stack to display and extract steady state response time 87
Figure 44: (a) Stack and system efficiency curves, and (b) Stack polarisation and power curves. 89
Figure 45: Example of parasitic load power consumption during step changes of stack power. 90
Figure 46: Cathode blower power consumption over stack power and air stoichiometry ratio. 92
Figure 47: Sensitivity analysis on the impact of air SR value – (a): SR = 2, (b): SR = 3, (c): SR = 4, (d): SR = 5, (e): full load test at SR = 4. 94
Figure 48: Flowchart describing the purging strategy's operation. 97
Figure 49: Outcome of hydrogen purging experiments without recirculation. 100
Figure 50: Hydrogen purging experimental outcome with recirculation. 101
Figure 51: CVM data for the stack with anode without recirculation: Figures a, b, c corresponding to events in (i), and recirculation: Figure d corresponding to (ii) 105
Figure 52: Block diagram of FCHEV propulsion system. 118
Figure 53: NEDC test cycle power, speed and acceleration profiles, with peak acceleration profile integrated in the end of the cycle. 119

Figure 54: WLTP test cycle power, speed and acceleration profiles with peak acceleration profile integrated in the end of the cycle. 119
Figure 55: NEDC traction and braking energies. 120
Figure 56: WLTP traction and braking energies. 120
Figure 57: Sankey diagram depicting surge of power regained through regenerative braking in a FCHEV, diagram extracted from Cruise Simulation with NEDC at 893s 122
Figure 58: Sankey diagram depicting power gained through regenerative braking on a FCHEV, diagram extracted from with WLTP simulation in Cruise at 1126s 122
Figure 59: FCHEV model architecture in AVL Cruise M™, highlighting electrical (orange) and mechanical (green) connections. 123
Figure 60: Electrical equivalent battery circuit model in AVL Cruise M 129
Figure 61: FC DC-DC converter equivalent circuit derived from AVL Cruise M. 130
Figure 62: Electric motor velocity vs torque map showing the efficiency 132
Figure 63: Efficiency 3-D surface chart of the motor. 133
Figure 64: Rule-based strategy state flow chart sequence diagram showing permissible transition between the four operating modes. 135
Figure 65: Detailed rule-based strategy showing transitions based on predefined rules 136
Figure 66: Toyota Mirai powertrain systems [128]. 138
Figure 67: Toyota Mirai powertrain configuration and components [129]. 139
Figure 68: RBS implemented in AVL Cruise M model depicting system operation with key parameters illustrated in multiple sections (numbered above the figure) within WLTP cycle. 142
Figure 69: CDCS controller behaviour based on WLTP cycle illustrating velocity profile, power curves, battery SoC and hydrogen fuel consumption. 146
Figure 70: Charge-Sustaining controller behaviour based on NEDC cycle illustrating velocity profile, power curves, battery SoC and hydrogen fuel consumption 148
Figure 71: Stack polarisation and power curves (FC operates at 200 to 350 V range) 149
Figure 72: FC stack operating points derived from Mirai test data and Cruise M model illustrating high frequency of usage in the low power region where FC is efficient. 150
Figure 73: Toyota Mirai histogram and system efficiency, data extracted from [129] 152
Figure 74: Model histogram and FC system efficiency 152

Figure 75: Description of CD mode illustration with small and large battery pack.....171
Figure 76: Description of CS mode implementation via DP in the EMS. Red lines indicate the upper and lower contraints on SoC.....173
Figure 77: Flowchart describing the sizing algorithm in charge depletion mode. 176
Figure 78: Net energy consumption at different rates of energy recuperation in the NEDC drive cycle replicating 45 iterations to complete the required range. 182
Figure 79: Net energy consumption at different rates of energy recuperation in WLTP drive cycle replicating 21 iterations to complete the required range.....182
Figure 80: Change in energy for each DoH value in NEDC drive cycle. 182
Figure 81: Change in energy for each DoH value in WLTP drive cycle.....182
Figure 82: Energy flow bar charts in NEDC drive cycle with charge rate of 0.5C and 2C respectively (a and c); WLTP drive cycle (b and d).....185
Figure 83: Hydrogen consumption across 45 NEDCs for net energy optimal solutions.....187
Figure 84: Hydrogen consumption across the whole vehicle range for net energy optimal solutions in WLTP.....187
Figure 85: DoH vs components size with 0.5C, 1C, 1.5C and 2C charging C-rates for NEDC profile.....189
Figure 86: DoH vs components sizing with 0.5C, 1C, 1.5C and 2C charging C-rates for WLTP profile.....190
Figure 87: Power split and SoC curves for optimal DoH combinations in the NEDC drive cycle.....192
Figure 88: Power split and SoC curves for optimal DoH combinations in the WLTP drive cycle.....193
Figure 89: Sizing in NEDC with high C-rate.....195
Figure 90: Sizing in WLTP with high C-rate. 195
Figure 91: Proposed optimal mass and volume solutions (NEDC). 196
Figure 92: Proposed optimal mass and volume solutions (WLTP). 196
Figure 93: System cost distribution for NEDC.....197
Figure 94: System cost distribution for WLTP. 197
Figure 95: Powertrain system cost with individual trend lines at every step of DoH. 199

Figure 96: UK average travel distance for a passenger car/driver- data extracted from [167]. 202
Figure 97: USA average travel distance for a passenger car/driver – data extracted from [166]. 202
Figure 98: NEDC PSCS control strategy results with 10C peak charging C-rate and 50% DoD window modelling on 4 consecutive cycles; a: net energy consumption, b: battery energy distribution, c: consumed and expended hydrogen, d: battery SoC for different battery capacities 206
Figure 99: WLTP PSCS control strategy results with 10C peak charging C-rate and 50% DoD window modelled on 2 consecutive cycles; a: net energy consumption, b: battery energy distribution, c: consumed and expended hydrogen, d: battery SoC for different battery capacities 208
Figure 100: Stacked plots depicting energy recuperation events for recharging the battery using hydrogen on-board the vehicle, a) NEDC profile b) WLTP profile. 210
Figure 101: Component sizing and cost derivation of FCHEV based on WLTP cycle; a: FC and battery sizing, b: system mass, c: system volume and d: system cost. 214
Figure 102: Test rig set up used for experimentation in this work, depicting various sub-systems 237
Figure 103: LabVIEW front panel view of the software, for control and data logging. 238
Figure 104: LabVIEW software program with cRIO embedded controller signal and data manipulation 239
Figure 105: NEDC and WLTP cycle data extracted from Toyota Mirai results available from Argonne National lab. 240

List of Tables

Table 1: Four commercially available different types of fuel cells with their characteristics. 28

Table 2: Summary of different types of on-board hydrogen storage vessels....35

Table 3: Classification and characteristics of EVs....37

Table 4: FC BoP components summary 49

Table 5: Indicative calculations based on the experiments on hydrogen purging. ...103

Table 6: NEDC and WLTP test cycles metrics 119

Table 7: Vehicle specification (inputs to the Vehicle block)....124

Table 8: Toyota Mirai Gen I specifications 140

Table 9: Controller functional behaviour description of four operating modes; E-Drive, charge, boost and power modes. 144

Table 10: Design optimisation techniques for a FC hybridised powertrains found in the literature....161

Table 11: Gravimetric, volumetric densities and costs of the components. 177

Table 12: Proposed optimal solutions data consisting component sizing, energy, fuel economy, mass & volume and cost parameters. 3-200

Table 13: CD mode results for WLTP cycle populated with battery and FC parameters....213

1 Introduction

There is a global drive to tackle the global warming issue. Though there are many causes contributing to the greenhouse gas (GHG) emissions, the mobility sector is seen as one of the main sectors where vehicle tailpipe emissions are a direct cause due to the usage of conventional fossil-based fuels. As a result, the automotive industry, followed by various others such as the energy, marine and aerospace industries, have begun to show a keen interest in carbon footprint reduction [1]. The effect of these harmful emissions, in particular the pollutant-based emissions, have proven to cause premature deaths and various respiratory problems in regions with polluted air quality [2]. Moreover, the problem is exacerbated due to the dependency on fossil fuel production on crude oil, which is prone to market fluctuations and only accessible to specific regions globally. In addition to this, causes such as increased energy demand and growing population have led to questions on energy security pertaining sole reliance on energy imports from oil producing economies. Moreover, road transport continues to see a growth globally. For example, the EU registered an annual growth of 2.1 % in a short span of 2017 to 2021 [3]. As a result, consumer behaviour and emission regulations globally are putting the automotive industry under increasing pressure to manufacture more efficient and less polluting vehicles. Thus, in order to tackle the above challenges the most favoured innovation in the mobility sector is electrification of the powertrain. Pure electrification in the

context of transport is applicable in mainly two types of electric vehicle (EV); battery and hydrogen fuel cell vehicle (FCEV) electrification. In the past decade, almost every major car manufacturer has released at least one urban style pure BEV. Although the FCEV industry faces numerous challenges and drawbacks, major car manufacturers have commercially released brands of FCEVs, in addition to having conducted a number of feasibility studies in form of a demonstration projects.

This chapter presents a detailed overview of the topic of integration and optimisation of polymer electrolyte membrane (PEMFC) powertrains hybridised with batteries. The rationale and advantages of the technology in question are also discussed in this report. Relevant comparison and technology gaps are highlighted. At the end of this chapter, the project scope in the form of research aim and objectives as well as format of this thesis are described.

1.1 Background and Motivation

1.1.1 The Need for Electric Vehicles

The concept of electrification is not a modern invention as it has existed long before the current advent of EVs. From a historical point of view, EVs made it to the roads in the late 18th century for the first time [4]. At that time, due to the immaturity of the technology, EVs failed to compete against conventional means of transport. With speeds of 15 km/h and range of 16 km EVs failed to excite the consumers over horse carriages. In the next couple of decades EVs suffered tremendously, compared to petrol cars, with range anxiety in particular. Especially when modernisation was at

its peak and longer travel distances were in demand across Europe and USA. A significant advancement in EVs at that time showed signs of their capability. The invention of regenerative braking made it possible for EVs to recover kinetic energy during braking, hence recharging the batteries - enhancing the vehicle range. Thanks to this concept the improvement in overall efficiency in urban driving mode commercialised in the form of hybrid electric vehicles (HEV).

EVs come in various forms but the main intent behind their growth is, undoubtedly, zero-emission at the point of use. Earlier in the last decade, there were an estimated one billion automobiles on the road globally whilst it is predicted that this number will double by 2030 [5]. Reasons for this could be attributed to global population growth and industrialisation in developing nations such as China and India. As a result, this increase in EVs poses a significant challenge to the automotive industry in terms of converting conventional vehicles into greener EVs whilst building an appropriate infrastructure. This in turn brings about a series of hierarchical challenges such as the consumer behaviour, meeting the electricity demand for recharging EVs and disposal and recyclability of energy storage devices [6]. If the current and historical trend continues to dominate the automotive market, i.e. employing conventional fuels such as diesel and petrol, then naturally a rise in GHG emissions and deteriorated air quality would be the result. Thus, there is a dire need for adopting vehicles with electrified powertrain as the solution.

The debate of battery electric vehicle (BEV) competing against FCEV is unreasonable. There now exists a consensus amongst fleet operators and academics that each technology has to be designated based on the application and user case. BEVs due to their unmatchable simplicity of operation and low component number are considered to be the most viable option for mobility solutions where short range is a requirement such as scooters, passenger and light duty vehicles. On the contrary, hydrogen fuel cell technology can be applied to mobility applications where high energy requirement is needed. For example, long range passenger vehicles, trucks, rail and heavy duty vehicles. Of course, every FCEV powertrain has to be hybridised with a battery pack in order to store and recuperate energy. Thus, a clear synergy of both technologies complementing each other is noticed currently.

1.1.2 GHG Emissions

According to a 'Mckinsey' report, approximately 83 % of CO_2 emissions are a result of combustion of fossil fuels [7]. The analysis concludes on seeing a replacement of ICE vehicles with full electrification by 2050, to tackle the current 75 % of all mobility GHG emissions from road transport. Furthermore, the three main culprits of the world's GHG emissions are coal, oil and natural gas [8]. In 2022, crude oil took the second position in emitting approximately 11.2 $GtCO_2$ equivalent, just next to coal in the first position of emitting 11.5 $GtCO_2$ equivalent (see Figure 1). While there were major pledges by leading economies in the 2015 Paris Agreement aimed at avoiding the further rise in global warming, 2022 recorded the fifth warmest year with

temperatures risen by at least 1.1 C since pre industrial times [9]. The biggest contributors are China, USA, India, Indonesia and Russia. Figure 2 displays graphically the historical comparison between the aforementioned nations in terms of GHG emissions. Although China currently heavily relies on coal for power, approximately corresponding to a 67 % share of fossil fuels based energy in electricity production, there are plans in the national climate target policy to achieve carbon neutrality before 2060 [10]. On the other hand, the USA being the second biggest emitter on an annual basis has passed a climate and tax legislation aiming to stimulate the green energy development, at the same time targeting to cut GHGs by almost half the 2005 levels by 2030. GHG emissions not only contribute towards global warming, but also deteriorate the air quality.

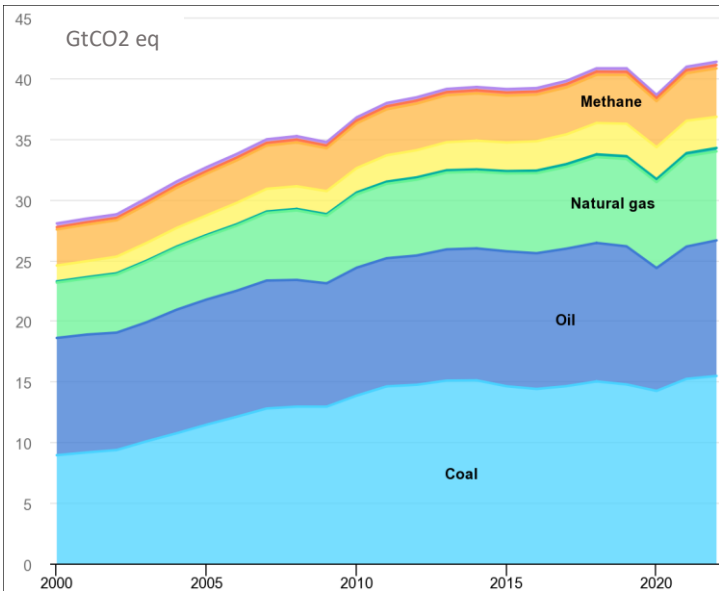


Figure 1: Global GHG emissions by fossil fuels from 2000 to 2022 [8]

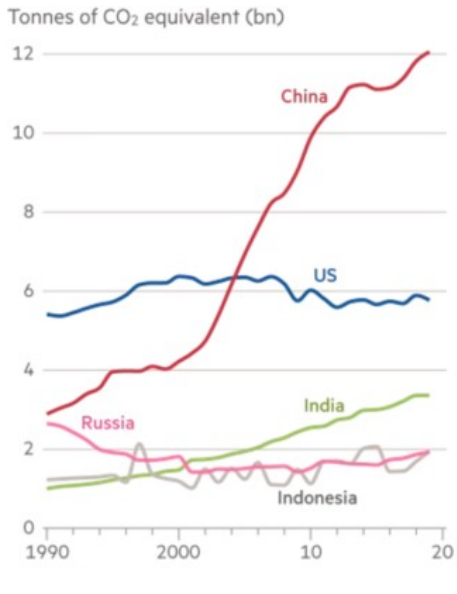


Figure 2: Graphically displays the historical top five emitters of CO_2 globally from 1990 onwards [10]

1.1.3 Energy Security

Security of supply is one of the essential pillars required for electrification, be it via BEV or FCEVs. The majority of the developed regions in the world still mainly rely on fossil based fuels in their energy systems. However, many of these developed economies, especially across Europe and US, are beginning to take initiatives towards making a gradual and long-term shift away from oil & gas. In particular, the rapidly growing renewables have offered an incentive as a solution towards this transformation. Specifically, these renewables sources include bioenergy, geothermal, hydropower, ocean, wind and solar. While most of these are seeing a gradual growth, wind and solar have seen rapid growth and development – mainly due to the declining cost which provide a good business case [11].

According to a recent report by the International Renewable Energy Agency (IRENA) [12], hydrogen as a fuel and energy vector could present itself as an energy disruptor, competing against the current energy mix. The last decade has noticed both an increased research and development activity. As a result of recent government policies globally, nations have conducted an increasing amount of innovation activities in hydrogen technologies and their value chain. This can be measured by observing hydrogen-related inventions in these regions, as illustrated in the form of flow of patents in Figure 3. Europe, Japan and the US take the lead on protecting inventions in the realm of hydrogen and its technologies, which revolve around fuel cells, hydrogen distribution, production and storage. Generally, this is

indicative of where there is scope for commercialisation. In addition, these are intended to cater for various markets such as energy, logistics, transport and industrial sectors. Although hydrogen technologies will not be cost competitive in the short term, the long term perspective could potentially be promising because of some key benefits. One of the most beneficial traits of hydrogen is that it can be produced at almost any location, provided there is a renewable source of energy. This, when considered in large-scale magnitude (in GW scale) can offer energy security for an economy which is currently subjected to fluctuations of fossil energy world trade prices. This topic is discussed in greater detail in the following chapter.

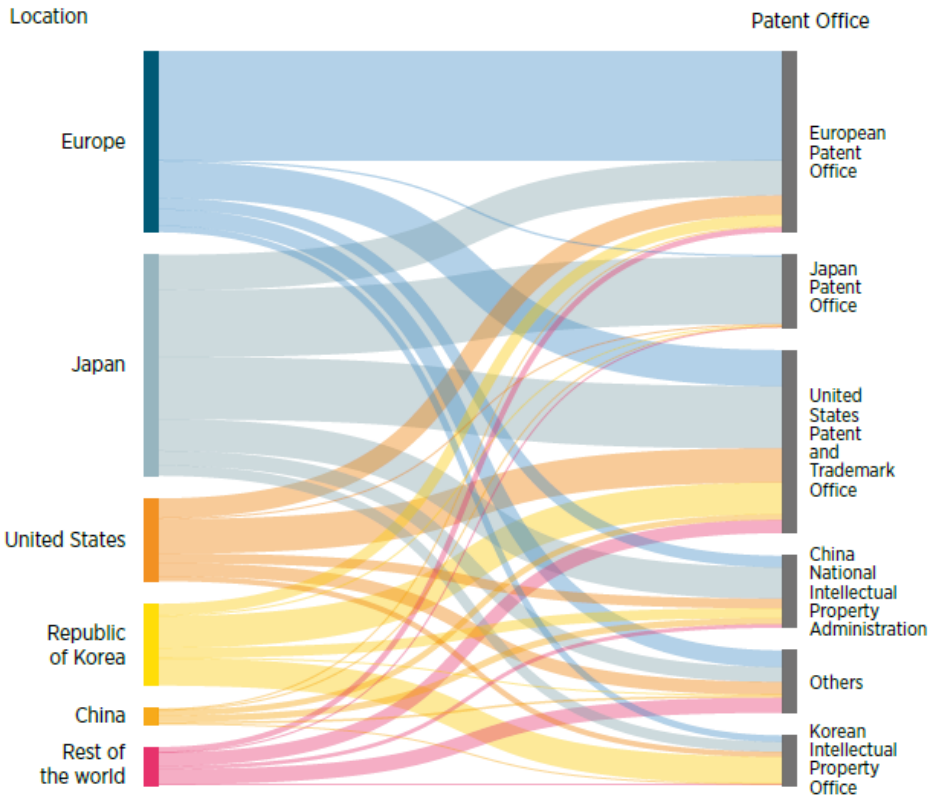


Figure 3: Invention flow as a result of R&D activity in the realm of hydrogen and its technologies between 2010 and 2020 [12]

Once produced, hydrogen can then be stored as gas for an indefinite duration chemically, or chemically in the form of other compounds, such as Ammonia, albeit

with substantial conversion losses. For this reason, experts and analysts are of the opinion that hydrogen conversion business has the potential to unlock cost competition [12].

The automotive industry is currently going through a major transition towards the electrification of vehicle propulsion powertrains. One of the main reasons for this can be attributed to reduction of the transport industry's reliance on fossil fuel based resources. In addition to global warming effect of greenhouse gas emissions from burning fossil fuels, limited resources and availability are also other drawbacks of fossil fuels. In the case of Europe, another major reason for the drive towards vehicle powertrain electrification is to rely less on the oil imports and showcase the technological improvements in the form of novel, pure electric powertrains. FCEVs are a good example which qualifies for zero tailpipe emissions, higher powertrain efficiency, longer drive range and short refuelling durations.

1.1.4 Challenges for Fuel Cell Vehicles

There have been immense developments in the recent years within the fuel cell hydrogen industry. In particular, the polymer electrolyte membrane (PEM) technology has seen great interest from leading industry players due to its applicability in various segments such as hydrogen production through electrolysers, and electricity supply to mobility through fuel cells. Despite these improvements there are still roadblocks preventing FCEVs from mass scaling and offering competiveness to other counterparts such as ICE and BEVs. The challenges

include cost, reliability of the stack, hydrogen supply, transportation and storage. However, of these challenges cost, storage and infrastructure continue to remain a hindrance in the upscaling of the hydrogen industry. Each of these three challenges is discussed in the following in more detail.

The cost of hydrogen fuel cells are, currently, expensive when compared to conventional or battery technologies. As of today, the latest generation of Toyota Mirai is commercially available with a price tag of $61,500. On the contrary, a Toyota Camry Hybrid is available for less than half of Mirai at $26,200. Moreover, a pure battery electric option such as Tesla with significant added values such as acceleration performance and semi-autonomous characteristics, but which much longer refuelling time, is priced at approximately $52,500. While it can be argued that the production rate of Mirai significantly differs from the other two options, the material costs of fuel cells remains high due to the need for platinum within in the membrane. The Toyota Mirai is reported to contain approximately 30 g of platinum in the fuel cell stack [13]. However, in the recent past the costs have been brought down thanks to the innovation and development in the electrocatalysts field leading to lower platinum loading of approximately 10g per 80 kW stack or 0.125 g/kW at rated power [14].

Although hydrogen has a high gravimetric energy density of 33 kWh/kg, its volumetric density is extremely low. Thus, traditional fuels such as petrol and diesel show ease of storage from a packaging. For storage on-board the vehicle, hydrogen

is compressed to high pressure range in order to store a desired mass for a pre-evaluated journey range. Liquefaction of hydrogen is also an emerging trend approaching within the automotive industry due to higher volumetric density capability. However, compression is by far the most prevalent method of storing hydrogen as a fuel on-board a vehicle and can be compressed to either a standardise pressure of either 350 bar or 700 bar pressurised vessels. Storage through compression is relatively efficient as liquefaction of hydrogen is energy intensive due to cryogenic temperature [15]. It is currently difficult for the emerging alternative fuels such as hydrogen to compete against conventional fuels without government subsidies.

Hydrogen infrastructure for consumers' use remains scarce and not well connected. This poses a challenge for fleet operators in terms of refuelling in between the routes, thus, discouraging wider adoption of hydrogen FCEVs for mobility. However, there are new government initiatives in developed economies to scale the hydrogen refuelling infrastructure to cater for long haul trucks and light duty vehicles. For example, the European Commission agreed to scale up the deployment of battery charging and hydrogen refuelling infrastructures [16]. For the latter, it is anticipated to have a wider deployment of refuelling stations at every 200 km in all urban nodes by 2030. Hence. this work aims to address the above challenges partly by undertaking the system integration and design optimisation, leading to economical and durability benefits.

1.2 System and Design Optimisation

An FCEV has an electrified powertrain which comprises of a fuel cell system as the primary and dominant power source while using an energy storage device as a secondary power source. The latter usually incorporates either a battery either pack or supercapacitor bank for automotive applications, in order to assist the fuel cell at times of peak power demand, as well as to store and recuperate energy. The multiple levels of control and management processes involved in such an electrified powertrain can be classified into two levels; low level system which manages the fuel cell system, and the supervisory level which encompasses the energy or power flow management.

The hydrogen fuel cell stack requires a system comprised of multiple sub-systems in order to function. This entire system is commonly known as the fuel cell balance of plant (BoP). The BoP has to deal with reactants supply, electrical conditioning of power and thermal management via heat exchangers. Underperformance in any of these sub-systems will have a direct effect on the overall system performance. This in turn will have an impact on the vehicle fuel economy or the running costs. Thus, any attempt to optimise and improve the low level control system could result in gains such as increased durability of the fuel cell stack, better fuel economy and cost savings.

Design optimisation refers to the sizing strategy of the power components within the powertrain. Over or under sizing these components will have an effect in the vehicle

performance. In the former case, this could result in increased costs, weight and volume, whereas in the latter case undersized power components will struggle to meet the transients, peak power demand, or complete the full range of the vehicle. This could also lead to enhanced degradation of the primary power source, resulting in lower operational hours or autonomy. Furthermore, it is imperative to have the energy management strategy (EMS) integrated and its operating strategy integrated within the design optimisation phase with the aim of taking realistic behaviour profiles into account. Most commonly, the EMS within the context of EVs would adopt either a charge-sustaining (CS), charge-depletion (CD) or the combination of the two strategies (CS-CD). These are applicable to both rule-based strategies (RBS) as well as model-based strategies such as model predictive control (MPC) which employ complex algorithms for optimality. The former is based on pre-defined rules from design experience or validation. RBSs have several advantages and shown good performance in commercial vehicles to date. Using these as the benchmark for further optimisation would allow a design engineer to benefit from realising the aforementioned gains. Moreover, the decisions made by the EMS will result in the desired split of the power flow from the different power sources for the traction requirements of the vehicle. Therefore, it is imperative that the EMS is integrated within the design study, with sufficient degree of complexity, to ensure that the achieved modelling results of the power components are realistic. Figure 4 below illustrates the different aspects of research work linked to fuel cell system and powertrain design optimisation. The research is focused between two key areas of

optimisation which have a direct impact on the overall system efficiency; the fuel cell system auxiliary control and the energy management strategy. In the former which can be referred to as 'system integration', the fuel and reactant gas supply and management are the key metrics whereas in the latter, 'design optimisation', the power flow between the fuel cell and the energy storage device is the focus.

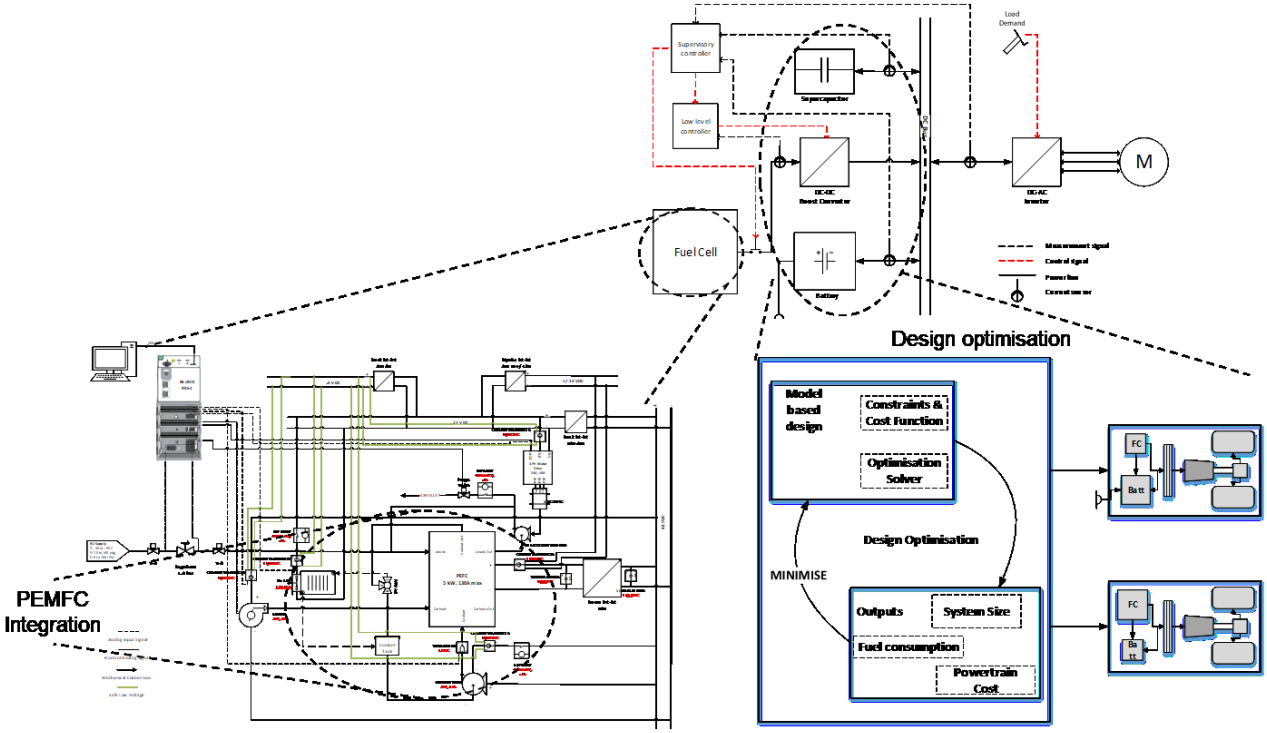


Figure 4: Research work visual compartmentalisation between fuel cell system and powertrain design optimisation.

1.3 Research Aims and Objectives

The hierarchical goal of this project was to undertake a holistic approach in the optimisation of both; the control and design of a FCEV hybridised with a battery pack. This research had an evenly split focus between the aforementioned optimisation aspects. Specifically, this included experimentally validated

optimisation techniques at a systems level within the fuel cell BoP and optimally sizing the power components through software modelling technique. The former required design and build of an experimental setup which offered an in-depth insight into system operation requirements in a laboratory-based environment, while the latter will used established methods of software optimisation based on a selected set of boundary conditions.

The following specific objectives were identified;

- Design and build of a 5kW PEMFC system with bespoke balance of plant enabling robust testing and validation.
- Experimental optimisation of the PEMFC system, specifically the anode hydrogen purging.
- Construction and implementation of detailed vehicle model to be used with an integrated rule-based and an optimisation-driven control strategies.
- Design optimisation of the fuel cell battery hybrid propulsion system via dynamic programming with the aim of optimal components sizing
- Evaluation and identification of the potential improvement to the already implemented fuel cell system, modelling and optimisation.

1.4 **Thesis Structure**

In this thesis, chapter one provides an introduction specifying the research aims and objectives along with an overview of the research topic. Since the thesis covers experimental and modelling aspects, the literature review is integration into the

respective chapters, beginning from chapter 4. The content of the following chapters is as follows:

Chapter 2 – Electrification through Hydrogen begins with the technical introduction of hydrogen fuel cells highlighting fundamental basis. These include theoretical principle of operation, construction and components that make up a fuel cell stack. The classification of electric vehicles, along with different powertrain architectures are showcased. Additionally, challenges such as low carbon hydrogen production and on-board hydrogen storage systems are discussed in this chapter. Finally, a comparison between the two most applicable energy storage technologies, battery and supercapacitor, is presented in the last segment of the chapter.

Chapter 3 – Experimental Work discusses the practical implementation of the design and build of a 5 kW polymer electrolyte membrane fuel cell system. Each sub-system's responsibility and tasks are described in detail. The development process of emulating a real system within a laboratory test bench is presented. This includes the instrumentation needed for safety, data sensing and logging and software to hardware interface for the control mechanism. Finally, the entire system processes used for experimentation in the subsequent chapter of the thesis will be explained.

In **Chapter 4 – PEMFC System Control** the implementation of the system control is carried out with the aim of conducting experimentation. Specifically, the fuel cell system's reactants gas management strategy is described and a novel anode purging

strategy is experimentally validated. Literature review on the topic is covered in the initial segment of the chapter. The rationale and process behind the strategy is discussed in detail. Finally, results of the purging strategy and the performance of the built system in chapter 3 are illustrated and scrutinised.

Work in **Chapter 5 – FCHEV Modelling and Simulation** undertakes the modelling and simulation study of a fuel cell vehicle hybridised with a battery pack. The chapter starts with a literature capture of previous work on rule-based control strategies, followed by conducting an analysis on two distinct drive cycles. An in-depth explanation of the model architecture build in AVL Cruise Software environment is provided. In addition, the chapter uses Toyota Mirai as the benchmark vehicle to analyse the developed model's behaviour.

The **Design Optimisation** topic is split into two chapters, **Chapter 6 and Chapter 7,** discussing strategy and implementation, respectively. The former chapter includes a literature review of the relevant work on the topic and description of the optimisation strategy developed in this work, based on chosen set of assumptions. The chapter introduces dynamic programming theory and its usage towards formulating an optimisation study. In the subsequent chapter, the devised sizing strategy is implemented and results are analysed with two control strategies integrated: charge-depletion and charge-sustaining.

The final **Discussion** chapter of this thesis summarises the conclusions of each chapter in a concise and succinct manner. In addition, further work with an aim to improve and refine the obtained results is proposed.

2 Electrification via Hydrogen

Hydrogen as an energy carrier is bound to be a promising fuel for various segments in almost all of the developed and emerging economies. Especially, in the mobility sector due to several advantages such as zero tailpipe emissions, competitive total cost of ownership post 2030, capability of offering longer range and forming a circular economy for rural applications. While hydrogen as a fuel has a superior energy density by mass compared to other fuels, the volumetric density of the fuel is considerably low. Thus, a targeted approach in the utilisation and implementation of this technology should be considered in order to establish a working business case. As such, major car manufacturers have taken the initiative to demonstrate the applicability of hydrogen technology in the automotive sector. Currently, several challenges remain and have hindered the uptake of this technology. Specifically, these include the low cost and low carbon production of hydrogen fuel with the aim of offering competitiveness with conventional fuels, and increased volumetric density of the on-board hydrogen storage systems.

In this chapter, an overview of the working principle of hydrogen fuel cells and hydrogen production via various pathways is discussed. Additionally, the chapter describes the classification of electric vehicles (EV), powertrain architectures and comparison between battery and supercapacitor technologies.

2.1 **Hydrogen Fuel Cells**

Polymer electrolyte membrane fuel cells (PEMFCs) electrochemically convert the chemical energy present in the fuel directly into electrical energy. Specifically, the hydrogen fuel is supplied into the fuel cells from the anode side and oxygen from the cathode side. Hydrogen is then oxidised into protons and electrons at the anode catalyst. The Nafion membrane is proton conducting and electronically insulating. As a result, the electrons are compelled to leave the anode side and pass through an external circuit in order to reach the cathode side, where the oxygen reduction reaction takes place [17]. The by-products of this reaction are heat and water, with no local carbon emissions, making PEMFCs zero-emission power. In addition, hydrogen fuel cell systems offer several superior features over conventional power systems such as high efficiency and power density, as well as low maintenance requirements and noise levels [18]. Fuel cell systems appear to be a viable alternative to traditional internal combustion engine or turbine power generators, linking with renewable energy sources to provide a sustainable energy system. However, in addition to the clear environmental benefits, fuel cells must also prove that they are a reliable and cost competitive alternative to the incumbent technologies. This will require fuel cell systems to have a compact design which can match the current requirements, especially in the automotive sector.

There are six different types of fuel cells, of which only four are widely commercially available at present. Hydrogen fuel cell systems offer numerous advantages over battery technology. These include higher efficiency, power density, scalability, indefinite electricity output provided there is fuel supply and lower power-to-weight ratio.

2.1.1 Fuel Cell Operation

There are mainly two chemical equations that describe the operation of a fuel cell. These equations are explained below. To fully understand the operation of hydrogen fuel cells the structure of the fuel cell must be considered. At anode, the hydrogen fuel is oxidised which in turn releases electrons and produces H^+ ions as shown in the equation below.

$$2H_2 \rightarrow 4H^+ + 4e^- \tag{2-1}$$

This reaction being an exothermic reaction releases energy in the form of heat. Furthermore, at the cathode oxygen reacts with the electrons acquired from the electrode and H^+ ions from the electrolyte to form water, as seen in the equation below.

$$O_2 + 4H^+ + 4e^- \rightarrow 2H_2O \tag{2-2}$$

Thus, the overall reaction which takes place in a hydrogen-air based fuel cell becomes;

$$2H_2 + O_2 \rightarrow 2H_2O + \text{heat} \quad (2\text{-}3)$$

There are other types of fuel cells that exist that are not as dominant currently as PEMFCs. These include alkaline (AFC), direct methanol (DMFC), phosphoric acid (PAFC), Molten carbonate (MCFC) and solid oxide fuels cells (SOFC). The aforementioned fuel cells are mainly distinguished based on the electrolyte material and operating temperature. In addition, the application for each type can generally be categorised as stationary or mobile application due to the system volumetric density and the auxiliary components required for safe operation (also referred to as the balance of plant).

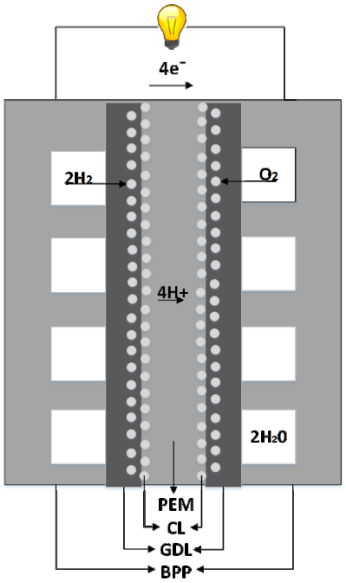
Table 1: Four commercially available different types of fuel cells with their characteristics.

FC Type	**AFC**	**PEMFC**	**SOFC**	**MCFC**
Electrolyte	Aqueous KOH solution	Solid polymer	Ceramic solid such as ZrO_2	KCO_3
Temperature [^oC]	<100	60-100	600-850	650-700
Fuel	Hydrogen	Hydrogen	Natural gas, hydrogen, coal gass	Natural gas
Mobile ion	OH^-	H+	O^{2-}	CO_3^{2-}
Bipolar plates	Ni coated	Graphite, coated stainless steel	Ceramic, stainless steel	Coated inconel

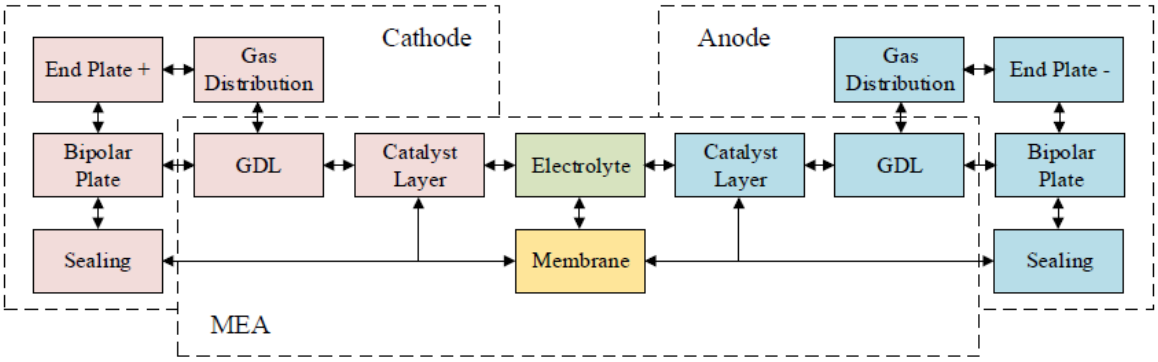
2.1.2 PEMFC Components

The polymer electrolyte membrane (PEM) fuel cell type of fuel cell consists of several layers of different materials. Each layer has a distinct function to contribute in the

operation. The PEM membrane, which is also considered as the heart of the fuel cell, is responsible for conducting protons and blocking electrons. The membrane material that is generally made from perflourosulphonic acid (PFSA), which is chemically based on polytetrafluoroethylene (PTFE), contains hydrophilic and hydrophobic regions. Furthermore, hydration of the membrane is a requirement for the transport of H+ ions. In addition, hydration has a strong influence on membrane conductivity. Normally, the conductivity increases by almost seven times when there is the membrane humidity level is increased from 10 % to 100 % [5]. The catalyst layer acts as an interface for the reaction to take place. The layer is generally made up of porous carbon support to which small platinum particles, typically of o size 2 to 3 nm, are loaded or dispersed onto. It should be noted that different loading proportions are used on anode and cathode sides, since the former, where the hydrogen oxygen reaction takes place has very high activity whilst the latter, where oxygen reduction reaction takes place has significantly lower activity. The main reason for using such nanoscale (0.2 mgPt/cm2 and 0.05 mgPt/cm2) loading is the high cost of Platinum. A labelled diagram of different layers, highlighting electron flow and microchannels, is illustrated in Figure 5a below. Figure 5b illustrate a block diagram of all the components and their interactions with each other.



(a)



(b)

Figure 5: Hydrogen fuel cell components, a: graphical representation of the cell within a stack, b: block diagram representation of FC components. PEM: polymer electrolyte membrane, CL: catalyst layer, GDL: gas diffusion layer, BPP: bipolar plate and MEA: membrane electrode assembly.

2.1.3 Hydrogen Production

One of the greatest advantages of hydrogen is that it can be produced from almost all primary energy sources, through either a chemical transformation process or electrolysis using electricity. The former category generally occurs in central large scale facility whereas the latter can also occur in a distributed facility. Low carbon production of hydrogen is possible through various methods. These include

conventional methods based on fossil fuels but with sequestration process (also referred to as carbon capture and storage). A well-to-tank (WTT) analysis of a particular fuel is generally a good methodology to calculate and compare GHG emissions. A report published by the Joint Research Centre under the EU Commission presents the emissions the hydrogen pathways as well as the WTT emissions [19]. The report allows for scrutinising the upstream and downstream emissions related to different hydrogen production pathways.

Hydrogen is also claimed as the fuel which could act as the facilitator of the integration of the various sectors of the energy system. Hence, maximising the decarbonisation effort requires low carbon hydrogen production considering the full life cycle analysis. There are multiple types of hydrogen production pathways which are defined based on the intermediate processes involved and carbon footprint [20]. Currently, most of the global hydrogen production is achieved through steam methane reforming (SMR) using natural gas [21]. This method of hydrogen production is commonly referred to as 'grey hydrogen', where CO_2 is released into the atmosphere. If, in this process, the CO_2 is captured and permanently sequestrated then the hydrogen production pathway is called 'blue hydrogen'. Furthermore, electrolytically produced hydrogen using renewable electricity such as solar and wind is classed as 'green hydrogen'. Other shades of hydrogen include 'turquoise hydrogen' which involves a methane pyrolysis process that generates carbon in a solid form and 'pink hydrogen' which utilises nuclear energy for water

electrolysis. Figure 6 below displays the different colours or shades of hydrogen production which are generally used as a reference in the industry.

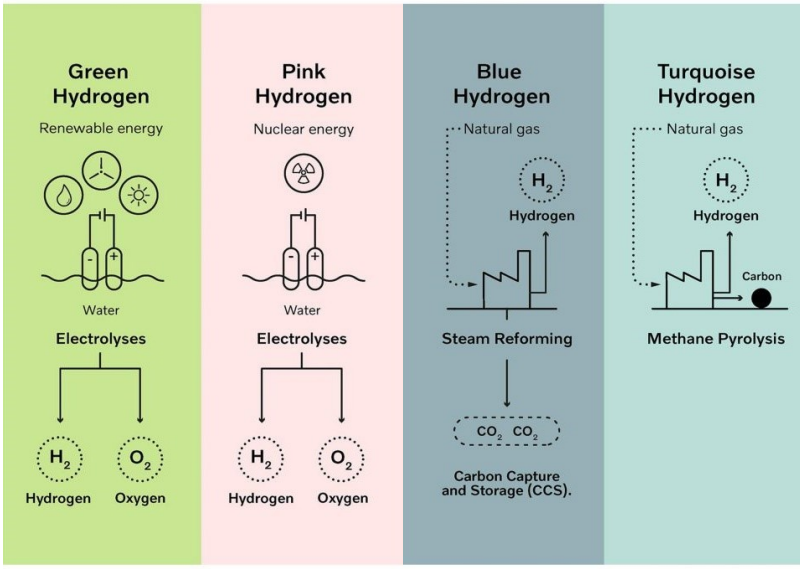


Figure 6: Different shades of hydrogen based on the source and process of production [20].

The UK government was one of the first globally to release a standard for the definition of low carbon hydrogen [22]. The document is meant to provide various industries guidance on the GHG emissions criteria when considering the production and usage of hydrogen. A general method of calculating the emissions within the scope 1 and 2 of the production process was expressed as below.

$$E_T = E_{feedstock\ supply} + E_{energy\ supply} + E_{input\ materials} + E_{process} + E_{fugitive\ non\text{-}CO2} + E_{CCS\ process\ \&\ infrastructure} - E_{CO2\ sequestration} + E_{compression\ and\ purification} \quad (2\text{-}4)$$

The standard takes into account considerations towards the supply of the feedstock, energy utilised in the form of electricity or heat, extraction of raw materials, energy for carbon capture and storage or sequestration as well as compression for storage. According to the UK's National Grid [23], hydrogen can lead the way in meeting the

net zero targets by contributing towards the whole energy system, as well as in the hard to abate sectors such as industries like steel industry. Figure 7 demonstrates the carbon emissions for each shade of hydrogen production. It can be seen that green, blue and pink hydrogen are below the UK low-carbon hydrogen limit while hydrogen produced from biomass combined with carbon capture even contributes towards negative emissions.

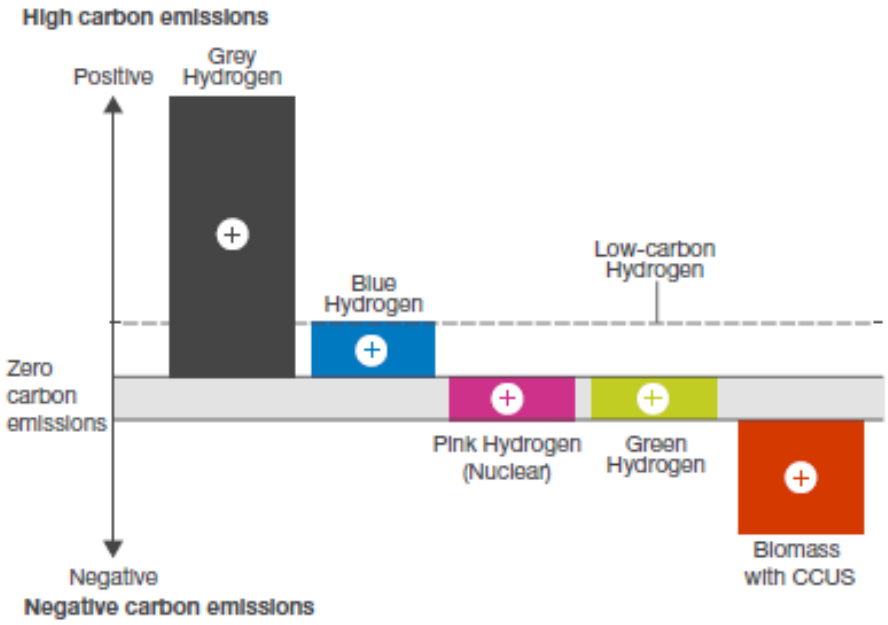
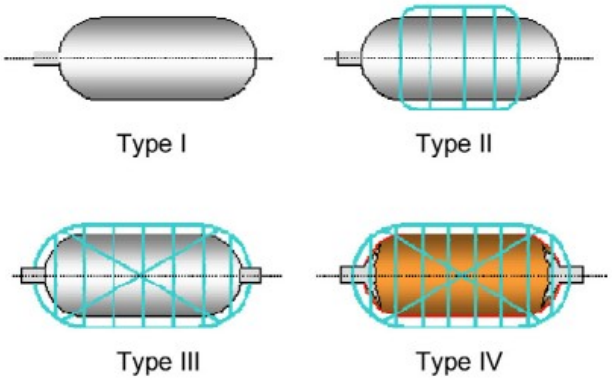


Figure 7: Carbon emissions for different shades of hydrogen, highlighting the low carbon hydrogen threshold [23].

2.1.4 On-board Hydrogen Storage

Hydrogen storage on-board a vehicle is critical and presents several challenges. So far, the preferred and most established method of storing hydrogen as a fuel in the automotive industry has been compressed hydrogen storage tanks. This method involves physical storage of hydrogen gas inside a high pressurised vessel. These vessels in the industry are classified into four different types; type I, type II, type III

and type IV (see Figure 8). The pressurised vessels are generally cylindrical in shape with different material and layering based on the classification. Type I storage vessels are all-metal material and are the heaviest of all categories, allowing up to a maximum of 50 MPa pressure. Type II vessels are similar to type I except there is an additional layer of glass fibre composite which allows for higher hydrogen content in the vessel, while having relatively lower tank weight. The metric, generally, used for this measure is the hydrogen fraction of the tank system, wt%. Type III compressed storage vessels are made of composite materials with aluminium liner around which carbon fiber is wrapped. Type III tanks have a tank density of approximately 4.2 wt % capable of storing at 70 MPa pressure. Type IV vessels are similar to Type III but have an additional layering with plastic liner which acts as the hydrogen permeation barrier and carbon fibre glass for structural load bearing (epoxy material), which enables this type of vessels to reach pressures higher than 70 MPa [24]. A concise summary of each type of compressed storage technology is presented in Table 2.



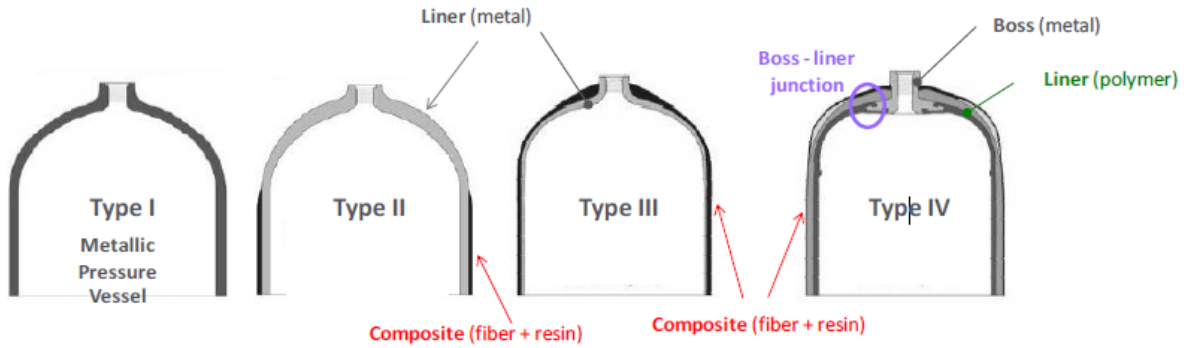


Figure 8: Different types of compressed hydrogen storage tanks and their manufacturing procedures [24].

Table 2: Summary of different types of on-board hydrogen storage vessels

	Type I	**Type II**	**Type III**	**Type IV**
Components	All metal construction	Steel Vessel with Glass fibre composite	Full composite overwrap with Metal (Aluminum) liner	Full Carbon-fibre or Carbon-glass composite with HDPE liner and metallic boss
Structural Load	Metal body withstands the whole load	Steel and composite materials share the load equally	The composite structure bears the most load, and the metal liner takes only about 5% mechanical load	Composite material carries the load
Storage Pressure	Up to 50 Mpa (500 bar)	Highest pressure Tolerance (similar to type I)	Up to 70 MPa (700 bar)	Up to 1000 bar
Gravimetric density	~ 1 wt%	< 2.1 wt %	< 4.2 wt%	4.4 – 5.7 wt%
Weight	High	30-40% less than type I	Half of type II	Lighter than type III
Cost	Low	Low	High	High

2.2 Electric Vehicles Classification

An EV consists of a powertrain which uses at least one electric motor for propulsion [25]. There are mainly two types of EVs which are classified on the basis of source(s) of propulsion and electrification level of the powertrain; hybrid electric vehicles (HEV) and pure electric vehicles (PEV). Figure 9 below illustrates a generic classification of EVs. By definition, fuel cell electric vehicles (FCEV) consist of a hybrid powertrain as they mostly include a battery and/or supercapacitors together with the fuel cell system. HEVs can then be further generally classified into four; micro-HEV, mild-HEV, full-HEV and Plugin-HEV (PHEV). Conversely, PEVs come in two forms; battery electric vehicle (BEV) and fuel cell electric vehicle (FCEV) [25]. The FCEV can be further classified into three; hybrid, plugin and range extender (REx) FCEVs. Furthermore, HEV and PEV have in them several strategies to save fuel, reduce emissions, extend vehicle range or ability to recharge the battery.

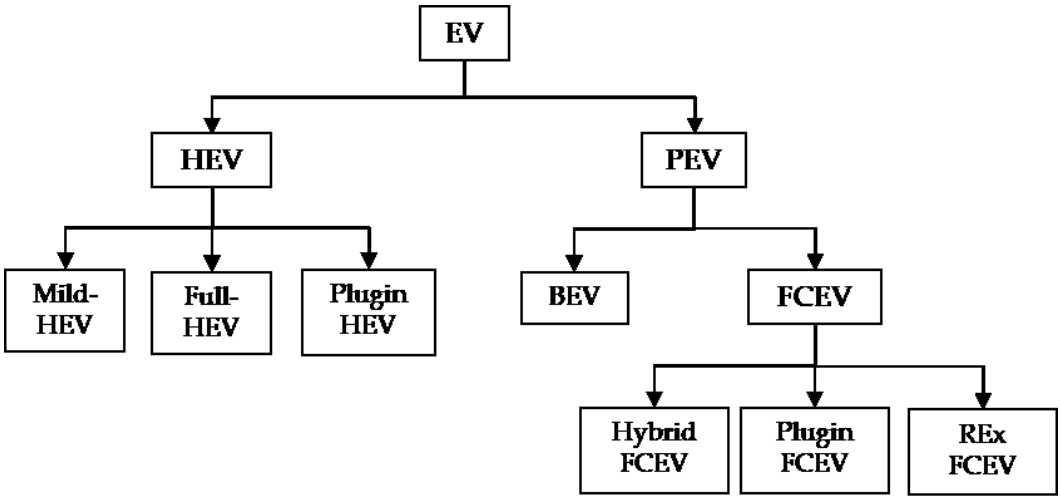


Figure 9: Electric vehicles classification.

Table 3 summarises the specific technical terms in the literature and EV industry standard. Idle-stop or stop-start is when the vehicle's ICE is turned off when the vehicle is at a standstill position. Power assist is when the electric motor in both types of EVs supplies propulsion in parallel to othe main power source, or also alone. Furthermore, regenerative braking is common in EVs with fairly large energy storage devices. Pure electric vehicle drive occurs when the propulsion from a hybrid powertrain is solely provided by a secondary source such as the battery pack. The plug-in option offers provision for the battery to be recharged from an external electricity supply.

Table 3: Classification and characteristics of EVs.

	Micro HEV	Mild HEV	Full HEV	PHEV	PEV
Stop/Start	⊙		-	-	-
Power assist		○	⊙	⊙	-
Regen-Braking		○	⊙	⊙	⊙
PEV Drive				⊙	⊙
Plug-in charge				⊙	⊙
Voltage	12	48+	300+	300+	300+

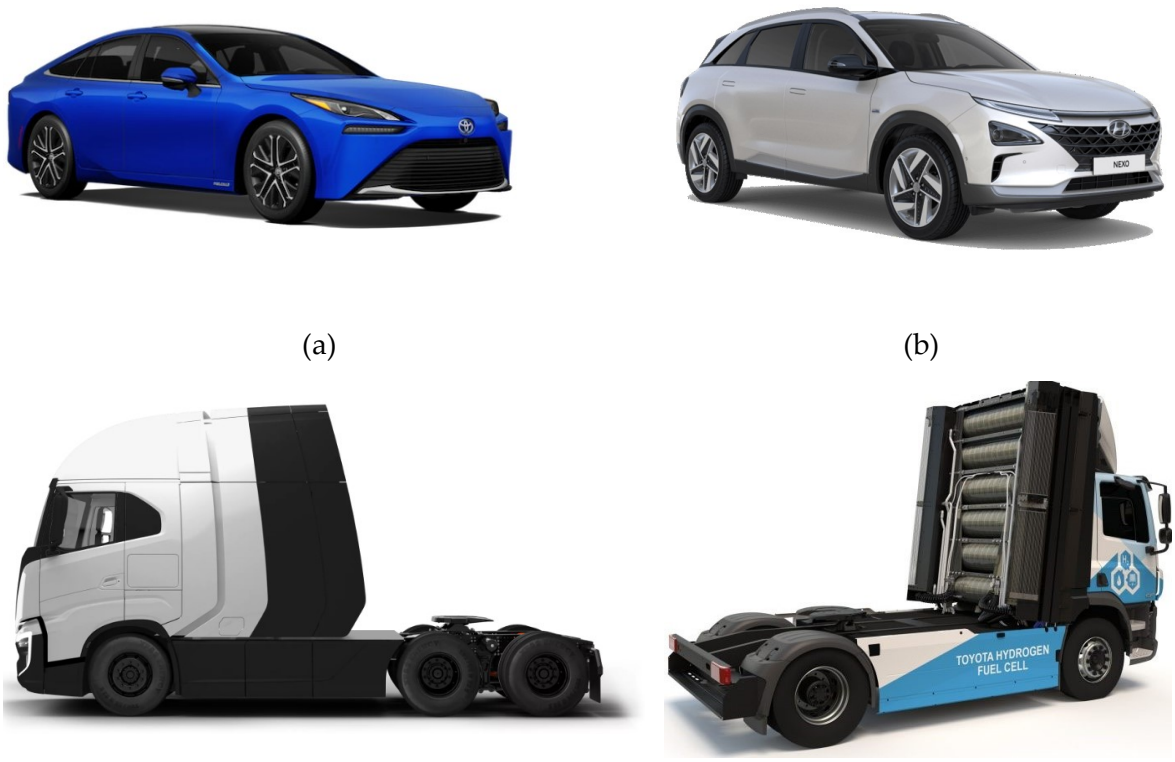
⊙: full capacity, ○: partial capacity, -: not applicable

2.2.1 Commercial FCEVs

Within the past two decades several automotive manufacturers showcased at least one concept FCEV. These include, amongst others, key players in the industry such as Toyota, Hyundai, Honda, Daimler, General Motors and BMW. Although, the

hype of hydrogen powered vehicles initiated from the passenger vehicle sector, the trend currently is also gaining momentum from the long haul and heavy duty trucks sectors [26], [27]. The primary reason for this shift can be attributed to the already existing market share and powertrain simplicity of the BEVs in the passenger vehicle industry. In addition, pure battery powertrain in the heavy duty industries is not technically feasible due to extremely low gravimetric energy density of batteries [28].

Figure 10 a & b display the second generation of Toyota Mirai and Hyundai Nexo which are currently commercially available in passenger vehicle industry for consumer use, respectively. Buyers of such vehicles can benefit from various incentives including free refuelling for a certain period of time after purchase. Figure 10 c & d display the examples of FCEV technology in the long haul truck industries offered by Toyota and Nikola respectively. Both on-board storage and refuelling infrastructure remain a challenge for trucks as the high power requirement means a large volume of storage system which may be constrained due to packaging requirements, especially with 350 bar pressurised vessels. The lack of refuelling stations has hindered the market take-off by various fleet operators. However, the infrastructure is currently being ramped in European regions.



(a) (b)

(c) (d)

Figure 10: FC technology adoption in passenger car and long haul truck industries. a: Toyota Mirai, b: Hyundai Nexo, c: Nikola TRE FCEV truck d: Toyota FC logistic truck.

2.2.2 Powertrain Architectures

The powertrain architectures in an FCEV can take various forms based on the number of power sources, their placement and sizing. A topology relying solely on a fuel cell for propulsion while having no energy secondary power source is called pure FCEV (see Figure 11a). This architecture presents several disadvantages such as lower fuel economy due to the stack operating at inefficient points, absence of braking energy recuperation and enhanced fuel cell degradation [29]. The most common topology, which is widely adopted in various industries, hybridises the fuel cell with an energy storage device, illustrated in Figure 11 b and c. Such a topology mitigates the disadvantages seen in a fully fuel cell architecture. The energy storage

system (ESS) incorporated could either take the form of a battery or supercapacitor pack. The former is the most common solution primarily due to relatively lower costs. In addition, the combination of both battery and supercapacitor within a fuel cell dominant powertrain is seldom seen and known as fuel cell tri-hybrid vehicle (shown in Figure 11 d).

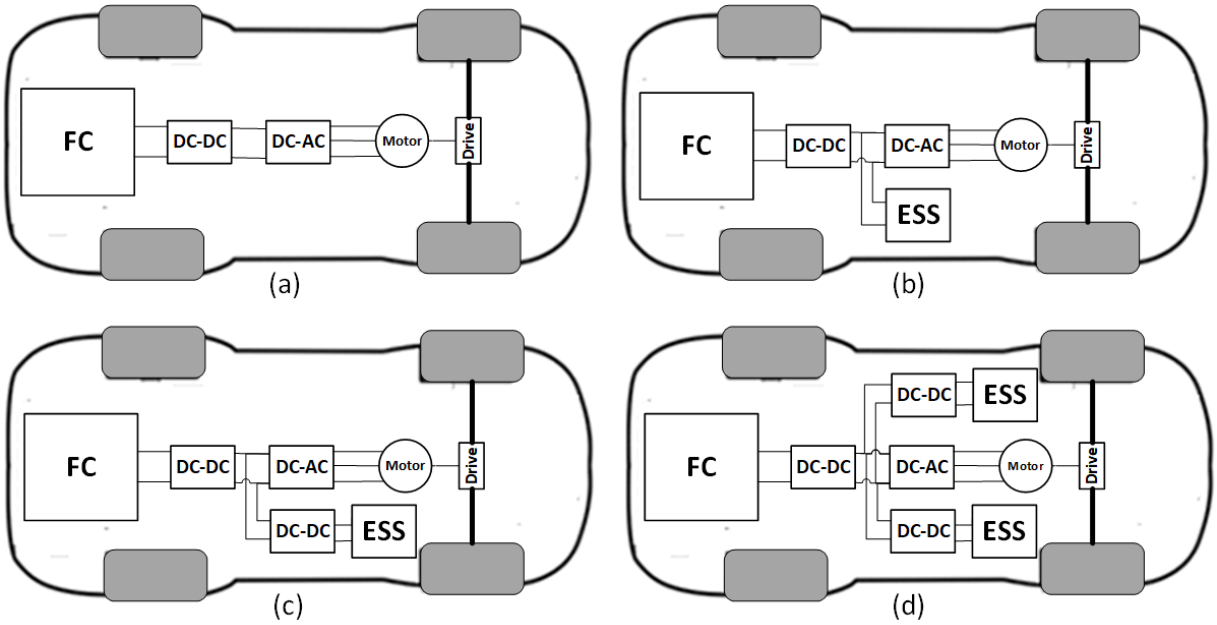


Figure 11: Different topologies applicable in an FCEV, a: standalone FCEV, b: fuel cell hybrid electric vehicle with passive control over ESS, c: fuel cell hybrid with active control over ESS and d: fuel cell tri-hybrid with active control over both ESSs.

The sizing of an FCEV can take place in three categories; hybrid, plug-in hybrid and range extender. In the hybrid architecture, the FC stack is dominant in power contribution and its size is significantly larger than the battery pack – which is used for transient peaks and energy recuperation. The plug-in hybrid option incorporates a large battery pack which can be recharged externally using the grid electricity. The rationale behind such an option is to consider the economic aspect based on the consumer prices of hydrogen gas and electricity at the refuelling or recharging

stations. The range extender architecture employs a small fuel cell, configured to maintain the relatively larger battery energy content.

2.3 Energy Storage Systems

A key component of a FCHEV is the energy storage system (ESS) which usually takes form of a battery or supercapacitor. The ESS is responsible for not only recuperating and storing energy, but also for supplementing the FC system in meeting the transient and peak power demands. Each of the aforementioned ESS technologies is discussed in detail in the following sections.

2.3.1 Batteries

There are a number of energy storage technologies, which can be used to supply and store energy on board. The system design of a propulsion system takes into account the selection criterion of an energy storage device based on several aspects such as cost, lifecycle, performance and size. Modern battery technologies have seen significant improvement in terms of cost, density and performance. Currently, there are three types of chemistries widely adopted within the automotive industry; lead acid, nickel metal hydride (NiMH) and lithium ion batteries. Almost all of the conventional vehicles use lead acid batteries for starting, ignition and lighting, while having a nominal cell voltage of up to 2 V. This type of battery chemistry, however, offers poor active mass utilisation and less favourable charge-discharge cycles which limits the practical energy content. NiMH chemistry played a role in the early years of EV industry offering a nominal cell voltage of up to 1.2 V with gravimetric and

volumetric energy densities of 80 Wh/kg and 250 Wh/L, respectively [30]. However, the coloumbic and energy efficiency of NiMH batteries are lower than even lead-acid batteries. For this reason, the emerging trend is a shift towards Lithium-ion batteries which have energy contents of up to 260 Wh/kg and 700 Wh/L with significantly higher Columbic (99%) and energy (up to 95%) efficiencies[31]. In addition, one of the main advantages of this battery chemistry is the possibility of having a vast range in the power to energy ratios when designing different powertrain architectures [32]. These improvements achieved in the battery technology were derived through innovation within the cathode chemistry which came as a result of the requirements from various sectors, through multiple generations as depicted in Figure 12.

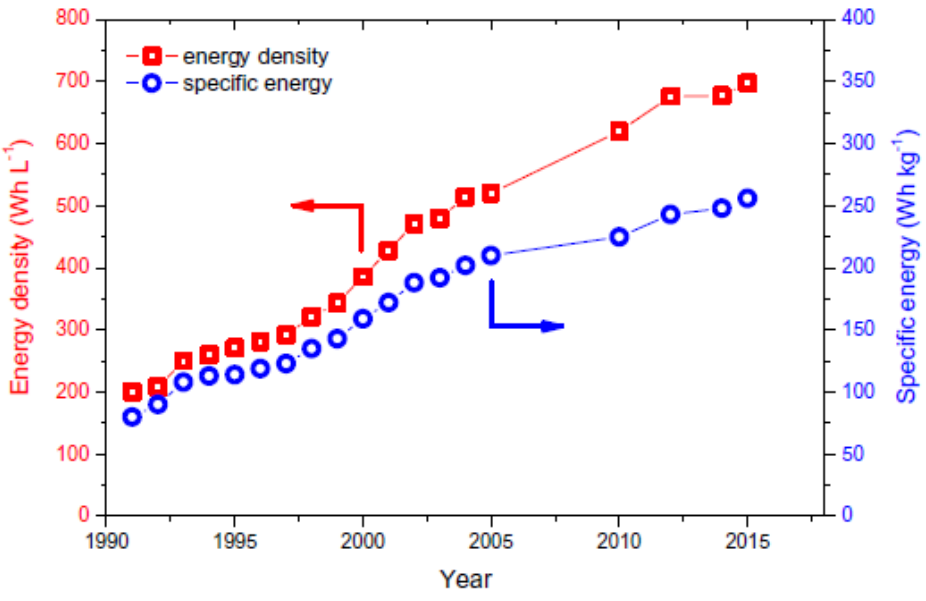


Figure 12: Gravimetric and volumetric energy densities evolution of Lithium-ion battery chemistry since 1990 to 2016 [31].

Additional key parameters in the selection of a particular battery chemistry are the discharge and charge rates (C-rate). In the context of automotive application, the former parameter plays an important role in the propulsion of the vehicle during acceleration, where the electric motor requires a surge of current. A high discharge C-rate allows for more power release from the battery pack. On the other hand, the charge C-rate of plays an important role when the battery is recharge during events such as regenerative braking and deceleration when the kinetic energy is recovered. Figure 13 depicts the disparity between the discharge and charge characteristics of a Lithium-ion Nickel Manganese Cobalt (NMC) high voltage battery pack (rated power of 110 kW for 18 seconds, with energy content of 14.1 kWh) integrated in Audi A6 PHEV [33]. It can be noted that the peak discharge C-rate of the battery equals approximately 8C, whereas the charge C-rate is almost half of the discharge figure. Conversely, in a HEV powertrain architecture, where the battery acts as a secondary device, the C-rate values are significantly higher due to higher power-to-energy ratio. For example, in the new generation of Toyota Mirai, the discharge C-rate for the Lithium-ion battery is 26C for a capacity of only 1.2 kWh.

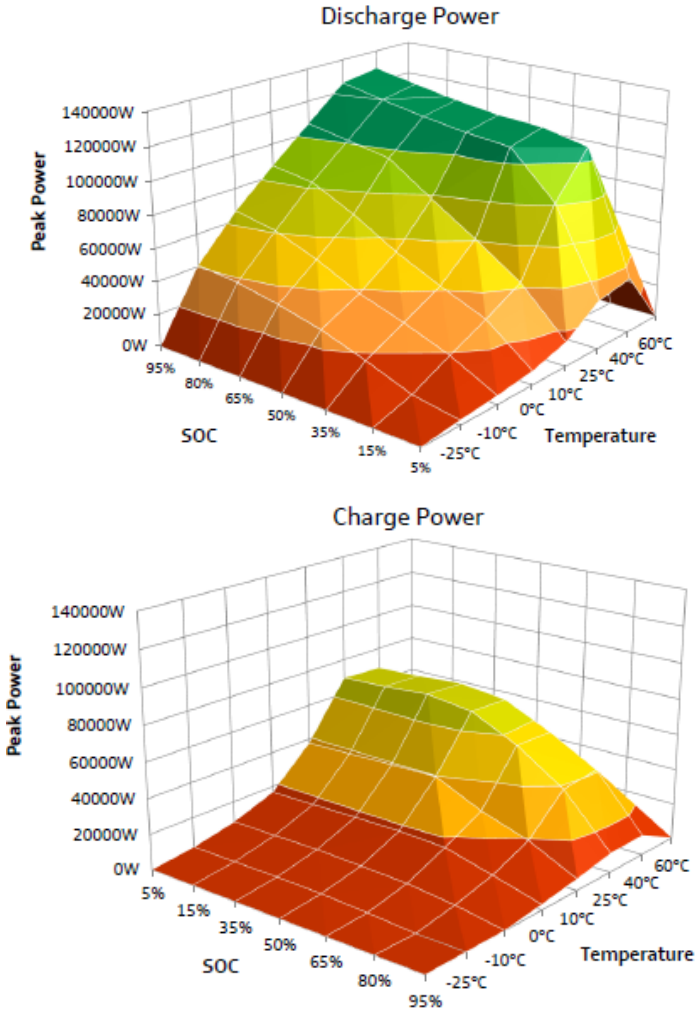
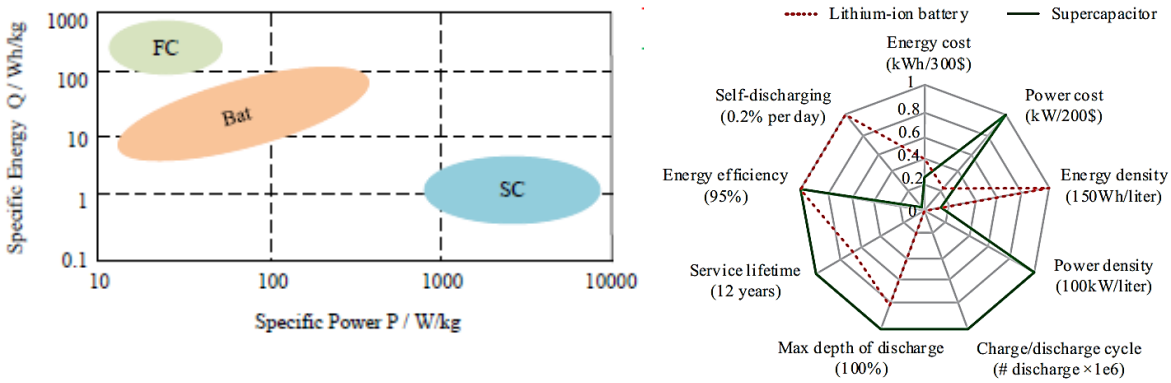


Figure 13: OEM integrated in Audi A6 PHEV high voltage battery discharge and charge power as a function of SoC and temperature [33].

2.3.2 Supercapacitors

Supercapacitors work on electrostatic principles with no chemical reactions and no internal moving parts. They avoid the lifetime issues associated with chemical storage of batteries or mechanical issues associated with fly wheels. The emerging and widely adopted type in the automotive application is electric double-layer capacitors (ELDC), commonly known as supercapacitors. They offer millions of charge and discharge cycles, higher efficiency due to low resistance and high power density. EDLCs, when compared to conventional capacitors, are technically capable

of storing up to a 100 times more energy per unit mass. Another category of supercapacitors are pseudocapacitors which involve reversible and fast Faradic redox reaction for charge thereby increasing the capacitance. In other words, this type of capacitor stores charge through a Faradic process involving the transfer of ions electrostatically. Pseudocapacitors incorporate metal oxides, metal-doped carbon and conductive polymer electrode materials which offer relatively higher capacitance and lower ESR and costs than EDLC type [34]. Figure 14a displays a comparison between various energy storage technologies applied on automotive application, highlighting the superiority of FC and batteries in terms of energy density per unit mass compared to supercapacitors. On the contrary, EDLCs have superior characteristics in terms of gravimetric power density. Furthermore, Figure 14b displays a techno-economic comparative summary of Lithium-ion and EDLC technology.



(a) (b)

Figure 14: Comparison of automotive energy storage technologies, a: Ragone plot depicting specific power vs specific energy, b: techno-economic comparison between Lithium-ion and EDLC energy storage systems [35].

3 Experimental Setup

A laboratory-scale test rig was designed and built for conducting experimental studies. A low temperature fuel cell stack procured from Ballard was repurposed for testing environment. This test rig involved construction of a 5 kW PEMFC system with bespoke Balance of Plant (BoP), which is responsible for gas supply, electrical and thermal management. Each subsystem was designed and programmed in order to realise various objectives. Where appropriate, some of the components were treated as 'black boxes', enabling simplicity. A number of components, such as the controller, sensors and converter, within the rig were either recalibrated or reconfigured upon procurement for enhanced accuracy purposes. The software-hardware interface selected was state-of-the-art and versatile, which can enable hardware in the loop (HiL) testing different settings. A robust embedded controller was used to control and run the system with fast processing power. The software architecture included reliable data monitoring and logging techniques within a sophisticated software programming system.

In this chapter of the thesis, details of the entire experimental setup involving physical systems integration, hardware interface and software programming are presented. It must be noted that the components' selection criteria did not take into account strict constraints such as cost, accuracy or size. Thus, imperfection in the context of system performance are bound to appear. Furthermore, the ambition

behind the system design and build must be emphasised, which was for testing purposes. In addition, the capabilities highlighted in this report are non-exhaustive, and thus encouraging of further improvements and studies.

The structure of this chapter begins with describing the complete FC system design and build phases. Where applicable, a detailed level of instrumentation and wiring diagrams presented for the appropriate sub-system.

3.1 **Fuel Cell System**

The fuel cell system consists of the stack and the four main sub-systems. These are cathode, anode, thermal management and electrical sub-systems. Each of these has different responsibilities but are inter-dependent. In other words, for a stable output from the system, all four sub-systems play an imperative role with constant communication with each other. The hydrogen storage employed was a passive storage system procured from an industrial supplier. Thus, monitoring the fuel storage level was not possible. The power is generated by stack with the help of the BoP as auxiliary components are needed for safe system operation. The system is controlled by the software from a computer with the aid of multiple communication protocols via an embedded controller (also referred to as the FC controller). Measurement signals can be monitored and recorded for further analysis based on a user-specified sampling rate. Where applicable, calibration of the components was performed in order to reduce excess or unsafe use. Moreover, safety procedures were adopted to avoid electrical faults, gas leaks and miscommunication between

subsystems. For example, hydrogen leak detection devices were installed near anode inlet and outlets.

The key stage of the design phase is the system integration. Where applicable, rationale and ratings of each component are determined and presented in this stage. The build phase is wherein the system is physically assembled based on process requirements. Hence, the work packages in this task included stack frame design, components selection and procurement, scaling of sensors for accuracy, electrical wiring, pipework for coolant liquid flow, and mechanical strength against vibration. Moreover, efforts were made to minimise alteration to the internal components of the stack to avoid unintended deterioration in performance. The specifications of the stack such as open circuit voltage (OCV), nominal and peak power, number of cells, stack design and material, dimensions, weight, coolant type, and pressure and flow are given in Table 4. Stack cell and active area geometries were not provided so estimates were made where applicable.

Table 4: FC BoP components summary

	Item	Value
PEFC Stack	Number of cells	58
	Open Circuit Voltage (V)	56.5
	Nominal Power (W)	5,000
	Peak Power (W)	5,600
	Estimated active cell area (cm2)	200
	Flow field material (design)	Graphite
	Weight (kg)	52
	Stack voltage range (V)	39 – 56.5
	Peak stack current (A)	130
Hydrogen/fuel supply sub-system	Controllable BLDC (*) diaphragm recirculation pump	24VDC, 2.5A
	Hydrogen feed pressure (bar)	1.3
	Purge solenoid valve (normally closed)	24 VDC
	Purge frequency at max power (DE mode)	10 per hour at 2 kW
	Purge frequency at max power (recirculation mode)	4 per hour at 2 kW
Air feed subsystem	Controllable BLDC* cathode air blower	48 VDC, 400 W
	Blower max. flow rate (lpm)	2,689
	Max required air flow rate (lpm)	658
	External/passive air humidifier	Shell & tube
Thermal management subsystem	Radiator	Air-cooled, fin type
	Coolant type	De-ionised water
	Coolant pump	48 VDC, 1.5 A
Data Acquisition/Control System	National Instruments	cRIO 9054
	Maximum Sampling rate	250 kS/s
Electronic Load	Modular variable DC (I-mode, U-mode or G-mode)	
	Max voltage and Current	800 V, 200 A
Sensors	Cell voltage monitoring (CVM) unit	
	Temperature sensor x 2	
	Current transducers x 6	
	Voltage transducers x 2	
	Pressure sensor x 1	
	Relative humidity sensor x 1	
	Mass flow meter	
	Hydrogen sensor x 1	

* Brush-less Direct Current

The experimental setup consisted of a liquid-cooled stack utilising dry hydrogen, and manufactured by Ballard Power Systems. The stack health at the time of conducting experiments was generally healthy, based on the OCV results obtained. The control system for the BoP was implemented on a test bench in a laboratory setting with mechanical strength provided by an aluminium frame design. The system included control of reactant flow and hydrogen purging, as well as and safety monitoring and the thermal management considerations. The BoP in question consisted of both passive and actively-controlled purpose-built units. LabVIEW software programming was adopted to represent the system control. In addition, data acquisition and software-hardware interfaces were implemented by using the modular, high-performance embedded controller compact RIO (cRIO) by National Instruments (NI). The main design objective of the BoP is to provide a stable maximum power output of up to 5 kW while catering to variations in external stimulus such as temperature or electrical load. In order for this to effectively take place the BoP requires mainly four subsystems; hydrogen fuel feed (in anode stream), oxidant feed (in cathode stream), thermal management and electrical subsystems. These are controlled and monitored using a software-based control system, interfaced with application-specific and fit-for-purpose instrumentation devices. The stack and the BoP were physically placed closed to each other to avoid excessive piping. Correct orientation of key components such as the blower, humidifier and purge valve is mandatory. Figure 15 and Figure 16 show CAD drawings of the FC stack with its BoP components attached to the front and rear

sides. An external coolant reservoir is required for the natural mixing and liquid storage. The rationale behind this is usually to avoid freezing of the coolant in sub-zero temperatures.

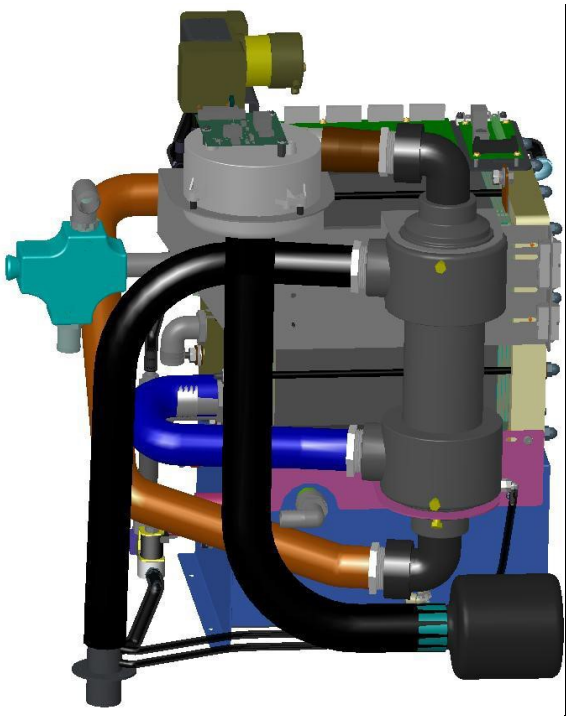


Figure 15: Fuel Cell stack with BoP rear CAD view

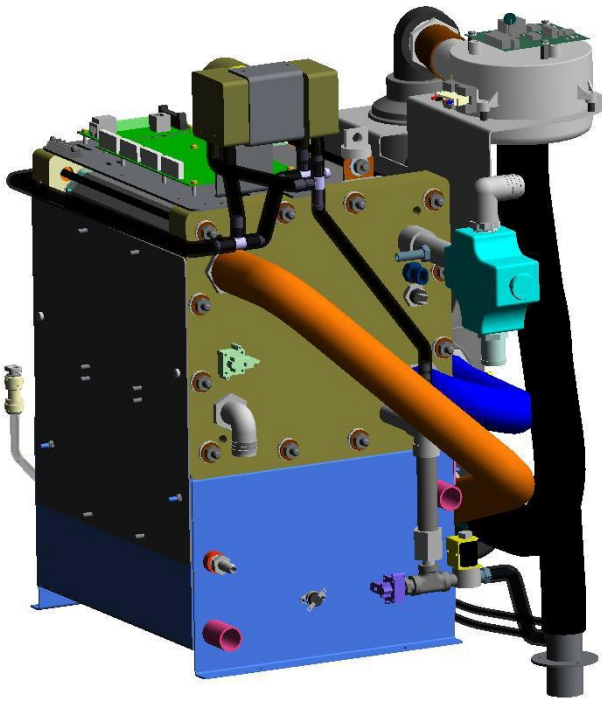


Figure 16: Experimental fuel cell stack with BoP frontal CAD view

3.2 **Anode Subsystem**

The hydrogen feed subsystem is an important part of the FC system. The subsystem is responsible for supplying fuel to the anode stream of the stack at a regulated pressure. During operation, the pressure at the stack inlet is maintained at a low and safe pressure of approximately 1.2 -1.6 bar with the help of a compact, diaphragm-based pressure regulator (see Figure 17). The principle operation of the regulator is such that when the downstream pressure is at or above the set pressure, the diaphragm valve helps to block the orifice and there is no flow of gas through the

regulator. On the contrary, when the downstream pressure drops the spring inside the pump is extended, enabling the valve plug to move away from the orifice, resulting in a flow of gas through the pump (see Figure 18).



Figure 17: Diaphragm based pressure regulator [36].

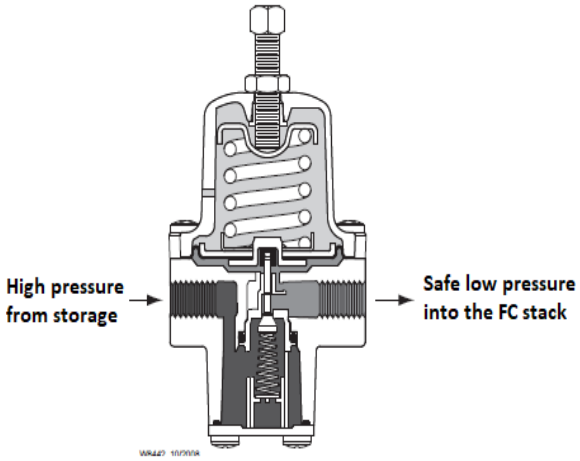


Figure 18: Internals of the medium to low pressure regulator [36].

In the experiments conducted, the hydrogen flow rate was unregulated by means of an injector and measured using a high capacity mass flow meter (MFM) connected in series with the main supply (see Figure 19) . Since the available MFM was calibrated for air, through numerical calculations the MFM was recalibrated for measuring hydrogen gas flow rate. Thus, a conversion factor (CF_V) relationship was formed and implemented in the software, as expressed in equation (3-1);

$$CF_V = \left(C_{p,1} \times D_{n,1}\right) \div \left(C_{p,2} \times D_{n,2}\right) \quad (3\text{-}1)$$

Where C_p and D_n are the heat capacity at constant pressure and normal density, respectively. As the mass flow is directly proportional to the densities and heat capacities, the flow at the outlet of the MFM can be determined using equation (3-2).

$$F_2 = \frac{F_1}{CF_V} \tag{3-2}$$

For safety purposes and emergency shutdown, solenoid valves and a hydrogen sensor (shown in Figure 20) were used. The latter device was procured due to its ability to provide signals for monitoring in the event of a gas leak within the system. Moreover, the compactness of the device meant that it could be installed within a close proximity of the locations most prone to leakages. The locations are usually at the inlets, outlets and recirculation joints.



Figure 19: Calibrated H2 MFM [37].

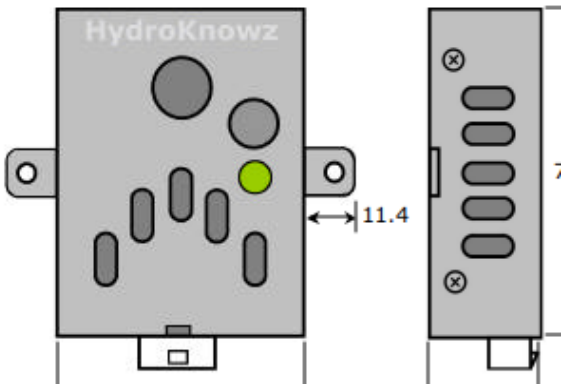


Figure 20: Hydrogen sensor [38].

A controllable, low power and compact diaphragm-based BLDC pump was used for the recirculation of hydrogen gas into the anode stream. The twin-headed natured of

the pump (see Figure 21) enables for higher flow capability of up to 66 LPM while consuming only about 70 W of power. The diaphragm material was EPDM with Neoprene gaskets. It should be noted that these materials are highly prone to embrittlement from gases such as hydrogen and therefore, care must be taken during inspection processes for fatigue and ruptures. The principle operation of the pump is such that the shaft of the motor is attached to the diaphragms, via a mechanical plate, which are synchronised to take advantage of the differential pressure build up. This is achieved through the suction and discharge ports on each head of the twin-headed pump. A graphical illustration is provided in Figure 22 of this phenomenon.



Figure 21: BLDC H_2 recirculation pump [39].

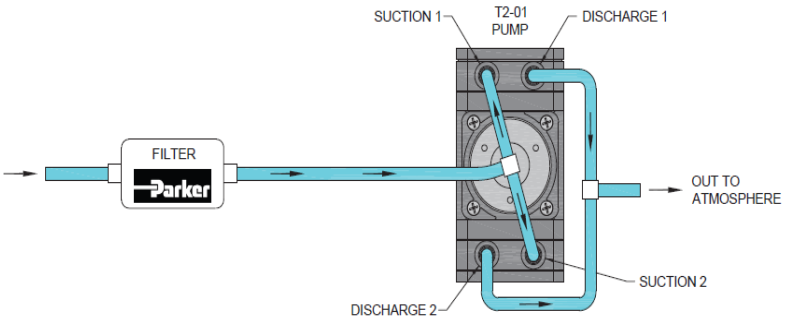


Figure 22: Recirculation process highlighting the suction and discharge ports of the recirculation pump [39].

It must be noted that, depending on the size of the fuel cell system and recirculation pump type, there will be an additional parasitic load demand. However, in the considered FC system, parasitic load due to hydrogen recirculation was minimal thanks to the compact and low power pump used. In the anode stream, periodic

purges from the channel were considered to be essential for avoiding inert gas accumulation and water flooding. In addition, recirculation of hydrogen into the anode stream is desirable for improving the fuel utilisation. A purging strategy, independent of time, was developed, experimentally implemented, and validated on the system. Furthermore, recirculation of the reactant in the anode stream facilitates with creating a constant flow. These aspects are discussed in greater detail later in this thesis in chapter 4.

3.3 **Cathode System**

The cathode sub-system has the responsibility of supplying enough air into the stack for the reaction to take place. Generally, this is achieved by employing a compressor or a blower. The former is predominantly used in the automotive applications where the response time is of importance due to the dynamics and the air stream has to be compressed for increased channel pressure. In smaller or stationary applications, a blower performs the similar job, however, without significant compression of the air. In this project, a controllable centrifugal blower was used. The blower has been tested and calibrated specifically to meet the needs of the stack. Specifically, to avoid fuel starvation an appropriate stoichiometric ratio value was experimentally scrutinised. Moreover, this posed a requirement of having a large scale flow rate meter in order to measure and validate experimentally. Thus, a test set up was prepared to carry out this task taking into the account the pressure drop due to the stack's cathode channel geometry. The flow meter was connected in series with the humidifier outlet and stack inlet, as shown in Figure 23. The control signal of the

blower is an analogue signal with a voltage range of 0 – 10 V, corresponding to off state at 0 V and full power at 10 V. It should be noted that due to the inertia requirement of the integrated BLDC motor, the blower requires at least 1.5 V as the base load signal to operate.

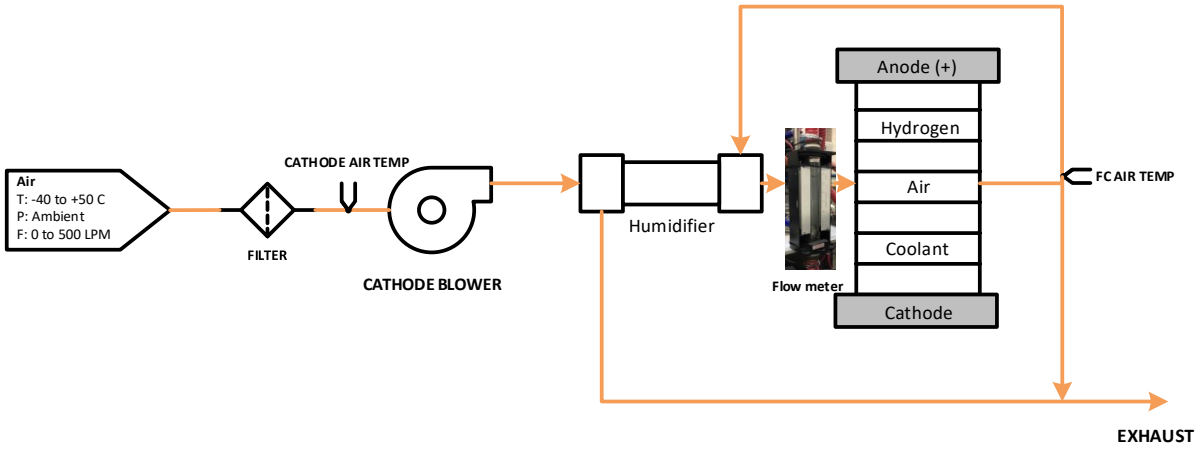


Figure 23: Blower calibration using experimental set up employing high flow rate meter.

The blower performance was observed through multiple step changes experimentally while monitoring and recording the blower flow rate and power consumption. This enabled for an appropriate way of controlling the blower based on the required air flow rate. Figure 24 displays the blower's responses to step changes controlled on the basis of stack's air flow rate requirement, which in turn is dictated by the air stoichiometric ratio (ASR).

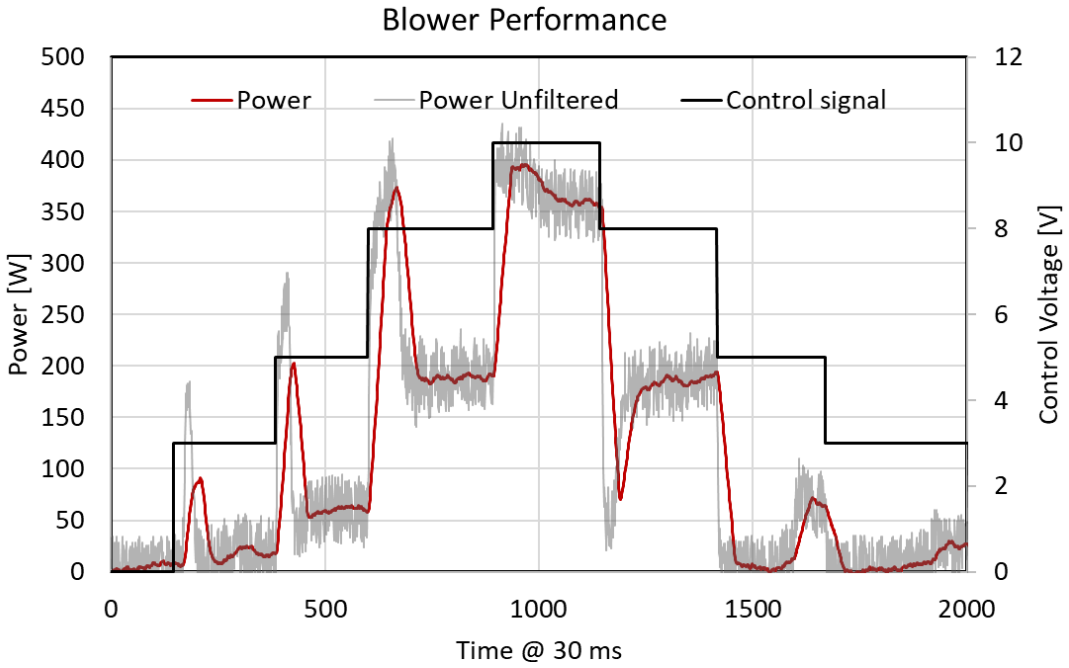


Figure 24: Cathode blower performance behaviour with step changes via analogue control signal

Thus, through the experimental work conducted it was possible to conduct a simplistic sizing study. This meant that for a given ASR value and stack's net power output, the flow rate measurements provided by the blower could be generated and recorded. Figure 25 illustrates the corresponding air flow rate, validated experimentally, as function of calculated stack power based on ASR value ranging from 2 to 6. In addition, the blower power is included to illustrate the non-linear behaviour in terms of power consumption which may lead to increased parasitic losses.

Thus, regions where the blower reaches to maximum capabilities restricts the operation of up to ASR value of 5. Beyond this, the blower can be deemed undersized, as highlighted in the figure. It can noted that the selection of ASR value

plays a crucial role in the meeting the desired as well as the mitigating the parasitic losses. This aspect is discussed in the following chapter of this thesis.

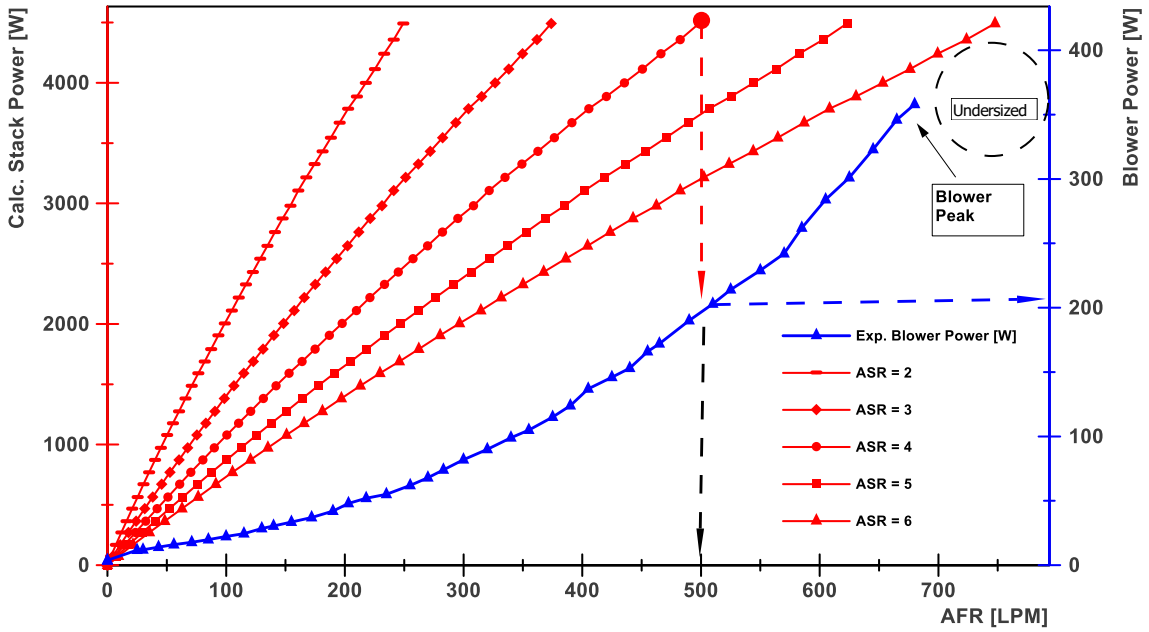
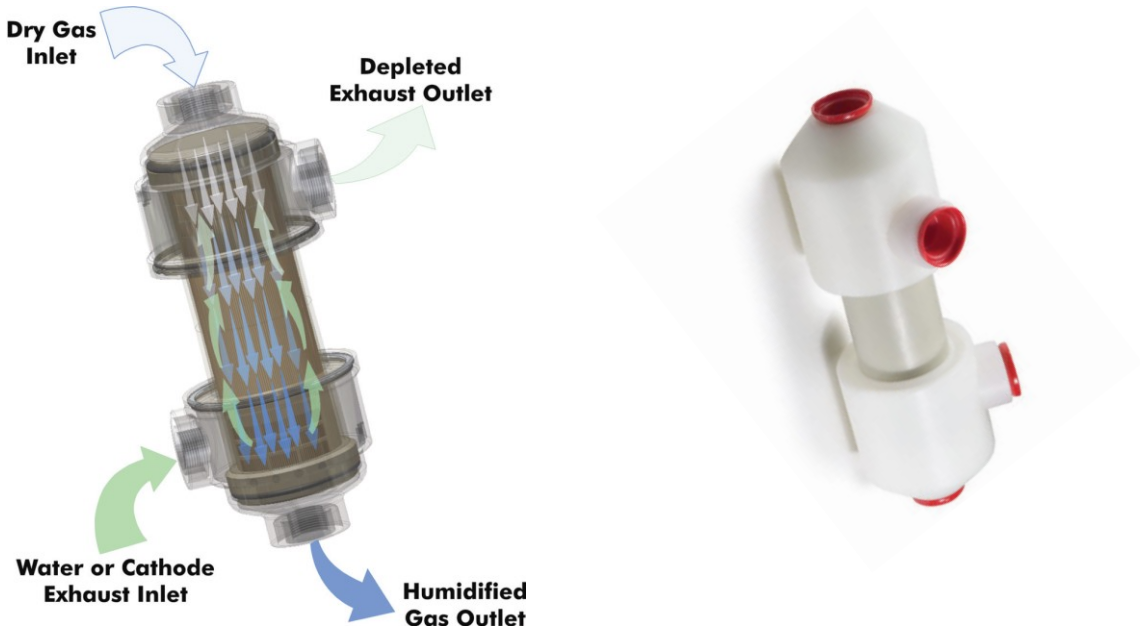


Figure 25: Cathode blower calibration based on the stack power and flow rate at different ASR values.

This sub system also requires a mechanism of humidifying the air intake from the ambient which enhances the ionic conductivity. The experimental test rig in this project employs an external passive tube-in-shell dual state (gas and liquid) exchangers that transfer heat and water vapour between two gas streams. These can also operate as water-to-gas or gas-to-gas moisture exchangers. The water molecule are absorbed onto the inner layer of the Nafion membrane tube and transported to the dry gas stream, which is driven by the difference in the partial pressures of water vapour on each side. Figure 26a and b shows the principle operation with annotation as well as the actual product integrated within the FC BoP, respectively. The water by-product from the electrochemical reaction is reused and fed into the humidifier, while the depleted gas is allowed to exit through exhaust of the system.



(a) (b)

Figure 26: Passive humidifier incorporated in the cathode sub-system: (a): principle operation description, (b): humidifier by Perma Pure brand used in the experimental test rig.

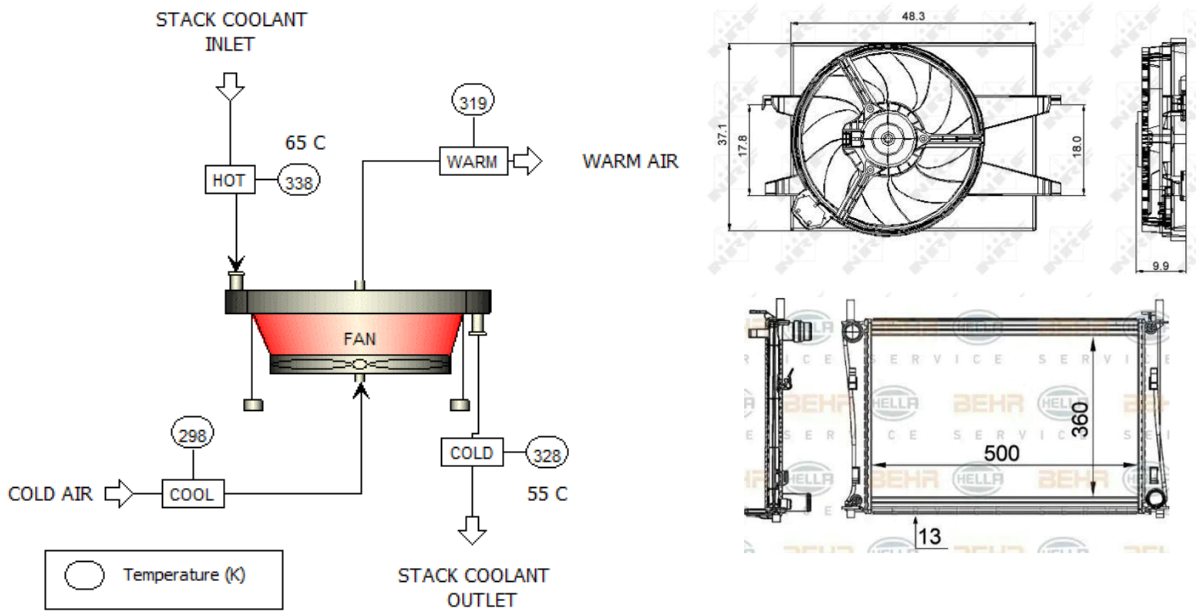
3.4 **Thermal Management**

Temperature is a critical parameter in the context of PEMFC as heat is produced during the operation of the FC stack. This can have a direct effect on the electrochemical reaction' kinetics and transport as well as other indirect effects such as conductivity, catalyst tolerance and thermal stress. Excessive operating temperature of the stack can lead to permanent damage to the membrane. Thus, the thermal management sub-system is responsible for maintaining the operating temperature of the system. This is achieved by incorporating a heat exchanger to cool down the stack. Generally, in medium-to-large (> 5kW) sized stacks convective heat transfer to liquid coolant is applied, in our case, via an air cooled cross flow liquid based radiator. The sizing procedure of the radiator was conducted in Aspen

Plus software which has a user-friendly environment and toolkit for heat exchanger design. Taking into account the efficiency and temperature difference, the heat duty was found to be 6.4 kW. As found in most automotive applications, a heat exchanger with aluminium fins attached to the tubes through which the coolant flow transfers the heat from the system with the help of a fan that has a cross flow arrangement. Figure 27a shows the model built in the software for deriving heat exchanger parameters. Thus, a relationship between the heat duty (Q), heat transfer coefficient (A) and logarithmic mean temperature difference ($LMTD$) is expressed as below.

$$\mathrm{Q} = \mathrm{U} \,.\, \mathrm{A} \,.\, \mathrm{LMTD} \tag{3-3}$$

The outputs from the model were found to be 850 W/m^{2}K, 0.3 m^2 and 24 K as U, A and LMTD, respectively. A heat exchanger from a Ford Fiesta (see Figure 27b) commercial vehicle was procured and integrated to suffice the needs of derived above.



(a) (b)

Figure 27: Heat exchanger details integrated within the FC system. a: Aspen Plus design model, b: procured heat exchanger used in Ford Fiesta commercial vehicle.

3.5 **Electrical System**

The electrical sub-system within the system involves conditioning of the power output. This is required in order to match the voltage level of the electrical bus by either stepping up or down the voltage of the stack. Devices capable of offering this are known as DC-DC converters. With the help of pulse width modulation (PWM) technology integrated within the converters, the duty cycle can be varied to control the input and outputs. The electrical DC bus in this project was set at 48 V level. The FC stack voltage output has to be stepped up to 48 VDC from as low as 34 VDC when operating at peak load of approximately 5 kW. Thus, a boost converter is required that can provide a regulated and controlled output. For this purpose, a high performance two-quadrant, double half bridge, interlaced boost converter by Zahn

Electronics was integrated. The converter is capable of delivering a switching frequency of 32.25 kHz at a 2:1 boost ratio, i.e. 24V to 48 VDC [40]. Figure 28a & b display the CAD drawings of the converter with functional parts such as inductive filter, control unit and the power distribution unit annotated. Figure 28c shows the wiring diagram with power sources and electronic load included in the test rig. It can be noticed from the figure that the input source, the fuel cell, shared a common node with the electrical load output.

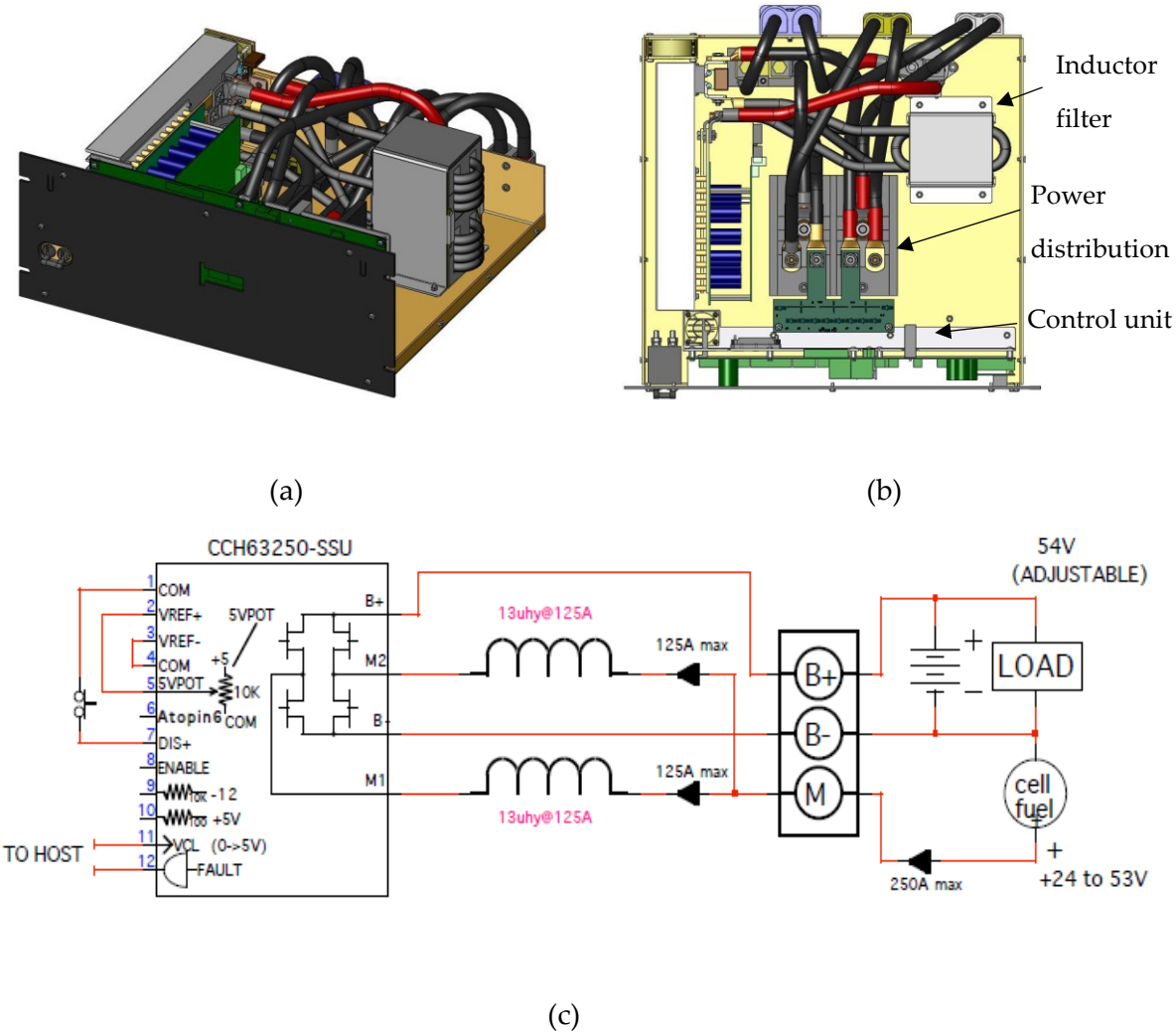


Figure 28: DC-DC boost converter, a: CAD side-view, b: CAD top-view with annotation, c: wiring diagram with load, battery and FC

Furthermore, the sub-system is also responsible for electrical safety of the power sources by making use of several devices such as fuses, relays, contactors and emergency shut down switches.

Figure 29 displays the operational behaviour observed during the experimental stage involving a battery system which deals with the power split deficit, depending on the converter current limit (CL) set point. At a constant load, it can be seen that the CL value defines the transition from a CL mode to pure voltage mode. Furthermore, the lower CL input to the DC converter suppresses the current ripples seen in the current and voltage at FC side. In addition, this parameter can be used to control the power flow from the two current sources, by varying the CL value based on the desired power split ratio [41].

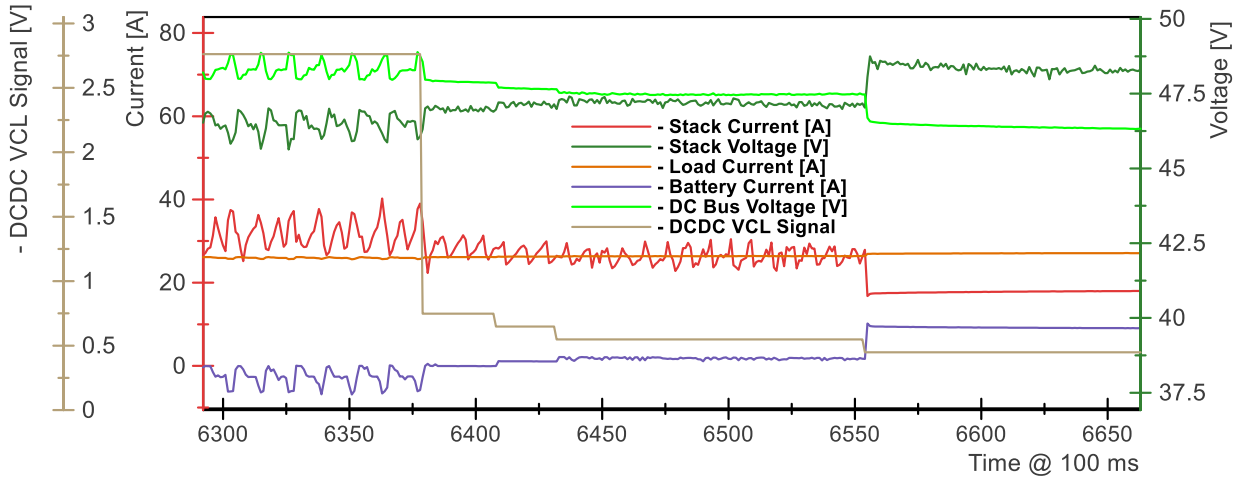


Figure 29: Operational behaviour of the DC-DC boost converter.

3.5.1 Sensors

The FC BoP requires numerous sensors for measuring crucial parameters. Sensors also facilitate data manipulation and logging as well as safe operation of the system.

The parameters that required a sensor include voltage, current, pressure, temperature, relative humidity (RH) and gasThe operational principle behind each of these

3.5.1.1 Current sensing

There are multiple current sensing technologies commercially available for accurate measurement. For automotive applications, these predominantly include hall effect and shunt resistor sensors. The former is based on the Lorentz force principle which senses the magnetic field produced by the device. Shunt resistor approach is a simple method which involves measuring of the voltage drop across the known resistor. To meet the needs of this project and attain accuracy (± 0.5%), a hall-effect sensor by LEM™ (model HTR 100-SB) was used. The working mechanism of the sensor is depicted in Figure 30.

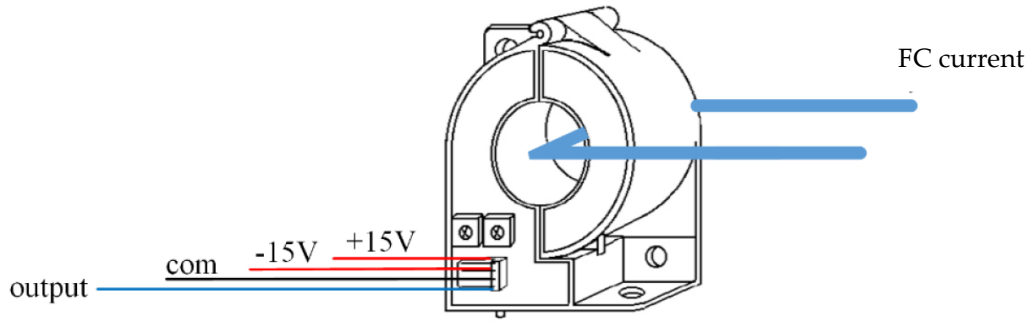


Figure 30: hall-effect sensor with input and outputs shown.

Using this sensor the FC stack current could be measured for before and after the DC-DC converter. The current transducer provides an analogue output signal of ±4 to 8 V, correspond to a scale of 100 A to 200 A. For this project's experimentation the

transducer was calibrated for 100 A, requiring a scaling factor of 25 as shown in the equation below.

$$I_{FC} = 25 \times v_{measurement}^{current} \quad (3\text{-}4)$$

3.5.1.2 Voltage sensing

The voltage output from the stack and the DC bus were measured using a voltage transducer. The output signal is ± 10V when powered by a 24 VDC supply. The voltage transducer by Phoenix Contact™ was calibrated to accept a voltage range of ± 80 VDC. Figure 31 depicts the input and output interface needed for obtaining measurements via the software environment devised within LabVIEW.

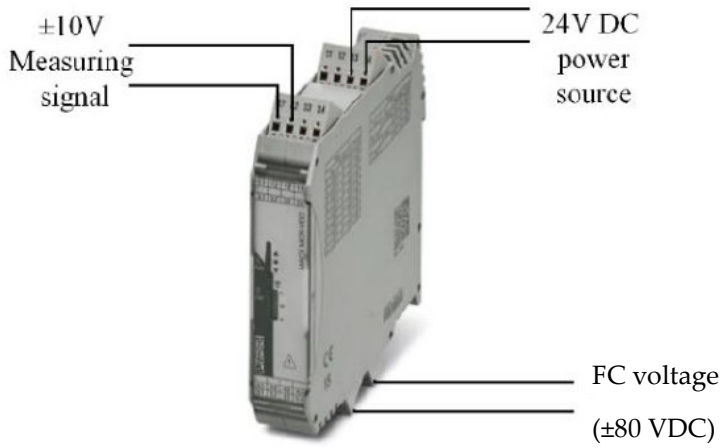


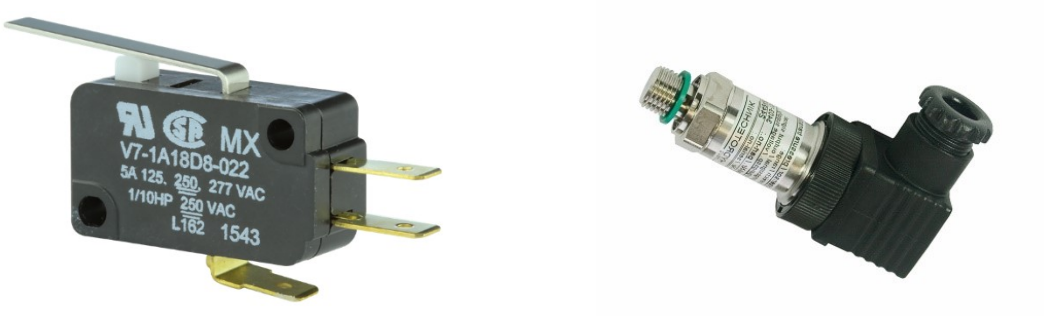
Figure 31: Voltage sensor with measurement signals illustrated.

Another transducer with similar specifications was used for measuring the DC bus voltage to monitor the out to feeding into the electronic load bank. Thus, the scaling of the devices can be mathematically expressed as in following equation.

$$V_{FC} = 8 \times v_{measurement}^{voltage} \quad (3\text{-}5)$$

3.5.1.3 Pressure sensing

The FC systems is required to go into shut down phase if the pressure built up reaches an unsafe value. Although in this project, neither the anode nor the cathode streams are compressed to high pressure, there could be instances where the stack can become pressurised. For example, in the event the exhaust or purge valve fails to operate. Thus, a mini pressure switch and sensor (pressure range of -1 to 6 bar) were integrated within the BoP of the stack for safe operation and regulation. These sensors depicting in Figure 32a and b.



(a) (b)

Figure 32: a: Mini pressure switch to shut monitor the anode pressure, b: pressure sensor to monitor pressure build up inside the stack.

3.5.1.4 Temperature sensing

Temperature control is an important aspect of the thermal management sub-system. Hence, a temperature sensor is required to constantly monitor and measure the operating temperature of the stack. A resistance temperature detector (RTD) type sensor was employed in this project (Figure 33a). The proportionality between the temperature and the RTD resistance allows for the measurement of the temperature using an external PT100 sensitive element. A transmitter (Figure 33b) was then used

to convert the readings into standard 4 to 20 mA analogue output (commonly known as 2-wire configuration). The length of the element was enough to maintain direct contact with the coolant at all times. The device was calibrated to measure between 0 and 100 C.

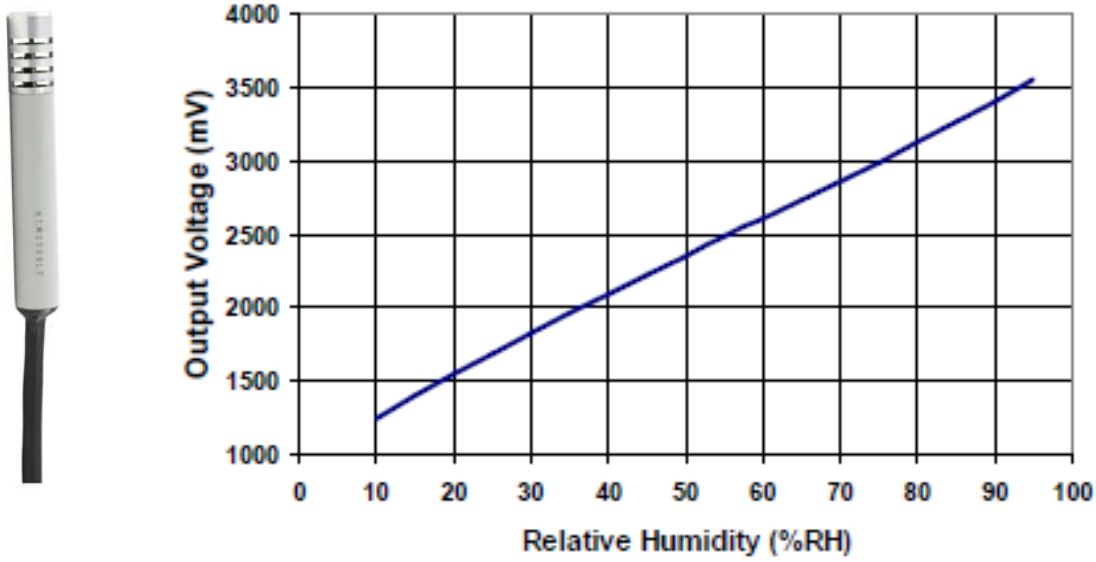


(a) (b)

Figure 33 Devices used within the thermal management sub-system[42]. a: RTD temperature sensor, b: high accuracy temperature transmitter [43].

3.5.1.5 Relative Humidity sensing

The ionic conductivity is a function of the relative humidity (RH). Maintaining a high RH level is beneficial in terms of stack performance. Hence, an RH module (displayed in Figure 34a) giving indication of humidification level in the cathode outlet was integrated within the pipework, perpendicular to the stream flow.



(a) (b)

Figure 34: RH sensing within the FC BoP. a: RH sensor by Measurement Specialties, b: RH level against output voltage signal [44]

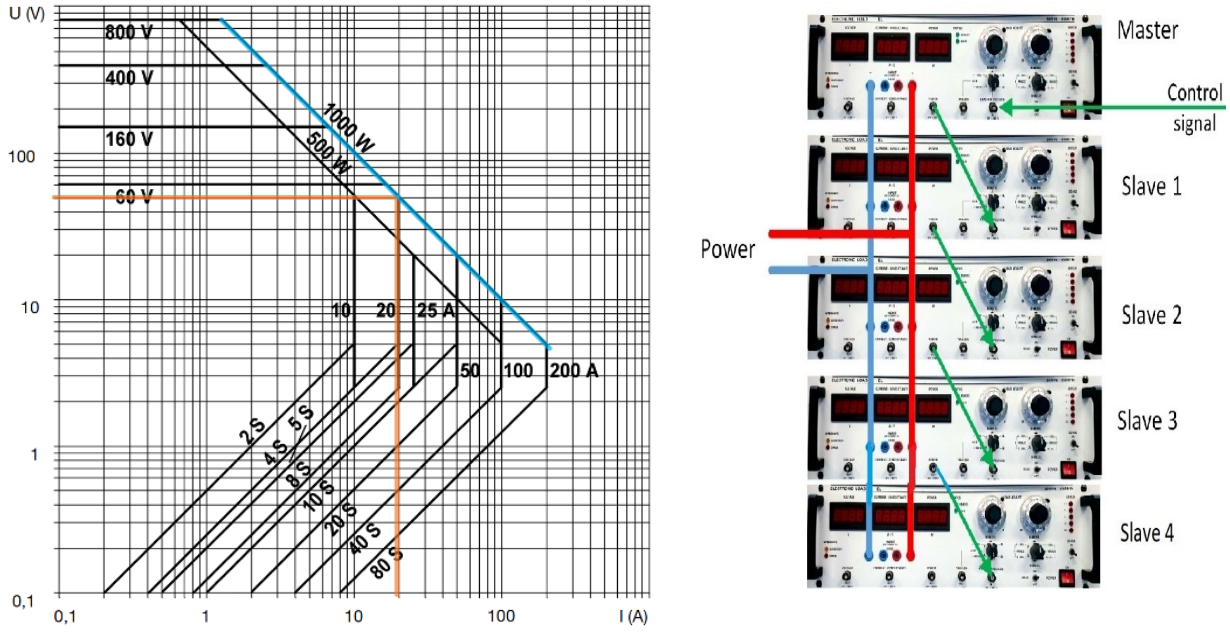
Figure 34b illustrates the relationship between the RH level and the analogue output signal detected in the embedded controller. The output voltage range is between 1.2 V and 3.5 V corresponding to RH level of 10 % and 95 % respectively. The manufacturer suggests a linear mathematical relationship to compute the RH value as in the equation below;

$$RH = 0.0375 * v_{measurement}^{RH} - 37.7 \quad (3\text{-}6)$$

3.5.2 Electrical Load Banks

A load bank is essential to draw current from the power sources. A bank of five electronic load banks (Zentrol-elektrik EL1000/800/20) connected in parallel were used to sink the drawn current. Although the maximum voltage and current level

accepted by each electronic load unit could potential be 800 V and 100 A respectively, the maximum current accepted at 48 V was restricted to 20 A as shown Figure 35a below depicts the current against voltage characteristics of the electronic load bank, with annotations illustrating the series limits of 20A at 50V for reaching a 1 kW power.



(a) (b)

Figure 35: Electrical load banks, a: current vs voltage characteristics, b: parallel connection in the lab set up illustration [45].

The individual units were connected in a master-slave configuration wherein the master unit was interfaced with the software with a control signal (0 to 10 V). Moreover, the units can be made to operate in three distinct modes; voltage, current and power modes. The power mode was selected because it did not interfere with the stack output regulation – what the DC-DC converter is tasked with. Thus, a relationship for scaling the power demand and the control signal was derived,

taking into account the number of load units and peak power per unit of 1000 W (corresponding to 10 V control signal).

$$v_{load}^{control} = \frac{P_{load}}{5\ x\ 100} \tag{3-7}$$

3.6 **Hydrogen Supply and Storage**

A high purity hydrogen corresponding to 99.999 % was supplied into the stack. The storage vessel was a Genie gas cylinder from BOC™ pressurised at 300 bar with a volume of approximately 5 m^3. The advantage of the having such tanks is that they are lighter and compact compared to Type I steel vessels. The pressure regulation takes place in multiple stages. The first pressure regulator steps down the pressure from 300 bar from the storage vessel to a medium range of 6 to 15 bar which is then passed into a medium to low pressure regulator with an output of 1.3 bar for the stack anode inlet. Figure 36 shows the stages using the regulators before feeding the fuel into the stack.

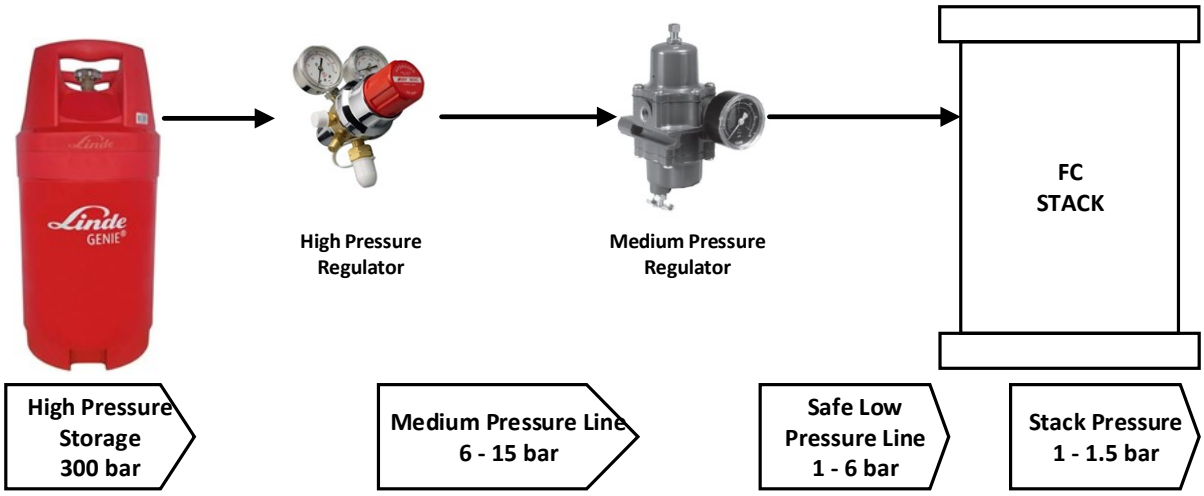


Figure 36: Pressure regulation from the storage tank to stack inlet with multiple stages illustrated.

3.7 **FC Controller**

An embedded controller available as CompactRIO by National Instruments™ (NI) was procured and programmed. This series of controllers is well-suited for laboratory environments and is designed to be robust. The controller (shown in Figure 37) can support three forms of programming modes; real-time via LabVIEW using a data acquisistion module, real-time scan requires external modules such as analogue or digital inputs and FPGA program mode for additional flexibility and timing choice. For the purposes of this project, the second programming mode of the C series controller was adopted for robustness and direct interface with the additional modules connected to the cRIO controller. Three sub-modules added into the main embedded controllers were; NI 9025 series for programmable analogue inputs and NI 9375 for digital input & outputs and NI 9264 for analogue outputs (shown in Figure 38). Their use corresponds to temperature and pressure sensor analogue inputs, contactor and relays digital switching and analogue control of all the motors in the system, respectively.



Figure 37: NI cRIO series embedded controller.



Figure 38: Additional modules for digital, analogue input and outputs for cRIO.

The software to hardware interface between the controller and the sensor devices is depicted in Figure 39 in detail (LabVIEW code in Appendix II and III). There are four types of connections that are used in the system; analogue input and output signals, low voltage supply and mechanical connections. There were several step down voltage converters employed, including bipolar DC-DC converters in order to power the voltage transducers. Furthermore, there is a dedicated current sensor for each of the FC auxiliary components; blower, recirculation pump, coolant pump and radiator fan. The coolant pump and fan require relay switches for interfaced with 24 V supply for safe transitioning between the on and off states. Similarly, a DC contactor was used for safely coupling and decoupling the FC stack with the DC bus.

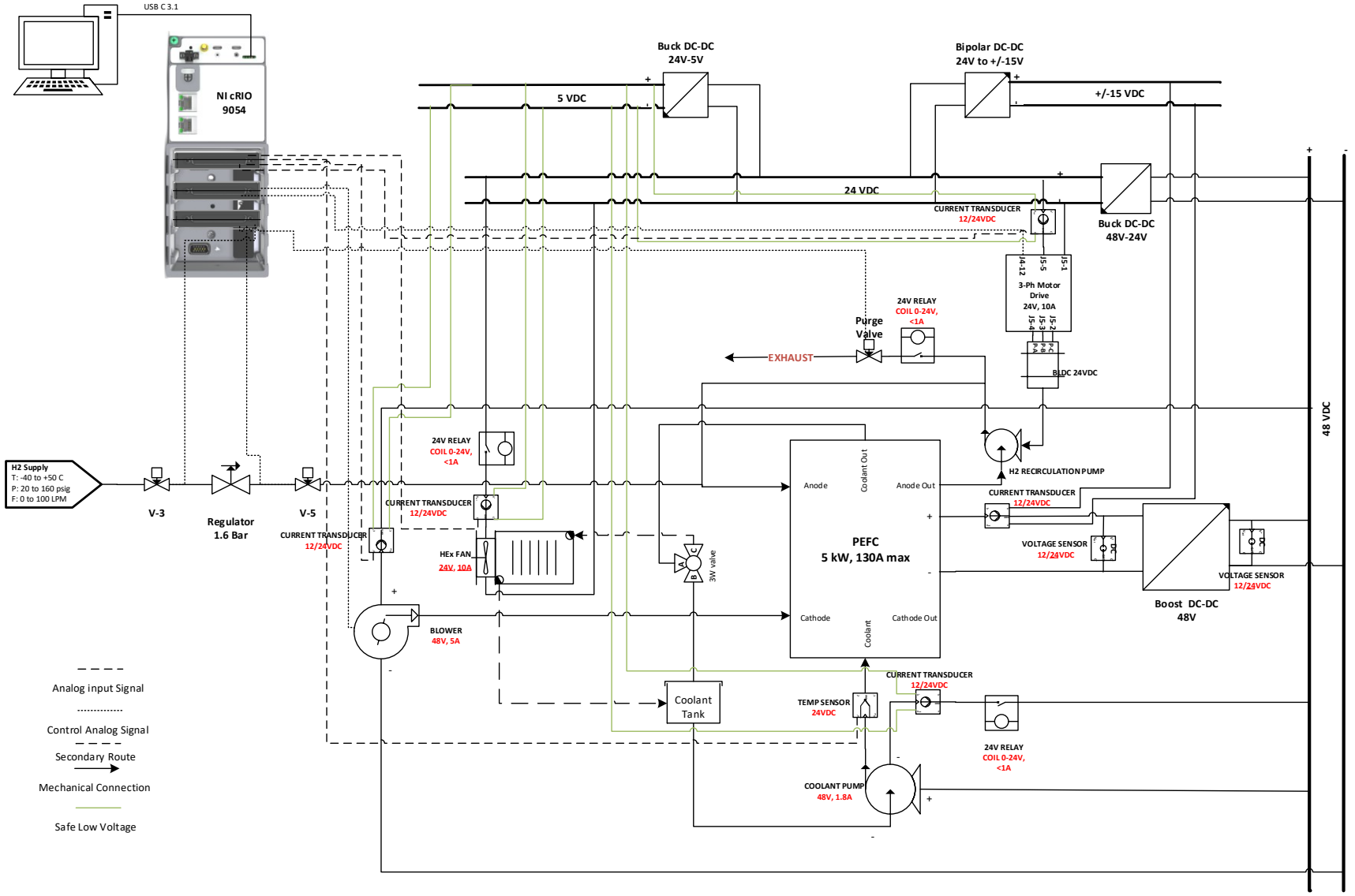


Figure 39: FC embedded controller interface with hardware devices in the lab test set up

3.8 System Process

The entire system process consists of the four sub-systems interfaced with the FC controller. The controller manages the decision making criteria based on prior calibration and defined rules. The system consists of passive components such as the air filtration unit, humidifier and 3-way valve which the controller has no interface with. The process can be said to begin with the reactants supply in both anode and cathode side with hydrogen and oxygen content from the ambient, respectively. The former has hydrogen recirculation mechanism in place for better fuel utilisation with the help of a controllable low power diaphragm pump and the latter uses an air blower for air intake. Both purged hydrogen and excess air are allowed to exit from the exhaust. The controller constantly monitors the stack temperature with the aim to maintain it at a specified level with the help of the radiator fan.

There are four electrical buses with different voltages corresponding to 48 V, 24 V, ±15 V and 5 V. The FC DC-DC converter is connected to the 48V electrical bus while most of the FC BoP components are connected to the 24V bus. The other two electrical buses are used for powering the electronic components. A diode is present in series with the DC-DC and the 48 V bus to protect the stack from negative currents. Furthermore, the five electric load banks are also connected to 48V bus to draw current from the stack based on a load profile input in LabVIEW software. A battery or a supercapacitor bank may be included in this bus for energy storage or assisting the stack with the transients. These details are

schematically depicted in Figure 40 with each subsystem segregated.

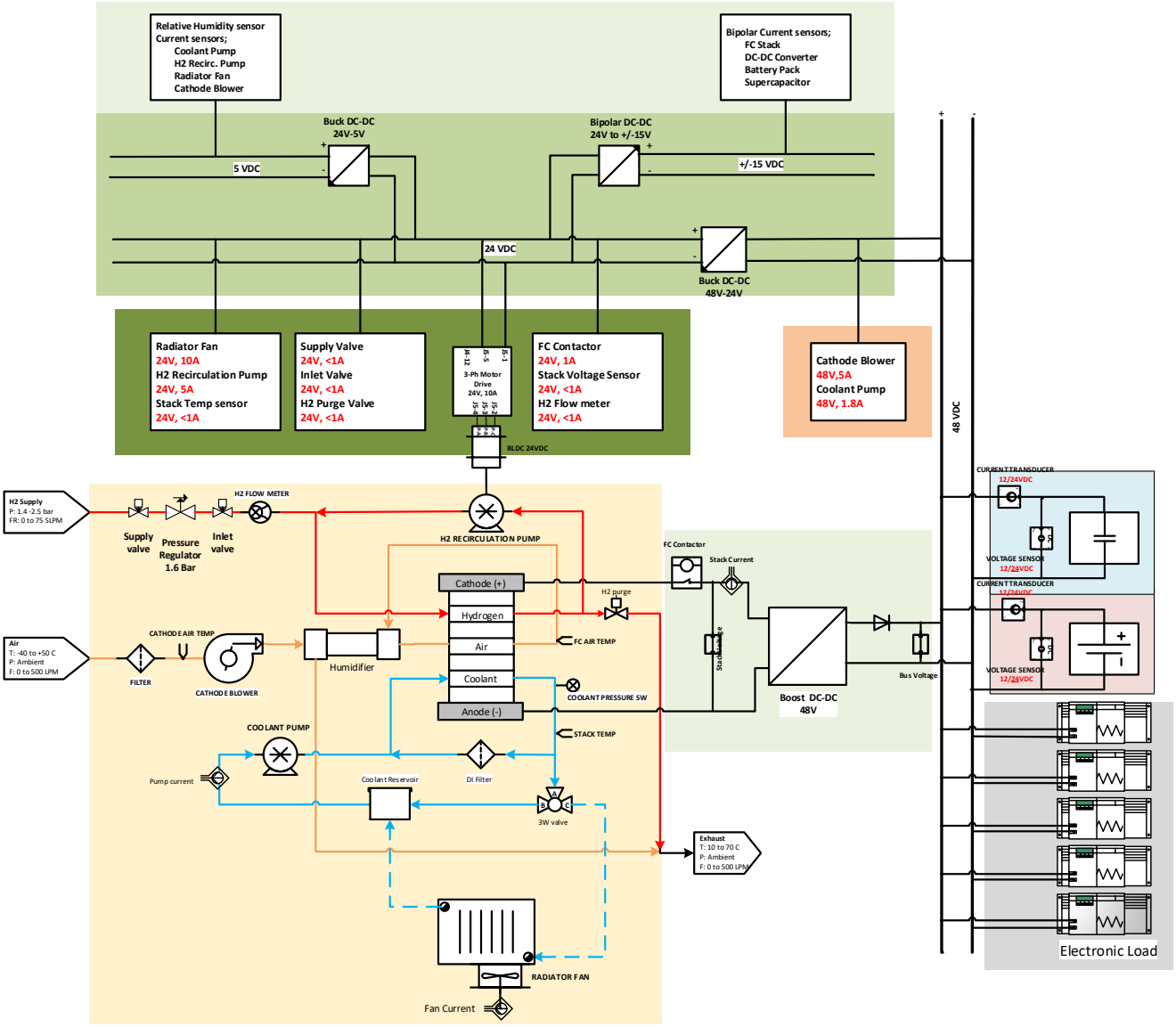


Figure 40: System process diagram depicting all the sub-system and the auxiliary components with each system distinctly segregated.

A photographic evidence of the laboratory test rig with the electrical and processes annotated is included in Appendix I.

4 PEMFC System Design*

This chapter presents a detailed overview of the fuel cell system control implementation. This includes the control mechanism of the entire balance of plant (BoP); including anode, cathode, thermal and electrical sub-systems. The identified strategies were derived and validated experimentally. Where applicable, a 'black-box' modelling approach was used. A key aspect presented in this chapter will be the system's reactant gas management strategy. In particular, the hydrogen purging strategy at the anode side considering both with and without recirculation. In this chapter we undertake a systems level approach in BoP analysis and gas management design with a focus on anode purging strategy. We present results through numerical simulation of the biggest contributor of parasitic loads. In addition, a novel and effective purging strategy using a single key parameter as input is proposed.

4.1 Introduction

Practically, all commercially available hydrogen fuel cell systems include a Balance of Plant (BoP) which requires a control system that manages the performance of the system. A crucial role of BoP control is to implement an appropriate reactant gas management strategy at both the anode and cathode

* This chapter was published in the *Energies* journal by MDPI, also provided in the Appendix
Khan, N.; Al-Sagheer, Y.; Steinberger-Wilckens, R. PEFC System Reactant Gas Supply Management and Anode Purging Strategy: An Experimental Approach. *Energies* **2022**, *15*, 288. https://doi.org/10.3390/en15010288

sides of the stack. Reactant gas and water management are an important aspect of Polymer Electrolyte Membrane Fuel Cell (PEMFC) systems and the key to achieving optimum performance. Generally, the issues of reactant gas flow and water management are interlinked. An uneven distribution of gases within the stack results in current density, humidity, and temperature inhomogenities, which will eventually lead to performance degradation [46] . Specifically, this occurs due to limitations in mass transport and thus undersupply of the catalytic sites with reactants [47]. Excess or lack of humidification in the membrane can have a similar result [47]–[50]. Therefore, a balanced approach has to be implemented between membrane drying and humidification to prevent fuel cell degradation and guarantee a high and homogenous performance level. Crucial parameters, when calibrated well, such as gas flow rates, operating temperature, and electrode inlet pressure can assist in mitigating the effects of flooding or fuel starvation.

Providing a homogeneous supply of fuel into a fuel cell stack is generally one of the core processes dealt with during the system design phase [18]. The decision in choosing a fuel supply design depends mainly on the application, availability, and fuel storage sub-systems. There are three main types of anode fuel feed designs: dead-end, open-ended, and semi-dead-ended or 'flow through'. In a dead-ended design there is no outlet from the stack anode. As a result, the entirety of the fuel gas flow into the stack has to be reacted and passed through the membrane. The purity of the fuel therefore has to be extremely high so as to avoid any negative

effect of the impurities concentrating in the anode compartment over time [51], the most noticeable affect being a decay of cell voltage due to decreasing fuel partial pressure cased by the impurities. This design is usually preferred for small scale systems where compactness and high fuel utilisation are most desired. In contrast, both semi-dead-ended and open-ended designs have an anode gas exhaust outlet. However, in the former design, a valve in the exhaust line on the stack outlet, is periodically opened in order to release any unreacted gas, taking the accumulated impurities with it. In the case of an open-ended or flow through design, the exhaust from the anode is always open in order to cause bleeding of hydrogen, though a restrictive orifice will increase the back pressure in order to control the anode stream [52]. The semi-dead-ended design is the most common one found in literature and is usually discussed synonymously with the dead-end design. Going forward, we will refer to it using the dead-end terminology in this paper. To reiterate, the main purpose of the anode fuel supply system is to uniformly distribute a sufficient amount of hydrogen gas throughout the membrane electrode assembly (MEA) active area. For this purpose, a hydrogen recirculation pump can be employed within the anode loop of open-ended designs. The type of pump employed depends on the scale of the system. Most commonly in medium sized systems, a low power brushless direct current (BLDC) pump is used, whereas in large scale systems a high power centrifugal pump will satisfy the high flow rate requirements.

4.2 Literature on PEMFC System

An extensive amount of work has been done in the past concerning PEMFC systems using a dead-end anode design with periodic purging [53]–[55], including experimental work to study the effects of operational parameters at cell level [56]. The authors concluded that the average intervals in a given purge cycle decreased with the decrease in of current density and the relative humidity on the cathode side. Experimental work on visually analysing the effect of water transport at the cell level has been reported in [57]. The authors visualised the effect of water accumulation back-diffused from the cathode side into the anode stream, and reported that a high air stoichiometric ratio reduced the cell voltage decay. Similar work at a stack level, employing a dead-end anode design with periodic purges was reported in [50], [58]. Additionally, crucial findings on nitrogen crossover in the membrane into the anode from the cathode side have been published [59], [60].

Most commercially available PEMFC systems have an anode recirculation loop to evenly distribute gas and improve fuel utilisation. Mainly this is to keep the hydrogen pressure at the anode outlet high and still have high system fuel utilisation. Some researchers have aimed to find the appropriate trade-off between impurity accumulation and fuel utilisation, while others have derived mathematical models to describe the performance of different anode gas supply strategies [53], [61]. Studies involving gas composition within the fuel supply system have also been performed extensively [62]–[64]. Comparative analysis on

anode recirculation incorporating periodic purges and bleeding has been reported and experimentally validated on a laboratory-scale system in [52]. Furthermore, He et al. [65] scrutinised the control aspect of a purging cycle whilst suggesting a model predictive control (MPC) approach instead of the conventional PID approach to regulate hydrogen recirculation based on a linearised model simulation. Their findings suggest that by manipulating the hydrogen recirculation rate the stack operation efficiency could be increased.

Another key aspect studies have paid attention to in the context of gas and water management is the purging criterion. The rules adopted in deciding when and for how long to purge, play an important role in terms of the sub-system's complexity and cost, and the loss of unused hydrogen [66]. According to available literature, a common way of triggering a purge event in the anode stream is based on allowable voltage drop [53], [54], [67], [68]. Some researchers have used the nitrogen partial pressure level in the anode stream to generate a trigger of when to purge [59], [69]. For example, Hu et al. used various tools such as an advanced cell voltage monitoring (CVM) unit and mass spectroscopy to monitor the nitrogen level. This allowed them to analyse the cell voltage drop due to impurity concentration and to devise a purging strategy [64]. The least complex anode purging strategy reported in the literature was the one involving current integration [55], [70]. However, there are no experimental results on a systems level found with this purging strategies. The approach only relies on the stack

current measurement integrated at the required sampling rate. With such a process parameter, the change in performance is only proportional to the operational time and is not effected by idle periods. Other variables such as hydrogen consumption and stack voltage will require additional executions in order to stop gas flow into the stack, thus, zeroing the stack voltage. In addition, such purging strategies require complex model based control designs, and additional instruments for the purpose of gas composition sensing.

On the cathode side, the blower injects oxygen content from the atmospheric air into the channels. Previous work on this aspect of BoP mostly covered numerical analysis. Experimental work related to accurately sized BoP with detailed rationale and discussion is scarce. Much of the reported work includes modelling and control of the cathode stream for PEMFC systems [71]. Theoretical work on cathode humidification was analysed by recirculating the exhaust gas, thereby removing the need to employ external humidifiers [72]. Similarly, work on dynamic modelling for PEMFC to investigate the transient response of the fuel cell to load changes has also been reported [73]. Optimised control strategies for the air supply system based on a fuzzy logic control strategy have been proposed and modelled [74].

4.3 Hydrogen Fuel Feed Loop

The hydrogen feed subsystem is an important part of the BoP. The subsystem is responsible for supplying fuel to the anode of the stack at a regulated pressure.

During operation, the pressure at the stack inlet is maintained at a low pressure of around 1.5 bar with the help of a compact, diaphragm-based pressure regulator. In the experiments conducted, the hydrogen flow rate was unregulated and measured using a high capacity mass flow meter (MFM) connected in series with the main supply. For safety purposes and to allow emergency shutdown, solenoid valves and a hydrogen sensor were used. A controllable, low power and compact diaphragm-based BLDC pump was used for the recirculation of hydrogen gas into the anode stream. Periodic purges from the channel were considered to be essential for avoiding inert gas accumulation and water flooding of the anode, by flushing through the exhaust [65], [75], [76]. Recirculation of hydrogen into the anode stream is essential for improving the fuel cell system utilisation [77], [78]. A purging strategy, independent of time, was developed, experimentally implemented, and validated on the system. This aspect is discussed in greater detail later in this chapter. The strong rationale for implementing the aforementioned was also due to the fact that without recirculation there was the requirement of frequent purge cycles in order to create a flow in the channel and avoid flooding, thereby reducing fuel utilisation [62].

As stated before, there are two main purging methods; the dead-end with and without recirculation mode. In the former case frequent periodic purges are require whilst in the latter case, due to continuous recirculation, the frequency of anode purging can be significantly reduced. Recirculation based configurations

can either allow bleeding of hydrogen or incorporating periodic purges. Based on previous work and our findings the latter mode is favourable due to advantages such as infrequent purges resulting in higher fuel utilization and controllable flow rate. Figure 41 below illustrates the hydrogen purging process with graphical representations of the setup for each type. It must be noted that, depending on the size of the fuel cell system and recirculation pump type, there will be an additional parasitic load demand. However, in the considered PEMFC system (described in chapter 3), the parasitic load due to hydrogen recirculation was minimal thanks to the compact and low power pump used. Figure 42a illustrates the complete dead-ended fuel supply with a recirculating anode subsystem involving a real-time data monitoring and logging setup used in this work..

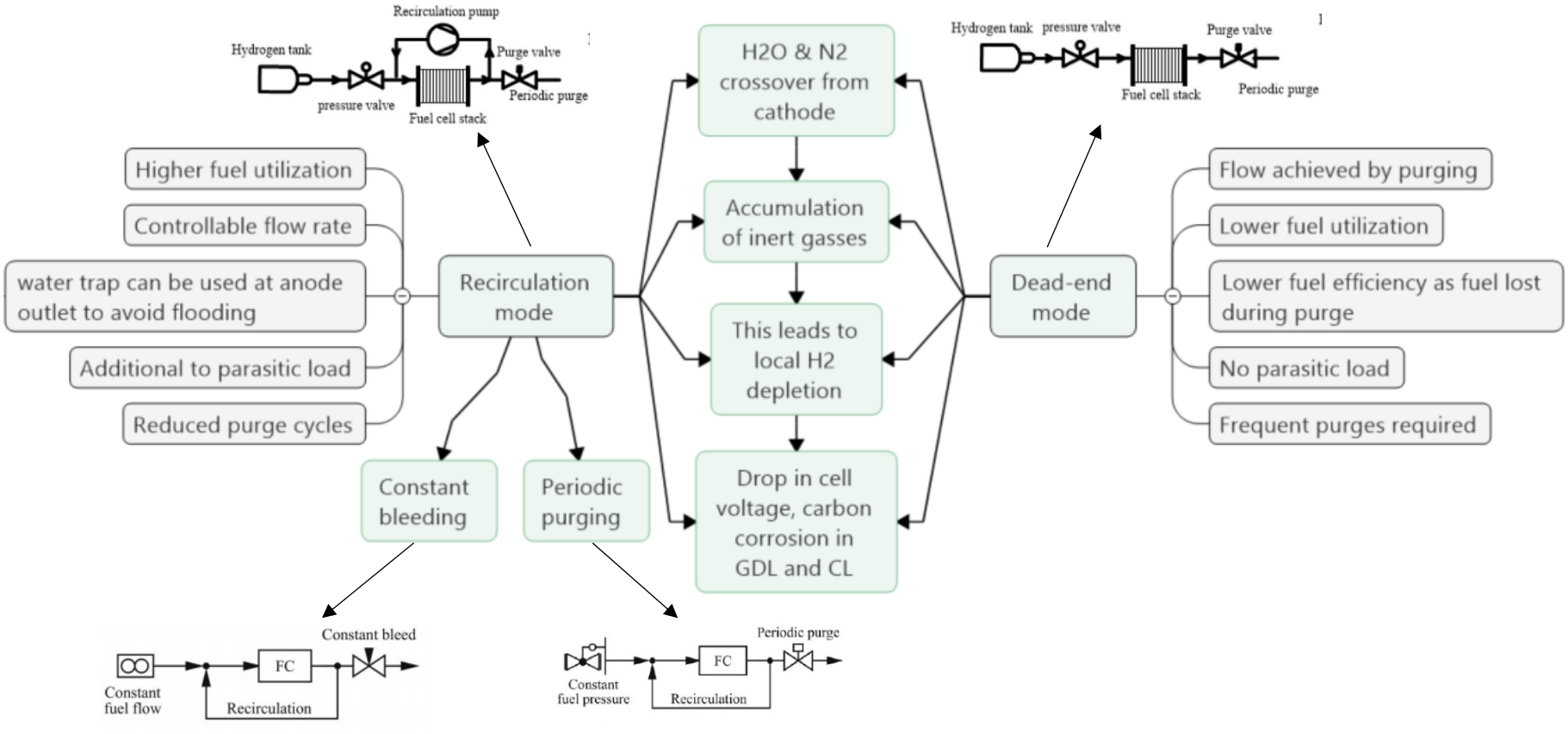
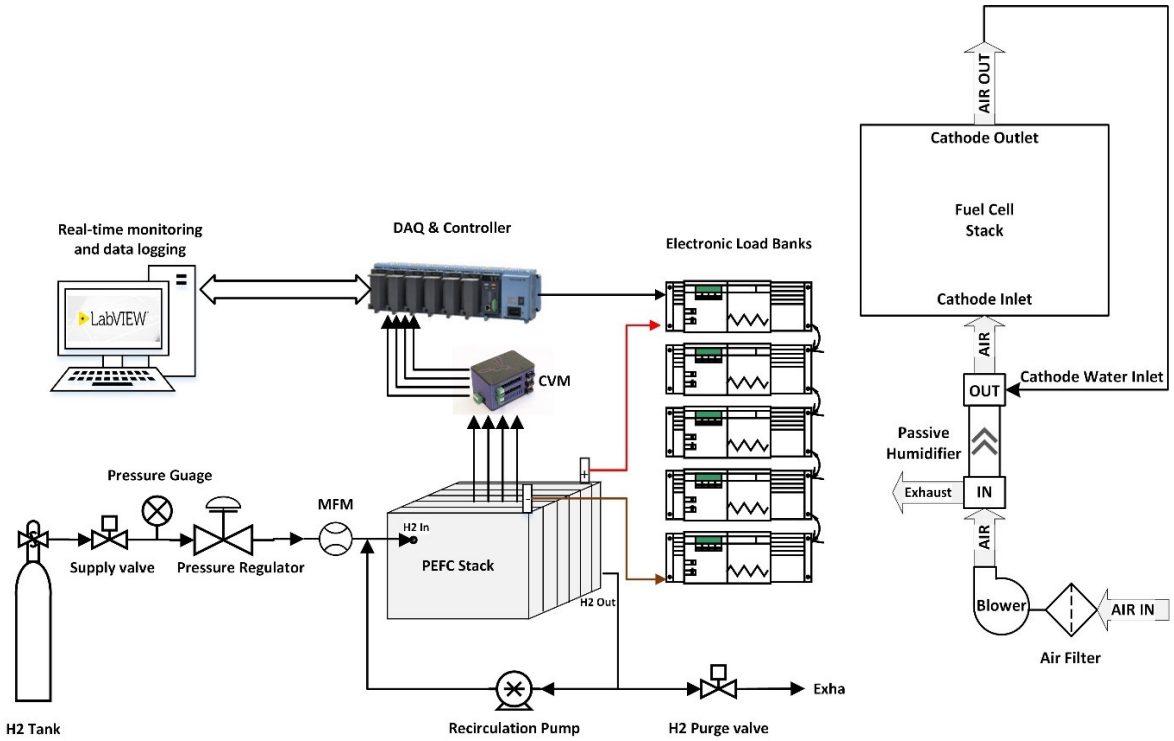


Figure 41: Illustrative classification of hydrogen purging process.

4.4 Oxidant Feed Loop

For the electrochemical reaction to take place, oxygen from ambient air is delivered into the cathode stream of the stack. This is achieved by using air compressors or blowers which, through suction or injection, provide ambient air into the stack. Fuel cell membranes only offer superior proton conduction when they are sufficiently humidified [79]. There are two main methods of humidification in a fuel cell; internal (also known as self-humidification) and external humidification. The former can be achieved by modifying the cell material composition and channel design [80], whereas the latter requires an external humidifier to cause humidification in the gaseous reactant flow prior to entering the cathode inlet. External humidifiers are capable of providing a certain level of regulatory control in maintaining the desired relative humidity level so as to avoid drying and/or flooding of the cell [81]. In this work, a passive external humidifier with shell and tube moisture exchanger containing a Nafion membrane was used – as shown in Figure 42b.



(a) (b)

Figure 42: (a) Anode subsystem experimental setup and (b) cathode sub-system design.

4.5 Temperature Management

It is imperative that the stack operates within a regulated temperature range for optimal performance [82]–[84]. The thermal management subsystem in the liquid cooled PEMFC in our setup was responsible for dissipating the heat produced by the stack effectively using a heat exchanger. As described in section 3.4, the subsystem consisted of an air-cooled radiator, a three-way passive valve to direct the flow of coolant into the heat rejector based on the stack temperature, a reservoir for the liquid storage and pressure compensation, and a coolant circulation pump.

4.6 Results, Comparisons and Discussion

4.6.1 Experiments

Prior to each experiment, a purging event was triggered in order to avoid the negative effects of inert gasses and water accumulation. The delay between each step change of 100 W was selected as two seconds in order to reach the steady state. This was experimentally determined by applying step changes to the stack with electrical load and observing the duration between the rising and falling edge and the steady state behavior, as displayed in Figure 43. In the figure, the slow rise in the stack voltage after reaching steady statue is due to the increase in temperature. The stack polarisation curve in Figure 44b was obtained using the LabVIEW software package to automate the voltage step changes with minimal duration so as to avoid an impact of temperature rise. The stack was made to operate at its ideal temperature of 60 °C.

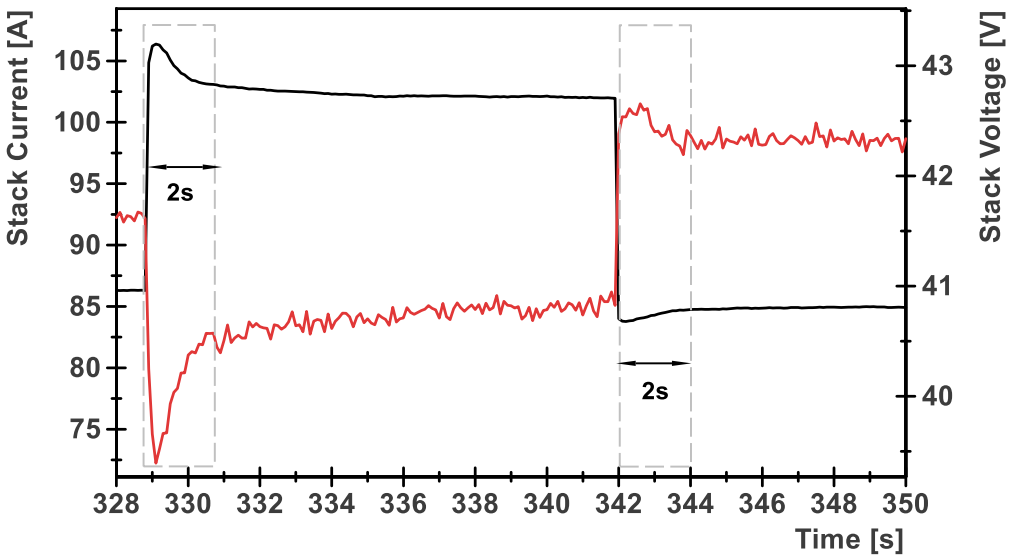


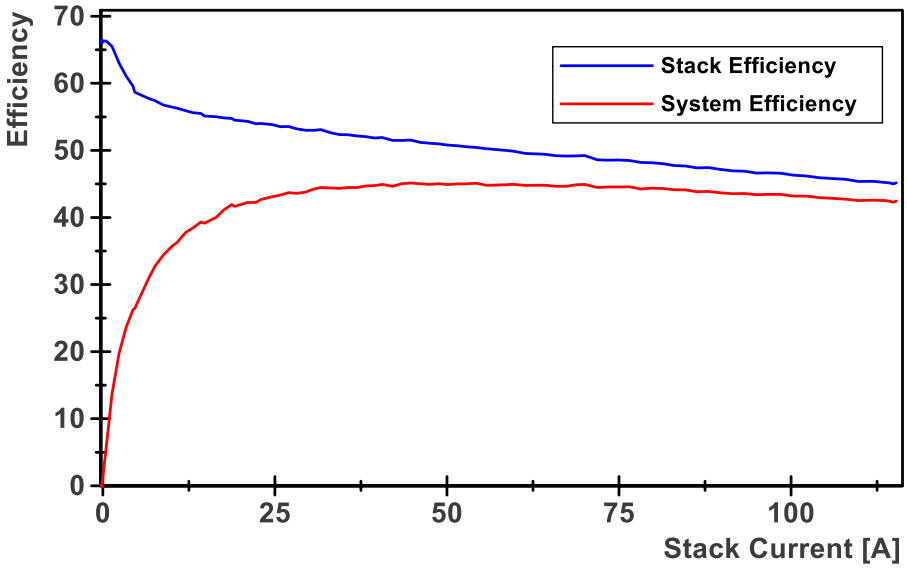
Figure 43: Step change experiment on the stack to display and extract steady state response time.

The stack and system efficiency curves were then obtained to showcase the best operating point of the stack Figure 44a. It can be seen that the stack efficiency at peak power was approx. 45 % while the system efficiency was approximately 40%. This reduced value of efficiency was attributed to the high parasitic loads at high stack power. Equations (4-1) and (4-2) describe the stack and system efficiencies, respectively.

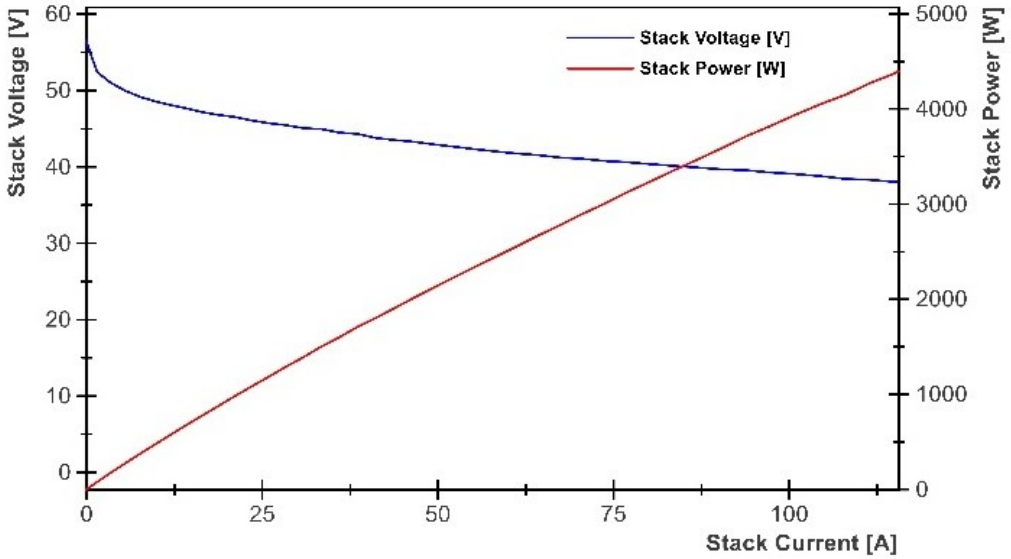
$$\eta_{stack} = \frac{V_{stack}}{1.48 \times N} \tag{4-1}$$

$$\eta_{system} = \eta_{stack} \times \frac{P_{stack}}{P_{stack} + P_{Blower} + P_{Coolant\ pump} + P_{Fan} + P_{H2\ pump}} \tag{4-2}$$

Where η_{stack}, η_{system}, V_{stack} and N are stack efficiency, system efficiency, stack voltage and cell number, respectively. The power elements in the system are stack power, P_{stack}, and auxiliary components.



(a)



(b)

Figure 44: (a) Stack and system efficiency curves, and (b) Stack polarisation and power curves.

4.6.2 Cathode Blower Experimental Modelling

System efficiency is closely related to the parasitic loads. Therefore, it is desirable to minimise the usage of active elements such as cathode air blower, heat exchanger fan, and hydrogen recirculation pump, while maintaining the stack performance. From Figure 45 it can be seen that at high electrical load (4 kW), the blower is the biggest contributor to parasitic loads. The coolant pump is usually left to a continuous operation for the precision of temperature measurement. Power consumed by the hydrogen recirculation pump is the lowest due to its small size. The heat exchanger fan is made to operate at its maximum power for a limited duration until the lower threshold of the dead band is reached.

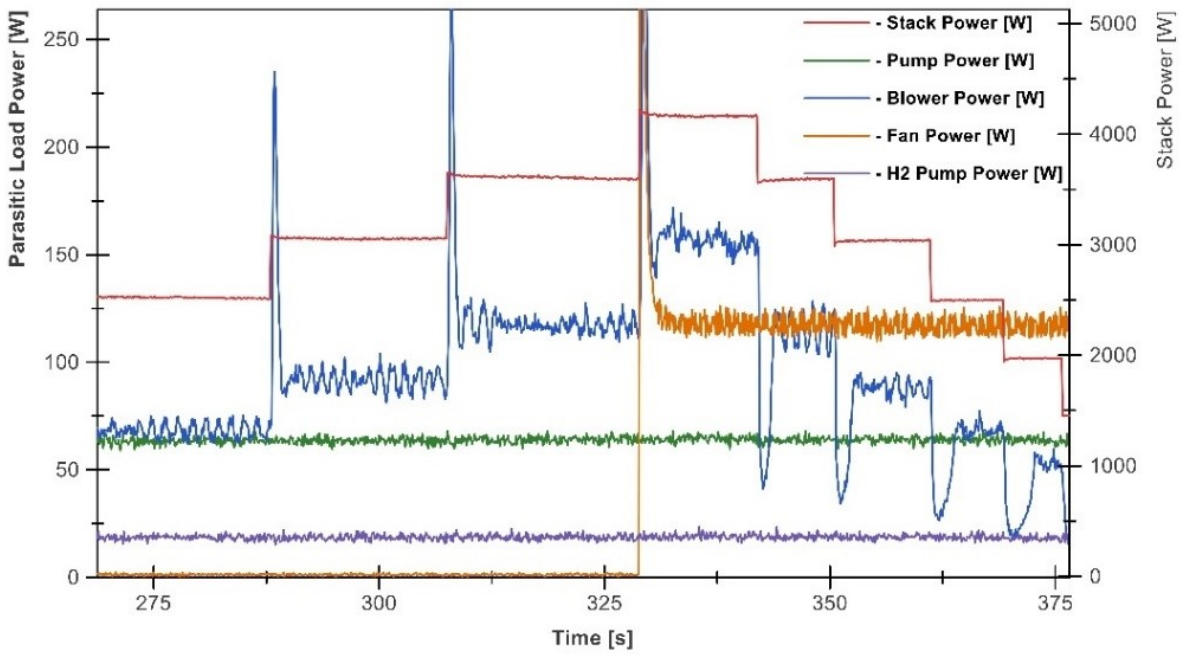


Figure 45: Example of parasitic load power consumption during step changes of stack power.

A 'black-box' modelling technique was adopted for developing a functional map of the cathode air blower. Black-box models are based on data acquired through statistical analysis or experiments wherein mapping of inputs to appropriate outputs is performed [85]. With this approach there is no need to rely on complex physical laws or governing equations. The disadvantage of this, however, is the inability to apply certain forms of optimisation techniques. The approach in this study involved taking measurements of the air flow rate at the outlet of the cathode manifold using a high range air flow meter. The large-scale flow meter enabled us to extract accurate air flow measurement values based on the control signal of the blower, without having to perform numerical modelling or requiring knowledge of the stack geometry. At the same time, power consumption values were noted against each flow rate value. These were all obtained at the steady-

state phase after every step change. Based on equation (4-3) the air usage of the fuel cell stack at a required electrical power output can be determined:

$$\text{AFR} = 3.57 \times 10^{-7} \times \lambda \times \frac{P_{stack}}{V_{cell}} \times 60 \quad [\text{LPM}] \tag{4-3}$$

Where λ is the air stoichiometry ratio, P_{stack} is the stack power and $V_{cell}$is the cell voltage. Figure 45 shows the flow rate requirement for the stack power at different air stoichiometry ratios, λ, values ranging between 2 and 6. These, when plotted against the blower power, present the capability of the blower with reference to stoichiometry ratio (SR) values. The calculated air flow rate requirements for the stack power were interpolated to fit the real AFR range of the blower, as shown below in the x-axis. The graph provides an operational map for the blower with respect to its electricity consumption and air flow rate for a chosen SR value and required stack power. These three parameters are imperative for the minimisation of blower energy use, especially in view of the non-linear behaviour of the aforementioned parameters. It can be seen in Figure 46 that the lowest and highest power consumption are attributed to SR values of two and six because of low and high flow rates, respectively. It can also be noticed that the blower is not capable of delivering the entire flow rate range with a SR of six due to it being undersized, as it exceeds the functional map of the blower.

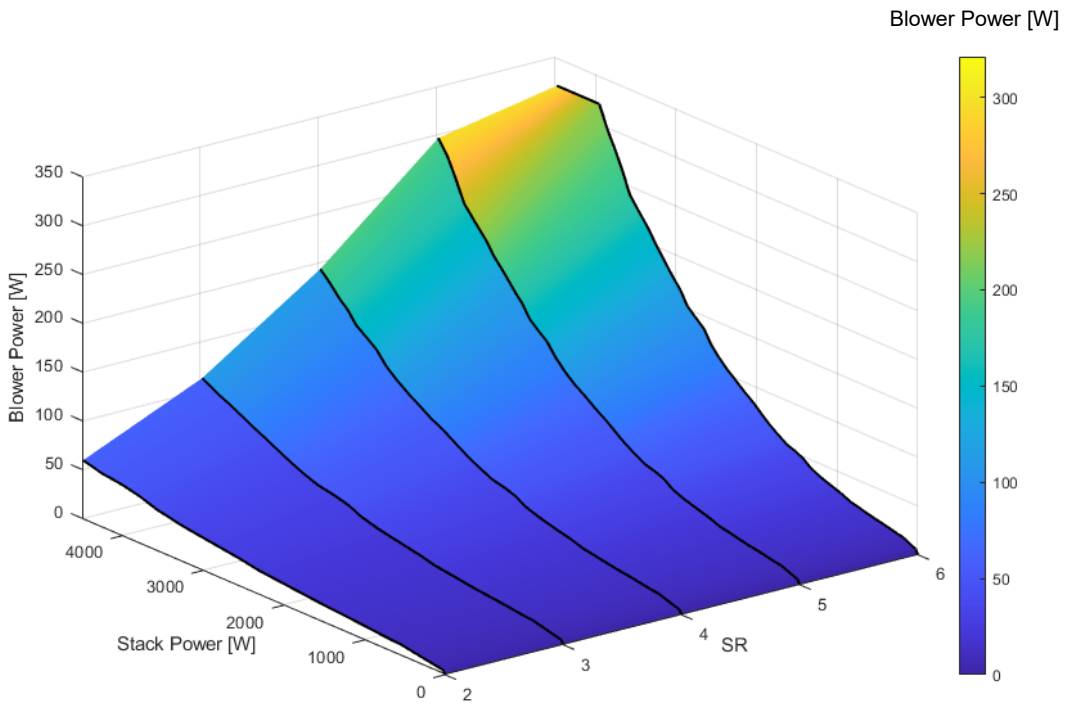
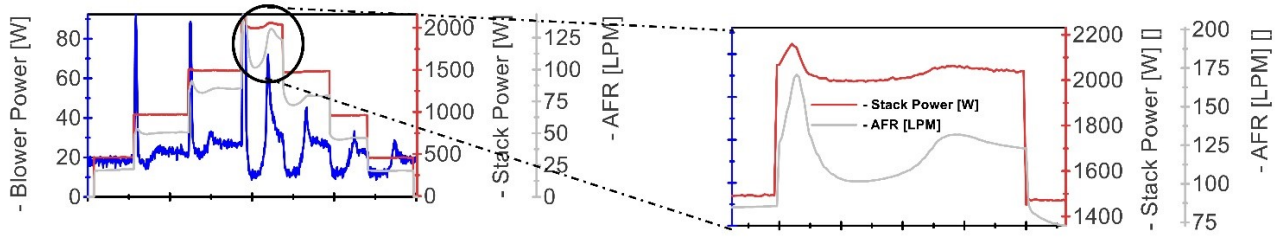


Figure 46: Cathode blower power consumption over stack power and air stoichiometry ratio.

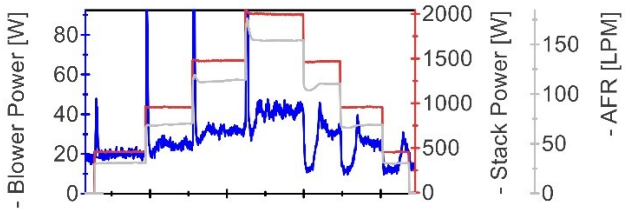
Selecting an appropriate value of air SR is crucial to deal not only with the electrochemical reaction but also for the purpose of water management. Moreover, deficiency in reactant gases, especially air on the cathode side, at high electrical loads can lead to fuel starvation. Fuel starvation is defined as the phenomenon of having insufficient supply or slow transport of the reactants to the reaction sites [86]. The reactant starvation phenomenon can be distinguished into two categories based on the starvation area and magnitude; local and overall starvation. Local starvation occurs at a cell level due to uneven distribution of gasses on the surface of the electrode. The effect of this is usually a drop in output performance [87]. Overall oxidant feed starvation occurs mainly due to external components such as compressors or blowers which, at a sudden change in demand, lag in supplying the stoichiometric value of air – thereby causing a major

reduction in performance [87]–[89]. In our work, we have aimed primarily at implementing an experimentally derived blower functional map so as to fulfil the required air flow rate without causing fuel starvation and significant effect on the system efficiency. Thus, neither optimisation nor dynamic calculation of the SR value were considered, as seen in the work done by some authors [90], [91].

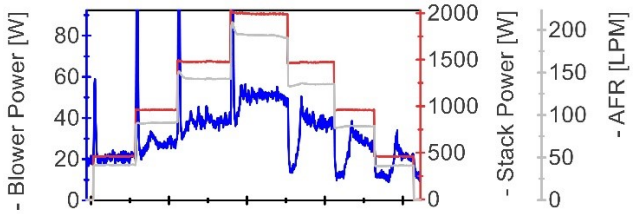
Figure 47 illustrates a sensitivity analysis performed in order to illustrate the effect of oxidant fuel starvation at a low air SR levels. The rationale for determining the optimal value is evident in the figure, where fuel starvation is seen with low air SR value of 2 at medium electrical load. Specifically, the step change in the electrical load value creates an abrupt demand for reactants. In the event of slow supply of reactants, and oxygen starvation is seen as illustrated in Figure 47a. Higher values of air SR resolve this issue (Figure 47b, c, d), however, the blower power consumption also increases. Although oxygen starvation is not seen when operating the stack with SR value of 3 or higher, an SR value of 4 is preferred because of the need to avoid water flooding in the cathode stream, thanks to the relatively higher flow rate. However, this comes with a small trade-off in terms of blower power consumption. Figure 47 (e) displays the high power demand being met with the aforementioned value of air SR, i.e. 4.



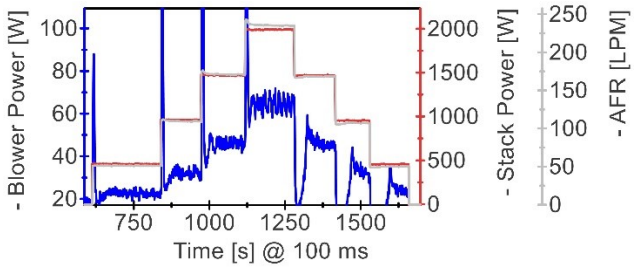
(a)



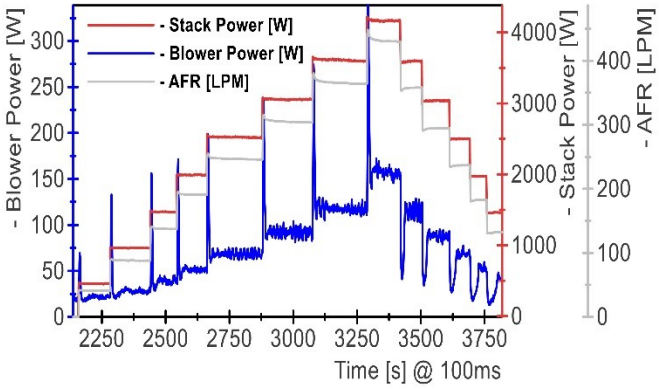
(b)



(c)



(d)



(e)

Figure 47: Sensitivity analysis on the impact of air SR value – (a): SR = 2, (b): SR = 3, (c): SR = 4, (d): SR = 5, (e): full load test at SR = 4.

4.6.3 Hydrogen Purging Strategy

The voltage drop caused by the accumulation of inert gasses and water formation in the anode can be recovered by purging the anode compartment. The frequency of this event will depend on the design of the hydrogen anode subsystem – as evident from the results presented later in this paper. The rationale and need for purging hydrogen has already been discussed in earlier sections. This section will describe the methodology adopted for determining when and how precisely to purge. Various purging strategies used in previous work by different authors involve complex models, additional sensing instruments and components such as water separators [92], [93]. Here, we propose a novel method which makes use of the stack current rather than cell voltage or nitrogen concentration within the anode stream. As a result, the purging event can be triggered when a certain value of Ampere-hour (Ah) is reached. The following equation (4-4) is used to determine the Ampere-hour (Ah) value:

$$\mathrm{Ah} = \sum I_{stack} \times \frac{T_s}{3600} \tag{4-4}$$

This equation allows to purge solely based on the current produced by the stack instead of devising fixed purge cycles. The justification for this is the underlying assumption that the level of impurities in relation to the hydrogen content is constant. Upon which the current, as a measure of hydrogen consumption, can be used as an indicator. With an anode recycle loop this will slightly vary. Therefore, purging strategy differed for dead-end and recirculation modes, mainly in terms

of frequency. In the recirculation mode, the recirculation pump was stopped during the purging event so as to allow a smoother passage for the exhaust gas stream. Figure 48 shows the flowchart highlighting the sequence of actions and processes concerning the anode purging strategy. The automated purging strategy involved constantly measuring and monitoring the stack current to be able to derive the Ah value and cumulate the value over every time interval. This Ah value, in real time, was reset once a pre-defined value was reached and after the purge duration was complete. The 'purge operation' began by changing the normally closed state of the solenoid purging valves to open, allowing a path for accumulated gasses and water to leave the anode stream. The purge valve was reverted to its original position as soon as the maximum purging duration was reached. Based on the electrical load, the purge duration was kept in the range of 0.5 to 0.8 s. Furthermore, having a variable and use-dependent purging strategy can save considerably on hydrogen fuel. For this reason, several authors have experimentally validated the correlation between the electrical load and purge duration or purge cycles [50], [62], [63], [94]. For example, Jian et al. [50] have conducted experimental work on a PEMFC stack with different purging durations at various current density values. Amongst their findings were that with longer purge durations at higher current density a more stable voltage trend was seen. Longer purge durations offer a larger window for the flooded water to clear from the anode side. Similar findings were reported where long purge durations were considered [62]. One of the key findings in the aforementioned report was that the

nitrogen content, as a result of backmixing, can be trapped inside the water volume and require long purge durations to discharge through the purge valve.

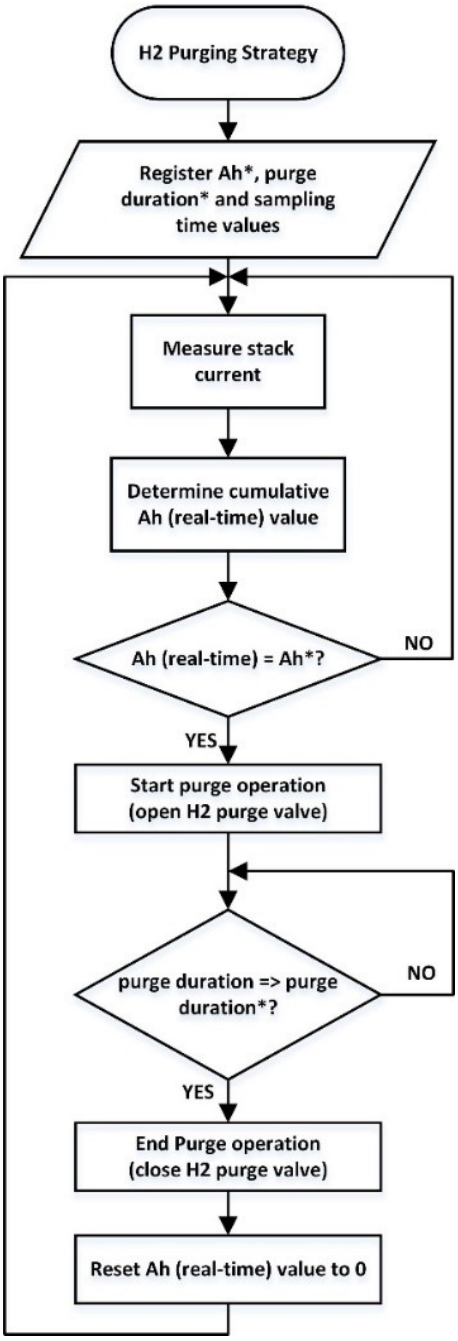


Figure 48: Flowchart describing the purging strategy's operation.

4.6.4 Comparative Analysis

In this sub-section, a comparative analysis will be presented, showing a clear distinction between the two most common anode sub-system designs; dead-end anode with and without recirculation. Also outlined in this section are the key benefits in terms of hydrogen utilisation and costs.

The most useful output parameter in identifying the effect of uneven gas distribution and water flooding inside the stack is the cell voltage. In the experiments carried out, the current drawn from a constant resistive load was programmed to operate in a current-controlled mode. Two separate experiments were carried out for each anode design in order to see the aforementioned effect. For safety of the stack health and to avoid any undesired negative impacts, the dead-ended anode experiments were carried out using a relatively low electrical load. The discussed purging strategy was implemented in both cases. Furthermore, the stack was operated at around the recommended operating temperature of 60 ^{o}C and anode pressure of 1.5 bar. The dead-band temperature setting for the experiments was between 54.5 ^{o}C (lower threshold) and 55 ^{o}C (upper threshold). The employed experimental setup and the software-hardware interface has been discussed in sections 3.4 and3.5, respectively. In order to avoid oxidant fuel starvation, the cathode blower was made to operate at a sufficiently high flow rate. The unregulated hydrogen flow rate was measured using a high capacity electronic MFM, well capable of measuring the maximum stack fuel flow

rate of up to 75 slpm. The real-time monitoring system had a sampling time of 100 ms. Individual cell voltages were monitored and logged using an advanced cell voltage monitoring (CVM) unit. Without this device, it was not possible to witness any of the stated effects clearly while being certain of their locations. The purity of hydrogen used in the experiments was of a high grade 99.99 %.

In the case with no recirculation, the results clearly demonstrated the need for frequent purges. Figure 49 shows the results obtained from an experiment on the stack with the aforementioned design at a medium level electrical load of 2 kW. The stack voltage clearly dropped, either after a short period of time, or upon drawing a certain number of Ah. This, as described in the previous section, was a result of accumulation of inert gases and water. When hydrogen was purged through the purging valve, indicated by a sharp spike in the flow rate measurement, the stack voltage reverted to its normal value. Thus, there are three instances during the experiments which show different voltage drop levels based on different Ah values. For example, in the middle region of the experiment it can be seen that there was a voltage drop of 0.63 V after drawing 47A for approximately 6.5 minutes or 5 Ah. This implied a purging event at approximately every 5 Ah of charge accumulation. Similarly, two other instances showed a smaller voltage drop of 0.28 V and 0.48 V with relatively lower Ah values. In order to minimise the effect of temperature rise the dead-band settings were such that a 0.5 to 1^{o}C difference was achieved.

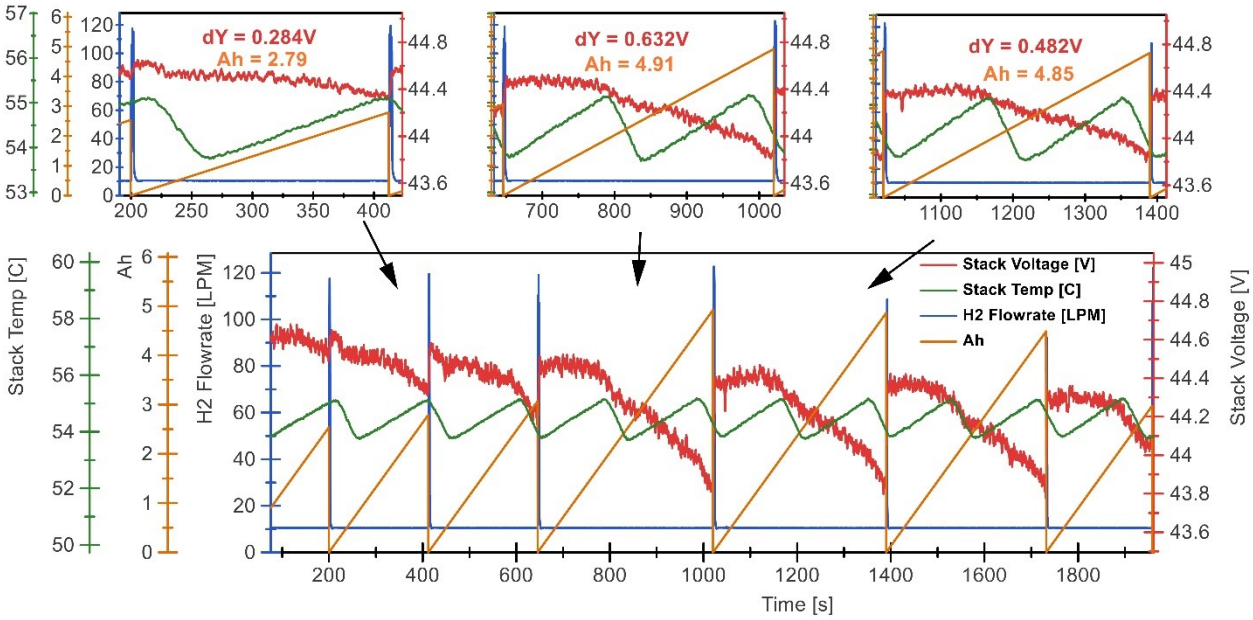


Figure 49: Outcome of hydrogen purging experiments without recirculation.

In contrast to the above design, employing the hydrogen recirculation pump in the anode stream helped in observing a significant improvement in stack voltage. Figure 50 shows the results of an experiment conducted under high electrical load of 4 kW - twice the value considered in the previous experiment. Similar configurations with regards to the electronic load were used. As shown, the results depict no evidence of voltage drop, after the start of the system which involves a purge event, until approximately 6.5 minutes of operation. This drop was found to be 0.08 V and can be considered negligible. The next two segments of the experiment shows a larger drop in stack voltage of 1.2 V, which suggests that a purge event in this range is ideal. This range having drawn approximately 100 A for the duration of approximately 15 to 20 minutes (where the evidence of at least 1.2 V drop is noticed) corresponded to 22 to 32 Ah range. Hence, a purge

event from the anode compartment within this range can be considered ideal in order to avoid seeing undesired performance. Furthermore, after the second purge in the experiment, a full recovery of the stack voltage (40.73 V) was observed. This purge event corresponded to 43 Ah, with a maximum voltage drop from the initial point of 1.3 V. The fluctuations seen in stack voltage readings are evidently due to the rise and fall of the temperature.

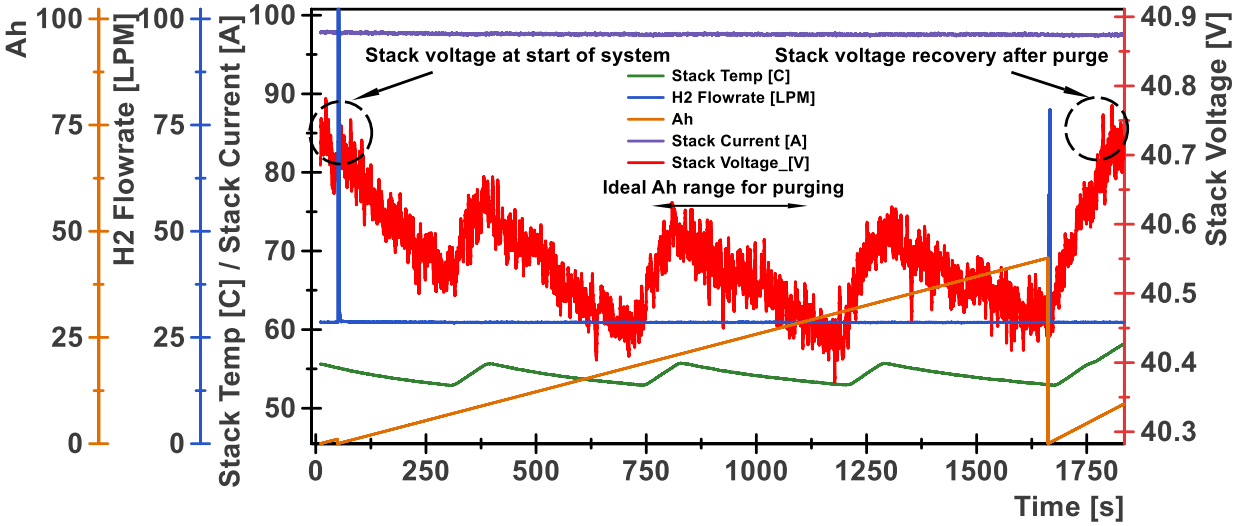


Figure 50: Hydrogen purging experimental outcome with recirculation.

The volumetric flow rate of hydrogen lost in the event of a purge equals the difference between the working flow rate of hydrogen into the stack inlet, $\dot{V}_{\text{inlet}}^{\text{H}_2}$, and the hydrogen consumed, $\dot{V}_{\text{cons}}^{\text{H}_2}$ - which is a function of the stack current. This can be mathematically expressed as below;

$$\dot{V}_{\text{loss}}^{\text{H}_2} = \frac{1}{t_{\text{open}}} \int_0^{t_{\text{open}}} \left(\dot{V}_{\text{inlet}}^{\text{H}_2}(t) - \dot{V}_{\text{cons}}^{\text{H}_2}(t)\right) \text{d}t \; [\text{ls}^{-1}] \qquad (4\text{-}5)$$

Where t_{open} is the duration the purge valve is open during which hydrogen is allowed to pass through the exhaust. The hydrogen used for operating the

recirculation pump can be computed based on the power of the pump, P_{pump}^{el}, for the complete operation of the stack, as expressed in the equation below.

$$E_{pump}^{el} = \int_0^{t=end} P_{pump}^{el}.\,\mathrm{d}t\ [\mathrm{Wh}] \tag{4-6}$$

Thus, an estimate can be obtained for the total cost in terms of fuel disregarded during purging over the period of stack operation using the relationship below.

$$\mathrm{Cost}_{\ \mathrm{purging}} = \dot{V}_{\mathrm{loss}}^{\mathrm{H_2}} \cdot \left(\frac{PM_{\mathrm{H_2}}}{RT}\right) \cdot \frac{t_{\mathrm{open}}}{t_{\mathrm{frequency}}} \cdot \mathrm{Cost}_{\mathrm{H_2}} \cdot t[\$] \tag{4-7}$$

Where $M_{\mathrm{H_2}}$, P, R and T are the molar mass of hydrogen, pressure, gas constant and cell temperature, respectively. The frequency of the purging, $t_{\mathrm{frequency}}$, is taken into account in the calculation.

In terms of fuel usage it becomes apparent that the dead-end without recirculation design requires at least ten additional purges, compared to the design employing recirculation, for the same length of experiment if operated at 2 kW electrical load. The operating cost of the small size recirculation pump, at mean operating power of 25 W, would amount to 0.025 kWh to operate for one hour. For recirculation in anode, this amount of energy consumed from hydrogen fuel is significantly less when compared to the frequently purged hydrogen. Table 5 presents results based on equations (4-5), (4-6) and (4-7) and the experiments discussed earlier in this chapter. The cost and amount of hydrogen used in the dead-end without recirculation design is more than two times that of the recirculation mode. This is mainly due to the fact that the former design requires ten purges whereas the latter requires only four. Thus, above set of experimental results clearly show the

frequency of purging events required in both scenarios which may be used for further optimisation that can lead to improved fuel utlisation values.

Table 5: Indicative calculations based on the experiments on hydrogen purging.

Test Parameters		
Stack Load	2 kW	
Operating time	60 minutes	
H2 flow rate	0.0017 kg/s	
Purge duration	0.8 s	
Anode Loop Design	**Recirculation**	**Dead End - without recirculation**
Pump energy requirement [in kWh]	24.9	N/A
H2 amount for operating pump [kg]	0.0006	N/A
Purge frequency	4	10
H2 consumed for purging [kg]	0.0055	0.0139
Cost of green H2 (at 9 $/kg) [$]	0.0557	0.1253

A clearer observation can be made by visualising the behavior at a cell level with the help of the CVM. The compact CVM incorporated in the PEMFC system was an advanced modular unit designed for fuel cell applications with a 12-bit resolution or 1 mV, and scan rate of up to 1 kHz. For the purpose of comparison, the experiments in Figure 10 had the exact same settings in terms of electrical load, purge duration and intervals. Observations in each experiment were split into three parts; the stage after the first purge, the middle stage and the recovery after the second purge. These completed an entire purge cycle operation, which enabled us to view both the negative effects and recovery. The contrast between the two anode feed modes is apparent in Figure 51. The experiments were

conducted at 2 kW electrical load under same operating conditions. Sub-figures (a), (b) and (c) correspond to dead-end without recirculation, whereas (d) corresponds to experiments including a recirculation pump. In the recirculation mode case, there was little discrepancy or fluctuation in cell voltages, whereas in the absence of recirculation evidence of performance degradation is clearly visible. For example, in Figure 51(b) some of the cells experienced a voltage drop of up to 0.15 V. Moreover, irregularity as a result of water and inert gasses accumulation starts to appear in the cells. A full recovery after purging is apparent in Figure 51(c). On the other hand, with the recirculation pump in operation, the voltage drop after the same amount of time or Ah value was minimal as shown in Figure 51(d). It can be noticed in Figure 51(i) that cell 1 experienced a relatively higher voltage drop due to flooding caused by excess water formation. In addition, this can also be attributed to the counter-flow channel design wherein cell one was on the opposite end from the cathode air inlet. Several authors in the literature have documented similar experiences, where an individual cell experiences irregularities as a direct result of flooding phenomena [58], [95]. Figure 51(ii) illustrates the uniform distribution effect of hydrogen recirculation in the anode side which results in a negligible voltage drop. In addition, as evident cell 1 offers a superior performance with improved voltage level of 0.685 V as opposed to 0.426 V in the previous case. Labels a, b, c and d correspond to instances where individual cell voltage measurements were taken.

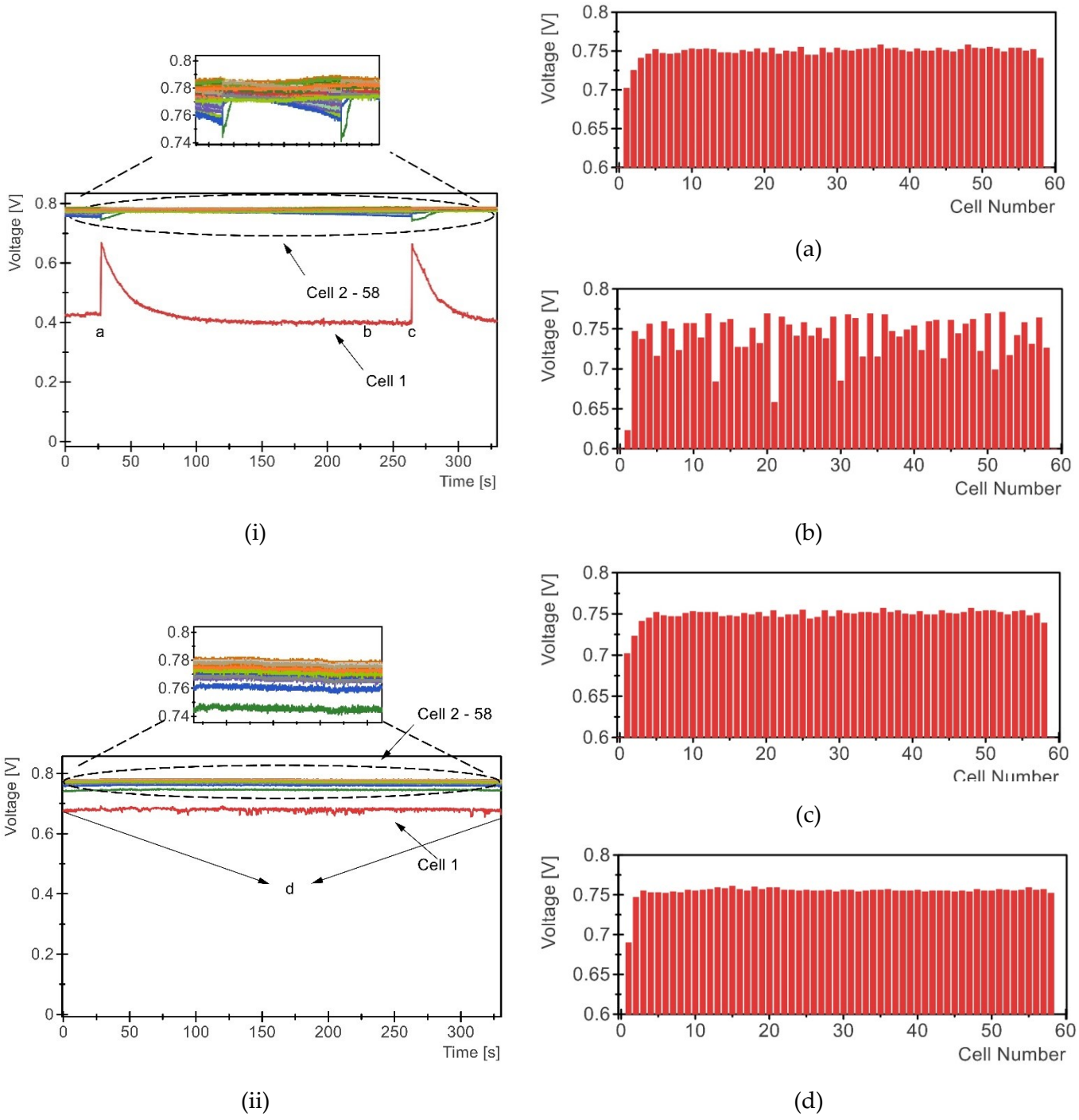


Figure 51: CVM data for the stack with anode without recirculation: Figures a, b, c corresponding to events in (i), and recirculation: Figure d corresponding to (ii).

4.6.5 System Control

The PEMFC system required a dedicated instrumentation and software-hardware interfaces for the purpose of implementing a control strategy. For the former, these included current & voltage transducers, relative humidity, hydrogen and

temperature sensors. For the latter, the LabVIEW software with a robust hardware interface was implemented. With such software-hardware interface inplace, a sampling rate of 1 μs was possible as well as real-time data monitoring and logging. The control system should react to events such as changes in electrical load demand by adjusting the cathode air flow rate, react to hydrogen gas leaks by initiating emergency shut down, and to a thermal imbalance due to temperature rise and buildup of inert gases or water in the anode stream by periodic purging. Figure 51 illustrates these events through an experiment conducted with the stack BoP connected to a 5 kW electronic load. It can be seen in the figure that label '1' depicts the cathode blower reacting to a step change in the electrical power of the stack by increasing the air flow rate. Similarly, label '2' depicts the stage where the BoP reacts to a temperature rise by turning on the radiator fan and adhering to 'dead band' threshold values of 55 ^{o}C and 54 ^{o}C. Label '3' shows the predetermined periodic purge cycles where the purging valve was opened for a set duration of time. The frequency of the purge cycle was based on the charge transfer of the stack (Ah value).

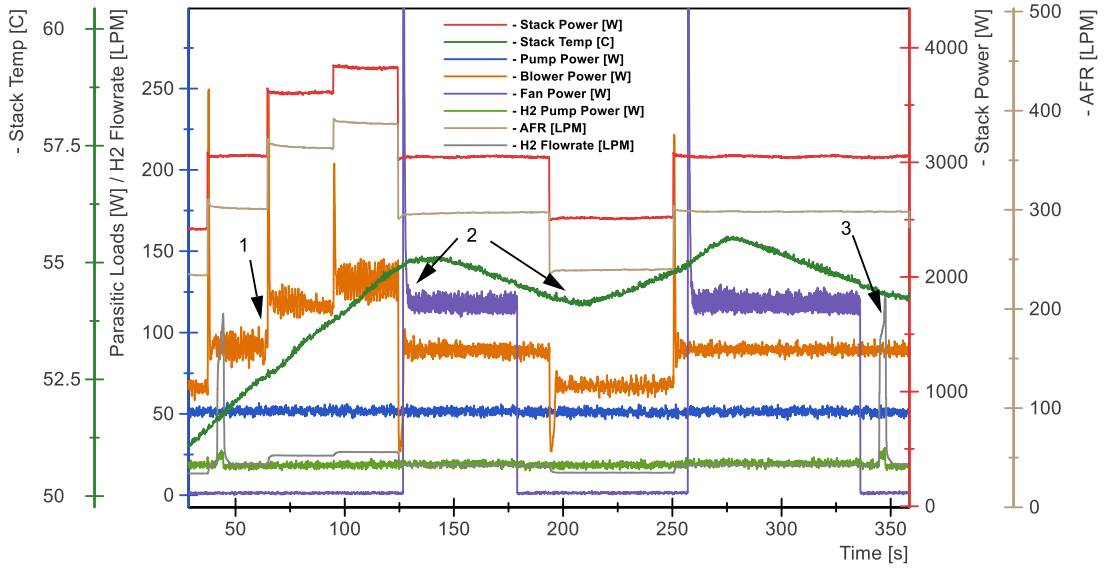


Figure 51: Illustration of PEMFC system control - 1: blower reacting to higher air flow rate requirement. 2: dead band temperature control, 3: purging event based on a set Ah value.

4.7 Conclusions

In this paper, a complete control system for a PEMFC BoP was proposed and validated experimentally. The cathode air blower, which was evidently also the biggest contributor towards PEMFC parasitic loads, was experimentally modelled with the goal of minimising its use. An appropriate air SR value was obtained through a sensitivity analysis. The rationale for having hydrogen recirculation was presented and a novel purging strategy based on the cumulative current flow parameter was evaluated. Our findings are in agreement with similar work by previous researchers and suggest that having a recirculation pump is advantageous. A sensitivity analysis on a key parameter, the air stoichiometric ratio, was performed. The specific findings are summarised below;

- A PEMFC BoP requires attention and programming in four different sub-systems, anode feed, cathode feed, thermal management and electrical

subsystem. Each of these require appropriately sized and calibrated devices. This was achieved by experimentally modelling the cathode blower to map the power consumer, air flow rate with stack's power. The blower also plays a crucial role in dealing with clearing excess water formation in the cathode stream. In addition, operating points where the blower was undersized were highlighted.

- A uniform reactant gas distribution in the anode channel reduces the need for frequent purges, thereby significantly improving the fuel utilisation. Additionally, our findings suggest that, with hydrogen recirculation, negligible voltage drop is seen for a limited period. An ideal range of Ah value between 22 and 32 Ah was experimentally investigated. However, there are capital costs attached to this scenario depending on the size and type of hydrogen recirculation pump.

- A novel purging strategy was proposed which was based on the cumulative Ah value. This parameter was acquired from the stack current using high accuracy current transducers and was independent of the stack operation time. Once the set value, present within identified ideal range, is reached the purge event is triggered and the Ah value is reset. The automated purging strategy was discussed and validated experimentally on the 5 kW PEMFC system while considering both anode feeding modes; dead-end anode with and without recirculation. It is evident from our

results that in the case of the former, a full recovery from stack voltage drop was achievable. Finally, through experimental data and numerical relationships, it was found that the magnitude of cost and amount of hydrogen needed for dead-end without recirculation mode is at least two times higher. This entailed less frequency of purge intervals in the recirculation design.

- Parasitic loads have a direct effect on the system efficiency, with the cathode air blower being the biggest contributor. It is, therefore, imperative to minimise its use while maintaining a stable performance. In our work, we presented a 'black-box' modelling approach to experimentally model and validate the blower's functionality. Our findings suggest that an air SR value of 4 is most appropriate for avoiding oxidant fuel starvation and at the same time not adding significantly to the parasitic loads.

5 FCHEV Modelling and Simulation

This chapter presents the design and simulation of the vehicle model environment used for developing a rule-based control strategy. A detailed model incorporating various subsystems is included within the model to take into account appropriate factors. AVL Cruise M was chosen and used to a forward-facing model which accurately represents the test vehicle in as much detail as possible. The rationale behind choosing this software package was based on the simplicity and calibration details available in blocks such as battery, E-motor, axle, and brakes. Data from experiments or manufacturer's datasheets could easily be integrated. In addition to these aspects, Cruise M allows convenient co-simulation with third party software such as Matlab. This feature will be exploited later in the design optimisation study in Chapter 7.

The structure of this chapter begins with a description of hierarchical modelling approaches as undertaken in this project. A detailed description of each of the component models provided. Following this, the chapter presents the results obtained by simulating a rule-based controller design implemented within the model, while highlighting the performance and, limitations and comparison with a benchmark vehicle, Toyota Mirai.

5.1 **Model Based Design**

Modelling of a system allows the designer to reap several types of benefits which include detail-specific scrutiny, shorter investigation time and cost-effectiveness. Based on experimental data or empirical studies, the model equations can be established, depending on the desired level of detail. Such models can then be integrated with other pre-built or pre-developed models to simulate the entire system such as an electric vehicle powertrain. This approach is generally known as Model Based Design (MBD). MDB can assist, and up to a certain degree, ensure safety, speed, repeatability and reliability. At the early stage of the system design, simpler models are built when specific key parameters of the project are unknown or are yet to be determined. Such models are also useful in studies such as component sizing where intricate details of certain sub systems do not affect the results. This model will offer simulation results, based on a state-machine control strategy, of a fuel cell powered vehicle hybridised with a battery pack.

Generally, there are two main approaches of implementing MBD; dynamic and quasi-static modelling. The former method uses differential and algebraic mathematical tools to describe a physical system. These equations consider the transient as well as static nature of the system operation. As a result of this, depending on the complexity of the model, the computational burden could be heavy. On the contrary, a quasi-static method runs the model in fixed time steps with constant system input such as velocity, acceleration, etc. A detailed analysis

of the different approaches has been presented in the literature [96]. Furthermore, the vehicle models can be classified into either forward or backward oriented models. Forward facing models differ from backward facing models such that the specified input such as the velocity and acceleration derived from a typical drive cycle. In this way, the actual velocity can be determined based on the reference value with the help of the controller. In this work, the forward facing modelling approach has been adopted due to the aim of studying controller behaviour.

5.2 **Literature Capture**

Every hybrid powertrain requires a sophisticated control system. In a conventional non-hybridised vehicle, the controller is usually calibrated to meet pre-defined operating points due to single power source on-board. However, the complexity level grows in a hybridised powertrain since the power demand can be fulfilled by multiple sources, as seen in an ICE-hybrid or FCHEV. This entails there is additional degree of freedom in terms of control system. Furthermore, the decision to maintain the state of charge (SoC) of the battery by replenishing it from the primary or the dominant power source is essential. All of these decision-making processes fall under the responsibility of the supervisory controller, which operates according to the energy management strategy (EMS) implemented in the design. There is strong dependency of the overall system efficiency on the controller. There is an extensive amount of investigative work found in the literature within the realm of rule-based or heuristic controllers and their

optimisation. A well-devised and implemented EMS within the controller has proven to offer multiple benefits such as better fuel economy [97]–[100]. Moreover, it can be said that the key role of the EMS is to manage, monitor and regulate the power and energy requirements from the energy storage devices on-board the vehicle. In the case of FCHEVs, using these energy storage devices acts like a buffer in order to meet transients, which in turn also mitigates fuel cell degradation [101]. Although the EMS is not directly in charge of the fuel cell, the decisions made by the supervisory controller - which is governed by the EMS – can have an effect on cell degradation. The US department of energy has set a target of achieving a 5,000 hour lifetime for fuel cell based vehicles [102]. Currently, PEM fuel cell type maximum lifetime reached is at least 4,130 hours [103] compared to 3,500 hours in 2012 [104]. This trend according many FC manufacturer is bound to exceed 5,000 hours [105]. In this context, there were two main strategies identified from the literature for mitigating fuel cell degradation; reduction of transient loading and avoidance of reactant starvation. Thounthong *et al.* [106] investigated and validated on a small-scale physical model the prevention of the fuel starvation phenomenon by liming supply of the peak power by controlling the fuel flow. Instead, the transient power demand is fulfilled by secondary energy sources such as battery and supercapacitor. Furthermore, their work proves the advantage of downsizing the fuel cell stack. Others, Pukrushpan *et al.* [107], Vahidi *et al.* [108] and Greenwell *et al* [109] employed a different strategy by controlling the oxygen flow to prevent fuel starvation.

There are numerous approaches to rule-based control strategies system engineers can employ for a variety of applications. The complexity of a strategy is defined by the practical implementation, especially in an automotive testing and validation environment. Furthermore, novel methods adopting machine learning based strategies such as neural networks, dynamic programming and game theory are gaining interest in the automotive industry, focusing on online optimisation techniques. These are considered to be better in terms of accuracy of results than heuristic methods because they adopt a vehicle model within the EMS for optimisation, while using a cost function [110]–[112]. For specific drive-cycle comparison and analysis, a more robust strategy known as Deterministic Dynamic Programming (DDP) is applicable. DDP maximises the performance of HEVs by designing a logical rule-based strategy [113]. In addition, Stochastic Dynamic Programming (SDP) is commonly employed to generate models which are dependent on the state of the system, by finding the optimal control action [114].

Heuristic EMS strategies are generally considered as robust and come in varying forms of complexity. They, however, require manual tuning and as a result can become time-consuming [101], [115]–[117]. These controllers use a pre-defined set of rules to determine the operating state of the system. Rule-based controllers are considered to be the simplest forms of control for energy management. Work done by Bauman and Kazerani [101] highlights a simple rule-based strategy to a charge the battery in the FCHEV powertrain only when the SoC is below 50 %. This is to

reduce the ohmic losses associated to DC/DC converters and cycling efficiency of the battery. Schaltz *et al.* [117] use a similar approach with the difference being that the fuel cell used as the primary source and controlled on the basis of load demand of the vehicle. Furthermore, Rousseau *et al.* [118] propose another approach by setting specific rules for each component in the powertrain as well as the fuel cell balance of plant.

As with every system, vehicle propulsion systems have multiple states which require specific rules for that particular state, generally referred to as state-based controller. These a more complex than rule-based because each state has its own control options devised and can sometimes use other state's variables to fulfil the requirements. For example, Schiffer *et al.* [119] have explored the strategy with four states; stationary, acceleration, constant speed and braking. Each of these states, dedicated control actions are designated. Similarly, Motapon *et al.* [120] have performed a comparative study of EMS controllers for a fuel cell hybrid emergency system for an electric aircraft. Their methodology involved state machines strategy based on the fuel consumption, battery and supercapacitor SoC and overall efficiency as cost functions.

Another method of implementing a rule-based control system is known as the Equivalent Consumption Minimisation Strategy (ECMS). This technique focuses on monitoring the fuel consumption related to the SoC fluctuation of the battery. The cost function is the addition of the primary fuel consumed and the equivalent

fuel consumed in relation to the use of the battery. This can be described from the equation, where $\dot{m}_f\left(P_E(t)\right)$ represents the fuel consumption and $\zeta(P_b(t))$ represents the fuel consumption equivalent of the electrical energy

$$J_t = \dot{m}_f\left(P_E(t)\right) + \zeta(P_b(t)) \quad (1)$$

ECMS offers the advantage of optimising the controller for fuel economy and at the same time maintaining the battery SoC. There are several reasons for the implementation of ECMS in the automotive industry at a wide range; they are relatively simple to implement for real-time control, optimisation of emissions, and drive-ability target [97]. Johnson *et al.* [121] have conducted work on real-time control strategy with the cost function being emission regulation. The use of theoretically derived graphs to map the fuel consumption to battery SoC was adopted. They concluded from their work that the SoC of the battery varying with vehicle operation, the equivalent amount of power supply from the battery can be enhanced, in addition to meeting the aforementioned targets. Validation of real world vehicles using a software model is scarce in literature, therefore, this work sets out to implement the control emulating a commercial vehicle and analysing the results. The developed model mimics the same type of vehicle architecture that suffices the requirements at a system powertrain level.

5.3 Vehicle Performance Considerations

5.3.1 Powertrain Configuration

The topology of an EV is described by the interconnection of the system components. There is a vast amount of literature dedicated to analysing different topologies [25], [122]–[124]. Generally, the placement and location of electrical systems such as the storage device and the DC-DC control unit distinguishes the type of topology adopted (series, parallel or power-split configuration). However, there can be other factors such as load characteristics, amount of regenerative braking energy available, DC bus voltage range and unregulated FCS voltage output that can dictate the operating point [125]. In this work, the propulsion system is comprised of only one DC converter connected in series with the FC system. This converter boosts or steps up the unregulated power output from the FCS to match the DC bus voltage. It should be noted that the power range of the primary power source and the energy storage device should always be maintained at the relevant voltage level. Hence, the boost converter requires the low voltage side to be lower than the high voltage side at all operating conditions to avoid mismatch in the shared DC bus with the battery. Figure 52 depicts the propulsion system block diagram adopted which is comprised of PEMFC stack with its BoP, battery pack, DC-DC converter, DC-AC inverter and E-drive unit consisting the motors.

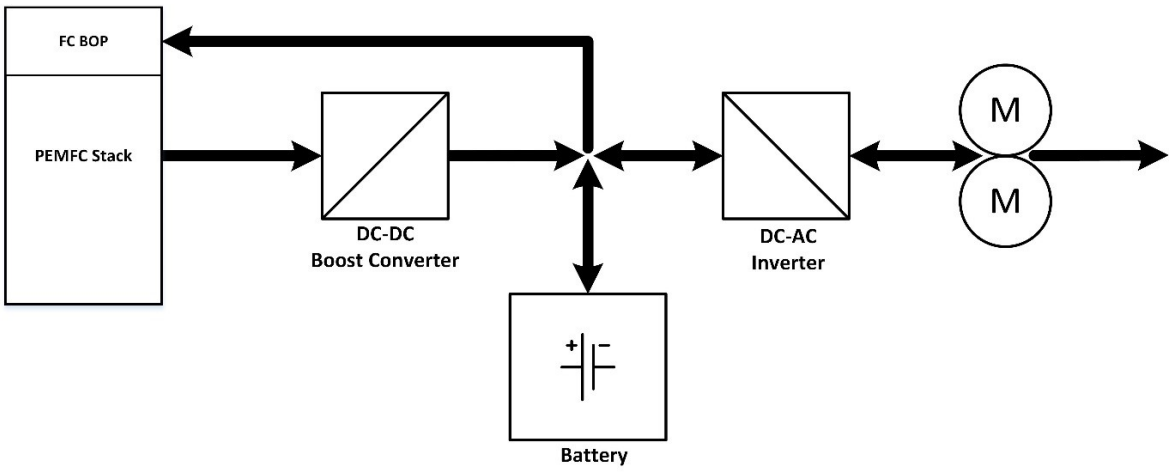


Figure 52: Block diagram of FCHEV propulsion system.

5.3.2 Drive Cycle Analysis

The two drive cycles in this work were the New European Driving Cycle (NEDC) and Worldwide Harmonized Light Vehicles Test Procedure (WLTP). The former is a drive cycle designed to represent typical driving conditions experienced in European countries while the latter replicates a more realistic scenario involving transients and unsteady accelerations. Historically, the NEDC test cycle was used to establish the fuel economy and emissions from passenger cars and light commercial vehicles running on conventional fuels such as petrol and diesel. The WLTP includes more transient phases as opposed to NEDC, the acceleration rates also better reflect real-world driving conditions. For this reason, it has replaced the NEDC cycle with the WLTP cycle. The average speed in the WLTP cycle is 46.5 km/h, compared to 34 km/h for NEDC testing, and the maximum speed for the former is 131.3 km/h compared to only 120 km/h for the latter. The cycle testing time ranges from 20 minutes for NEDC to 30 minutes for WLTP. The trip journey is 23.25 km (14.5 miles) distance during the WLTP test, as opposed to 11 km (6.8

miles) for the NEDC. The WLTP cycle comprises of four phases distinguished based on the vehicle speeds. Table 6 summarises the key metrics of the two considered test cycles while Figure 53 and Figure 54 illustrate the power, speed and acceleration profiles.

Table 6: NEDC and WLTP test cycles metrics

	NEDC	WLTP
Maximum Speed (mph)	74.5	81.5
Distance (miles)	6.8	14.5
Average Speed* (mph)	20.7	28.8
Idle time (s)	267	234
Full duration (s)	1180	1800
Peak Acceleration (m/s2)	1.04	1.58

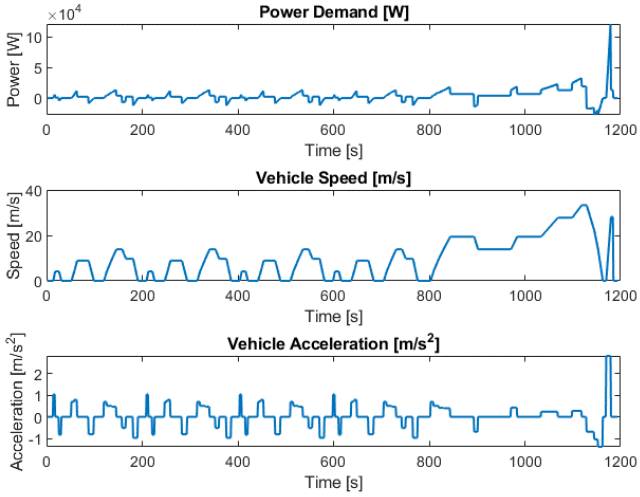


Figure 53: NEDC test cycle power, speed and acceleration profiles, with peak acceleration profile integrated in the end of the cycle.

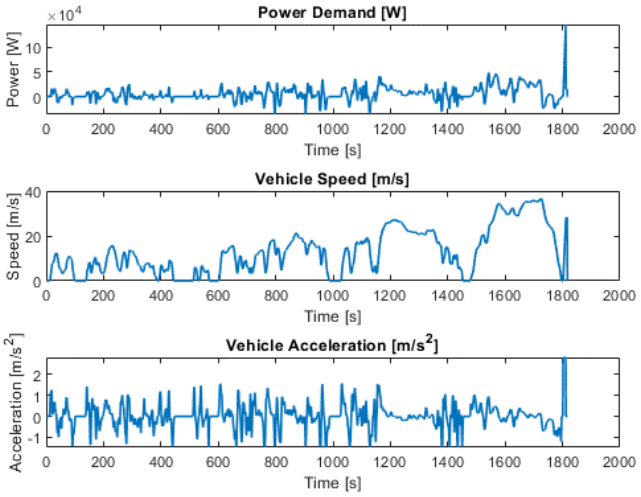


Figure 54: WLTP test cycle power, speed and acceleration profiles with peak acceleration profile integrated in the end of the cycle.

5.3.3 Regenerative Braking

One of the most important advantages of pure EVs, HEVs and FCHEVs is their ability to recuperate kinetic energy through braking. This is achieved by having the electric motors operate as electric generators to convert the potential energy of vehicle mass into electric energy as the vehicle moves but power feed to the motor is zero. This, otherwise wasted energy, can be stored in an energy storage device and then reused for vehicle acceleration or propulsion. A significant amount of energy is dissipated by frequently braking a vehicle. In particular, public transport busses or trams are a good case having; frequent braking and heavy chassis. Specifically, in the context of FCHEV, the possibility of storing energy into the battery pack through braking allows for an enhanced fuel economy. The sizing of the energy storage device is usually based on vehicle driving pattern. The tractive energy demand in WLTP is almost twice in excess of what is required in the NEDC, as evident from Figure 55 and Figure 56.

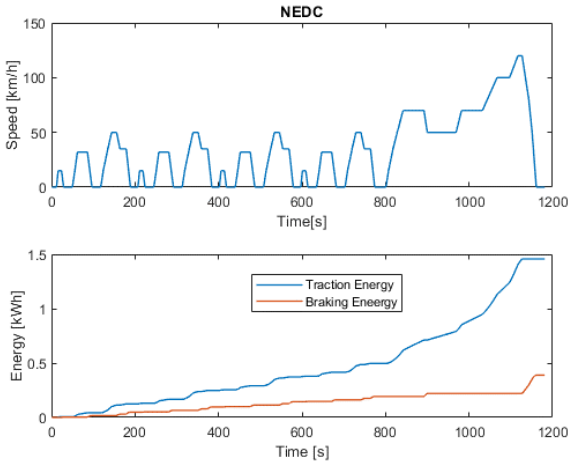


Figure 55: NEDC traction and braking energies.

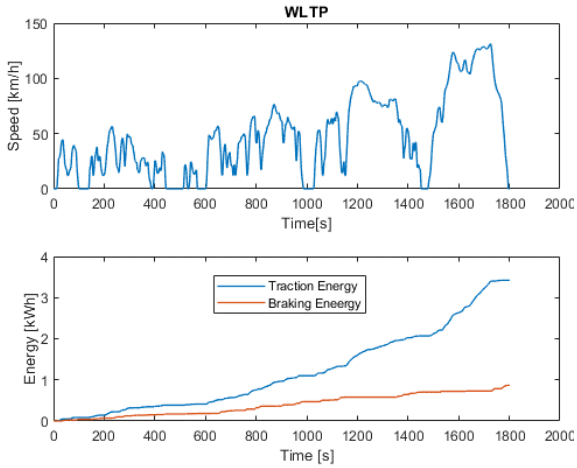


Figure 56: WLTP traction and braking energies.

Braking energy dissipated at low vehicle speeds is insignificant and usually the motor is made to disregard operating in the generator mode. In fact, the low electromotive force at low speeds in the electric motor makes energy recuperation difficult. The demonstration of this concept was attempted in AVL Cruise environment depicting the energy flow in and out of the power sources. Figure 57 depicts a sankey digram with power sources and sinks for an FCHEV running an NEDC test cycle. It can clearly be seen that the kinetic energy recuperated during a braking event at the point of 893s in the cycle produces a surge of approximately 15 kW. Most of this power is redirected into the traction battery which accepts approximately 10 kW of this power, subject to braking losses which have an efficiency range of 40-80% from mechanical to electrical energy conversion [29]. Other avenues of power sinks in a FCHEV are FC, e-drive, transmission, brake, power converters and auxilliaries' losses. Similarly, Figure 58 shows results from WLTP cyles at the 1126s of the simulation, wherein a higher surge of power, 20 kW, is noticed as a result of energy recuperation. Other power sink in the diagram include FC auxilliaries, consumer power and mechanice losses within the transmission or the final drive.

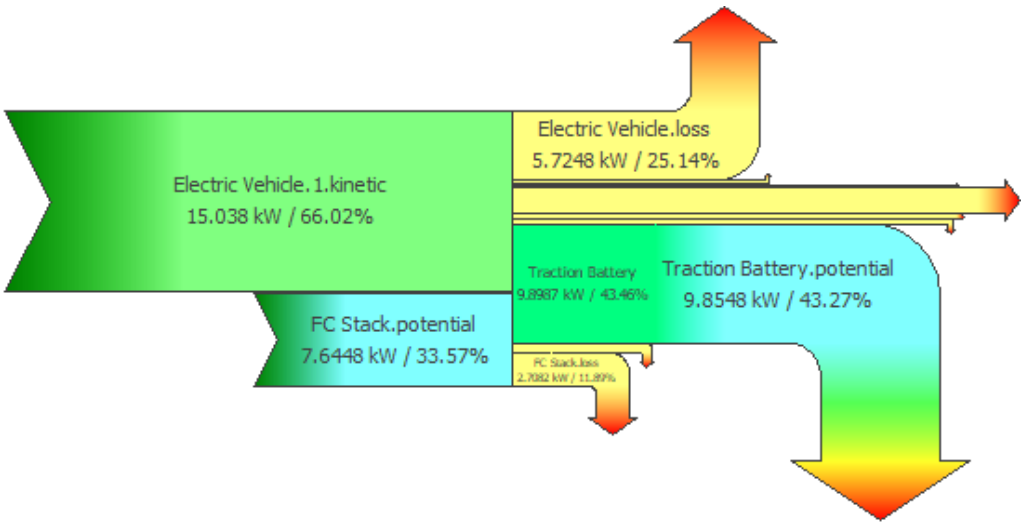


Figure 57: Sankey diagram depicting surge of power regained through regenerative braking in a FCHEV, diagram extracted from Cruise Simulation with NEDC at 893s

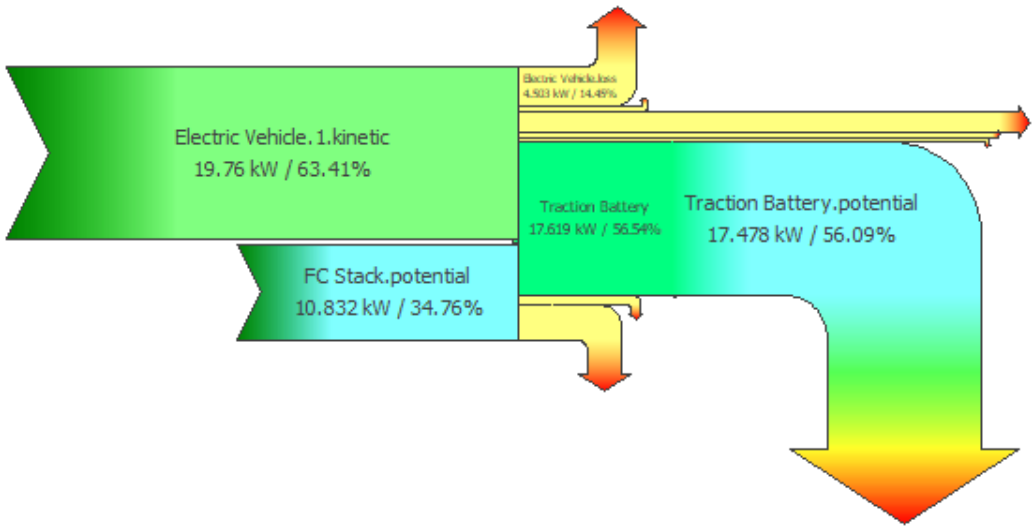


Figure 58: Sankey diagram depicting power gained through regenerative braking on a FCHEV, diagram extracted from with WLTP simulation in Cruise at 1126s

5.4 Model Architecture

The architecture of the model involves and is dependent on various several sub systems. These sub-systems communicate between each other to carry out relevant decisions and signal acquisition. AVL Cruise M provides a multi-disciplinary platform for simulation which also imitates the real world systems within a FCHEV powertrain which have a shared Controller Area Network

(CAN) bus for data transmission. Figure 59 illustrates the system level architecture of the model built within Cruise M™ platform.

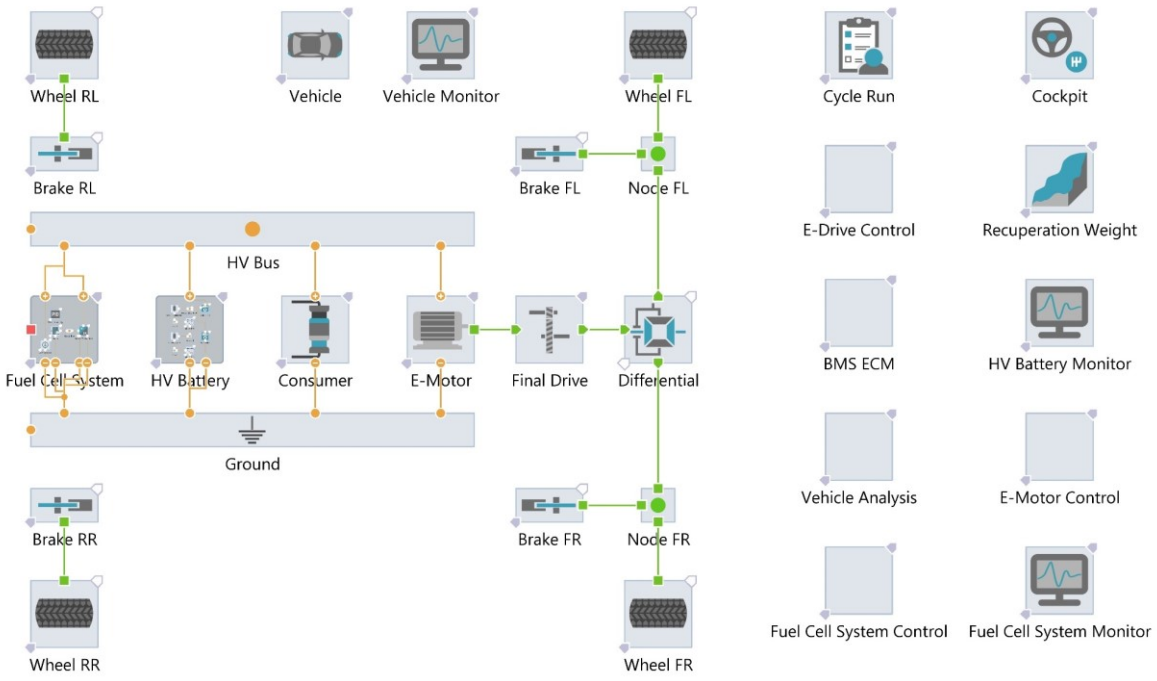


Figure 59: FCHEV model architecture in AVL Cruise M™, highlighting electrical (orange) and mechanical (green) connections.

The vehicle specifications are fed into the model as inputs via the Vehicle Block in the model. Data in this block includes physical parameters of the vehicle such as the nominal vehicle dimensions, weights, driving resistances, frontal area, drag coefficient, etc., as well other characteristics like towing. Table 7 below summarises the vehicle specifications used in this work. Connections between the blocks can be electrical or mechanical. For example, all sub systems connected to the high voltage (HV) bus have electrical connectors while the sub systems connected to the final drive are mechanical. The HV bus has a regulated electrical power being fed into it from the fuel cell system and HV battery pack. The power

is then, primarily, drawn by the motor and auxiliary electrical loads, labelled as consumer in the model.

Table 7: Vehicle specification (inputs to the Vehicle block)

Parameter [SI Unit]	**Value**
Frontal area (A_f) [m]	1.85
Vehicle glider mass [kg]	1400
Gross weight [kg]	1980
Aero-dynamic drag coefficient (C_D)	0.29
Tyre Coefficient (μ_T)	0.015
Wheelbase (front/rear)	1.53/1.52
Range [miles]	312
Drivetrain	FWD

5.4.1 Vehicle model

The vehicle model provides a prediction on the power requirement for a given vehicle specifications. This is achieved through calculating the different types of resistances and the load required at the wheel of the vehicle. The AVL Cruise M software package was used to model and simulate the vehicle model. The software tool provides a detailed system level approach in modelling dynamics with less computational burden and short simulation periods. The model can be expressed in a mathematical form as a combination of equations (5-1) to (5-4).

$$F_D = \frac{1}{2}\, C_D\, A_f\, \rho\, v^2 \tag{5-1}$$

$$F_R = m\,\mu_T\,g \tag{5-2}$$

$$F_G = mgsin(\theta) \tag{5-3}$$

$$F_A = ma \tag{5-4}$$

Where F_D, F_R, F_G and F_A are the aero-dynamic drag, tyre friction due to rolling, and inclination and acceleration resistance, respectively. The aerodynamic drag is a function of vehicle speed, v, vehicle frontal area (A_f), drag coefficient C_D and air density ρ. The rolling resistance, F_R, is caused by the hysteres in the tyre material and is a function of vehicle mass, m, and rolling resistance tyre coefficient (μ_T). The inclination resistance, F_G , produced due to the weight of the vehicle, is either opposed to the forward motion (grade climbing) or assistive (grade descending). F_A is the acceleration force exerted by the vehicle. Thus, the tractive power, (P_v) required to overcome these forces can be expressed by equation;

$$P_v = (F_D + F_R + F_G + F_A) \cdot v \tag{5-5}$$

5.4.2 Fuel Cell

The fuel cell system consists of an electrical PEM fuel cell block which is pre-built based on electrical-equivalent equations derived from the polarisation curve of the PEMFC. The outputs of the block take into account the oxygen and proton transport losses. These are affected by operating parameters such as relative humidity, temperature, and gas pressure on the cathode side. The voltage of the fuel cell model is calculated as;

$$U_{\text{cell}} = V_{OCV} - \eta_{cathode} - j_0 R \tag{5-6}$$

Where $U_{OCV}, \eta_{cathode}$ and $j_0 R$ are open-circuit voltage also known as the Nernst potential, cathode voltage losses and ohmic loss of the fuel cell. The cathode voltage loss is caused by a combination of reaction activation and gas transport limitation inside the cell – both within the catalyst layer (CL) and gas diffusion layer (GDL), as described in the equation below.

$$\eta_{cathode} = \eta_{activation} + \eta_{transport,CL} + \eta_{transport,GDL} \tag{5-7}$$

$$\eta_{activation} = b \cdot \operatorname{arcsinh}\left(\frac{\left(\frac{{j_0}^2}{j_a}\right)}{2\frac{c_h}{c_{ref}}\left(1 - \exp\left(\frac{-j_0}{2j_*}\right)\right)} \right) \tag{5-8}$$

where b is the Tafel slope, c_h is the oxygen concentration in the cathode channel, and c_{ref} is the oxygen concentration in the channel inlet. j_a is a function of volumetric exchange current density and CL's proton conductivity. In the cathode, the gasses are a mixture of nitrogen, oxygen, and water. Thus, the molar flow of gas on the cathode side will mainly be attributed to these three gases. The transport losses that occur within the GDL can be described as;

$$\eta_{transport,GDL} = -b\ln\left(1 - \frac{j_0}{j^*_{lim}\frac{c_h}{c_{\text{ref}}}}\right) \tag{5-9}$$

Where j^*_{lim} is the limiting current density due to oxygen transport in the GDL. A detailed description of transport losses in CL and GDL models are available in [126].

Thus, the ohmic losses in a fuel cell stack can be defined as;

$$j_0 R = I_{\text{stack}} / A_{\text{area}} R \tag{5-10}$$

where j_0 is the current density which is a function of cell active area, A_{area} . I_{stack} and R are stack current and ohmic resistance, respectively. The stoichiometric ratio (SR) is defined as the precise ratio between the amount of oxygen supplied to the fuel cell to the amount of flammable gas or vapour to which the combustion or reaction takes place. In this mode, SR is used to compute the total amount of hydrogen and oxygen consumed by the fuel cell system based on the electrical current drawn. The SR is a function of mass flow of the reacted hydrogen, oxygen;

$$m_{reacted,H_2} = \frac{I_{\text{stack}} * n_{\text{cells}}}{2 * F} * M(H_2) \tag{5-11}$$

and

$$m_{reacted,O_2} = \frac{I_{\text{stack}} * n_{\text{cells}}}{4 * F} * M(O_2) \tag{5-12}$$

where $M(H_2)$ and $M(O_2)$ are molar masses of hydrogen and oxygen. The total amount of reactants fed into the stack based on the SR, as described the equations below;

$$m_{\text{flow},H_2} = m_{\text{reacted},,H_2} * SR_{H_2} \tag{5-13}$$

and

$$m_{\text{flow},O_2} = m_{\text{reacted},,O_2} * SR_{O_2} \tag{5-14}$$

The stack voltage, V_{stack}, is proportional to the number of cells, n_{cells}.

$$V_{stack} = V_{cell}.n_{cells} \tag{5-15}$$

and the power output from the stack will equal

$$P_{stack} = V_{cell}.I_{stack}.n_{cells} \tag{5-16}$$

with a power loss of

$$P_{loss} = (V_{ocv} - V_{cell}).I_{stack}.n_{cells} \quad (5\text{-}17)$$

corresponding to a cell efficiency of

$$\eta_{cell} = \frac{(U_{cell})}{U_{ocV}} \quad (5\text{-}18)$$

AVL Cruise M uses a compressor model within the fuel cell system. This block within the model can be parameterised through experimentation and validation. Generally, this is realised using power consumption maps of the compressor. Theoretically, the power consumption of a compressor can be estimated using the following equation.

$$P_{\text{compressor}} = m_{\text{flow,in}} \cdot \frac{1}{n_{s,C}} \cdot c_p \cdot T_{in} \cdot \left[\Pi^{\frac{k-1}{k}} - 1\right] \quad (5\text{-}19)$$

Where T_{in} and k, are inlet gas temperature and ratio of the heat capacity at a constant pressure to the heat capacity at a constant volume, respectively. Also, c_p and n_s are the isentropic efficiency and specific heat at constant pressure between the inlet and outlet of the compressor, respectively, while Π is the pressure ratio.

5.4.3 Battery

An electrical equivalent circuit model is implement in the model to represent a battery. This model allows for estimation of the output voltage, state of charge (SoC) and temperature. Using these parameters, a systems level analysis can be conducted post results generation. AVL Cruise M offers two options, a simple (adopted in this work) and an advanced with cascaded RC networks for better accuracy. In addition, individual cells are connected appropriately to form a

module in the model. Figure 60 represents the battery electrical equivalent circuit model used in the vehicle modelling study.

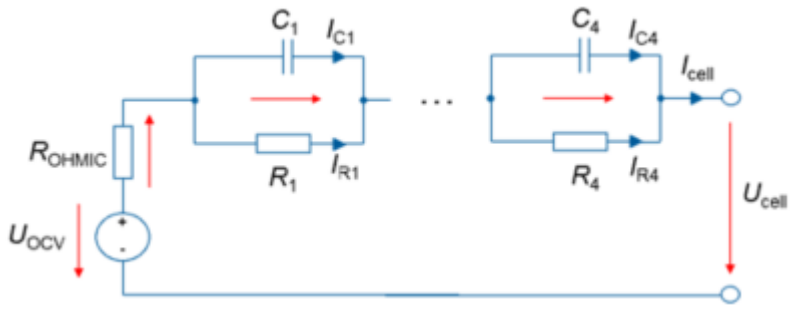


Figure 60: Electrical equivalent battery circuit model in AVL Cruise M

The model takes into account the open circuit voltage (U_{OCV}), ohmic resistance (R_{ohmic}) of the battery. The SoC of the battery is function of the OCV and resistance, which can be evaluated using current drawn from the battery cells.

$$SoC = \int I_{cell}\,\mathrm{dt} \tag{5-20}$$

The cell voltage can be estimated using the following mathematical relationship based on the electrical equivalent circuit mode;

$$U_{\text{cell,battery}} = U_{\text{OCV,battery}} - I_{\text{cell,battery}} \cdot R_{\text{OHMIC}} - \sum_{i=1}^{n} \frac{Q_i}{C_i} \tag{5-21}$$

Where n, C_i and Q_i are the number of RC components, capacitance and charge of the capacitor in the RC circuit, respectively. Hence, the voltage of the battery would be dependent on the SoC, taking into account the maximum charge of the battery, Q_{max}.

$$Q_{\text{cell}} = Q_{\text{max}}.SoC \tag{5-22}$$

In addition, the power output from the battery pack can be computed using the individual cell voltage and current as shown in the equation below;

$$P_{\text{bat}} = U_{\text{cell}} \cdot I_{\text{cell}} \cdot n_{\text{series}} \cdot n_{\text{parallel}} \tag{5-23}$$

The power loss seen in battery can be estimated using the following mathematical relationship with the battery internal resistance, R_i.

$$P_{\text{loss, cell}} = I_{\text{cell}}^2 R_{\text{Ohmic}} + \sum_{i=1}^{n} I_{Ri}^2 R_i \tag{5-24}$$

5.4.4 DC-DC Converter

The DC-DC converter in series with the FC matches the voltage to that of the electrical DC bus by stepping up or down. This device also regulates the power out of the FC stack and can offer controllability over its operation. In most cases, the converter is designed to match the target current requirement by following the load demand. This phenomenon is known as load following strategy.

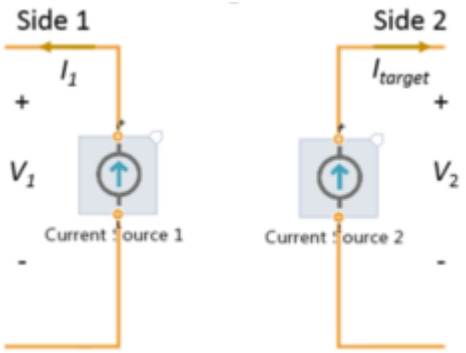


Figure 61: FC DC-DC converter equivalent circuit derived from AVL Cruise M.

Thus, the equivalent circuit of the DC/DC converter with target current control can be represented using the following mathematical relationship;

$$V_1 \times I_1 \times \eta_{DC-DC} = V_2 \times I_{\text{target}} \tag{5-25}$$

Where I_{target} is the target current on the DC bus side and η_{DC-DC} is the converter efficiency. The model has to be fed several inputs such as the rated bus voltage

and current as well as the peak values, in order to set limitations for safe operation.

5.4.5 Electric Motor

The electric motor modelling approach adopted is a simplistic one. The output of the sub-system delivers the requested torque based on the mechanical load request. The power losses are added to this in order to compute the electrical power output, based on the efficiency map of the motor. The angular speed of the motor, ω_{EM}, is calculated using the vehicle speed, v, the final drive ratio, r_g, and the rolling radius of the wheel, r_r, as described in the mathematical equation below;

$$\omega_{EM} = v\frac{r_g}{r_r} \tag{5-26}$$

The motor torque is a function of torque demand at the wheels and rotational speed of the motor. As a result, the propulsion effort on the motor can be computed using the following equation.

$$F_w = \tau_{EM}\frac{r_g}{r_r} \tag{5-27}$$

where τ_{EM} is the motor torque and F_w is the tractive effort required from the motor. In addition, the current drawn from motor can be described considering the efficiency of the motor, η_{EM}, torque output and supply voltage, V_{EM}.

$$I_{EM} = \frac{\omega_{EM}\tau_{EM}}{\eta_{EM}V_{EM}} \tag{5-28}$$

Thus, for a permanent magnet synchronous (PMS) electric motor the maximum available torque in the motor has a dependency on the operating temperature of the machine. Hence, the following relationship can be expressed;

$$T_{EM,max,PSM} = \left(1 + \beta_{EM,rem}\left(T_{EM} - T_{EM,L}\right)\right)\tau_{EM,max}. \quad (5\text{-}29)$$

Where $\beta_{EM,Rem}$ is the temperature coefficient of the resonance induction within the motor, T_{EM} is temperature $T_{EM,L}$ is the layout temperature and $\tau_{EM,max}$ is the maximum torque of the PMS machine. In this work, a motor efficiency map is used as illustrated in a two-dimensional format in Figure 62.

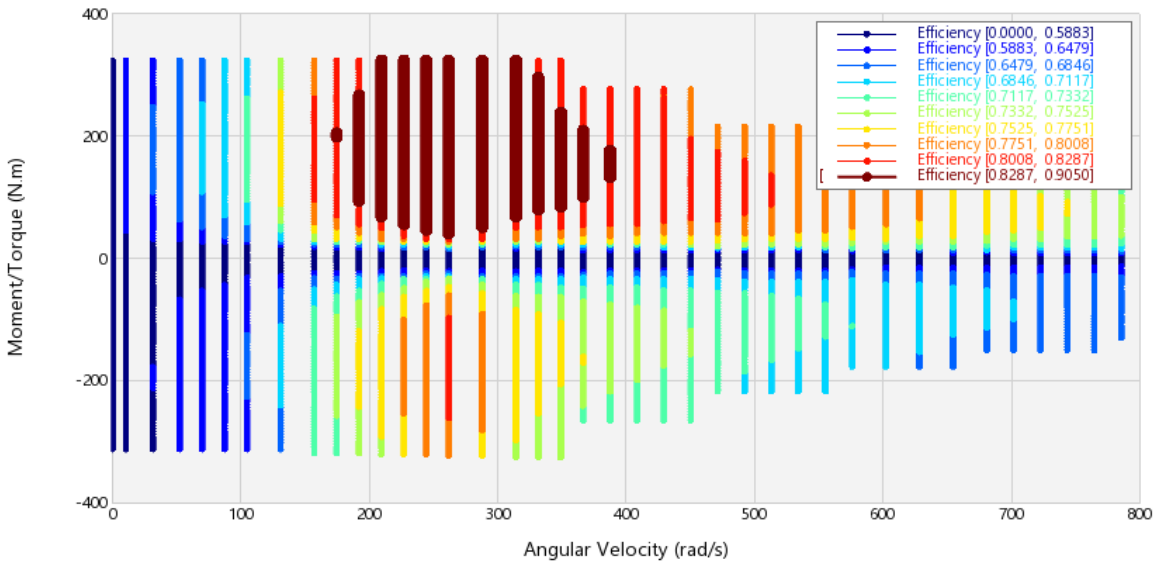


Figure 62: Electric motor velocity vs torque map showing the efficiency

The most efficient points are highlighted at motor speeds between 200 and 400 rad/s. In Figure 63, the efficiency of the motor is presented in a 3-D format as a function of motor torque and speed.

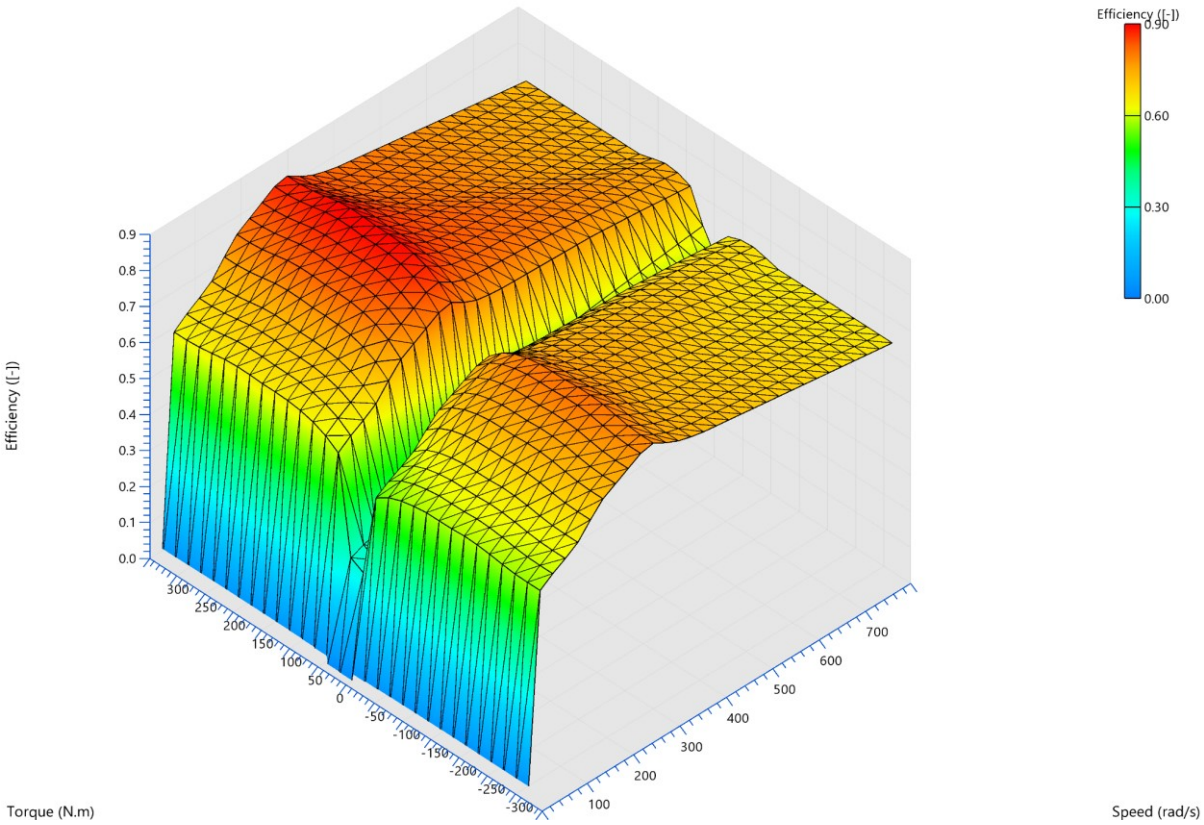


Figure 63: Efficiency 3-D surface chart of the motor.

5.5 **Heuristic Controller**

A heuristic or rule-based strategy (RBS) is implemented in order to have a control over the flow of energy between the power sources, as well as allowing the vehicle performance to adhere to the functional specifications. These specifications or rules are defined based on previous experience and design knowledge of the functional system. In this work, a complete vehicle model incorporating a RBS was developed within the AVL Cruise M™ software. The purpose of the model was to acquire power requirement results based on the considered vehicle specifications and multiple test cycles. After this, depending on the calibration of the sub-systems, the behaviour of the entire model could be observed and

assessed. Moreover, the electrical equivalent models of the sub-systems enabled acquisition of realistic results at a systems level.

The operating strategy implemented in the model was based on a typical 'load following' strategy where the fuel cell system was made to dominate the load demand. This was achieved by having in place a fuel cell activation threshold window, matching the power curve of the fuel cell stack. Hence, the control logic included four different operating modes; E-drive, charge, power and boost modes. The E-drive operating mode was active when the vehicle was stationary, when the power demand was below the FC activation threshold and the battery SoC within the operating window. In this mode the FC was not active or assisting in vehicle propulsion. The charge mode is activated when the current SoC of the battery reaches the minimum threshold value (SoC_{ON}), thereby requiring the FC to assist in recharging. In this mode both FC and the motor, via regenerative braking, charge the battery pack. The boost mode was initiated when the actual vehicle power demand is above the FC activation threshold value, whilst the power mode was triggered when the average vehicle power demand was higher than FC activation threshold value. Since the goal in these mode was to have most of the power demand fulfilled by the FCS, the SoC of the battery is maintained. In both cases, the FC power can reach its peak value. However, the battery peak power at the defined discharge C-rate can only be seen in the E-drive and power modes of operation. This is because these are the two modes which are can transition into

charge mode, subject to the the SoC value reaching the threshold point. **Error! Reference source not found.** below shows the high level state-machine diagram illustrating all the possible transitions between each state/operating mode and regions where each power source is active. This is then followed by actioning certain variable definitions such as the FC activation threshold, and battery SoC operating window.

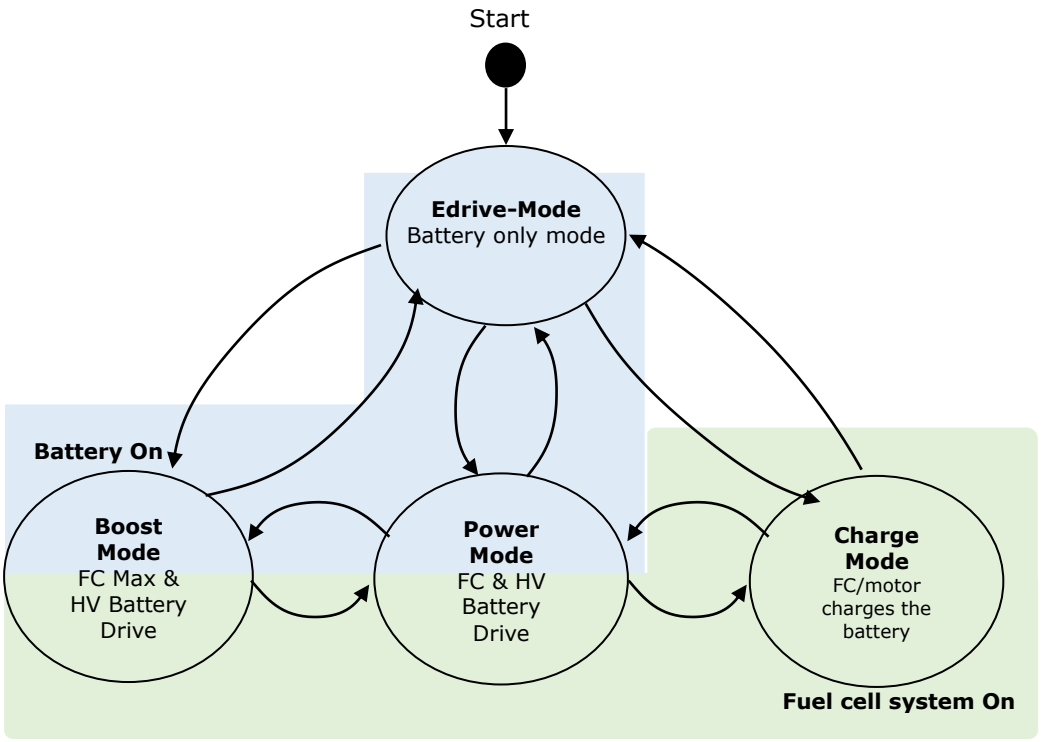


Figure 64: Rule-based strategy state flow chart sequence diagram showing permissible transition between the four operating modes.

A detailed flow chart showing the logic for transitions between the operating modes is presented in **Error! Reference source not found.**. The state-machine control logic procedure begins with the computation of average over a certain consecutive time steps and actual vehicle power demands for the determination of operating modes.

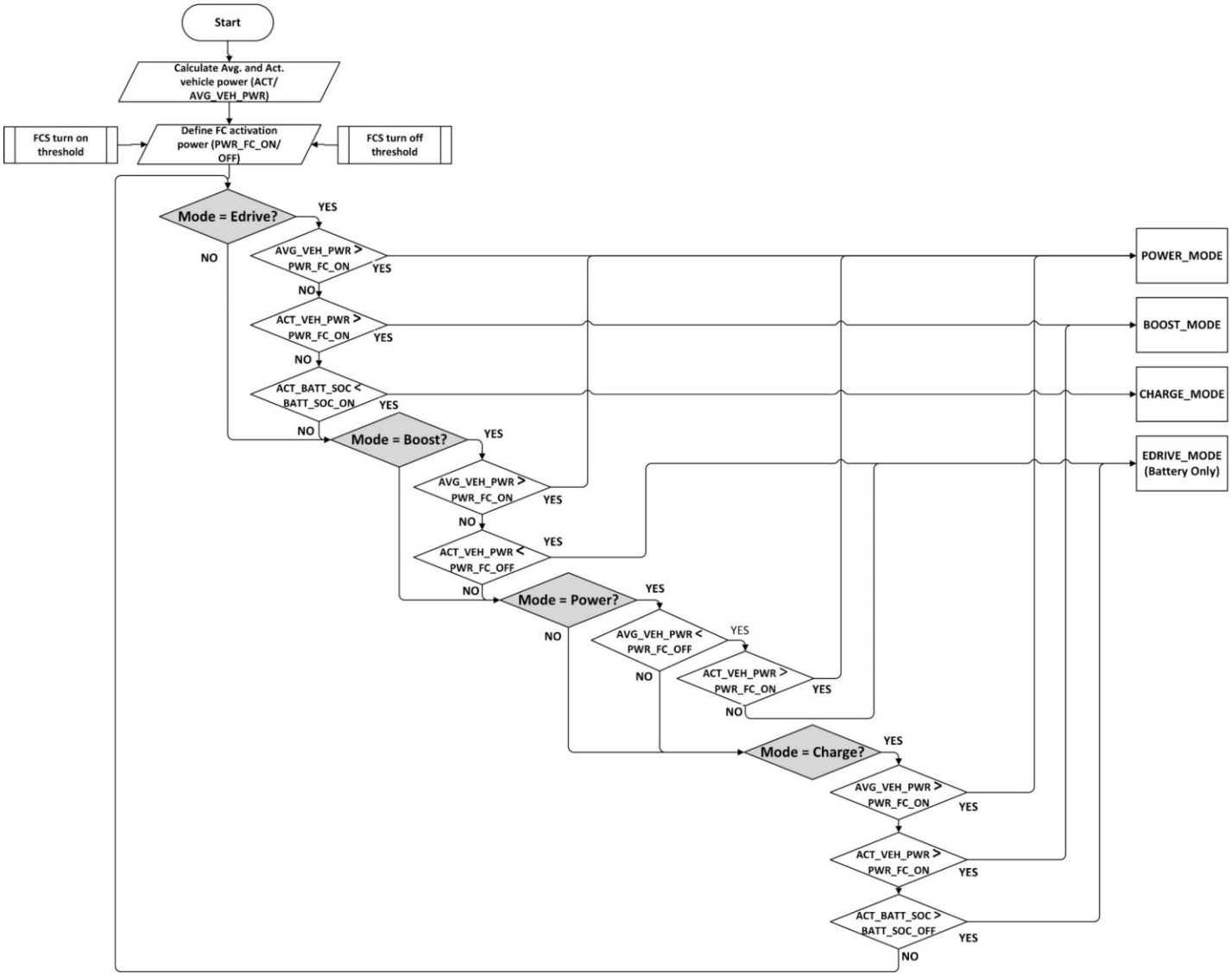


Figure 65: Detailed rule-based strategy showing transitions based on predefined rules

5.6 **Toyota Mirai Case Study**

The Toyota Mirai was one of the first FCEVs to become commercially available in the automotive market. Although numerous other OEMs had demonstrated FCEV technology, only Toyota and Hyundai offered a commercial product to customers. So far there have been two generations of the Mirai and Nexo, Toyota and Hyundai's FCEV brands respectively. Furthermore, extensive research lead to key innovations such as self-humidification, modern design of flow field channels and improvement in the mass fraction (wt %) of storage systems [127]. These innovations resulted in a better gravimetric and volumetric stack density, from 1.4 kW/L in the first prototype to 4.4 kW/L in Toyota Mirai gen II. However, with such drastic innovation within the powertrain, there still exists complexity in aspects such as energy management, packaging and hydrogen storage. The Toyota Mirai powertrain consists of the FCS, high voltage battery pack, electric drive unit and hydrogen storage system. The communication between all of these sub-systems takes place in a supervisory control unit. Figure 66 depicts the components as well as the improvements seen in the generations of Toyota Mirai. Notably, these include increased fuel storage, Lithium-ion battery chemistry and, better stack performance.

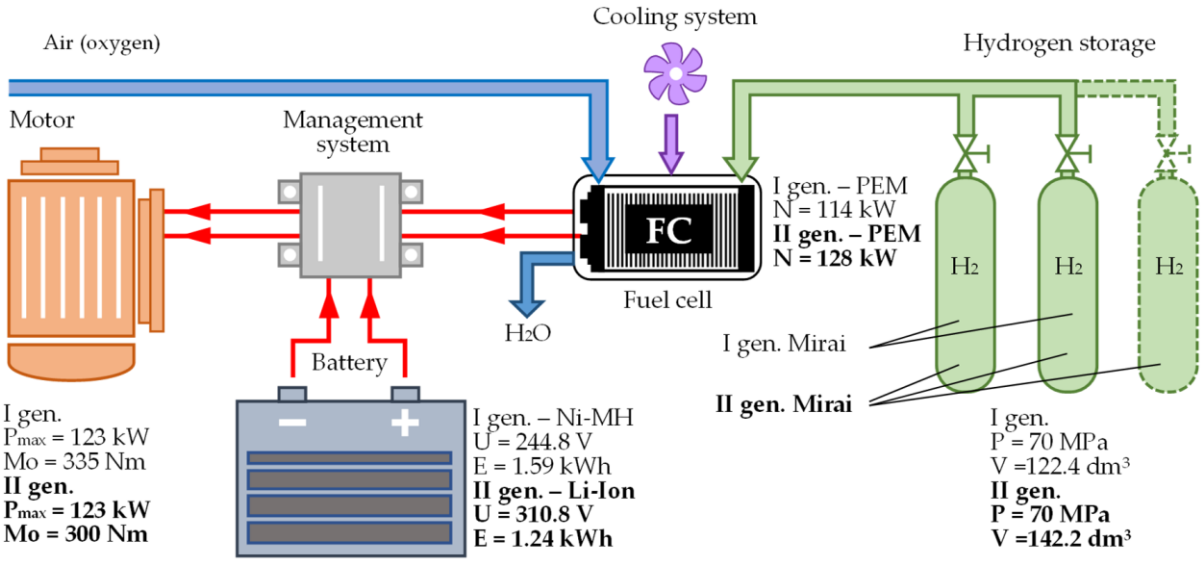


Figure 66: Toyota Mirai powertrain systems [128].

In this work, the first generation of Mirai will be considered for comparison purposes, as extensive test data is available for only this model. Argonne National Laboratory have conducted several key tests on Toyota Mirai Gen I with open access to the data (see Appendix IV). This enabled an in-depth scrutiny of powertrain components and their behaviour, for example, the C-rates of the battery, mass fraction of the storage systems and control system behaviour [129].

The Mirai gen I fuel cell stack uses a solid polymer with 370 cells in series resulting in an electrical output of 114 kW. The integrated battery holds a small capacity of 1.6 kWh and is responsible for contributing to the dynamics during acceleration and for energy storage from regenerative braking. The humidifier-less configuration allows the system to reuse the by-product water from within the cells to humidify the cathode stream.

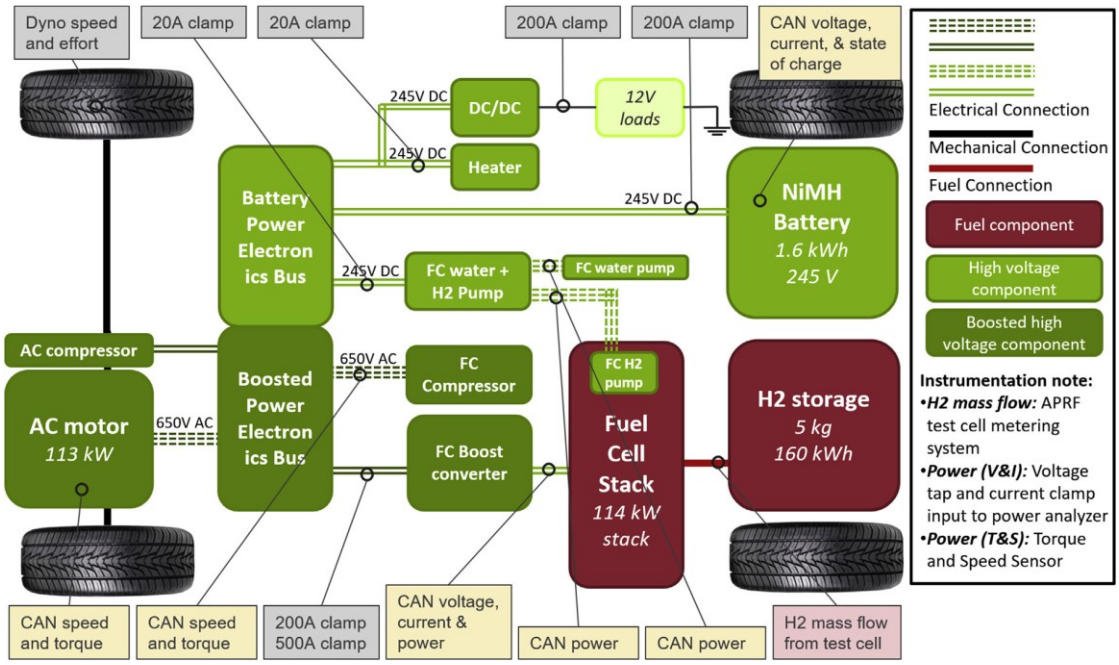


Figure 67: Toyota Mirai powertrain configuration and components [129].

The Mirai powertrain (See

Figure 67) employs a liquid-cooled boost converter to step up the stack voltage to 650 V to match the electrical bus voltage. This converter regulates the output from the stack based on the supervisory control decisions. The hydrogen storage system in Mirai stores 5 kg of hydrogen in two separate tanks, taking up 122.4 L of space. The pressure of compressed storage is 700 bar, as a result the weight of the tanks becomes heavier due to carbon fiber reinforced layering. Based on the 5.7 mass fraction of the storage tank, the total weight is calculated as 88 kg. It should be noted that this value takes into account the weight of the fuel, and auxiliary components such as piping and valves. Table 8 summarises the specifications of the Toyota Mirai Gen I collated from various sources in terms of FC, battery, hydrogen storage and electric motor.

Table 8: Toyota Mirai Gen I specifications

	Vehicle Parameters	Value	Unit
Fuel Cell	Max power output	114	kW
	Power density by volume	3.1	kW/L
	Power density by weight	2	kW/kg
	Volume	37	L
	Weight of stack	56	kg
Battery	Cell capacity	6.5	Ah
	Pack capacity	1.6	kWh
	Configuration	34s1p	34 series 1 parallel
	Cell voltage	7.2	V
	Battery pack voltage	244.8	
	Cell number	34	cells
	Weight	46.9	kg
	Peak power for 10 s	~30	kW
	Nominal power @ 1C	1.6	kW
H2 Storage	Number of tanks	2	
	Type	type 4	
	Max filling pressure	87.5	Mpa
	Normal operating pressure	70	Mpa
	Tanks Size/Volume Front	60	L
	Tanks Size/Volume Rear	62.4	L
	Total tank size volume	122.4	L
	Fuel mass	5	kg
	Tank storage density/mass fraction	5.7	wt%
	Tank storage weight with 5kg H2	88	kg
	Tank volumetric density	1.6	kWh/L
Motor	Motor type	PMS AC	
	Peak Power (@4500rpm)	123	kW
	Max output (hp)	112646	W
	Torque (lb-ft)	247	

5.7 Simulation Results

The simulation results depict the performance of the vehicle based on the RBS defined within the model. The main purpose of this section of the report is to analyse the obtained results from the point of view of the controller functionality rather than optimisation of the design. There are several key parameters, which can be calibrated to fit the vehicle design and requirements, which are used to implement a logical transition between the four operating modes of the controller. These include FC activation threshold, battery SoC window and target SoC values, and actual and average electric power. The actual electric power is the power demand of the motor for traction, in addition to consumer loads. The average electric motor power is derived from an internal Cruise M fixed step windowed average function over a pre-defined buffer window. Furthermore, all of the aforementioned parameters are dependent on the current state and magnitude of the motor power demand as well as the battery SoC.

5.7.1 Controller Functional Behaviour

The simulation model can be classed as a backward-facing model. The reason for this is the ability of the model to meet the requirements of the input, i.e. the drive cycle. Thus, the control system comprises of three sub-components; the drive cycle, the driver, and the supervisory controller. The first two mentioned sub-components are tasked with controlling the speed of the vehicle in order to match the target speed, while the controller is responsible for regulating and managing a

safe and efficient output from the FC, as well as the SoC of the battery pack. According to the parameters set, the RBS controller can accept a target SoC value to implement a charge-depletion (CD) followed by charge-sustaining (CS) behaviour of the battery. If a target SoC input is defined for the controller, for example to emulate a range extender powertrain - then the battery is forced to maintain the SoC_{Target} value recharging by the FC and regenerative braking. The system operation and behavioural performance of the control strategy, based on the conditions defined earlier are presented in Figure 68.

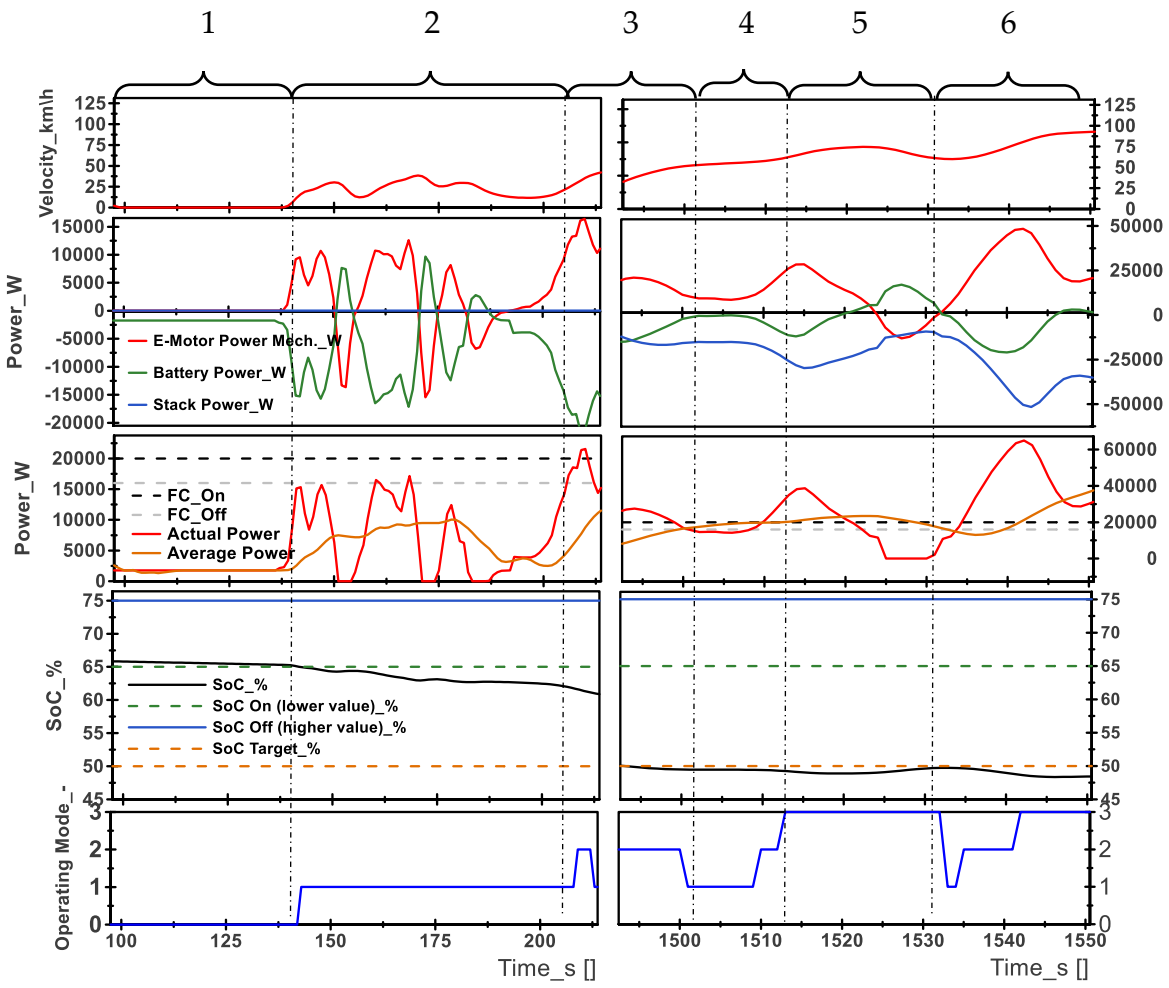


Figure 68: RBS implemented in AVL Cruise M model depicting system operation with key parameters illustrated in multiple sections (numbered above the figure) within WLTP cycle.

Illustrated in the figure are the key parameters, which are registered at every time step in order to enter one of the four operating modes. Furthermore, precedence of certain conditions over others occurs, for example, reaching and maintaining the SoC of the battery towards the target value is prioritised over other conditions such as FC activation power. In our case, the SoC target value selected was 50 % and the FC activation power 20 kW, with an initial SoC of 70%. Varying these thresholds can result in different transitions of the operating modes as these values are integrated into the EMS, which has control over the regulated output from the FC DC-DC converter. The FC system also takes into account reserve power needed to power its BoP. The battery discharge and charge rates are restricted to 30 kW and 25 kW, respectively. The FCS BoP includes a simplistic compressor model based on a current source block controlled by the stack current parameter. The compressor operation in our model mimics lookup table based on the predefined generic specifications which is not dynamic in nature. The electric machine operates as both motor and generator. In the former mode, the maximum current for the traction is defined by the peak current of the battery as it is passively connected to the electrical bus. In generator mode, the current is limited based on the battery charge C-rate value. Similarly, recirculation of hydrogen was not included in the developed model for the sake of simplicity. Table 9 below summarises these observations based on the operation mode.

Table 9: Controller functional behaviour description of four operating modes; E-Drive, charge, boost and power modes.

Region	Operating Mode	Scenario	Fuel Cell	Battery	Observation
1	Edrive-mode (mode 0)	Initial propulsion of the vehicle after start-up	Off	Discharging	This control state allows the battery to discharge from its initial SoC for consumer load until transition
2	Charge-mode (mode 1)	Battery ready to accept charging at powers below FC threshold	Off	Discharging & charging	The battery can be charged through regen braking only as the FC activation power has not been reached.
3	Boost-mode (mode 2)	Battery can either provide sole propulsion power or in tandem with the FC, subject to logic statements	On/Off	Discharging	Although actual power can be greater than FC activation, if $SoC_{Current} > SoC_{Target}$ is not met then the FC remains inactive and vice-versa.
4	Charge-mode (mode 1)	FC charges the battery while supplying propulsion and consumer loads	On	Charging	To maintain the SoC_{Target} the FC charges battery, actual power reaches above the FC activation threshold.
5	Power-mode (mode 3)	FC and battery supply traction power	On	Discharging /charging	Provided the average power is greater than the FC threshold and SoC is lower than the threshold window, this logic is activated.
6	Charge, power & boost modes	FC and battery supply traction power	On	Discharging /charging	Key parameters used to create transitions between the three operating modes.

5.7.2 System Operation

The modelling results presented in this section of the report are attributed to two of the most common control strategies applicable to rule-based strategies. The system operation can be measured using power curves of sources and motor, SoC of the battery and hydrogen fuel consumption by the stack. The WLTP and NEDC drive cycles were used to generate results based on charge-depletion/charge-sustaining (CDCS) and charge-sustaining (CS) control strategies, respectively. In CDCS mode, the battery system, provided it is above the higher threshold of the SoC operating window (SoC_{ON} parameter) and vehicle power demand is below the peak discharge power of the battery, provides the motor traction power. The FCS becomes active under certain condition which are highlighted in Table 9. Figure 69 illustrates simulation results based on the WLTP cycle. The results depict the depletion of the battery since the beginning of the cycle to reach the minimum allowable limit or the SoC_{Target} of 50 %. The actual SoC is then maintained near the target value with the help of the FC and electric motor (braking energy recuperation), until the end of the journey. This is achieved by employing PID controller to match the current value of the SoC to that of the target value. The hydrogen consumption curve follows the stack output, showing higher fuel consumption in the charge-sustaining region of the cycle (post 500 seconds). This is due to the need for the battery to be recharged by the FC and the reduced contribution towards motor traction power. Thus, resulting in cumulative

hydrogen consumption of 0.6 kg. However, it should be noted that in reality, this figure would be lower due to the recirculation of unreacted hydrogen.

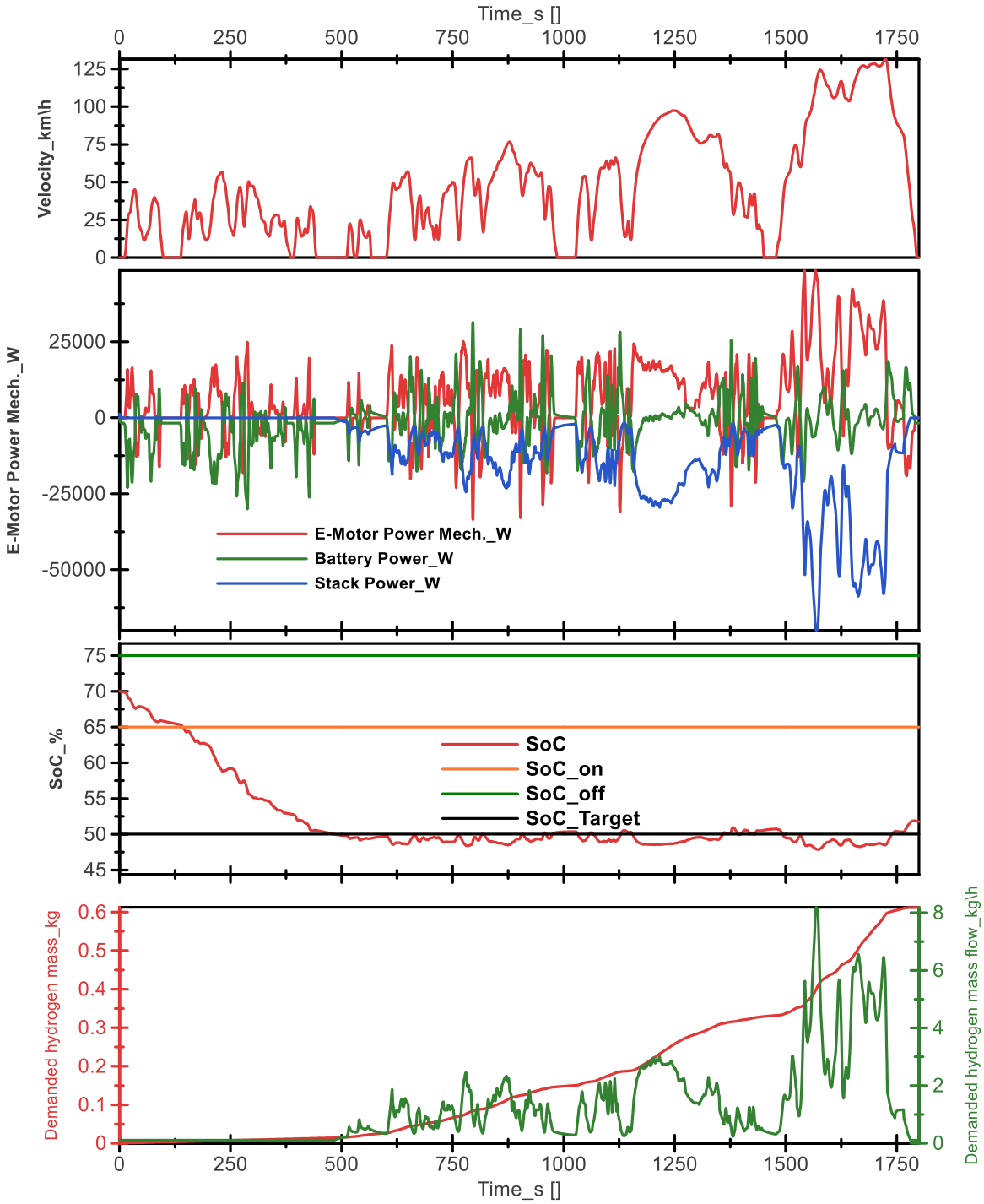


Figure 69: CDCS controller behaviour based on WLTP cycle illustrating velocity profile, power curves, battery SoC and hydrogen fuel consumption.

In CS control mode, the battery assists in fulfilling the transients as well as the lower than the FC activation power requirements throughout the cycle. This allows the FC to operate at more efficient operating points, in the low-to-medium current range. NEDC profile was used to display CS control, as shown in Figure 70. Furthermore, it can be noticed that the FC system is activated in events where the traction power exceeds the FC activation (FC_{ON}) threshold, a parameter only applicable in this control strategy. At this point, the FC supplies the motor with traction power required for propulsion and at the same time attempts to recharge the battery in order to equate the final SoC value to that of the initial value. The SoC_{Target} value is dictated by a PID control mehanics within the FC control block in the model to respond the to the actual SoC input in events where the FC is active. This is further evident from the hydrogen fuel consumption curves in synchronisation with SoC and the SoC_{Target}. For example, at approximately 800th second of the cycle there occurs a surge of power for traction, which is fulfilled by the FC stack in addition to charging the battery. Similar to the previous case, the SoC windows are for safe operation of the battery pack which, depending on the chemistry of the battery technology, vary to wider operating window. Furthermore, using equation (5-13) hydrogen flow into the stack can be computed based on a predefined stoichiometric ratio. Hence, the demanded hydrogen mass in this cycle was found to be 0.35 kg. The power losses or the inefficiencies described in equations (5-8), (5-9) and (5-10) are considered when power from the stack is delivered, thus, resulting in delivery of a larger magnitude – as shown in

the power curves below. The rationale for displaying CS control in the NEDC cycle was to clearly illustrate the SoC_{Target} instances.

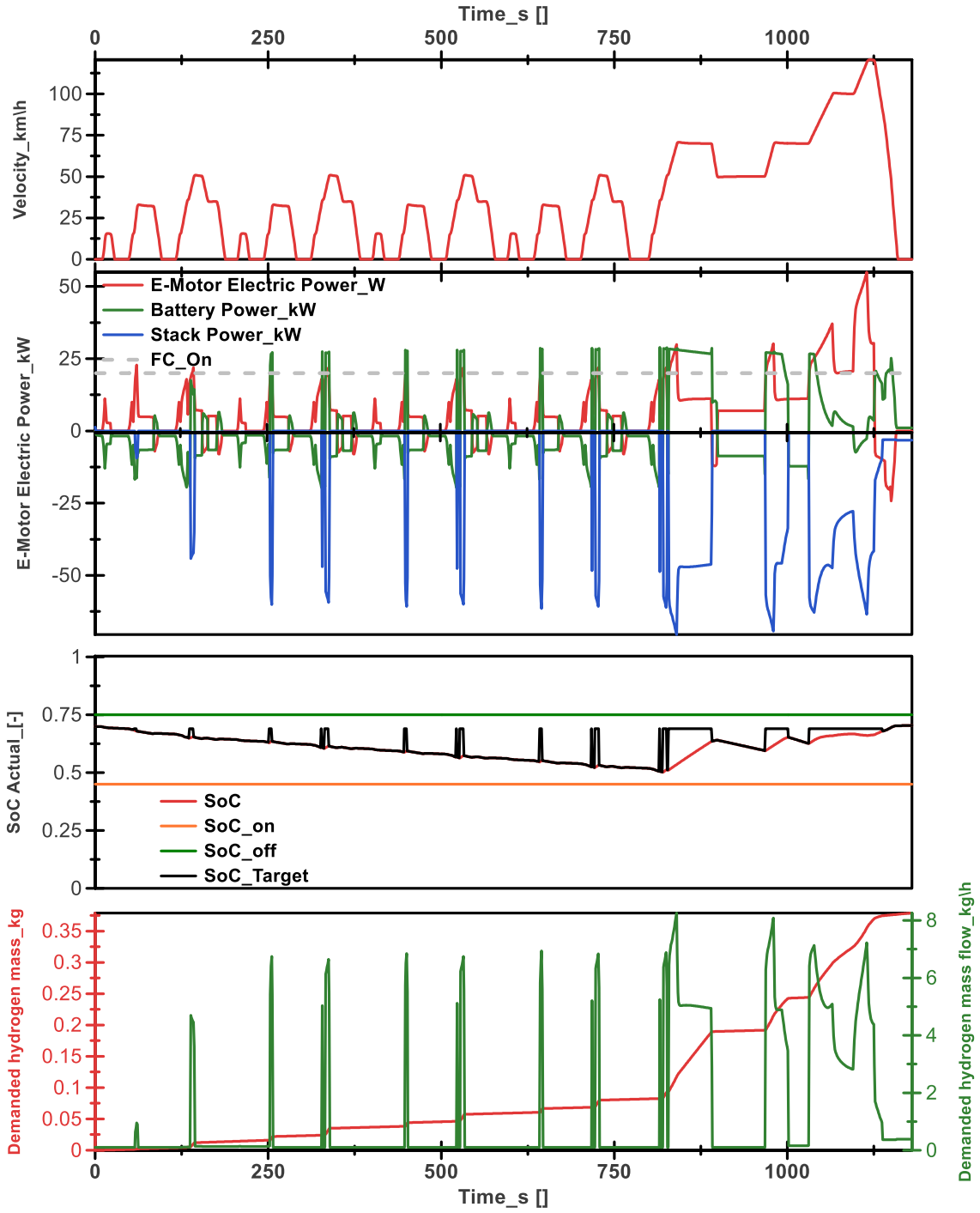


Figure 70: Charge-Sustaining controller behaviour based on NEDC cycle illustrating velocity profile, power curves, battery SoC and hydrogen fuel consumption

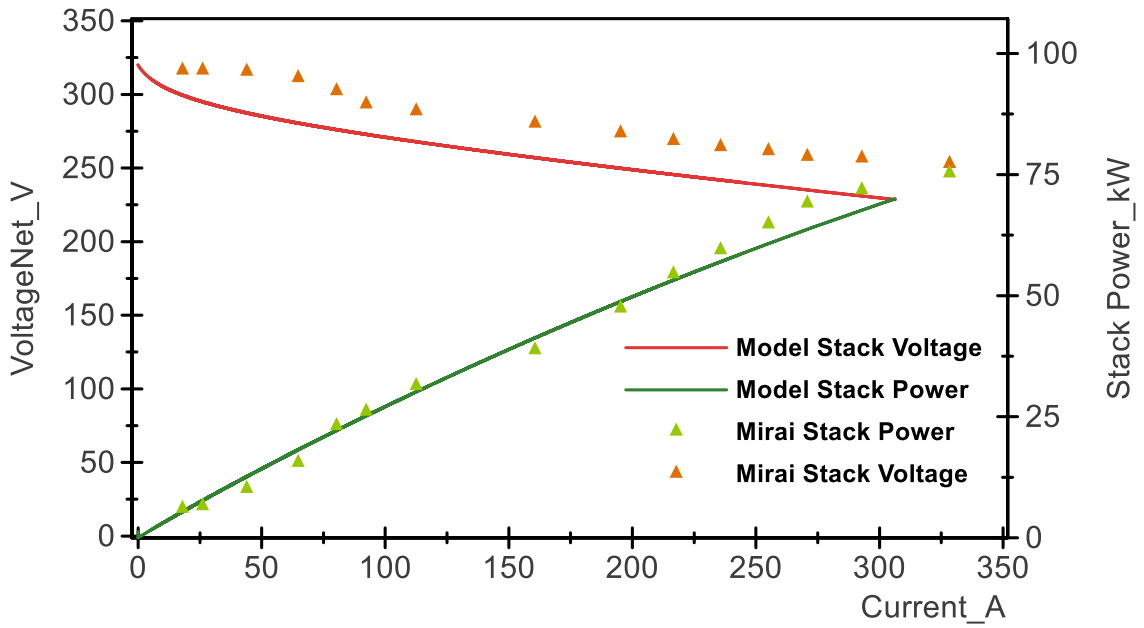


Figure 71: Stack polarisation and power curves (FC operates at 200 to 350 V range)

The stack polarisation and power curves are presented in Figure 71, derived from Mirai test data and also from the model - based on a WLTP drive cycle. Having these superimposed in a graphical format, a difference in the stack voltage level is observed. This could be attributed to the fact that the model does not consider dynamic parameters such as temperature and pressure range of the fuel cell stack.

5.7.3 Usage Envelopes

The results from the model can be compared against the test data available for the Toyota Mirai. This scrutiny will provide verification of the vehicle and the controller model. The operating points of the stack entails whether the usage is under the efficient region of the curve. FC stack operating points running a WLTP cycle for both Mirai test data and model results are plotted in Figure 72. The figure shows consistency in frequency of operation of the stack in regions where stack efficiency is high.

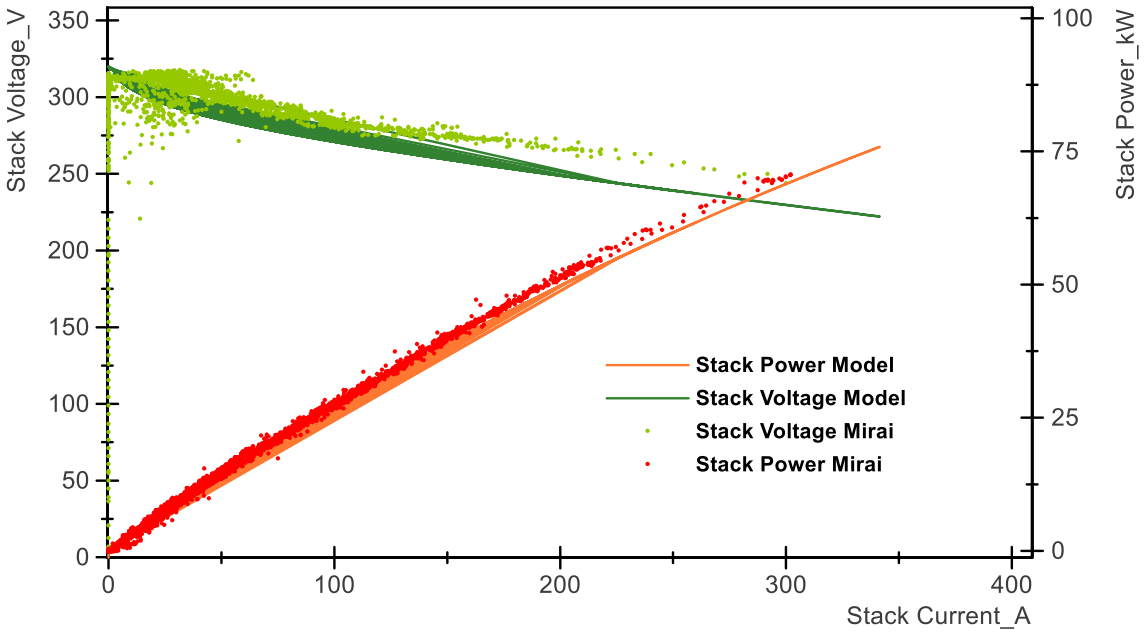


Figure 72: FC stack operating points derived from Mirai test data and Cruise M model illustrating high frequency of usage in the low power region where FC is efficient.

In addition, the Mirai generates slightly higher power at lower currents, which results in higher voltage levels – as evident in the stack voltage curve. This in turn has an effect of an increased system efficiency. At low power, the FC stack also provides power to its auxiliaries such as the compressor, pump and radiator fan. This power is known as the reserve or auxiliary power or 'base load'. The base load can be computed by deducting the stack power from the aforementioned auxiliary powers. Moreover, the model does not consider other dependencies such temperature and pressure, which play an important role in the calibration process of FC mapping. The usage of FC system can be further quantified by observing the normalised frequency of the operating points against power requirement in the drive cycle. Again, using Toyota Mirai as the benchmark vehicle, Figure 73 is produced illustrating a histogram and system efficiency.

It can be noted that FC is made to operate mostly in regions where efficiency is highest. Similarly, Figure 74 shows the histogram and system efficiency produced from Cruise M modelling simulation results. Upon analysis, good correlation between the two cases can be observed in terms of controller behaviour and FC system operation, as well as the system efficiency points. The peak power reached in the case of Mirai was found to be approximately 70 kW corresponding to a low efficiency of 30 % (high parasitic load due to high voltage compressor). On the hand, the model has a similar pattern with peak power of approximately 75 kW with ~ 50 % system efficiency (with no parasitic losses integrated). The increased system efficiency in the model is because of the lack of appropriate compressor look up table consuming high power with high electrical load demand. In addition, the model is based on an electrical-equivalent block rather than an electrochemical model, which would consider mass transport losses more accurately. This study entails the effectiveness of the controller is ensuring stack operating points reside in the regions which would result in better fuel economy.

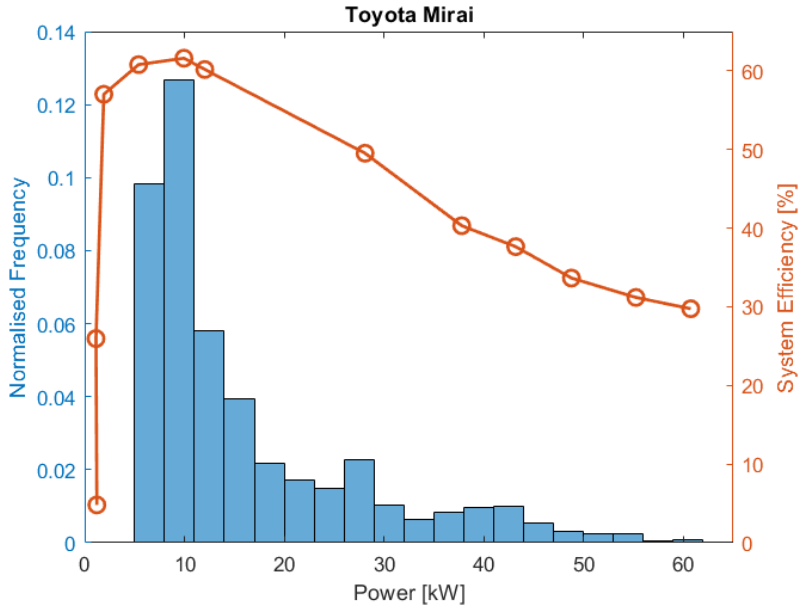


Figure 73: Toyota Mirai histogram and system efficiency, data extracted from [129]

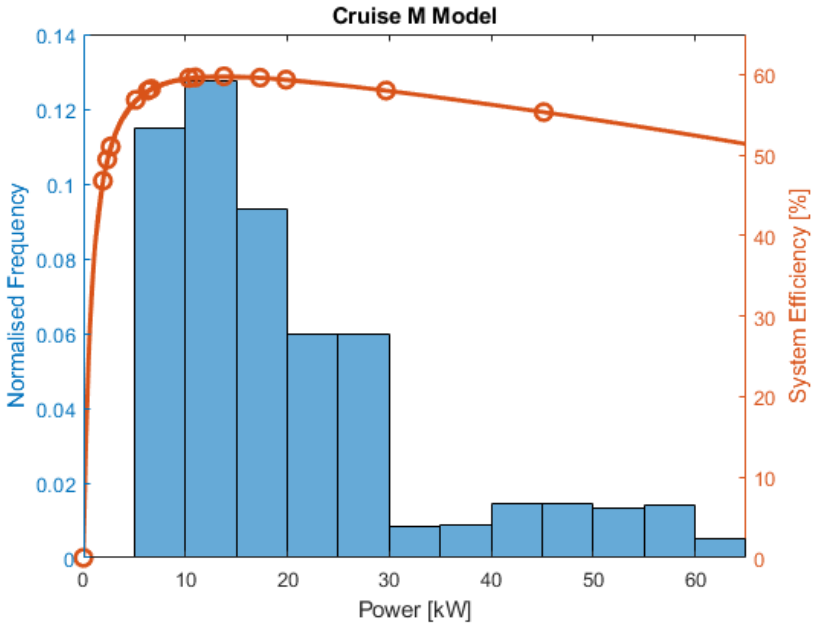


Figure 74: Model histogram and FC system efficiency

5.8 **Summary**

This chapter presented the methodology and considerations needed for implementing a rule-based or heuristic controller within an energy management system. The latter consideration included powertrain configuration, drive cycle analysis and energy recuperation via vehicle braking or deceleration. The model included sub-models of the fuel cell stack, battery pack, DC-DC converter and electric motor. The controller was made to perform in two different test cycles in order for a broader assessment. Dynamo test data of the Toyota Mirai was obtained. Moreover, this vehicle and its performance was used as a benchmark for comparison purposes in terms of the controller operation. The results show a realistic performance of the controller in each operating mode. The controller also responds well to certain pre-defined limits such as the FC activation and battery SoC windows. Furthermore, in CDCS operating mode, the controller behaves as intended upon reaching the SoC_{Target} value. In CS control mode, the initial and final SoC values found were 0.70 and 0.69, respectively. Finally, a good correlation between the operating points of the fuel cell system when compared against Mirai, implying realistic behaviour of the controller. Since, optimisation of the controller was not within the scope of this chapter the fuel economy sensitivity analysis was not carried out.

6 Design Optimisation Part I: Strategy

6.1 Introduction

The concept of combining multiple sources of power in a propulsion system is known as hybridisation. In Fuel Cell Electric Vehicles (FCEV), the primary and secondary power sources are typically hydrogen fuel cells and battery, respectively. The primary is the dominant power source whereas the secondary is mainly used to supplement or store energy on-board the vehicle. There are several benefits for having a hybridised vehicle powertrain. These include faster response time to varying load dynamics and downsizing of the primary power source. With no optimisation of the hybridisation ratio a vehicle powertrain can display an increased mass and volume as compared to a conventional vehicle, oversized components leading to increased costs and lack of performance. Thus, it is necessary to obtain an optimal hybridisation ratio which will also result in improved fuel economy can be achieved. One of the methods of implementing the optimisation is by employing dynamic programming.

While there are several versions of battery hybrid electric vehicle (HEV) based on the size of the battery pack installed, similarly, there are generally three versions of hybridisation in the context of FCEVs. These include fuel cell hybrid electric vehicle (FCHEV), plugin FCHEV, and range extender vehicle (REx FCEV). The difference between a standard and plugin FCHEV is that the latter has a relatively

larger battery capacity than which can be charged from the grid electricity via a charging cable. This results in cheaper running cost as the price of electricity is cheaper than the cost of green hydrogen for mobility in the current market condition. However, this scenario is anticipated to change in the future with the uptake of hydrogen production through renewables energy sources such as solar and wind. The REX- FCEV incorporates a relatively smaller FC stack than the battery pack and made to operate at a constant power level, mainly responsible for the recharging the battery pack.

This chapter sets out to present a design optimisation methodology for a propulsion system within a FC hybridised powertrain. Using the already built vehicle model in section 5.4, research will focus on devising a strategy which employs an optimisation techniques found in the literature. The sizing study shall incorporate the Energy Management Strategy (EMS), to a level of minimal complexity so as to have a correlation between design optimisation and operating conditions.

Specific objectives of this aspect of research work are;

- Conduct a literature review of the methods of sizing the power sources from a range of engineering literature databases.
- identify the key requirements needed in order to conduct a design optimisation study for an FCHEV powertrain.

- produce sizing results in terms of power ratings for the power sources on-board the vehicle.
- Evaluate the applicability of the obtained results in powertrain architectures.

The above sub-objectives relate to the design optimisation thesis objective stated in the chapter 1 of the thesis.

6.2 Literature Review

Design optimisation of a FCHEV encompasses the procedure of evaluating its power source component ratings and sizes. There are several parameters such as cost, fuel economy, power source degradation, compactness and vehicle performance which are addressed during design phase. Generally, an energy management system (EMS) is also implemented during this phase. EMSs are classified into two main categories: using rule-based or optimisation-based strategies. Rule-based optimisation strategies typically use state-machines for devising different operating modes while optimisation-based strategies use component models, most commonly employing dynamic programming technique [97]. There are numerous methodologies found in the literature which describe the procedure of sizing the FC stack or system, battery pack or supercapacitors such that the aforementioned variables are either minimised or maximised.

Most of the research and developments found in the literature had a sole focus on fuel economy improvement [97], [108], [111], [115], [118], [119], [130]–[132]. Many

authors have focused on forcing the operation of the FC system into an optimal efficiency point. This requires an oversized stack in order to have a wide enough window of operation to meet the load demand, not reaching the low efficiency points at high current densities. Moreover, the system efficiency of the fuel cell is dependent on the auxiliaries, such as air compressors, radiator fans and coolant pumps [118]. When there is an increased load on the fuel cell system the utilised power from the ancillaries can be considered as negligible, however, the ohmic losses increase. Similarly, the mass transport of reactants and gasses within the fuel cell starts to restrict the voltage output, thereby significantly limiting the overall efficiency. Rousseau *et al.* [118] have shown this in their work when comparing the efficiency of a fuel cell and a conventionally powered vehicle. The EMS has a direct relationship with and a decisive impact on the fuel economy of an FCHEV. For this reason, it has been found that a well-designed EMS strategy with complex control system can result in up to 30 % improvement in fuel economy compared to simplistic load following EMS with no optimisation [133].

Numerous strategies were found in the literature which were aimed at fuel economy improvement. Guezennec *et al.* [97] have done work on possibilities to improve the system efficiency of an FCHEV using hybridisation techniques at a powertrain system level. They have employed an Equivalent Consumption Minimisation Strategy (ECMS) technique. An improvement of 48 % in the fuel economy was seen by running the fuel cell at its optimal operating point during

most of the drive cycle and also minimising the idle-time of the fuel cell. Although, as a trade-off, the peak power of the fuel cell was significantly reduced. Furthermore, Schiffer *et al.* [119] looked at the optimisation of the fuel economy in an FCHEV incorporating supercapacitors (SC). In their work, they investigated several state-based strategies and concluded that SC, when utilised optimally for acceleration and regenerative braking, can result in 25 % reduction of fuel consumption as opposed to a vehicle powered solely by a fuel cell. Some authors use pure numerical modelling tools while using quantitative data to size components whereas others use optimisation or minimisation algorithms. For example, authors in [134] have utilised the Pontryagin's minimum principle to obtain the component sizing for a PHEV hybdridised with SC and batteries. Furthermore, several sizing algorithms have been proposed in the literature wherein a multi-objective optimisation problem was formulated aimed at minimising numerous parameters of FC and battery hybrid powertrain vehicle [90], [135]–[140]. For example, Zhang et al. [140] have proposed a sizing procedure to maximise the fuel economy and system durability, and minimise component cost and battery volume in the optimisation problem for a city bus. Their method involved an elimination process for non-feasible solutions and obtained results on FC rating and battery capacity based on the NEDC drive cycle. Hu et al. [141] and Sim et al. [142] proposed a framework for component sizing for an FCEV. In the former case, the authors carried out optimisation with a criterion of minimising the energy consumption and system cost. In the latter case, the authors conducted

a sizing study of an FC powered truck, having an objective function which minimised the total cost of ownership. Similarly, sizing optimisation work on range-extender FC powertrains with plug-in feature was also found in the literature [137], wherein a novel powertrain architecture was proposed involving FC hybridisation. Furthermore, studies in the literature highlight other intricate considerations such as regenerative braking, transient response, and efficiency that are required when sizing the primary or secondary power sources [139], [143]–[145]. Component size affects powertrain weight which in turn has an effect on the tractive requirements. Thus, research on the effect of added mass on the FCHEV propulsion system has been conducted in the literature [139]. The findings of the authors were based on the Dynamic Programming (DP) optimisation technique to obtain a hybridisation ratio aimed at reducing fuel consumption. An alternative to batteries acting as a secondary power source as well as an energy storage device in a FCHEV are SC. The benefits and disadvantages of SCs have been discussed in earlier sections of the thesis (section 2.3.2). In some cases SCs are used as a complementary device to battery packs. Extensive research work on sizing a SC-FC powertrain is found in the literature [125], [146]–[148]. Applications where SC are employed mostly have a duty profile which incorporates significant amount of regenerative braking, for example, in city bus transport systems. This allows higher magnitude of energy storage on-board and response during peak acceleration. Table 10 below summarises the literature

collection pertaining to different architectures employing FC and at least a battery or SC.

Research work that involves both system level control logic and component sizing integrated in one modelling package was lacking in the literature. As a result, this works fills this gap by devising a simple power split control logic between the fuel cell and the battery, while feeding into the model the dynamic inputs with the aim to sizing the powertrain components.

Table 10: Design optimisation techniques for a FC hybridised powertrains found in the literature.

Approach	Aims & Objectives	Powertrain	Reference
Dynamic Programming	Optimal component sizing by minimisation of fuel consumption	HEV – FC & Battery	[138]
Dynamic Programming	Design optimisation to obtain balanced degree of hybridisation	HEV – FC & Battery	[139]
Multi-objective optimisation	Design optimisation algorithm considering fuel economy, durability, cost and volume.	HEV – FC & Battery	[140]
Heuristic search	Design optimisation by minimisation of hydrogen consumption and system mass	HEV – FC & SC	[125]
GA	Design optimisation by cost minimisation of a battery-SC hybrid system	HEV – Battery & SC	[147]
Rule-based algorithm	Optimal component sizing by minimisation of capital and running costs	PHEV – FC & Battery	[149]
Deterministic algorithm	Design optimisation by system mass and cost minimisation	HEV – FC & Battery	[150]
Multi-objective GA	Optimal component sizing by minimising hydrogen consumption and cost	PHEV – FC & Battery	[151]
Dynamic programming	Design optimisation by maximising the efficiency and minimising the cost and mass	HEV – FC & SC	[146]
Non-linear branch & bound search	Sizing methodology based on minimisation of mass of the system	HEV – Battery and SC	[148]
Non-linear branch & bound search	Design optimisation based on minimisation of total cost of ownership	HEV – FC and ESS	[152]
Dynamic programming	Design optimisation with embedded EMS. Objective function included fuel consumption minimisation	HEV – FC and Battery	[153]
Particle Swarm	Design optimisation by minimising the vehicle cost and fuel consumption	PHEV – FC & Battery	[154]
Multi-objective Particle Swarm	Design optimisation based on the minimisation of the vehicle total cost and fuel economy	HEV – FC & battery	[155]

6.3 Energy Management System (EMS) and Its Strategy

The role of an EMS within a vehicle powertrain is to act as a decision making criteria. The objective is to compute, either based on pre-defined sets of rules or prediction-based models, the power that must be supplied to the motor from each of the power sources. In this study, a power split controller technique was embedded in order to control the power distribution.

6.3.1 Optimisation Theory

There are multiple methods of implementing optimisation techniques. However, the techniques are generally adopted in order to find a set of design parameters, $x = \{x_1, x_2, \dots, x_n\}$, which can be classed as optimal. The lowest degree of optimisation usually occurs in the form of minimisation or maximisation of the system characteristics that rely on x. In an advanced scenario, an objective function, $f(x)$, is formed and subjected to equality constraints, $G(x) = 0$; inequality constraints, $G(x) \leq 0$; and including lower and upper variable bounds, x_l and x_u. A generic problem in the context of optimisation can then be expressed as

$$\min_x f(x),$$

subject to

$$G_i(x) = 0; i = 1, \dots, m_e,$$

$$G_i(x) \leq 0; i = m_e + 1, \dots, m,$$

Where x is the vector of length n design variables (also known as decision variables). This, when entered into the objective function, $f(x)$, should return a

vector of length m which consists of constraints evaluated with respect to x. The linear nature of the objective function and constraints classifies the optimisation problem as a linear programming problem. The problem becomes a quadratic programming problem when the aforementioned elements have a non-linear nature. Non-linear programming solutions are generally obtained via an iterative procedure which enables a search criterion at every iteration. Furthermore, Matlab software toolboxes offer readily available solvers such constrained minimisation (fmincon), quadratic programming (quadprog), Linear programming (linprog), etc. The fmincon function aims to find the minimum of a constrained non-linear multivariable problem function, whilst quadprog and linprog deal with constrained (both equality and inequality constraints) functions. Quadratic solution allows for faster response in solving a quadratic problem, without having the need to adopt sophisticated techniques such as symbolic functions.

6.3.2 Dynamic and Quadratic Programming

Dynamic Programming (DP) is an algorithm-based technique that attempts to find the optimal control sequence with the aim of either minimising or maximising a given cost function. The cost function usually has constraints attached in order set boundary conditions. The DP method is considered to be computationally expensive in terms of simulation time. In some cases, this approach is not practical enough to be implemented due to extensive amount of data. Thus, requiring pre-built third-party mathematical solver such Gurobi™, which has simplified

function inputs to formulate a problem. Generally, the DP approach adopts a recursive optimisation procedure which attempts to reach optimality over an *N*-stage problem space by sequentially solving one stage of the problem at a given time interval until the overall optimisation is complete. Furthermore, DP is capable of dealing with nonlinearity or with a quadratic nature of the objective function. A quadratic programming (QP) problem minimises a quadratic function which can be subjected to linear equality or inequality constraints in the following form;

$$\min_x \frac{1}{2} x^T H x + f^T x$$

such that

$$Ax \leq b,\ Aeq\ x = beq,\ l \leq x \leq u$$

where H, A and Aeq are matrices corresponding to linear quadratic matrix term which is symmetrical sparse, inequality and equality constraint matrices with M (number of inequalities)-by-N (number of variables in x) size. These input arguments into the optimiser have to take form of symmetrical matrices and optional arguments such as the choice algorithm, tolerances and Hessian multiplier.

6.3.3 Fuel Cell System

The power component of a PEMFC stack can be obtained using numerical equation which are found in the literature [18], [156]. This curve describes the electrochemical technique of characterising the performance of the FC, both at single cell and stack level. Moreover, the polarisation curve indicates the

activation (η_{act}), ohmic (η_{ohm}) and concentration (η_{conc}) losses that occur at different operating conditions. Thus, the stack voltage is a function of the Nernst potential (E_{Nernst}) and total number of cells as expressed in equation (6-1).

$$V_{FC_{stack}} = [E_{Nernst} - \eta_{act} - \eta_{ohm} - \eta_{conc}] \cdot N_{cell} \quad (6\text{-}1)$$

The FC stack efficiency, η_{FC}, is defined as the ratio of the electrical power generated by the stack to the electrical energy content available in the hydrogen fuel, as expressed in (6-2).

$$\eta_{FC} = \frac{P_{FC_{stack}}}{P_{H_2}} \quad (6\text{-}2)$$

$$P_{FC_{stack}} = V_{FC_{stack}} . I_{FC_{stack}} \quad (6\text{-}3)$$

$$P_{H_2} = \dot{m}_{H_2} . \Delta H \quad (6\text{-}4)$$

$$\dot{m}_{H_2} = \frac{M_{H_2} I_{FC_{stack}}}{n \cdot F} \quad (6\text{-}5)$$

$$\eta_{FC} = \frac{V_{FC_{stack}} . I_{FC_{stack}}}{\frac{M_{H_2} . I_{FC_{stack}}}{n \cdot F} \cdot \Delta H} = \frac{V_{FC_{stack}}}{1.48 \times N_{cell}} \quad (6\text{-}6)$$

Where $\dot{m}_{H_2}$, ΔH, M_{H_2}, F and n are the rate of hydrogen consumption, enthalphy of the electro-chemical reaction, molar mass of hydrogen. Faraday's constant and number of electrons generated during the reaction, respectively. Thus, equation (6-2) can be quantified as (6-6) based on the derivations presented in (6-3), (6-4) and (6-5). The stack cell number, N_{cell}, is taken into account when computing the stack efficiency. The auxiliary components that make out the balance of plant

(BoP) partly require electricity (blowers and pumps) which is supplied by the stack. This lowers the overall system efficiency as described in equation (6-7).

$$\eta_{system} = \eta_{FC} \times \frac{P_{FC_{stack}} - P_{BoP}}{P_{FC_{stack}}} \tag{6-7}$$

6.3.4 Battery Model

The battery model used in this study was based on the Lithium-ion chemistry to predict the state of charge (SoC). The discrete model was based on power integration of the battery based on the drive cycle load and battery contribution dictated by the cost-function. The current SoC value of the battery at time *t* was estimated based on the previous time step ($t - \Delta t$). This can be mathematically represented as in equation (6-8).

$$SoC(t) = SoC(t - \Delta t) - \eta_{Bat} \frac{P_{Bat}(t)}{Q_{Bat}} \Delta t \tag{6-8}$$

$$\eta_{Bat} = \begin{cases} 1/\eta_{dis} & P_{Bat} > 0 \\ \eta_{ch} & P_{Bat} < 0 \end{cases} \tag{6-9}$$

Where the efficiency of the battery (η_{Bat}) varies in discharging and charging modes as described in (6-9). This is discussed in greater detail in section 2.3.1. In addition, temperature, internal resistance and SoC have dependencies on the battery efficiency. However, for the sake of having simplicity in the design algorithm, battery efficiency is not considered in this study. Moreover, the discretised form of the equation for predicting the SoC of the battery can be written as equation (6-10).

$$SoC^i = SoC^0 - \sum_{i}^{N} \frac{P_{Bat}^i \cdot t^i}{3600 \cdot Q_{Bat}} \quad (6\text{-}10)$$

Where SoC^0 is the initial SoC of the battery, i is the current sample point and t is the sampling time and Q_{Bat} is the nominal battery capacity. The battery configuration depends on the vehicle powertrain configuration.

6.3.5 Problem Formulation

The dynamic programming problem for the design optimisation will consist of a cost function limited by a pre-defined boundary conditions. Thus, the optimisation problem can be formulated in a standard form for a set of decision variables x and a cost function $f(x)$. The optimiser aims to search values of x that minimise the f subject to defined optimisation constraints G. The former represents the power contribution from the fuel cell and the battery, respectively. The cost function includes several performance indices which penalise the power supply with respect to the load demand. In this study, the implemented cost function consists of four performance indices as shown in equation (6-11).

$$min\, f = \sum_{i=1}^{N}. \left[w_1 \left(P_v^{k+i} - \eta_c P_{PC}^{k+i}\right)^2 + w_2 \left(P_v^{k+i} - P_{Bat}^{k+i}\right)^2 + w_3 \left(P_{PC}^{k+i}\right)^2 + w_4 \left(P_{Bat}^{k+i}\right)^2 \right] \quad (6\text{-}11)$$

The represented variables P_v, P_{FC}, and P_{Bat} are the vehicle, FC and battery powers respectively. The DC-DC converter is connected in series with the FC unit having an efficiency η_c. The variable k represents the sample number in the global optimisation cycle. The weighing parameters w_1, w_2, w_3 and w_4 are the performance indices which can be used to either tune or penalise the FC and

battery contributions in terms of the energy management strategy. The cost function is subject to several constraints which maintain the functional behaviour of the vehicle and restrict the optimisation from violating the boundary conditions set and individual component limits.

$$P_{load} = P_{FC} + P_{Bat} \tag{6-12}$$

$$0 \leq P_{fc} \leq P_{fc,max} \tag{6-13}$$

$$-P_{bat,min} \leq P_{bat} \leq P_{bat,max} \tag{6-14}$$

$$slew\ rate \leq \Delta P_{fc} \leq slew\ rate \tag{6-15}$$

$$SoC_{min} \leq SoC \leq SoC_{max} \tag{6-16}$$

The required constraints restrict solutions to the problem based on a realistic behaviour of the FC and battery pack. The two types of constraints are applied: equality and inequality constraints. The former forces the optimisation to compute the minimised power values for the FC and battery while following and not exceeding the load profile, as described in equation (6-12). There are limits set on the maximum and minimum status for each power source. In the case of the FC system , in equation (6-13), only positive power can be drawn from the stack whereas the battery has the ability to charge in the negative power region (see equation (6-14)) . A constraint in equation (6-15) to demonstrate a realistic behaviour of the FC dynamics is applied. This is called the 'slew rate' or ramp-up

rate, used 10 kW/s value based on experimental findings. In addition, the constraint in equation (6-16) restricts the SOC of the battery within a window of operation between a maximum and minimum made. Appendix V provides the detailed structure of matrices used in Matlab.

6.3.6 Assumptions

In this study and analysis the following assumptions were considered;

- Only the sizing of the power sources and storage was considered. Thus no sizing of the electric motor or other vehicle components considered.
- The nominal efficiency of the fuel cell system was assumed to be 55 %.
- The nominal efficiency of the DC-DC converter was assumed to be 95%.
- The fuel cell system model did not use any penalty for start-up and shutdown.
- Compressed hydrogen fuel technology for on-board storage.
- The power split between the FC and the battery was based on the cost parameter.
- The effect an increased powertrain volume has on vehicle was not been considered in this study.
- Charge-rates of the battery are chosen based on manufacturers updated recommended values (see section 2.3.1).
- The battery pack variables used already incorporates the DC-DC controller.

- The definition of degree of hybridisation (DoH) used is described in the equation

$$DoH = \frac{P_{FC_{max}}}{P_{FC_{max}} + P_{Battery_{max}}} \quad (6\text{-}17)$$

6.3.7 Charge Depletion Mode

Charge depletion (CD) mode is an operating mode wherein the SoC of the battery continuously decreases. The window of operation is usually given by the maximum and minimum SoC values. For the safety of battery operation the SoC threshold values are based on the maximum depth of discharge (DoD) allowed for a specific type of battery chemistry. In this study, the assumption was that the battery was fully recharged only after completing the full range of the vehicle. Moreover, the power split controller enabled the depletion of the battery in such a way that the capacity of the chosen battery helped complete the full journey. The size of the battery pack plays a significant role in the amount of energy that can be recuperated through regenerative braking. The larger the battery size, the larger the surges of current the battery pack can accept due to the C-rate parameter (applicable to large battery pack such as in Plug-in hybrid configurations), thereby capturing more energy content. Figure 75 illustrates this procedure graphically highlighting the number of drive cycles achievable with a small and large battery pack. It can be noted that the battery pack with a smaller capacity reaches the final DoD sooner thereby not completing the full desired range (~36 cycles or 245

miles). This is dependent on the choice battery capacity based on the type of powertrain topology. For example, in the RExFCHEV powertrain a larger battery pack would be incorporated, allowing a longer journey or range [137].

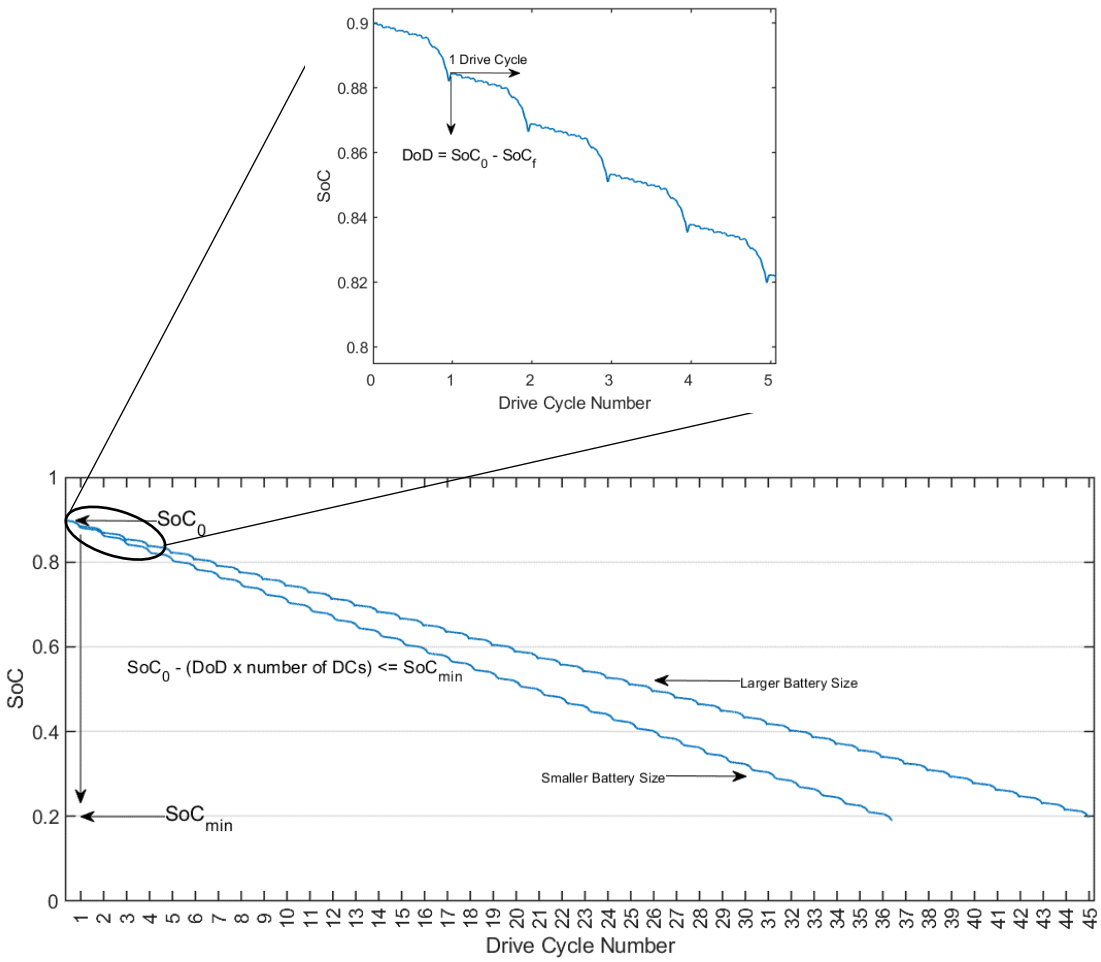


Figure 75: Description of CD mode illustration with small and large battery pack.

From the figure, the battery pack with larger capacity completes the full range of 45 drive cycles or 312 miles before reaching the maximum DoD. Thus, a relationship can be formulated in order to acquire the correct battery size value while adhering to the safe SoC operating window and vehicle range. The DoD after completing the drive cycle, *i*, can be expressed as.

$$DoD_i = SoC_i^0 - SoC_i^f \quad (6\text{-}18)$$

where SoC_i^0 and SoC_i^f are the initial and final SoC values with the drive cycle. Since the driving behaviour repeats itself identically, just one drive cycle can be used while incrementing the size of the battery at each iteration. This approach required a conditional statement which measured the DoD. Thus, quantifying this relationship further, using the vehicle range, provided the model presented in equation (6-19).

$$SoC^0 - DoD \times N_{cycles} \leq SoC_{min} \quad (6\text{-}19)$$

With N_{cycles} being the number of repeat drive cycles. In CD operating mode the primary power source, i.e. the FC system, must be sized with an aim to fulfil the maximum vehicle performance requirements. This is because, in the absence of a recharging opportunity for the battery pack from the grid (when considering a plug-in configuration), the responsibility for meeting the power demand is solely on the FC.

6.3.8 Charge Sustaining Mode

In charge sustaining (CS) control mode, the SoC of the battery is maintained at a target value while using the primary source of power (FC in this case) to recharge the battery. In other words, CS operating mode allows fluctuation in the SoC within the allowed operating window while resulting zero in the net energy consumption across the whole drive cycle. This achieves the goal of having battery energy level at the beginning of the drive cycle equalling to the energy

level at the end of the drive cycle. Furthermore, it must be noted that the sole source of energy onboard the vehicle is the hydrogen fuel, when there is an absence of regenerative braking or plug-in recharging is not considered during the journey. Figure 76 below illustrates the CS operating mode strategy implemented via dynamic programming within the EMS.

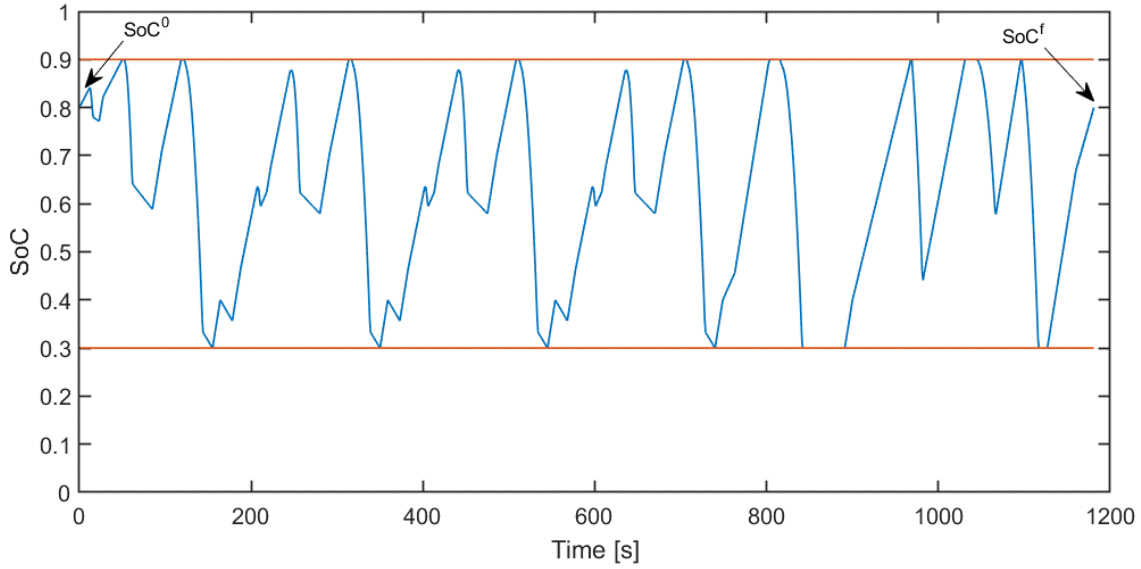


Figure 76: Description of CS mode implementation via DP in the EMS. Red lines indicate the upper and lower contraints on SoC.

It can be seen that the initial SoC equals the SoC at the end of the drive cycle in this example. The constraints on the minimum and maximum SoC operating window, 0.3 and 0.9, respectively, were adhered to by the optimisation algorithm. The equality constraints ensured that once the battery depleted to the minimum threshold, the FC recharged the battery if energy recuperation through deceleration was not available. Most commercially available HEVs adopt this control strategy as it is the simplest rule-based control strategy.

6.3.9 Sizing Strategy

The sizing algorithm is a sequential process wherein the optimisation steps are dependent on a number of decision variables used to obtain optimimum results. Specifically, the algorithm aims to find the rating of the fuel cell system, battery pack capacity, and the system mass and volume. Through a dynamic programming based EMS the fuel consumption is minimised. The entire procedure is illustrated in the Figure 77 flowchart. The sizing procedure begins with setting user-defined boundary conditions such as vehicle range, power and energy densities, initial hydrogen level in the storage tank, and drive cycle profile. The algorithm has two main loops for different purposes. The outer loop manipulates the power split ratio fed into the algorithm. By varying the contribution between the two power sources a range of DoH can be obtained. In this work, this defined as power split (PS). Furthermore, the inner loop contains a detailed vehicle model and DP-based EMS. The former provides the power requirement profile based on the vehicle specifications and the drive cycle, while dynamically accepting the optimal powertrain mass as an input post optimisation. The latter performs model-based optimisation with decision variables, subject to equality and inequality constraints. Within this loop a recursive iteration process is followed until a convergence is seen in the powertrain system variables such as the mass and volume.

In order to complete the desired range, which is also an input to the model, a large number of drive cycles are required. This presents the challenge of heavy computational burden and at times impossible to be completed. Thus, devising the EMS with consideration towards computation structure and embedded control strategy is imperative.

The algorithm computes the optimal size (in kW) of the fuel cell system based on the peak power of the load. It should be noted that the drive cycle incorporated includes the acceleration profile required to achieve the performance criterion stated in the earlier chapter (see section 5.3.2). Thanks to this added full load acceleration profile, the peak in power requirement is seen which enables the sizing of FC system. Similarly, the optimal battery capacity (in kWh) is found, based on the DoD to complete the full range. Since the DoD depends on the SoC operating window, the higher the DoD the larger the battery capacity will be – as described in equation (6-18). Hence, equation (6-20) below provides a mathematical expression for computing the size of the battery ($Q_{Battery}$) using DoD and total energy, E_{Total}, is the total net energy delivered to the wheels of the vehicle by the battery pack.

$$Q_{Battery} = \frac{E_{Total}}{3600 \times DoD} \text{ [Wh]} \tag{6-20}$$

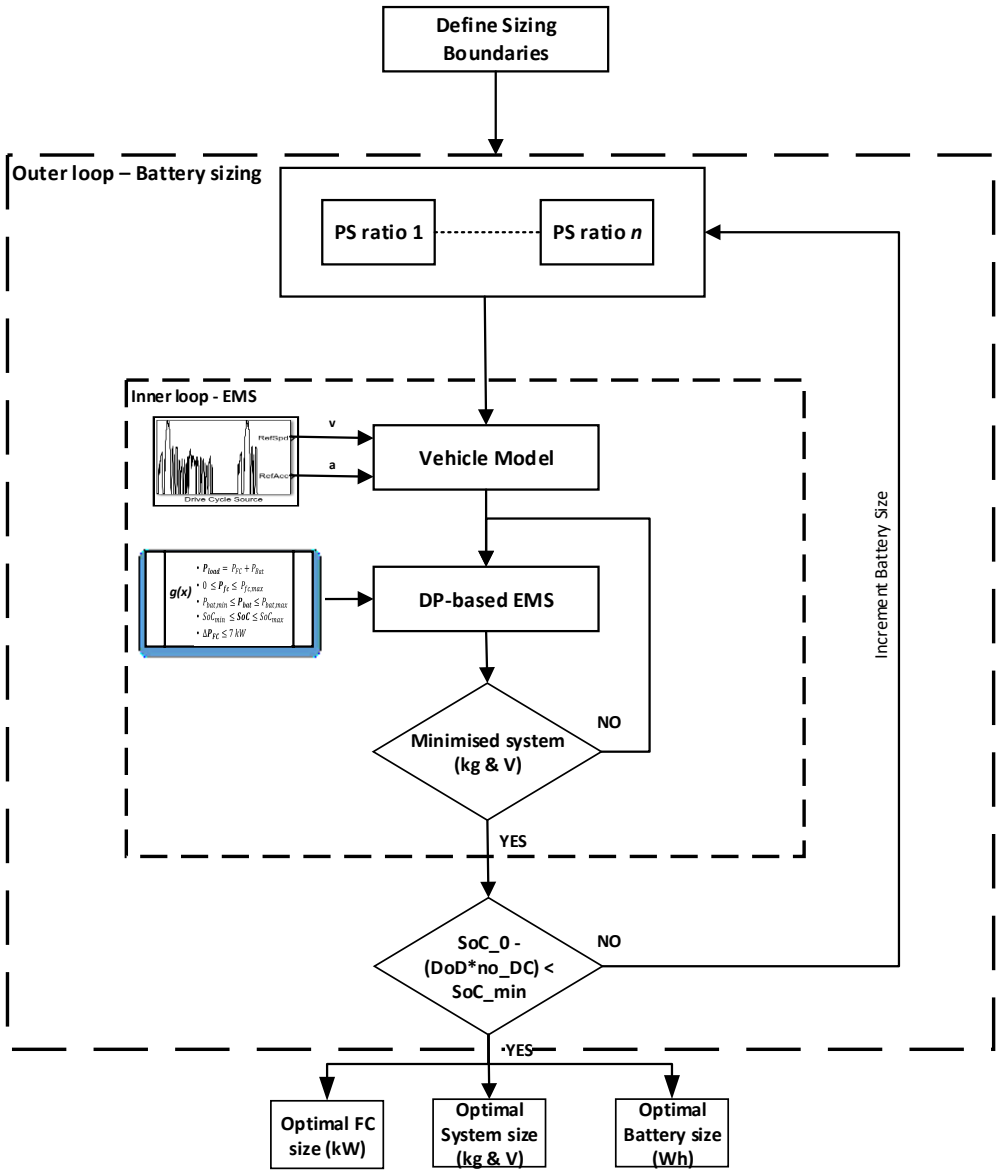


Figure 77: Flowchart describing the sizing algorithm in charge depletion mode.

The system mass includes FC stack, FC BoP, FC DC-DC converter, hydrogen storage and battery pack. Drivetrain system which includes the E-drive unit including the electric motor and transmission is not considered in this study. In order to find the FC stack mass, specific power density values (gravimetric and volumetric) based on the latest Toyota™ Mirai FC stack are used. Similarly, based

on the wt% value of the storage tanks in the Mirai the algorithm computes the mass required for the storage of compressed hydrogen gas on-board the vehicle. Furthermore, the difference between the FC system and stack unit densities results the FC BoP mass and volume, which includes all the auxiliaries except the storage and power conditioning units. Specific density values for the FC DC converter were extracted from the literature and implemented in the design process (Table 11) Thus, the total system mass can mathematically be expresses as equations (6-21) and (6-22);

$$M_{System} = M_{FC_{stack}} + M_{FC_{BoP}} + M_{FC_{DC-DC}} + M_{H_{2Storage}} + M_{Battery} \quad (6\text{-}21)$$

$$M_{System} = \frac{1}{\rho_{P,FC}} \cdot P_{FC,max} + \beta . P_{FC} + \frac{1}{\rho_{P,DC-DC}} \cdot P_{FC,max} + \frac{kgH_2}{wt\%} + \frac{1}{\rho_{E,Bat}} \cdot E_{Battery} \quad (6\text{-}22)$$

Table 11: Gravimetric, volumetric densities and costs of the components.

Component	Specific power [kW/kg]	Power density [kW/L]	Specific Energy [kWh/kg]	Energy Density [kWh/L]	Cost♣ [$]
PEMFC stack	2.46 [157]	4.40 [157]	-	-	22 $/kW+ [158]
PEMFC system	0.86 [158]	0.64 [158]	-	-	50 $/kW [158]
Li-ion Battery Pack	0.7 [159]	1.83 [159]	0.24 [160]	0.67 [160]	132 $/kWh [161]
DC-DC Converter	0.75 [162]	1.20 [162]	-	N/A	50 $/kW [162]
Type IV CH_2 tank	-	-	1.50* [163]	1.56 [157]	333 $/kg H_2 [163]

* Values normalised for comparison purposes based on a 5.6 kg of H2 at LHV FC system considering BoP excluding the storage tank.

+ At 100,000 units per year production rate

♣ Cost is determined on set targets and based on roadmaps and comparable baseline

- Not applicable

7 Design Optimisation Part II: Implementation and Analysis

Having discussed the methodology of the design procedure in the previous chapter, this chapter will set out to implement the design optimisation. The presented results will use previously developed relevant models, extracted parameters and discussed control strategies; charge depletion (CD) and charge sustaining (CS).

7.1 CD Control Mode Results

Based on the models formulated in section 6.3, subjected to multiple equality and inequality constraints, the optimisation problem was solved. The results presented are structured based on the two different types of EMS, CD and CS modes. These are the most commonly used types in the automotive industry. These are then applied to two drive cycles: NEDC and WLTP in order to clearly view the effect of regenerative braking. First, the report will present the optimisation results for the CD EMS, extracted from the energy and power data. Then, results based around the system mass and volume will be discussed and analysed sequentially in the same order. Finally, the optimal results are summarised with explanation.

The optimisation aimed to minimise the power requirement from the two power sources in the powertrain. This minimisation in turn reduces the hydrogen consumption by the FCS. The adopted procedure provides a global optimum by

emulating a power split controller embedded in the EMS. The results from this section of the analysis show the energy consumption, component behaviour and size, based on the different DoH values.

7.1.1 Energy Consumption

The energy consumption of an FCHEV has several critical dependencies. These include components' sizing, which dictate the mass and volume of the powertrain system, and the amount or rate of energy recuperation from regenerative braking. In other words, the battery's ability to accept high surges of current in the above events. In addition, the system cost plays an important role in commercialising the product. Thus, a trade-off must be made in order to meet the desired targets within the design phase, which is based on the powertrain configuration. The net energy consumption of the vehicle illustrates the effect of regenerative braking and variation in system size. This parameter is also strongly reflective of the propulsion system's fuel economy and drive cycle characteristics. Two distinct drive cycles, NEDC and WLTP, were employed while varying the DoH, based on equation (6-17). An analysis of the two drive cycles in terms of tractive effort and net energies has been performed in section 5.3.2. The obtained DoH values were selected in the range of 0.1 and 0.9, corresponding to battery and FC dominance, respectively. In other words, regions where the DoH was greater than 0.5, it can be can be classed as a FC-dominant region whereas DoH less than 0.5 can be classed as a battery-dominant. This range reflects the power split controller

behaviour. The cost function weighing parameters w1 to w4 (in equation (6-11)) were varied at every outer loop within the sizing algorithm in order to split the power contribution. Figure 78 and Figure 79 show the net energy consumption from the combination of both power sources at four different scenarios depicting four levels of regenerative braking energy at different C-rate values. For this effect to be implemented, the charging C-rate of the battery was varied in steps of 0.5 between 0.5C and 2C. The obtained results depict a specific trend, which is common in both drive cycles while indicating both: the effect of increased system mass and energy recuperation via regenerative braking. Shifting away from FC to battery dominance highlights this effect. An FC dominant powertrain will have a smaller battery pack due to which only a limited amount of energy recuperation is possible. Furthermore, as we start to move towards a more battery dominated powertrain, the net energy consumption starts to decay until a rise because of the increased battery mass. In addition, it can be noticed from the four different trend lines, based on four different C-rates, that the rate of this decay varies. In the NEDC profile the distance is relatively lower than in the WLTP cycle and therefore requires a higher number of drive cycles to fulfil the range required. Also, in each case there is a difference in the magnitude of tractive and braking efforts as described in earlier section 5.3.3 of this report. Upon further scrutiny, it can be noticed that each scenario has only one optimal solution across the whole DoH range. This becomes more apparent by visualising the change in energy (ΔE) across the entire DoH range with respect to the FC dominant powertrain (DoH =

0.9) as presented in Figure 80 and Figure 81. It can be seen that the decay in the net energy consumption occurs faster in higher C-rate values until the effect of increased battery mass demands more tractive effort. Moreover, the energy recuperation from the given drive cycles reaches a stagnation point. Each value of the DoH will have additional varying dependencies in terms of system mass, volume and costs, which are discussed in the following sections of this chapter. Each DoH step has a different capacity of the battery and FC rating, thereby limiting the amount of energy that can be stored from regenerative braking at different C-rates considered in this study. These rates are adjusted based on the recommendations from different manufacturers. A lower C-rate will restrict the battery from absorbing high currents during braking or deceleration intervals in the drive cycle whereas battery with larger C-rates can accepted higher values of currents. Most commercially available EV battery packs recommend a low C-rate for charging [159], [160]. In some cases, exceeding these could result in cell degradation. However, modern battery chemistries such as Lithium-ion batteries are capable of accepting short pulses of high current surges. These pulses usually have a short duration lasting only seconds. However, this comes at the cost of cell degradation and complexity in thermal management system for the battery [164].

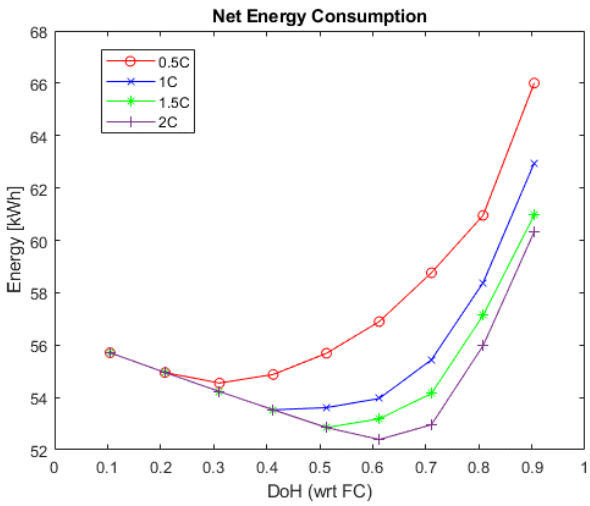


Figure 78: Net energy consumption at different rates of energy recuperation in the NEDC drive cycle replicating 45 iterations to complete the required range.

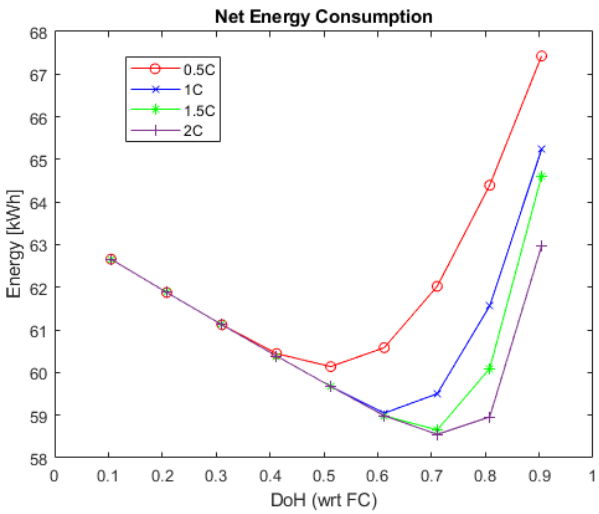


Figure 79: Net energy consumption at different rates of energy recuperation in WLTP drive cycle replicating 21 iterations to complete the required range.

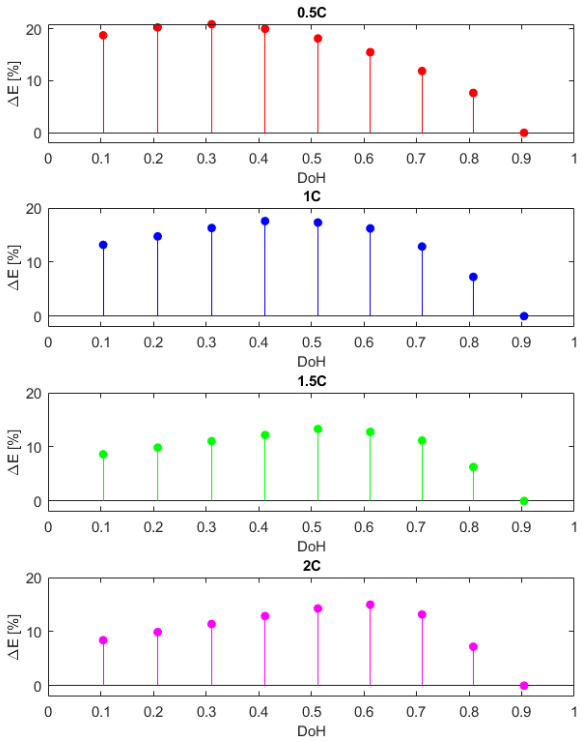


Figure 80: Change in energy for each DoH value in NEDC drive cycle.

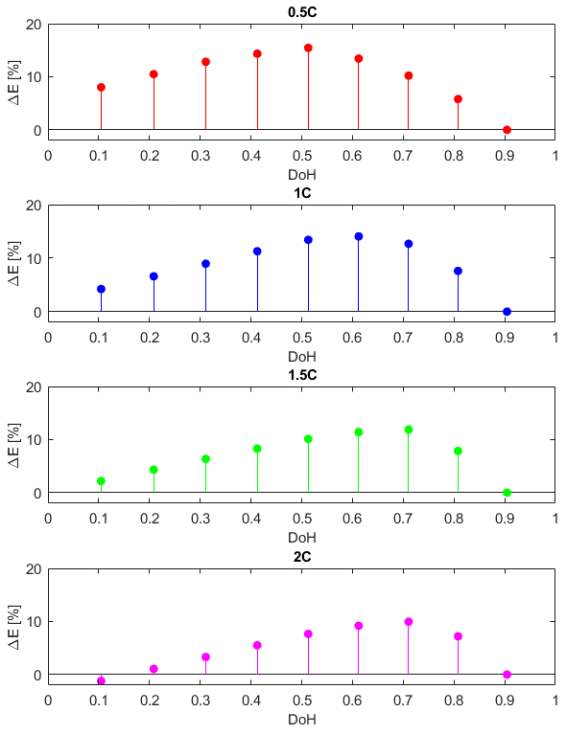


Figure 81: Change in energy for each DoH value in WLTP drive cycle.

A closer look into the individual contributions of FC and battery pack in terms of energy flow is provided in Figure 82. Only the two extremes of charging rates, i.e. 0.5C and 2C, are displayed for a clearer contrast in each duty profile. The battery-

electric range (BER) is the distance which the vehicle can travel solely relying on the battery as an energy source and can be expressed mathematically as equation (7-1).

$$BER = \frac{Vehicle\ Range\ [\text{miles}]}{Energy_{Battery}\ [\text{kWh}]} . Q_{Battery}[\text{kWh}] \quad (7\text{-}1)$$

This option is mainly applicable to plug-in hybrid vehicles where the driver can opt to choose which power source to use. Alternatively, this decision can be made by the supervisory energy management system based on the driver inputs – via the car in-built satellite navigation system, for example, in case where the journey distance is short. Figure 82a and c show the energy distribution and BER along with the corresponding vehicle fuel economy (miles/kWh) in NEDC drive cycle while Figure 82b and d show the equivalent results for the WLTP drive cycle. Although the results in both drive cycles suggest similar pattern of energy flow, the optimal solution in WLTP is found at a more FC-dominant DoH. The reason for this is the increase in magnitude of energy demand which has a direct effect on the system mass. Although the BER values are bound to be similar due to the vehicle range input being the same, the vehicle efficiency differs because the net ratio of traction energy to braking energy in WLTP is higher than in NEDC (as shown in 5.3.2). It can be noticed in the energy flow bar charts that the stagnation point in terms of braking energy is reached later towards the battery dominant region with a smaller C-rate and earlier with a higher C-rate. Thus, a high C-rate can enhance the rate energy recuperation but this may cause the issue of range

anxiety in battery-electric mode for batteries with small capacities. For example, for a DoH of 0.3 and 0.6 in NEDC the battery sizes at 0.5C and 2C are 29 kWh and 25 kWh, respectively.

While these could be the optimal solutions in terms of energy consumption, the BER these can offer is restricted to approximately 200 and 70 miles, respectively. Furthermore, the regenerative braking energy produced by at the FC-dominated region (at DoH 0.9) is 5 kWh and 10 kWh at 0.5C and 2C, respectively. This significant difference in charging rate or the amount of recuperated energy can help in downsizing the battery pack. Depending on the powertrain configuration, this can also help in lowering the system cost. On the contrary, the WLTP optimal solutions are obtained at the mid-point (DoH = 0.5) or closer to the FC-dominant region, where the BER is lower than approximately 130 miles. The hydrogen consumption of the vehicle can be computed using (6-5). For the sake of clarity, only the optimal solution which have the least net energy consumption, corresponding to different amounts of energy recuperation, in both drive cycles are presented in the following section.

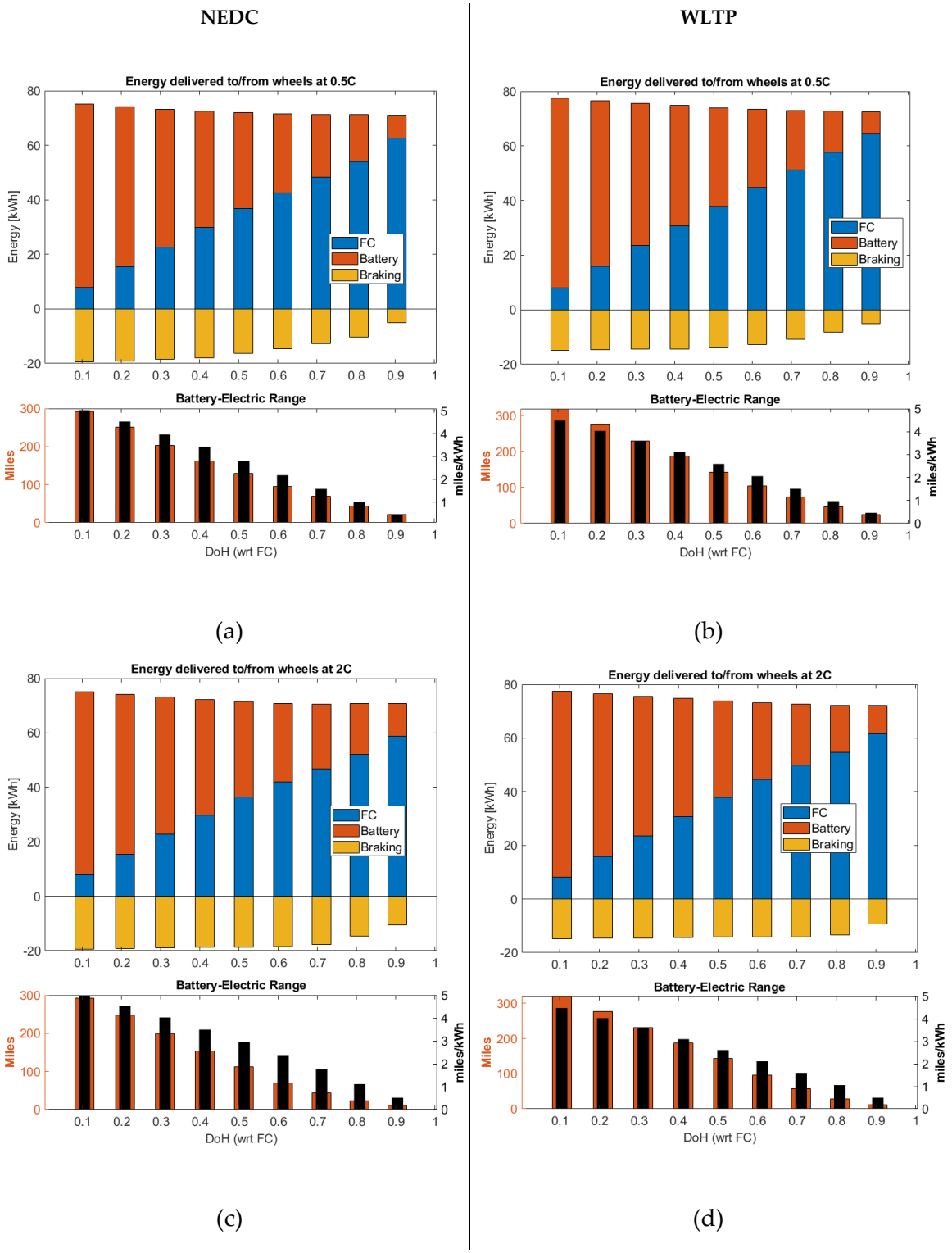


Figure 82: Energy flow bar charts in NEDC drive cycle with charge rate of 0.5C and 2C respectively (a and c); WLTP drive cycle (b and d)

Figure 83 depicts the hydrogen fuel consumed by the FC stack across the full vehicle range, which approximately equals 45 NEDC cycles. The behaviour of the curve remains the same in every iteration until the conditional statement

described in equation (6-19) is triggered. Each curve (colour-coded) corresponds to the DoH which results in the least net energy consumption based on Figure 78. The FC dominant powertrain (with DoH of 0.6) has a higher fuel consumption rate due to a larger contribution made by the FC system. Conversely, the battery dominant powertrain (with DoH of 0.3) has a lower fuel consumption rate as less effort is made for propulsion by the FC system. Thus, hydrogen consumption for DoH values of 0.3, 0.4, 0.5 and 0.6 are 1.1 kg, 1.5 kg, 2.1 kg and 2.4 kg, respectively. Similarly, Figure 84 shows results obtained using the WLTP load profile. The latter results imply variation in the DoH values corresponding to 0.5, 0.6, 0.7 and 0.7 with hydrogen consumption of 2.0 kg, 2.3 kg, 2.5 kg and 2.4 kg respectively. The slight variation in quantity of hydrogen consumption in each case can be attributed to the power requirement difference.

In addition, in WLTP, it can be noted that same DoH values will result in the same fuel consumption rate due to the power split ration for the FC being the same. The repetitive behaviour of the cycles indicate the same power utilisation. Thus, for NEDC 45 iterations will complete the desired range whereas for WLTP 21 iterations are needed. The former drive cycle shows two optimal solutions occurring in the battery dominated region while the latter drive cycle shows optimal solution at and after the mid-point of hybridisation favouring the FC. Key considerations with such results will assist in identifying the amount of fuel

required on-board and the volume for its storage. This aspect is discussed in later sections of the chapter.

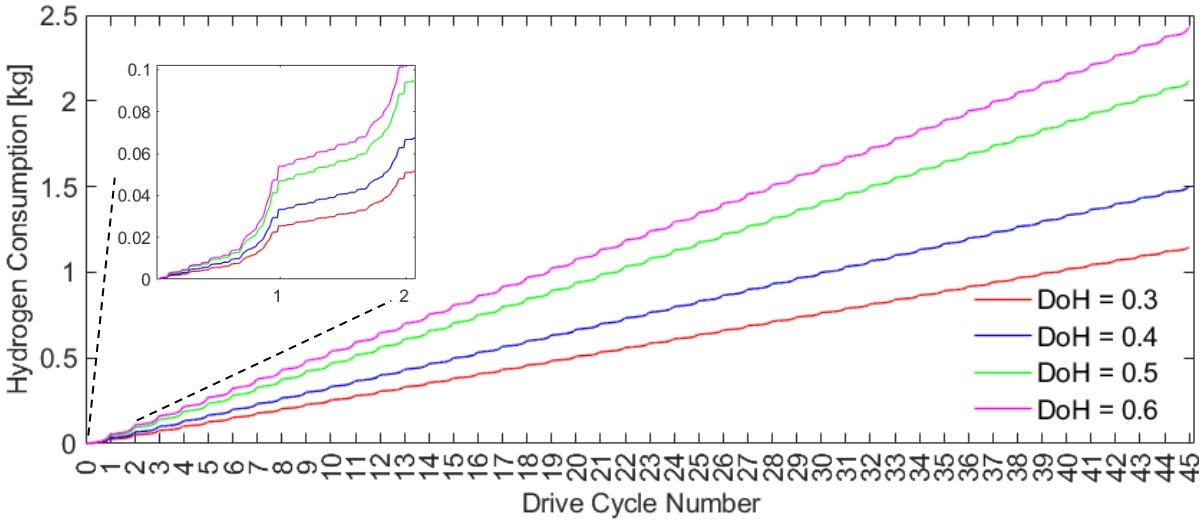


Figure 83: Hydrogen consumption across 45 NEDCs for net energy optimal solutions

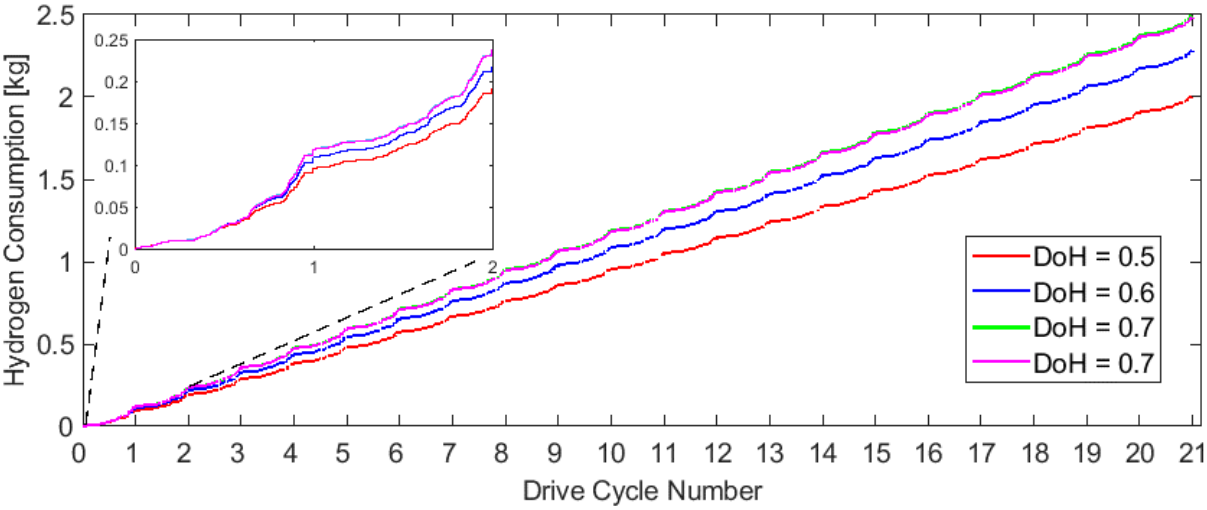


Figure 84: Hydrogen consumption across the whole vehicle range for net energy optimal solutions in WLTP

7.1.2 Component Sizing

Improper sizing of the power source components (FC and battery) can lead to undesired outcomes such as degraded performance in acceleration, lower fuel economy and overly costly powertrain. The sizing of the components has a direct effect on several crucial parameters such as system weight, net fuel consumption

and the overall system cost. Hence, an optimisation-based sizing strategy enables design of the components to be more effective. Component sizing usually concerns the two power sources on-board a hybridised powertrain. One of these is generally classed as the primary power source while the other is classed as the secondary power source. The former is rated or designed such that it is capable of delivering sufficient power for traction at any time with little or no reliance on the secondary source under any circumstance. During the sizing stage, the anticipated vehicle performance and the drive cycle adopted play an important role. The component sizing of such powertrains in the proposed sizing strategy is governed by peak power and energy requirements, which in turn are dependent on vehicle performance criterion such as acceleration, gradeability and range. As clarified in previous sections, vehicle acceleration takes precedence over other factors when rating the power requirements, whereas the range depends on the energy content of on-board storage. This scenario is generally true for road passenger vehicles. The battery sizing considers the DoD which during the optimisation is controlled by the minimum and maximum SoC values set. Figure 85 and Figure 86 show the FC system size (kW) and battery capacity (kWh) against each DoH for the two considered drive profiles, NEDC and WLTP, respectively.

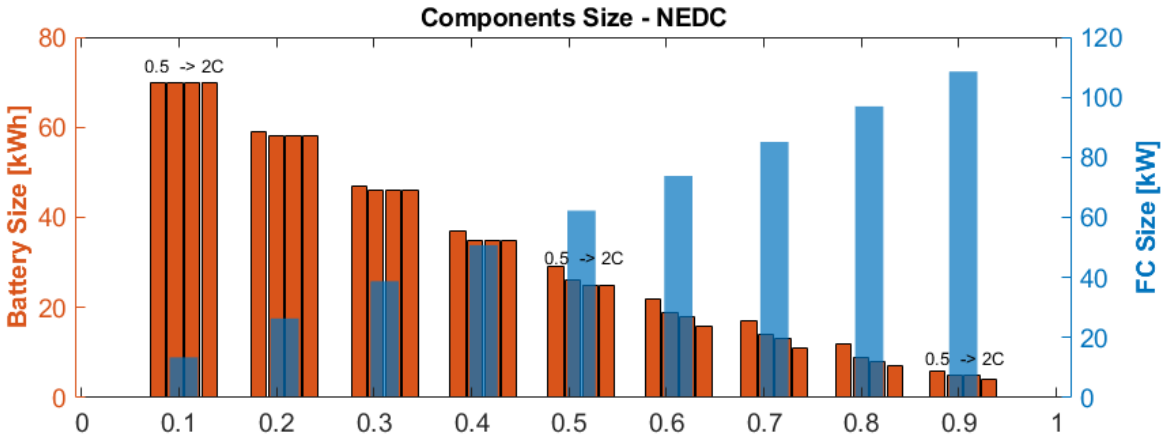


Figure 85: DoH vs components size with 0.5C, 1C, 1.5C and 2C charging C-rates for NEDC profile.

In the case of the former, it is evident from the chart that with a higher charge rate the size of the battery can be reduced by up to 41%, for example, in DoH of 0.7 where the difference between batteries with low and high C-rates is 6 kWh. However, the energy recuperation, based on the drive cycle, braking losses and vehicle dynamics reaches a saturation point. Once this is noticed, further increasing the size of the battery in the sizing algorithm is then dictated by compactness, cost and BER range requirements. A similar pattern is seen in the case of the WLTP drive cycle but saturation in terms of energy recuperation occurs earlier than in the NEDC. In addition, the relatively lower capacities in this scenario is due to a higher energy recuperation factor, which helps in component sizing aspect.

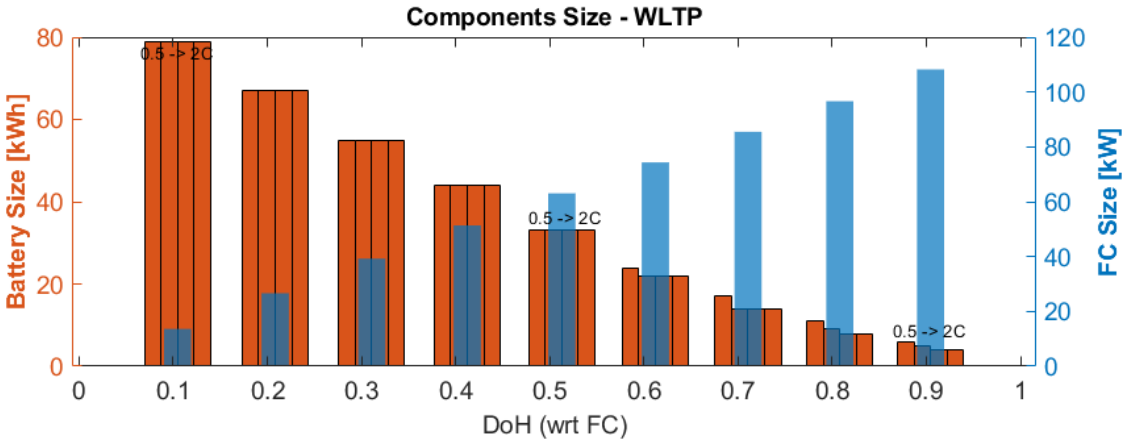


Figure 86: DoH vs components sizing with 0.5C, 1C, 1.5C and 2C charging C-rates for WLTP profile.

7.1.3 Power Split Curves

The PS control mechanism is based on the weighting factors described in (6-11) in the previous chapter. By varying the parameters in the aforementioned function control over the vehicle propulsion in terms of power from each of the power sources on-board the vehicle can be attained. Moreover, with the presence of embedded constraints in equations (6-12) to (6-16) and using the performance indices within the cost function, a range of PS ratios can be achieved to solve the problem. The optimal output results are visualised in the form of power curves in relation to the load. Each iteration will have a different system mass value, depending on the hybridisation ratio of the powertrain. Thus, the power demand at the motor side will see a small increase.

Figure 87 illustrates the power curves of FC, battery and load requirement for a single NEDC profile with the four optimal net energy DoH combinations at different energy recuperation or charging C-rates. The presented results show

different PS ratios between the power sources, hence, resulting in different DoH. It can be noticed that most of the braking energy in the negative cycle of the power requirement is recovered via regenerative braking in all the presented cases. This, in the low C-rate scenario of 0.5C, occurs in the battery-dominant region where there is larger scope of recuperation than in FC-dominant regions, as evident in Figure 82a and c. The SoC curve for a single cycle shows small variations depending on the size of the battery. It can be seen in the figure that the power split ratio in DoH 0.3 favours the battery in meeting the load demand, whilst in the opposite is seen in DoH 0.6 where the FC is meets most of the load demand. In the event of DoH 0.5, the load demand is evenly split between the power sources. The battery pack capacities presented in the NEDC scenario results below have capacities of 47 kWh, 35 kWh, 25 kWh and 16 kWh, corresponding to peak charge power of 23 kW, 35 kW, 37.5 kW and 32 kW respectively. Figure 88 shows similar sets of PS results for WLTP cycle wherein signs of limitation on braking energy recuperation are seen in the 0.5C C-rate with battery size of 33 kWh. The battery pack capacities presented in the WLTP scenario results below have capacities of 33 kWh, 22 kWh, 14 kWh and 14 kWh, corresponding to peak charge power of 16.5 kW, 22 kW, 21 kW and 28 kW respectively.

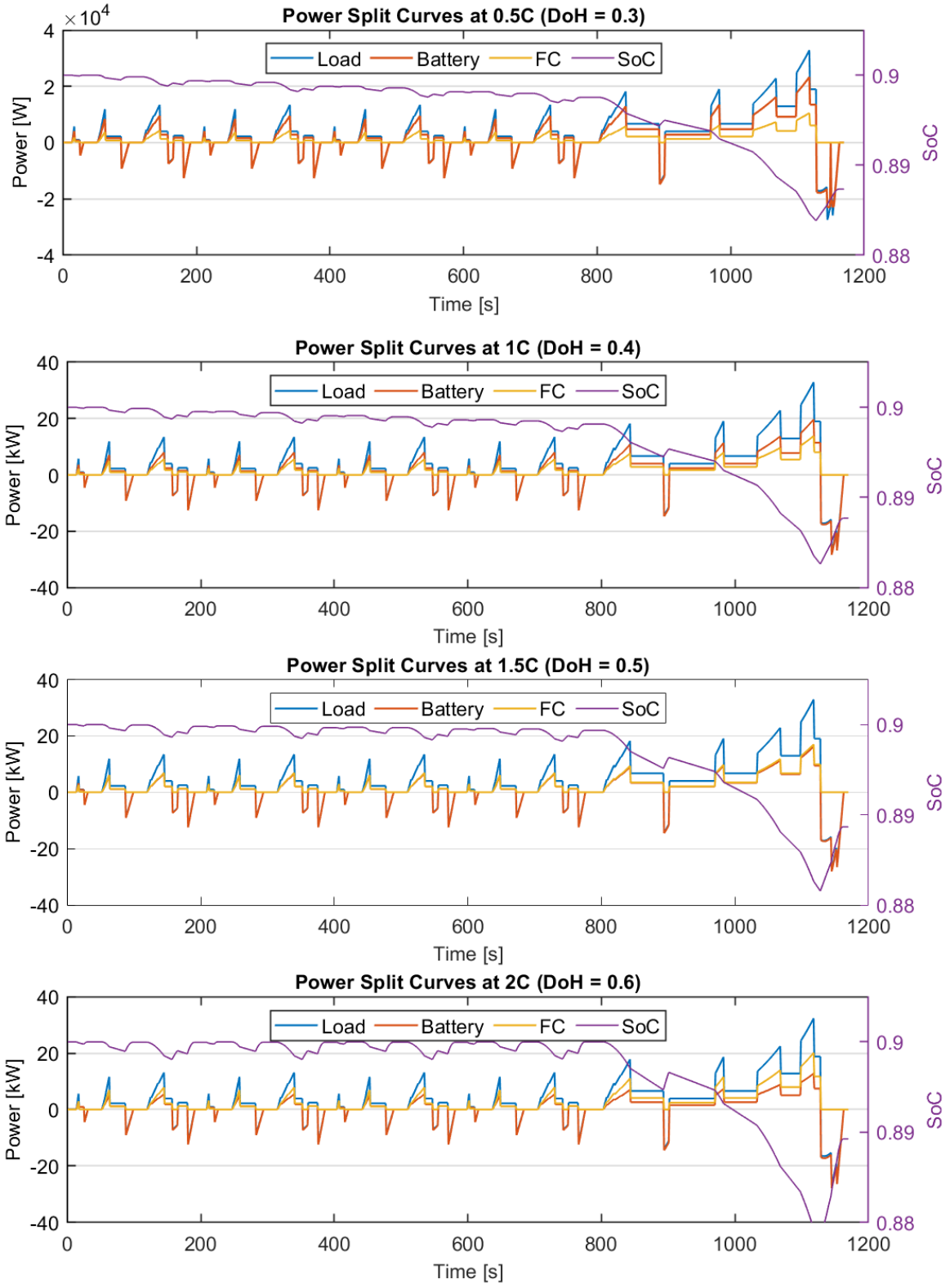


Figure 87: Power split and SoC curves for optimal DoH combinations in the NEDC drive cycle.

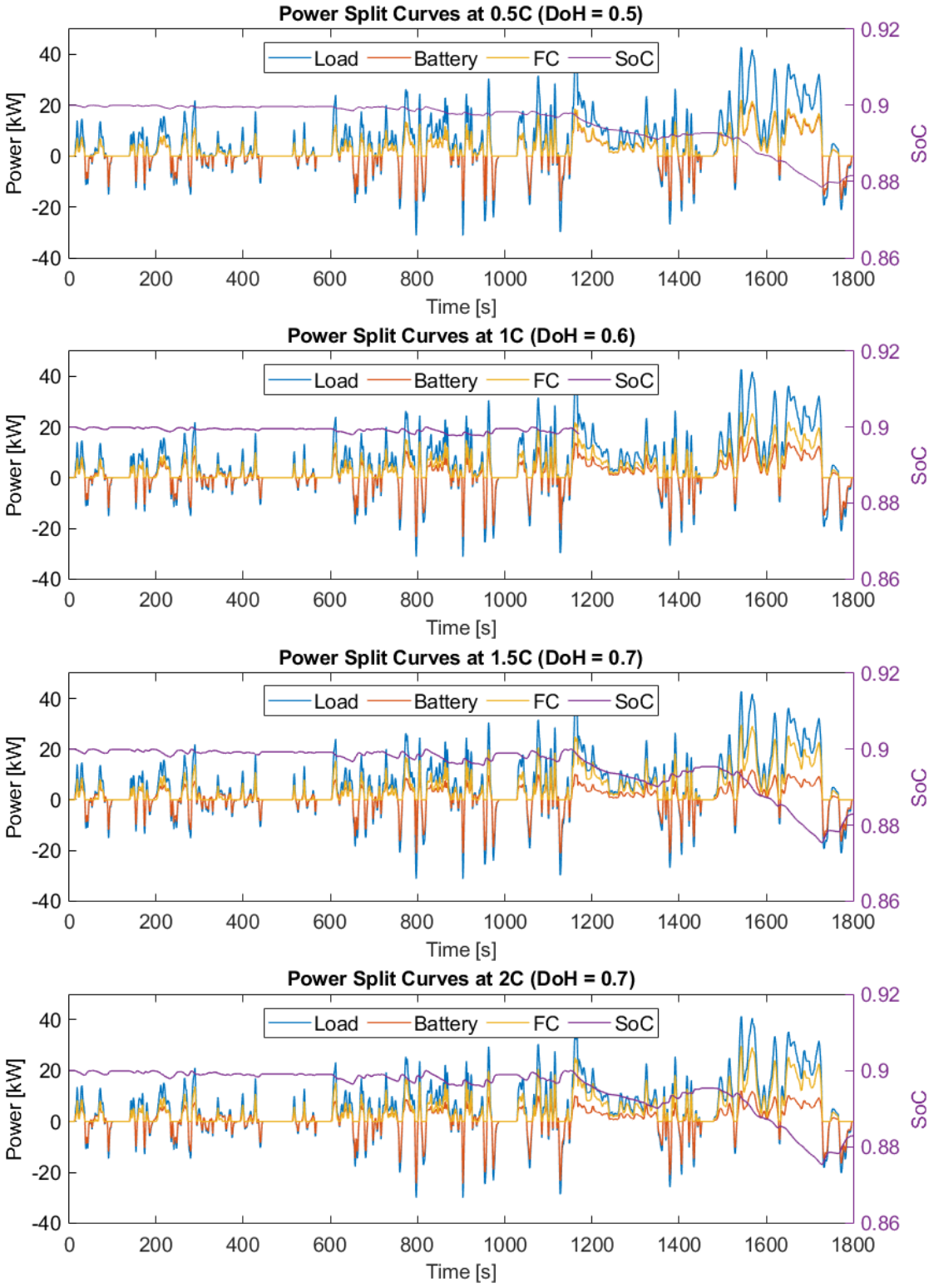


Figure 88: Power split and SoC curves for optimal DoH combinations in the WLTP drive cycle

7.1.4 System Mass and Volume

The system mass and volumes are dependent on the power source ratings, DoH and hydrogen fuel storage. The methodology adopted for computing the mass and volume of each powertrain component is highlighted in equation (6-22). The FCS size is mainly dominated by the auxiliaries which are required to form the entire system. These include BoP components, FC DC-DC converter and hydrogen storage tank. The battery pack size is reliant upon the number of modules and thermal management subsystem which are taken into account for in the gravimetric and volumetric densities. The power conditioning unit for the battery is assumed to be included within the battery pack parameters. Figure 89 shows powertrain system mass and volume with individual contributions from each component. It is evident that the larger the FC stack is, the larger the size of FC auxiliaries. For example, a FC-dominant powertrain (DoH 0.9) of net power 108 kW and having a stack size of 44 kg and 25 L requires auxiliaries amounting to 158 kg and 239 L. Furthermore, batteries having significantly lower specific gravimetric and volumetric energy densities results in higher mass when scaled up. However, the volumetric energy density of batteries offer an advantage, as can be noticed in the presented results. Thus, increasing both the battery capacity beyond the energy recuperation saturation point and the FC stack rating will result in an increased system mass. On the contrary, a high capacity battery pack

will take up almost half the space a complete FCS will take due to its relatively lower volumetric energy density.

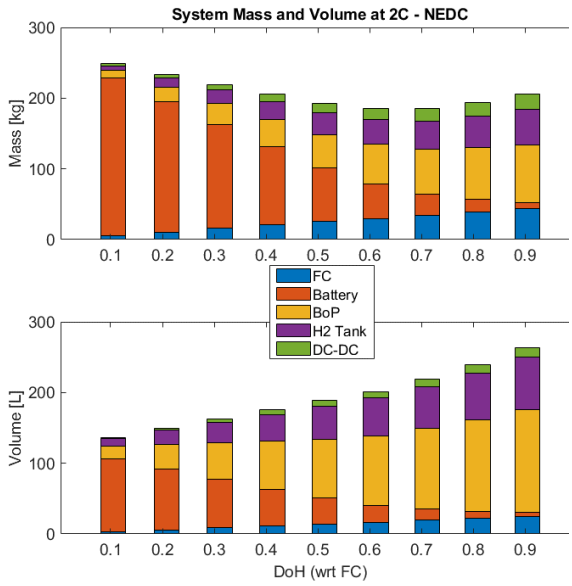


Figure 89: Sizing in NEDC with high C-rate.

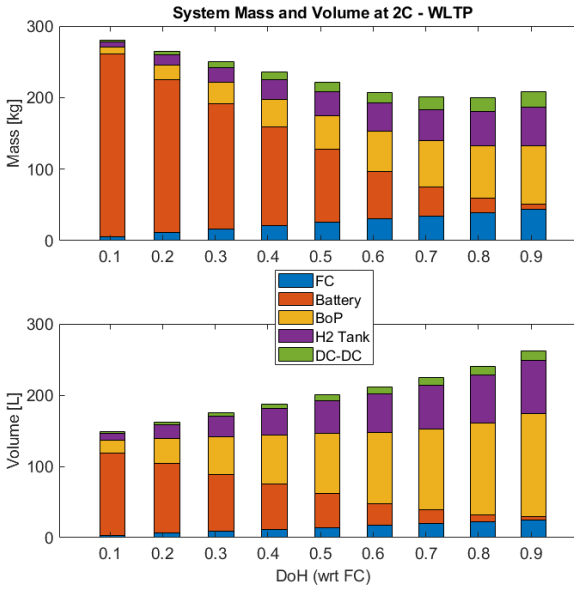


Figure 90: Sizing in WLTP with high C-rate.

In the WLTP cycle, the tractive effort required per cycle is twice as much as in the NEDC, thus requiring a higher capacity battery that has a direct effect on the mass. Figure 90 shows the increased battery mass reaching almost 300 kg with the higher BER and battery dominated powertrain. Moreover, it can be noticed that the least system mass options appear closer in the FC-dominated space at DoH of 0.7 and 0.8. For the sake of clarity, Figure 91 and Figure 92 were plotted to illustrate the system mass and volume for the proposed optimal solutions based on the net energy consumption graphs, corresponding to each C-rate value presented in Figure 78 and Figure 79.

Both scenarios illustrate similar trends in terms of mass and volume variation against the selected DoH. Favouring a battery dominant powertrain shows an

inversely proportional relationship between the mass and volume, and vice versa for a FC dominant powertrain. Thus, from a design perspective a trade-off has to be reached in order to meet specific requirements such as maximum allowable mass, compactness and hydrogen fuel storage based on a predefined range of the vehicle.

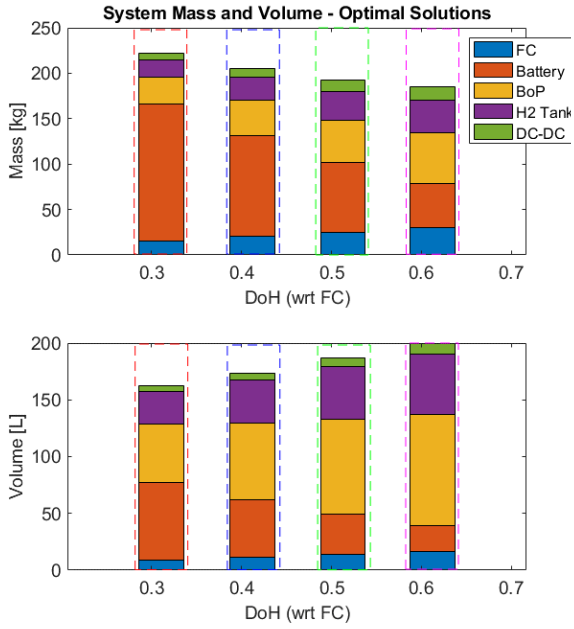


Figure 91: Proposed optimal mass and volume solutions (NEDC).

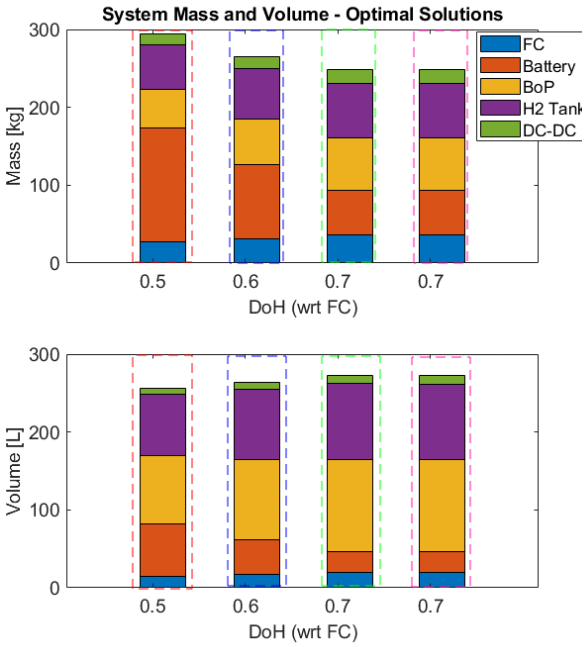


Figure 92: Proposed optimal mass and volume solutions (WLTP).

7.1.5 System Cost

The results obtained from the component sizing can be further scrutinised to compute system costs. Although, the objective function used in the optimisation problem is not a function of the cost, the component ratings offer an estimate of the distribution of the system cost. Thus, equation (7-2) and (7-3) can be used to compute the total powertrain system costs, C_{System};

$$C_{System} = C_{FC_{stack}} + C_{FC_{BoP}} + C_{FC_{DC-DC}} + C_{H_2 Storage} + C_{Battery} \quad (7\text{-}2)$$

$$C_{System} = \left[C_{Stack} \cdot P_{FC,max}\right] + \left[C_{BoP}.P_{FC,max}\right] + \left[C_{DC-DC} \cdot P_{FC,max}\right] + \left[C_{Tank} \cdot Mass_{H_2}\right] + \left[C_{Battery} \cdot Q_{Battery}\right] \quad (7\text{-}3)$$

Where C_{Stack}, C_{BoP} and C_{DC-DC} are dependent on the peak power rating of the fuel cell and C_{Tank} is based on the hydrogen content required for on-board storage. The battery cost, $C_{Battery}$, is mainly dependent on the energy content or the capacity (kWh). Figure 93 and Figure 94 depict the distribution of the system cost for NEDC and WLTP drive cycles. In each case individual contributions from the FC stack, BoP, storage tank, DC-DC converter and battery are highlighted. The two depicted scenarios do not show much difference in the total costs, however, the magnitude of varies mainly because of the sizing of the battery pack. Specifically, this occurs in the battery-dominant space.

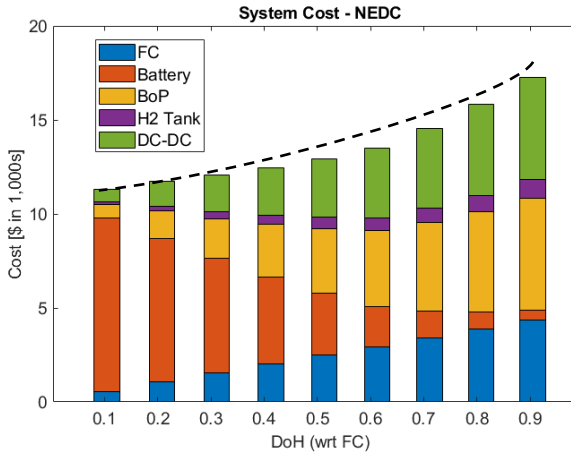


Figure 93: System cost distribution for NEDC.

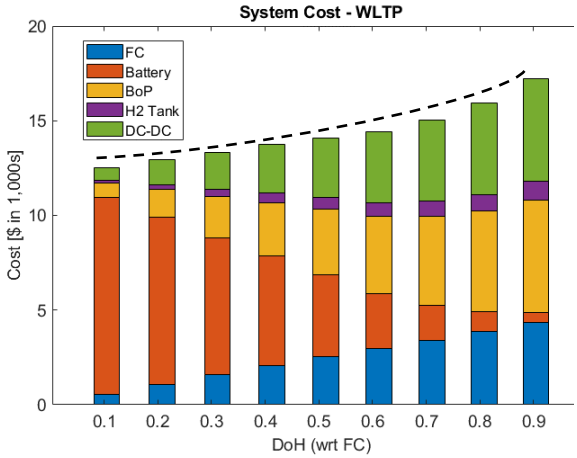


Figure 94: System cost distribution for WLTP.

For the sake of further clarity, the total cost with individualised trend lines of each component cost are plotted for the WLTP case in Figure 95. The cost of FC system

is dependent on the rate of production and are directly proportional to the size of the stack and capacity of hydrogen storage on-board the vehicle. As a result, costs of FC and its dependencies such as the FC DC-DC controller, BoP and hydrogen tank are plotted at production rates of 10,000 units, as well as 100,000 units. The corresponding costs of FC at the above production rates are $ 40/kW and $ 18/ kW [165].

Costs of FC system components used were presented in Table 11. It can be noted from the graph that, at high production rate with a range of DoH 0.4 to 0.7, the total system cost can be lower than a more FC or battery dominated powertrain. However, this is not true at a lower production, which has high FC and auxiliary component's costs. Table 12 is populated with and categorised by power component rating, energy, fuel economy, size and cost data of the optimal solutions (DoH 0.4 for this the discussed type of control method. The table is segregated into component rating, energy, fuel economy, mass and volume and cost for the two considered drive cycles.

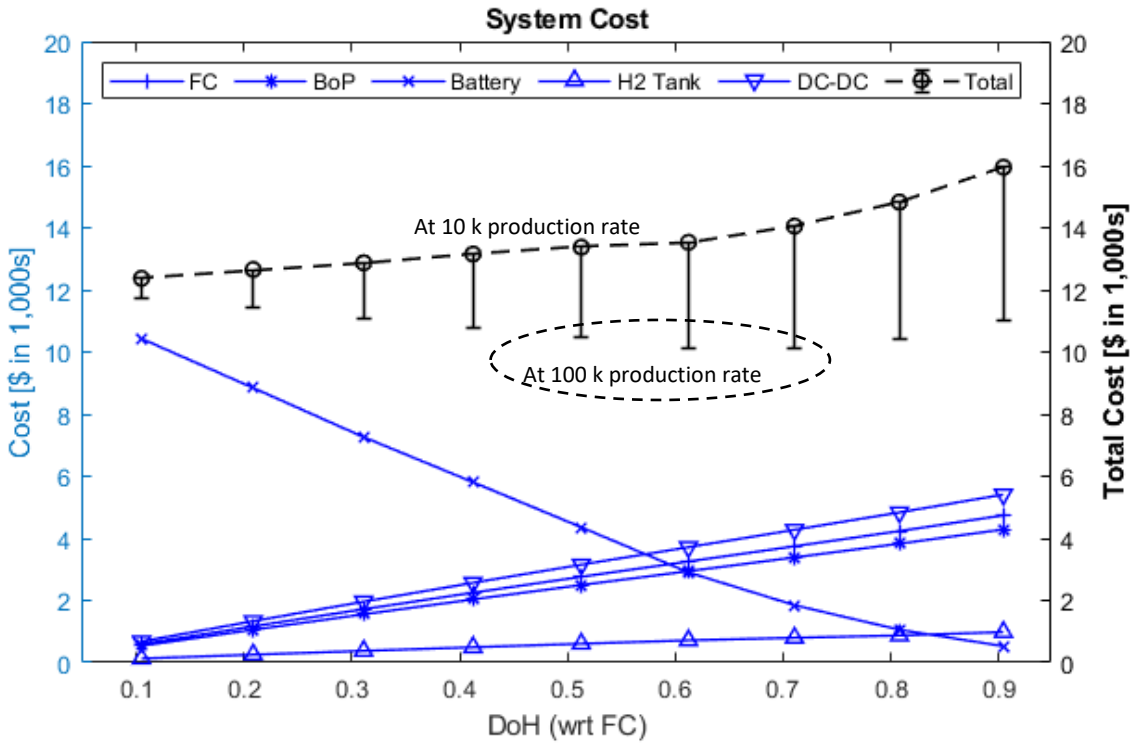


Figure 95: Powertrain system cost with individual trend lines at every step of DoH.

Table 12: Proposed optimal solutions data consisting component sizing, energy, fuel economy, mass & volume and cost parameters.

			Component Sizing			**Energy**		**Fuel Economy**		**Mass & Volume**		**Cost**
Drive Cycle	C-rate	DoH	FC size [kW]	Battery Size [kWh]	Net Energy [kWh]	Energy Savings[a] [%]	Energy Recuperation [kWh]	H2 Consumption [kg]	BER [Miles]	System Mass [kg]	System Volume [L]	System Cost[b] [$]
NEDC	0.5 C	0.3	39	47	54.55	20.87	18.379	1.14	220	222.47	162.55	12,022
	1 C	0.4	51	35	53.53	17.58	18.741	1.49	154	205.65	173.79	12,214
	1.5 C	0.5	62	25	52.85	13.30	18.566	2.11	112	192.27	187.11	12,629
	2 C	0.6	74	16	52.39	14.98	18.471	2.42	69	185.03	199.82	13,124
WLTP	0.5 C	0.5	66	33	60.14	15.44	29.794	3.75	143	293.77	256.63	16,354
	1 C	0.6	77	22	58.98	14.05	29.752	4.26	97	265.16	264.11	16,076
	1.5 C	0.7	88	14	58.64	11.89	29.606	4.79	59	248.56	273.29	16,155
	2 C	0.7	88	14	58.54	9.95	29.999	4.79	58	248.17	272.75	16,146

[a] saving with respect to the FC-dominant rating at DoH 0.9.

[b] at 100 k production rate of FC systems.

7.2 CS Control Mode Results

In the CS control mode the battery is recharged during the journey in line with matching the target value of SoC at the end of the journey. This control scheme is mainly applicable to a FC-dominant hybrid vehicle, wherein the only source of energy is hydrogen. Moreover, one of the major differences when employing this control strategy, compared to PSCD, is the size of the battery pack. In addition to energy storage and recapturing energy from braking, the purpose of the battery is to provide assistance during high and transient load dynamics. Thus, most of the tractive energy effort is fulfilled by the FC and, therefore, the capacity of battery can be kept small whilst maintaining a high power-to-energy ratio. For this reason, specific driving distance has to be known in order to compile a drive cycle. Data extracted from Department of Transportation offers the daily driving miles per driver for a light-duty or passenger vehicle in the UK and USA [166], [167]. The data is visualised in Figure 96 and Figure 97, implying that at least 80 % of the journeys have a daily distance of up to 25 miles. This metric can assist the design phase of passenger vehicles.

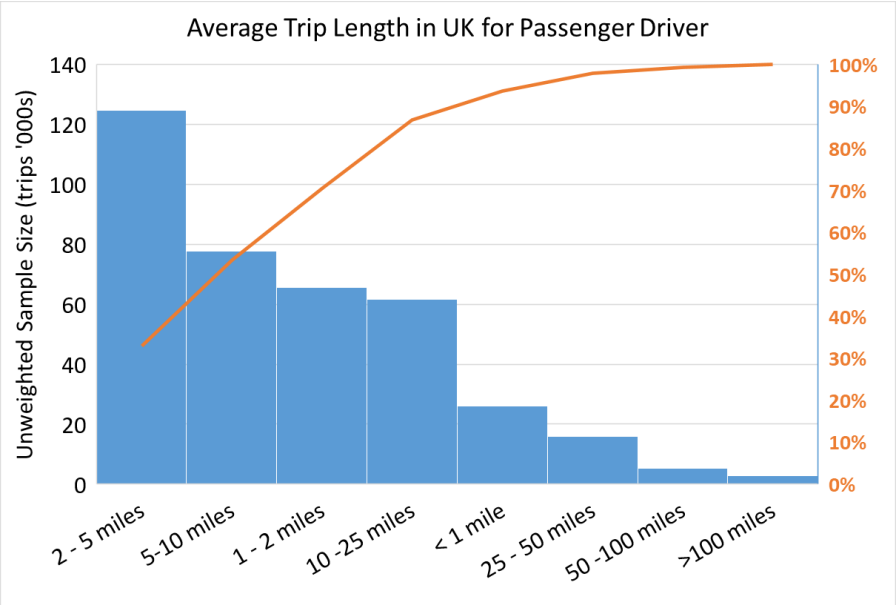


Figure 96: UK average travel distance for a passenger car/driver- data extracted from [167].

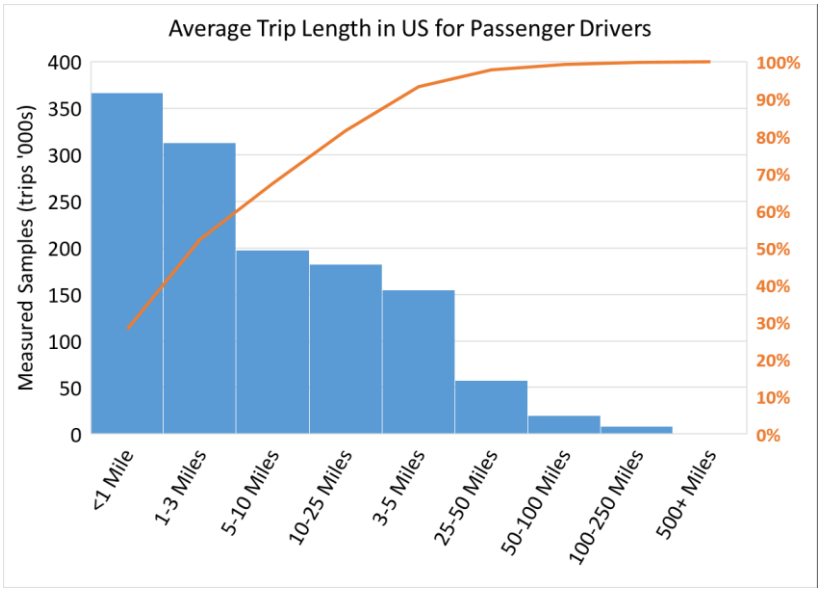


Figure 97: USA average travel distance for a passenger car/driver – data extracted from [166].

7.2.1 Energy and Fuel Consumption

The energy and fuel consumption results depend on the vehicle range entered into the sizing algorithm. Similar drive cycles, i.e. NEDC and WLTP, were used but with different lengths in order to match the daily average journey distance. The fuel cell having a larger contribution towards the vehicle propulsion will result in the DoH to always be above 0.5. This would mean that the power-to-energy ratio of the battery would be high. Specifically, for FCHEV where the FC is the dominant source, unlike pure EV or PHEVs. This can be further evidenced from the experimental data extracted for Toyota Mirai in Chapter 5. The peak charge rate used in the sizing algorithm was taken from Samsung batteries. The peak discharge and charger power of the battery are based on the C-rates available from commercially available vehicles such as the Toyota Mirai and literature [168].

The ratio between the discharge and charge rates extracted from the above sources corresponds to a range of 1.5 to 2. Thus, this power-to-energy ratio aligns closely with that of the battery pack installed in the 1st generation Toyota Mirai is used. The vehicle battery pack (1.6 kWh) is capable of 25.5 kW peach discharge power for 10 to 15 seconds, which corresponds to approximately 15C discharge rate. With the aforementioned ratio of 1.5, this results in a peak charge C-rate of 10 C. Figure 98 depicts the NEDC plots for energy and fuel consumption, battery energy distribution (discharged, charged and recaptured energies) and SoC for a

DoD of 50%. Five battery capacities ranging from 1 kWh to 3 kWh are considered, resulting in a DoH range between 0.6 and 0.9.

Figure 98a shows the net energy consumption of the FCHEV vehicle with a charge and discharge C-rates of 10C and 15C respectively. For example, with these rates the 3 kWh battery is capable of reaching peak charge and discharge power values of up to 30 kW and 45 kW. Although these peak figures are realistically only applicable for limited duration (typically ranging between 15 to 30 s), the battery surges appear within in this period for both NEDC and WLTP scenarios. Moreover, the net energy consumption will always be higher in a FC-dominant powertrain wherein the battery charge rate is restricted because of a smaller power-to-energy ratio.

In the case of NEDC, the net energy consumption peaks at 58.6 kWh with the majority of contribution made by the FC (DoH 0.88). The figure then reaches a stagnation point at 56.5 kWh below 0.7 DoH. In addition, as all energy on-board comes from hydrogen every case should have the same net energy; but as the smaller batteries in large DoH are limited in absorbing braking energy, they require more hydrogen in the splits as highlighted in Figure 98b. This is due to the regenerative braking energy reaching a stagnation point once the peak charging power reaches or exceeds the maximum available negative power based on the power profile. The results show that a higher energy recuperation rate results in lesser amount of expended hydrogen acquired in Figure 98c. In our work, this

amount of hydrogen consumed or used to recharge the battery is referred to as 'expended hydrogen'. The expended hydrogen sees an increase after the drop as a result of inversely proportional contributions from the FC and battery. At DoH of 0.66 the FC stack size is reduced, limiting the peak stack power, while the battery size is increased thereby resulting in a relatively higher peak charge and discharge powers as well as energy content. This is to match the initial and final SoC towards the end of the drive cycle in charge-sustaining mode as validated in Figure 98d. Since the NEDC has relatively higher magnitude of deceleration and frequent braking from high speeds, the SoC does not approach the SoC_{min} threshold value. On the contrary, the SoC_{max} threshold is reached at multiple times, after which the control algorithm restricts battery charging beyond this point. The global optimisation algorithm determines the optimal intervals of recharging the battery by using hydrogen fuel and regenerative braking. Four NEDC cycles were simulated in order to reach the identified daily required distance.

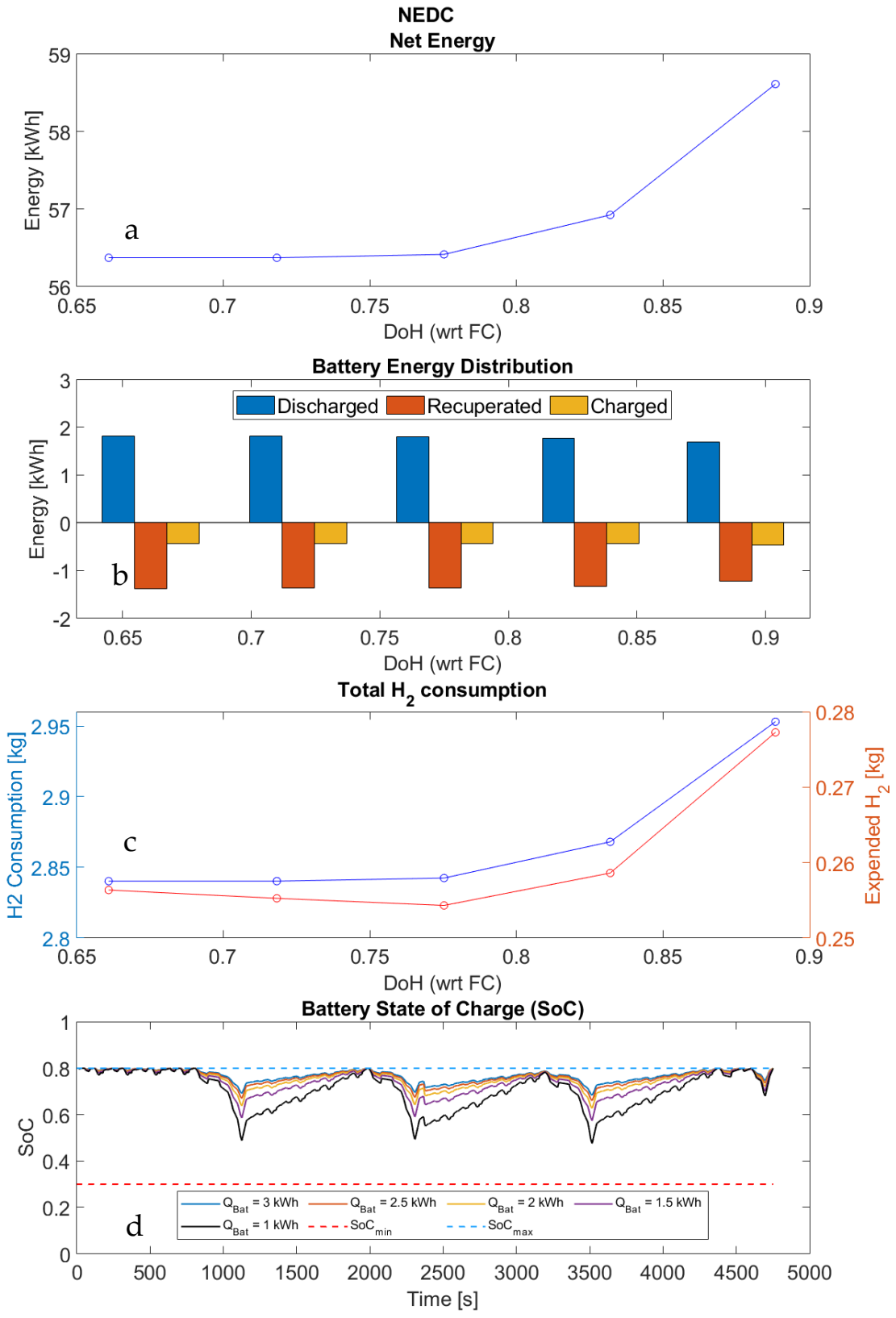


Figure 98: NEDC PSCS control strategy results with 10C peak charging C-rate and 50% DoD window modelling on 4 consecutive cycles; a: net energy consumption, b: battery energy distribution, c: consumed and expended hydrogen, d: battery SoC for different battery capacities

Plots in Figure 99 show similar modelling results with the WLTP drive cycle. Battery parameters such as its size, DoD, charge and discharge C-rates are kept the same as in the previous case. Moreover, the tractive effort requirement in WLTP is higher per cycle. The distance travelled per cycle equates to approximately 29 miles. As a result, only two WLTP cycles are compiled per simulation to produce the following results. Then, the scaling variable is rounded to achieve the full length of the journey taking into consideration the number of drive cycles needed to fulfil the whole journey. Thus, most of the results produced a similar trend as in the NEDC cycle simulation.

The net energy consumption seen in this scenario is slightly higher due to the profile behaviour with faster dynamics and higher tractive effort requirements. In addition, the battery contribution and energy recuperation via braking is higher, thereby enabling the battery to be recharged less from the FC. In the FC dominant region the net energy consumption is seen the highest with 69 kWh (see Figure 99a). Furthermore, the stagnation point in the net energy consumption occurs earlier than in the previous case, thanks to a higher amount of regenerative braking. The magnitude of this energy recuperation into the battery ranges between 1.6 kWh and 1.8 kWh in FC and battery dominant regions, respectively (see Figure 98b).

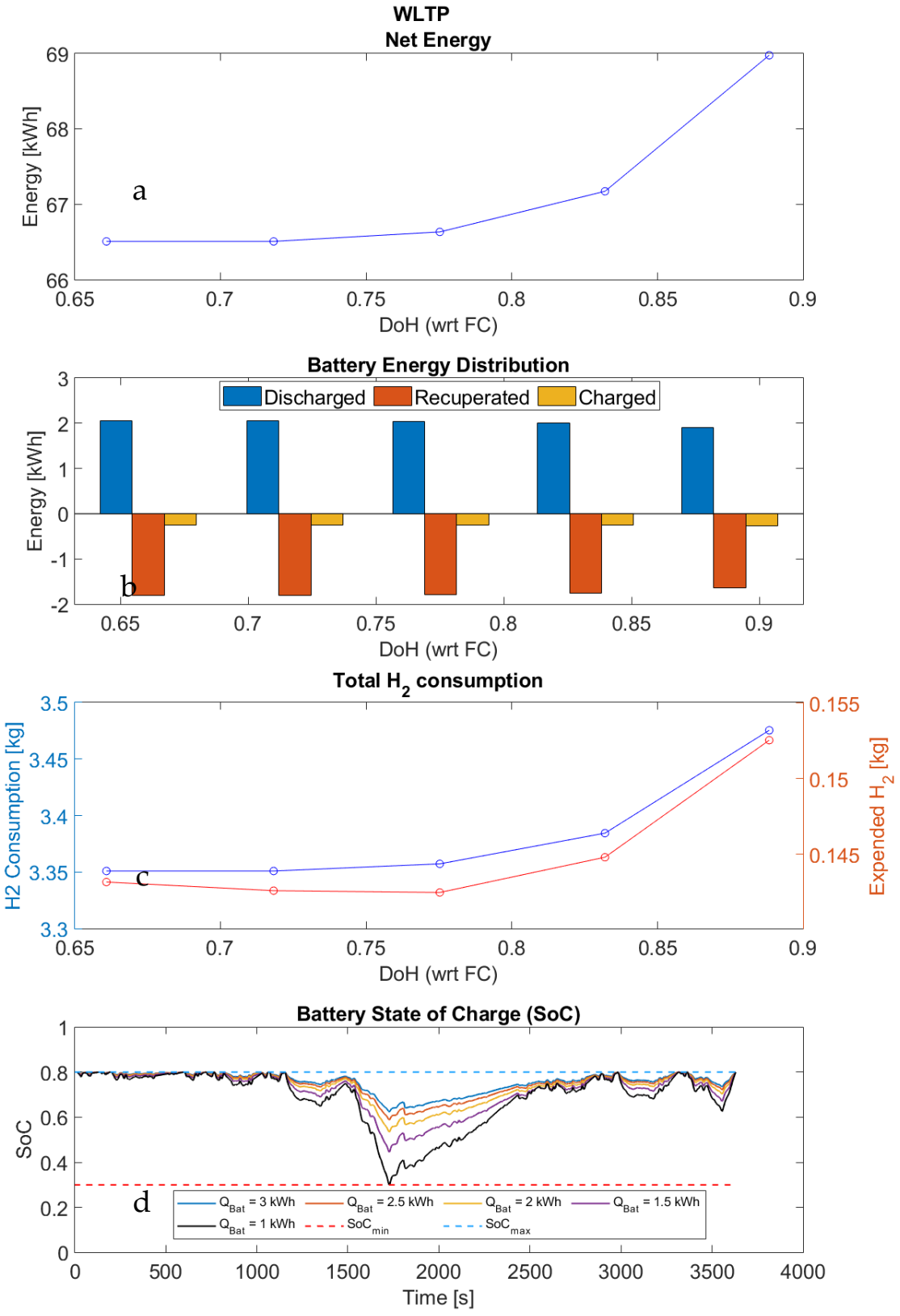


Figure 99: WLTP PSCS control strategy results with 10C peak charging C-rate and 50% DoD window modelled on 2 consecutive cycles; a: net energy consumption, b: battery energy distribution, c: consumed and expended hydrogen, d: battery SoC for different battery capacities

The total hydrogen consumption seen across the full vehicle range results in 3.5 kg and 3.3 kg with DOH values of 0.88 and 0.66. Added into this consumption is the expended amount of hydrogen which is used to recharge the battery, employing a charge-sustaining control strategy. It can be noticed that a lower magnitude of expended hydrogen is seen (ranging between 0.15 kg and 0.14 kg) as a result of higher rates of energy recuperation as shown in Figure 98c. Figure 99d shows the SoC of the battery for the modified drive cycle which aims to complete a daily driving range. The global optimisation adheres to the constraints registered (described in section 6.3.5) as seen when reaching the maximum and minimum threshold values. In addition, the final battery SoC value equals the initial value, adhering to the equality constraint set. The battery pack with the smallest capacity of 1 kWh sees higher discharging due to the power requirements. Thus, a smaller battery pack than this would be undersized for this particular range and power profile, reason being, insufficient peak power capabilities.

Figure 100 visualises the occurrences where the battery is recharged using the hydrogen fuel on on-board the vehicle. The plots are stacked on each occurrence for a given battery pack. This is derived based on conditional statements where vehicle deceleration is seen, and battery power is in the charging mode region. The battery has a limit on accepting limited surges of current which are dictated by the charging C-rate, for a specified short duration given by the manufacturers. This behaviour is clearly reflected in the plots below which showcase the events

based on the aforementioned conditions. The NEDC profile shows higher frequency of battery recharging events having energy magnitudes within the range of 3.8 kWh and 20.7 kWh for battery capacities of 1 kWh and 3 kWh respectively (see Figure 100a and b). Conversely, the WLTP cycle has lower frequency of events but with higher energy magnitudes and durations. Since the size of the battery as well the FC differs inversely, larger battery packs will see a larger magnitude of recharging in the simulation.

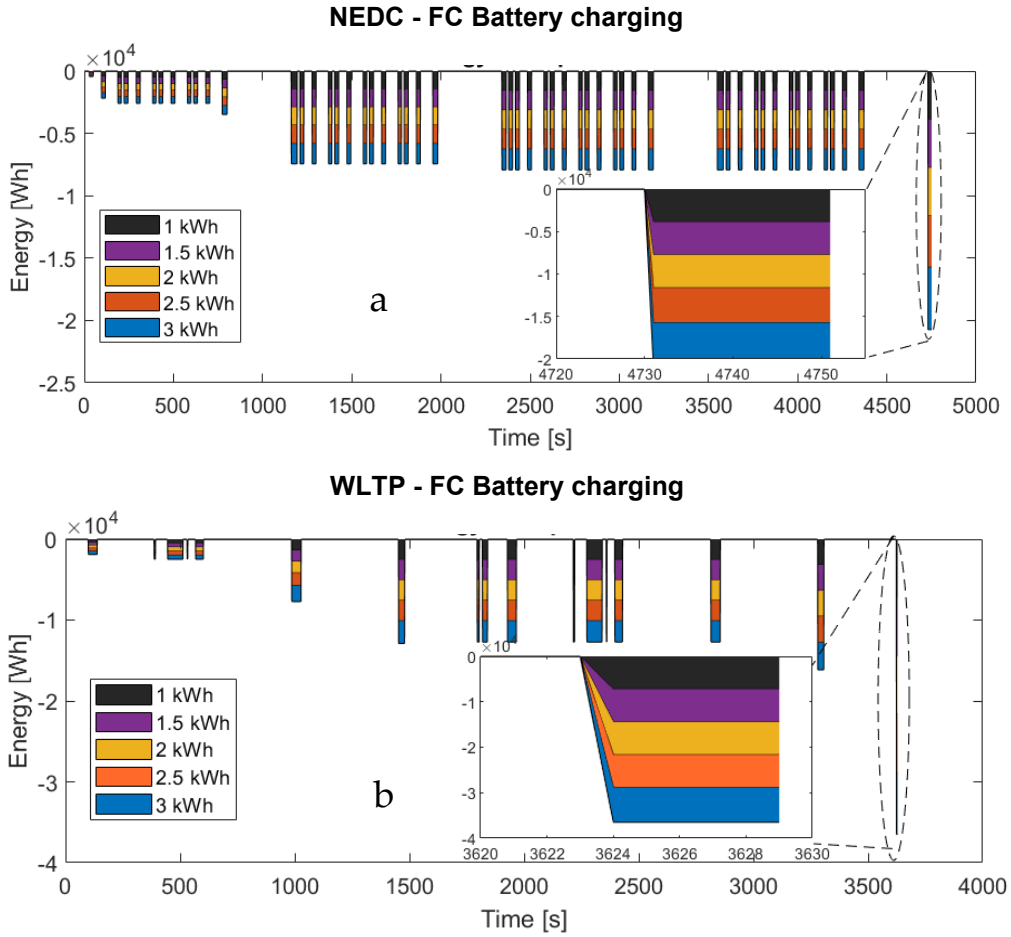


Figure 100: Stacked plots depicting energy recuperation events for recharging the battery using hydrogen on-board the vehicle, a) NEDC profile b) WLTP profile.

7.2.2 System Sizing and Cost

The sizing of the components, battery pack and FC system, is achieved based on an iterative optimisation process. A FCHEV typically incorporates a battery pack with small capacities and large FC stack for propulsion. Similar to previous analysis, the components' mass and volume are derived based on the gravimetric and volumetric densities obtained from the date in Table 13. Since the changes between the two drive cycles will result in small changes, only the WLTP results will be presented Figure 101 shows the component sizing and system cost wherein the DoH ranges between 0.66 and 0.88. This range represents the dominance of FC system in meeting the tractive effort. From Figure 101a it can be seen that the FC size is 120 kW close to the DOH 0.9 (FC dominant region) and 87 kW close to 0.66 DoH. Although the difference between the extremes is just 2 kWh battery capacity, a 26 % downsizing in FC power is seen. Figure 101b displays the mass of the entire system in kg for a non-plugin FCHEV. It can be noticed that there is no major change in the total mass magnitude, corresponding to approximately 250 kg in all cases. The variations occur in the masses of the FC BoP components, battery and stack, all of which are dependent on the peak power output rating. The FC system BoP contributes the most reaching 36 % contribution of the entire system mass in DoH 0.88. In contrast, the total system magnitude varies across the DoH axis, showing highest volume of 300 L at the FC dominant region (see Figure 101c). Moreover, it can be seen that the FC system BoP takes up 159 L of

powertrain space. Figure 101d illustrates the system costs at two rates of production. The first rate of production of 10,000 units per year offers a higher total cost, where as a mass production rate of 100,000 units per year reduces the cost by up to 30 %. The values of costs assumed through mass production of FC stacks and FC system BoP were $ 21.52/kW and $27/kW, respectively [165]. Cost values for DC-DC converter, H2 tank and battery packs were extracted from the target values presented by DoE [163]. The results show similar trend lines in each DoH case for the FC stack and its auxiliaries such as BoP and DC-DC converter. The cost of the aforementioned is directly proportional to the size of the FC stack. For example, the total cost of the system (119 kW stack and 1kWh battery) with a DoH of 0.88 is $ 17,200 (at 10k production rate) and $ 11,730 (at 100k production rate).

Table 13: CD mode results for WLTP cycle populated with battery and FC parameters.

DoH	**0.66**	**0.71**	**0.77**	**0.83**	**0.88**
Pbmin [kW]	30.00	25.00	20.00	15.00	10.00
Pbmax [kW]	45.00	37.50	30.00	22.50	15.00
SoC_min			0.3		
SoC_max			0.8		
SoC_0			0.8		
SoC_final	0.7991	0.7990	0.7991	0.7990	0.7990
C-rate			10.0		
D-rate			15.0		
Q_Bat [kWh]	3.00	2.50	2.00	1.50	1.00
FC size [kW]	87.71	95.61	103.50	111.39	119.29
Fcmax [kW]	87.71	95.61	103.50	111.39	119.29
H2 Consumed [kg]	3.33	3.33	3.33	3.36	3.46
Expended H2 [kg]	0.26	0.26	0.25	0.26	0.28
FC Energy [kWh]	66.51	66.51	66.63	67.17	68.97
Net Energy [kWh]	66.51	66.51	66.63	67.17	68.97
System Vol [L]	237.12	249.70	262.45	275.72	290.64
System Mass [kg]	245.51	245.55	245.71	246.26	248.01
Total Cost at 10k rate [$]	13,212	14,199	15,188	16,185	17,202
Total Cost at 100k rate [$]	91,65	97,98	10,433	11,074	11,734

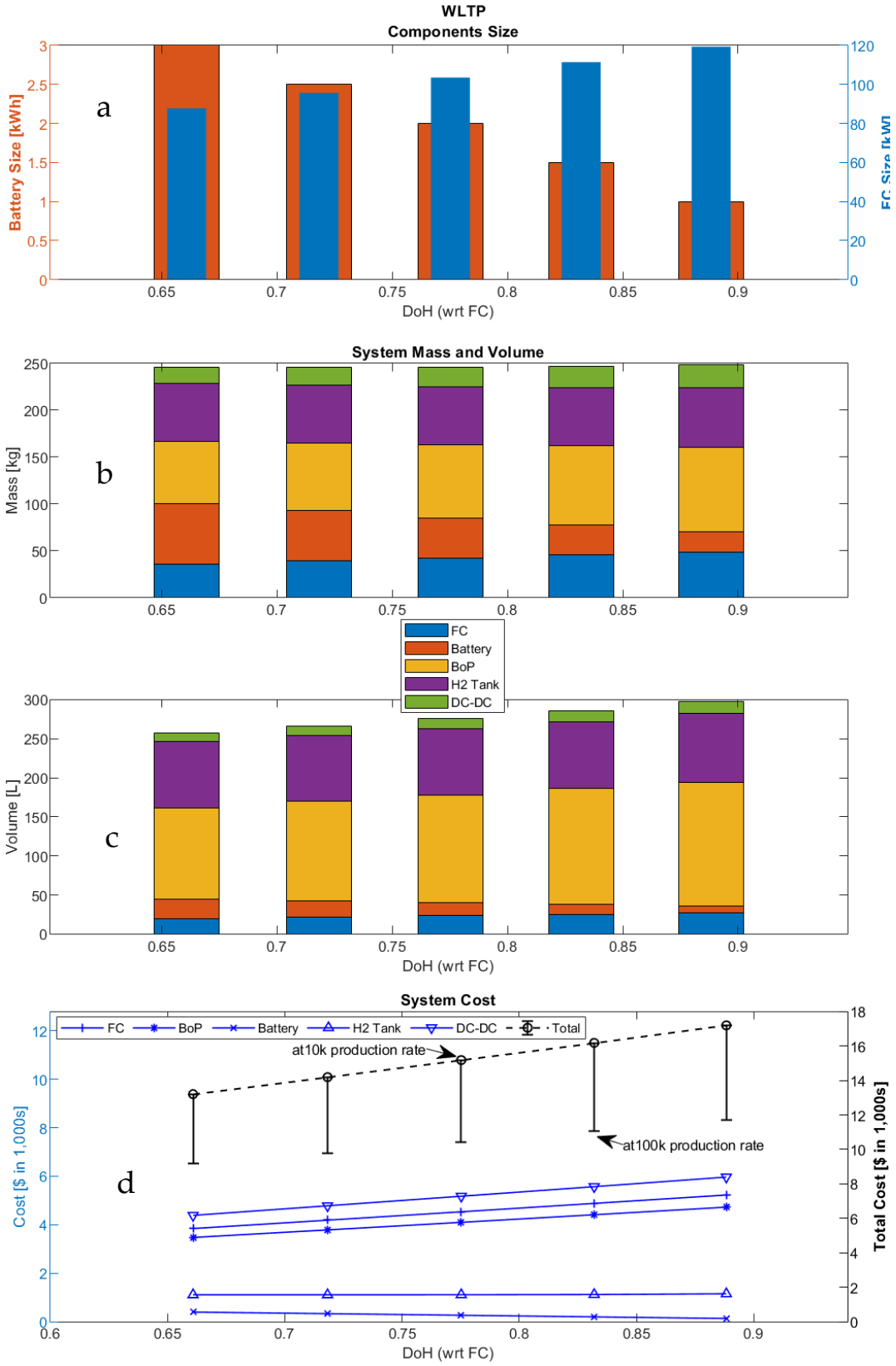


Figure 101: Component sizing and cost derivation of FCHEV based on WLTP cycle; a: FC and battery sizing, b: system mass, c: system volume and d: system cost.

7.3 **Summary**

This chapter presented a novel sizing strategy for a fuel cell hybrid powertrain. Low temperature hydrogen fuel cell systems on their own introduce, in terms of economic, performance and compactness, challenges. Thus, hybridisation using a battery with high power-to-energy ratio can assist in energy recuperation and fuel cell downsizing.

The approach began with the creation of a vehicle powertrain model followed by an optimisation using dynamic programming which used a variety of input parameters. Having acquired a benchmark vehicle specification to feed into the vehicle model built in Chapter 5, power requirement based on specific drive cycles were obtained. An optimisation problem with pre-defined equality and inequality constraints, along with upper and lower boundary conditions with accepted tolerance levels, was formulated. It was found that the sizing of components could have a direct effect on the mass and volume of the powertrain. Thus, observing sensitivities around scaling of each components within the propulsion system enables the design optimisation to reach an optimal degree of hybridisation. An important aspect when hybridising is the capability of a battery pack to accept current surges in event of vehicle braking or deceleration. Since there are several battery chemistries, Lithium-ion chemistry is predominantly used in the automotive industry due to its power density and charging C-rates.

Two different widely applicable control modes (CD and CS) were illustrated based on two distinct drive cycles. In the CD control mode, the strategy allows for contributions from both power sources for propulsion, while restricting the use of hydrogen for battery recharging. This requires the battery on-board to have a plug-in charging feature. Hence, the powertrain configuration is classed as a plug-in hybrid. Moreover, the battery pack incorporated is sized to have a larger capacity such that the desired range is fulfilled on a single full charge. In addition, this configuration offers a relatively longer BER. With four different charging C-rates (0.5C, 1C, 1,5C and 2C) considered in the study in each drive cycle, the results vary slightly. The results indicate that there is a strong correlation between the battery's ability to accept high currents (at high charging C-rates) and its capacity, gravimetric and volumetric densities. Although a larger pack offers a longer BER, but the with significantly higher added mass on to the powertrain. Conversely, a FC dominant powertrain may reduce the system mass, however, the volume requirement will be higher due to auxiliaries such as the BoP, storage tanks and power conditioning units. This outcome could present a challenge in terms of packaging, which may lead to higher drag on the vehicle.

In CS mode, the strategy aims at recharging the battery pack using the hydrogen fuel on-board the vehicle such that the final SoC equates the initial SoC. In this FCHEV configuration, the plug-in option is absent and thus sizing is done based on a daily average distance travelled. This enables the battery pack to be sized

considerably smaller than in the previous case. However, the peak discharge and charge C-rates of such high power-to-energy ratio based batteries are high. In our case, 15 C for discharge and 10 C for charging were used. The results show that the cost function for the power split controller adheres well towards the constraints and delivers minimisation based on the strategy described in 6.3.9, resulting in DoH range of 0.66 to 0.9. The optimality in this range was found to be at DoH 0.77 due to the least amount of hydrogen consumption and expended into the battery.

8 Conclusions

8.1 Summary and conclusions

This thesis presented work, in the form of experimentation, modelling and simulation, on two aspects; systems integration of a PEMFC system and implementation of design optimisation strategy on a fuel cell hybridised with battery powertrain. Any optimisation in these two areas resulting in fuel savings, and cost savings, is advantageous in providing hydrogen electrification solutions such as the fuel cell technology the cost competiveness it needs. Unlocking cost competitiveness of fuel cell system remains a challenge, thus optimisation in the system integration to minimise the system cost by optimal sizing is required. On the system integration side, a liquid cooled 5 kW low temperature polymer electrolyte membrane fuel cell (PEMFC) system with a bespoke balance of plant (BoP) was designed and integrated, as discussed in Chapter 3. The design involved all four sub-systems consisting anode, cathode, thermal management and electrical power conditioning sub-systems.

Following this, a control system for the built system was developed in LabVIEW graphical software environment interfaced with a robust embedded controller (cRIO). This laboratory-scale set up was then used in carrying out experimentation with the aim of devising a hydrogen purging strategy needed in the anode compartment of the fuel cell stack, all of which was extensively presented in

Chapter 4 of this thesis. The devised anode purging strategy procedure was independent of time or the duration of operation. Instead, a new parameter (Ah), relying solely on the current drawn from the fuel cell stack, was proposed in the study. The conclusion of this aspect of the thesis was the identification of an ideal range between 22 to 32 Ah function with an anode design employing a recirculation pump.

Modelling work enables easier analysis and provides relevant scrutiny of real world systems. For this reason, vehicle modelling, consisting of relevant sub-systems such as the electrical-equivalent fuel cell, battery, DC-DC converter, electric motor, was conducted in Chapter 5 using the AVL Cruise M software package. A rule-based or heuristic control strategy was developed and simulated in the software, using the Toyota Mirai as a benchmark vehicle. An extensive amount of raw data on this fuel cell vehicle was available that allowed us to conduct a comparative study on the obtained modelling and simulation results. The results showed similar pattern in the functional behaviour of our rule-based controller and how Toyota Mirai operates in the NEDC and WLTP drive cycles.

In Chapter 6, the design optimisation strategy aimed at finding optimal component sizing solutions within a range of varying degree of hybridisation (DoH), employing two different control modes; charge sustaining (CS) and charge depletion (CD). Problem formulation through dynamic programming, mimicking a model-based energy management strategy (EMS) was implemented and

analysed, utilising the already built vehicle mode in Chapter 5. Furthermore, the applicability of these control modes depend on the powertrain configuration, be it a plug-in fuel cell hybrid electric vehicle (FCHEV) or a fuel cell dominant FCHEV. The adopted non-linear constrained global optimisation process was iterative in nature, thereby enabling extraction of minimised parameters. The findings from the design optimisation study are summarised as below;

- The integration of the EMS with the component sizing phase of the powertrain plays a vital role. In our case, the power split ratio embedded within the control mechanism dictated the DoH, having a direct effect on fuel cell and battery sizing.
- Charge depletion control results suggest that, with low power-to-energy ratio and C-rates (0.5 C, 1C, 1.5C and 2C) of the battery pack based on Lithium-ion chemistry, a plugin-in FCHEV powertrain configuration is more appropriate. In this configuration, the battery can be recharged using the grid electricity, while offering a battery-only electric range (BER). The criteria used for identifying optimal solutions was the net energy consumption of the vehicle throughout the entire vehicle range. Of course, this parameter being a function of the regenerative braking energy, the charging C-rates play a vital role in the rate of recapturing the energy and storage. The DoH with optimal results corresponding to the aforementioned battery charging C-rates were found to be 0.3, 0.4, 0.5 and

0.6 in NEDC and 0.5, 0.6, 0.7 and 0.7 in WLTP cycles, respectively. The former set of DoH resulted in larger battery size than in the latter case due to magnitude differences in the magnitude of energy recuperation which effects the energy consumption. Finally, the costs as well as the gravimetric and volumetric size of the power components, including the BoP, were found to be directly proportional to the power and energy ratings of the fuel cell and battery, respectively.

- In CS control mode, the C-rates were significantly higher due to the need of having larger power-to-energy ratio in the battery packs. This gave a DoH range of 0.66 to 0.88. Hydrogen being the only source of energy on-board the vehicle, the battery is allowed to be recharged by the fuel cell using the hydrogen fuel. This added 'expended hydrogen' parameter in the criteria of proposed optimal solutions.

8.2 **Future Recommended Work**

Although the experimentation and modelling work in this research project achieved their goals with satisfactory results, there can be further improvement and work in the two segments. On the PEMFC system side, the anode purging strategy can be further developed by carrying out statistical manipulations on the individual cell voltages. To avoid cell flooding in the anode side, the system could be integrated with additional flow rate, temperature and relative humidity sensors at the outlet of anode. Furthermore, although the hydrogen recirculation pump in

the current system had very small power consumption, a passive high flow rate hydrogen injector can be employed to replace the pump.

The physical system can be demonstrated in a prototype vehicle with a battery pack or supercapacitor bank. The powertrain can be attached to a dynamometer test rig for emulating real world conditions. With this approach, the design optimisation can be employed and validated depending on several parameters such as the battery chemistry, drive cycle and vehicle specifications. Since the undertaken optimiser already uses model-based systems, it can be further modified to adopt the model predictive control (MPC) theory with the aim of greater minimisation. MPC within the supervisory controller will require a prediction horizon for optimisation which, in the case of an electric vehicle, can be acquired from the satellite navigation systems data on board.

In addition to the above recommended work, a sensitivity analysis using the algorithm can be made. This should include a different type vehicle powertrain such a heavy duty or long haul truck. In this case the battery chemistry can play a vital role. Lithium-ion batteries have multiple different cathode materials such as nickel manganese-cobalt (NMC), lithium iron phosphate (LFP) and lithium titanium-oxide (LTO). Each of these will slightly differ in power and energy density, cost and cycle life. Hence, integrating these variables into the design optimisation strategy, in the form of constraints, will result in obtaining a feasibility region that can allow for better applicability.

References

[1] International Maritime Organization (IMO), "Acting to cut emissions from ships," *Cutting-GHG-emissions*, 2019. [Online]. Available: https://www.imo.org/en/MediaCentre/HotTopics/Pages/Cutting-GHG-emissions.aspx. [Accessed: 02-Sep-2022].

[2] WHO, "Air pollution," *Ambient air pollution: Health impacts*, 2019. [Online]. Available: https://www.who.int/airpollution/ambient/health-impacts/en/. [Accessed: 13-Sep-2018].

[3] Eurostat, "Road freight transport by journey characteristics," *Transport statistics at regional level*, 2022. [Online]. Available: https://ec.europa.eu/eurostat/statistics-explained/index.php?title=Road_freight_transport_by_journey_characteristics#Average_distance_travelled_per_tonne_of_load. [Accessed: 01-Jan-2022].

[4] R. Matulka, "History of Electric Vehicles," *Department of Energy*, 2014. [Online]. Available: https://www.energy.gov/articles/history-electric-car. [Accessed: 01-Jan-2019].

[5] S&P Global, "EV Chargers: How many do we need?," *Mobility*, 2023. [Online]. Available: https://www.spglobal.com/mobility/en/research-analysis/ev-chargers-how-many-do-we-need.html. [Accessed: 01-Jan-2023].

[6] Statista, "Number of cars sold worldwide from 2010 to 2022, with a 2023 forecast," *Vehicles & Road Traffic*, 2023. [Online]. Available: https://www.statista.com/statistics/200002/international-car-sales-since-1990/. [Accessed: 11-May-2022].

[7] McKinsey Global Institute, "The net-zero transition," *Sustainability*, 2022. [Online]. Available: https://www.mckinsey.com/capabilities/sustainability/our-insights/the-net-zero-transition-what-it-would-cost-what-it-could-bring. [Accessed: 02-May-2021].

[8] IEA, "Global energy-related greenhouse gas emissions, 2000-2022," *IEA, Paris*, 2023. [Online]. Available: https://www.iea.org/data-and-statistics/charts/global-energy-related-greenhouse-gas-emissions-2000-2022. [Accessed: 11-Jun-2023].

[9] IPCC, "Climate change widespread, rapid, and intensifying.," *IPCC, Geneva*, 2021. [Online]. Available: https://www.ipcc.ch/2021/08/09/ar6-wg1-20210809-pr/. [Accessed: 02-Feb-2022].

[10] D. Clark, S. Joiner, and S. Bernard, "How each country's emissions and climate pledges compare," *Financial Times*, 18-Jan-2023.

[11] Bloomberg NEF, "New Energy Outlook, Global renewable energy trends: solar and wind move from mainstream to preferred," *The New Energy Outlook 2022*, 2023. [Online]. Available: https://about.bnef.com/new-energy-outlook/. [Accessed: 01-Jan-2023].

[12] IRENA, *Geopolitics of the energy transformation: the hydrogen factor.* Abu Dabi: IEA Publications, 2022.

[13] Heraeus, "Platinum demand from fuel cell cars – dream or reality?," *Heraeus Precious Metals*, 2018. [Online]. Available: https://www.heraeus.com/media/media/hpm/doc_hpm/precious_metal_update/en_6/20181031_PGM_Market_Analysis.pdf.

[14] DOE, "Technical Targets for Polymer Electrolyte Membrane Fuel Cell Components," *Hydrogen and Fuel Cell Technologies Office*, 2019. [Online]. Available: https://www.energy.gov/eere/fuelcells/doe-technical-targets-polymer-electrolyte-membrane-fuel-cell-components. [Accessed: 01-May-2022].

[15] IEA, "Technology roadmap: Hydrogen and fuel cells," *Technology Reports*, 2015. [Online]. Available: https://www.iea.org/reports/technology-roadmap-hydrogen-and-fuel-cells.

[16] European Commision, "European Green Deal: ambitious new law agreed to deploy sufficient alternative fuels infrastructure," *Press Release Brussels*, 2023. [Online]. Available: https://ec.europa.eu/commission/presscorner/detail/en/ip_23_1867. [Accessed: 01-Jun-2023].

[17] A. Jayakumar, "A comprehensive assessment on the durability of gas diffusion electrode materials in PEM fuel cell stack," *Front. Energy*, vol. 13, no. 2, pp. 325–338, 2019, doi: https://doi.org/10.1007/s11708-019-0618-y.

[18] A. Dicks and J. Larminie, *Fuel cell systems explained*, 2nd ed. West Sussex, England: John Wiley & Sons, 2003.

[19] Joint Research Centre, Institute for Environment and Sustainability, R. Edwards, L. Jean-Francois, and B. Jean-Christophe, "Well-to-wheels analysis of future automotive fuels and power trains in the European context: report version 3c, July 2011," *Publ. Off. Eur. Union*, 2014, doi: /10.2788/79018.

[20] Volvo. "What are Hydrogen Fuel Cells?" *Hydrogen that reduce CO2 emissions*. Accessed: 12.10.2023. [Online]. Available: https://www.volvogroup.com/en/sustainable-transportation/responsible-business/climate/hydrogen-fuel-cells.html

[21] Hydrogen Council, "Hydrogen scaling up: A sustainable pathway for the global energy transition,"Report, November, 2017.

[22] Department for Business, Energy & Industrial Strategy (BEIS), "UK Low Carbon Hydrogen Standard," London, 2022.

[23] National Grid, "Future Energy Scenarios," Report. 2022. [Online]/ Available: https://www.nationalgrideso.com/document/283101/

[24] T. Smolinka and J. Garche, *Hydrogen Production by Water Electrolysis*, 1st ed., Elsevier, 2021.

[25] G. Wu, X. Zhang, and Z. Dong, "Powertrain architectures of electrified vehicles: Review, classification and comparison," *J. Franklin Inst.*, vol. 352, no. 2, pp. 425–448, Feb. 2015, doi: 10.1016/J.JFRANKLIN.2014.04.018.

[26] Hyundai Motor Group, "Hyundai Motor's XCIENT Fuel Cell Heavy-Duty Trucks to Hit German Roads," 2022. [Online]. Available: https://www.hyundaimotorgroup.com/news/CONT0000000000046014. [Accessed: 01-Sep-2022].

[27] European Commision, "Heavy-duty trucks drive clean hydrogen to the next level," *Horizon: The EU Research & Innovation Magazine*, 2022.

[28] Hydrogen Insight, "Hydrogen will be preferred solution for long-haul trucks, but all cars will be battery electric: Shell's new 2050 scenario," *Transport*, 2023. [Online]. Available: https://www.hydrogeninsight.com/transport/hydrogen-will-be-preferred-solution-for-long-haul-trucks-but-all-cars-will-be-battery-electric-shells-new-2050-scenario/2-1-1423292. [Accessed: 01-May-2023].

[29] M. Ehsani, Y. Gao, S. Longo, and K. Ebrahimi, *Modern Electric, Hybrid Electric, and Fuel Cell Vehicles: Fundamentals*, 3rd ed. CRC Press, 2018.

[30] K. Beard W., *Linden's Handbook of Batteries*, 5th ed. New York: McGraw Hill, 2019.

[31] T. Placke, R. Kloepsch, S. Dühnen, and M. Winter, "Lithium ion, lithium metal, and alternative rechargeable battery technologies: the odyssey for high energy density," *J. Solid State Electrochem.*, vol. 21, no. 7, pp. 1939–1964, 2017, doi: 10.1007/s10008-017-3610-7.

[32] P. Meister, H. Jia, J. Li, R. Kloepsch, M. Winter, and T. Placke, "Best Practice: Performance and Cost Evaluation of Lithium Ion Battery Active Materials with Special Emphasis on Energy Efficiency," *Chem. Mater.*, vol. 28, no. 20, pp. 7203–7217, 2016, doi: 10.1021/acs.chemmater.6b02895.

[33] Audi AG and S. Lehnert, "Lithium-Ion Battery for Audi A6 PHEV," 2017. [Online]. Available: http://cii-resource.com/cet/AABE-03-17/Presentations/BATO/Lehnert_Steve.pdf. [Accessed: 01-Sep-2019].

[34] M. E. Şahin, F. Blaabjerg, and A. Sangwongwanich, "A Comprehensive Review on Supercapacitor Applications and Developments," *Energies*, vol. 15, no. 3, pp. 1–26, 2022, doi: 10.3390/en15030674.

[35] Q. Xun, Y. Liu, and E. Holmberg, "A Comparative Study of Fuel Cell Electric Vehicles Hybridization with Battery or Supercapacitor," *SPEEDAM 2018 – Proc. Int. Symp. Power Electron. Electr. Drives, Autom. Motion*, Amalfi, Italy, pp. 389–394, 2018, doi: 10.1109/SPEEDAM.2018.8445386.

[36] Emerson, "Series Instrument Supply regulators," 2019. [Online]. Available: fisher.com. [Accessed: 01-Mar-2019].

[37] Bronkhorst Ltd., "EL-Flow Thermal Mass Flow Meters and Controllers," *EL-FLOW Select Mass Flow Meters / Controllers for Gases*, 2020. [Online]. Available: www.bronkhorst.com. [Accessed: 20-Jul-2020].

[38] Neodym System Inc., "Gas detection systems for sage energy," *HydroKnowz Catalytic hydrogen monitor with optional relay*, 2022. [Online]. Available: http://www.neodymsystems.com/n_hydroknowz.shtml.

[39] Parker Hannifin Corp., "High Flow Diaphragm Pumps (air/gas)," *T2-04 Miniature Diaphragm Pump*, 2020. [Online]. Available: https://ph.parker.com/us/en/product-list/t2-04-miniature-diaphragm-pump. [Accessed: 11-Sep-2019].

[40] Zahn Electronics, "Step Up Converters 9,000W-15,200W," 2019. [Online]. Available: https://www.zahninc.com/dc-dc-converters/dc-dc-step-up-converters/dcdc-step-converters-9000w-15200w/. [Accessed: 01-Jan-2019].

[41] Y. Al-sagheer, "Fuel Cells and hydrogen for balancing renewable energy fluctuations: A control-oriented approach," University of Birmingham [PhD Thesis], 2017.

[42] Hydrotechnik UK Ltd, "TSOK Threaded Temperature Sensor," *Threaded Sensors*, 2020. [Online]. Available: https://www.hydrotechnik.co.uk/tsok-threaded-temperature-sensor. [Accessed: 09-Sep-2019].

[43] RS Pro, "High Accuracy Temperature Transmitter," 2019. [Online]. Available: https://uk.rs-online.com/web/p/temperature-transmitters/1852284. [Accessed: 06-May-2019].

[44] TE connectivity, "Humidity Temperature Transducer," *Humidity Transducers & Assemblies*, 2020. [Online]. Available: https://www.te.com/usa-en/product-CAT-HSA0001.html. [Accessed: 01-Aug-2020].

[45] Zentro-elektrik GmbH, "Electronic DC Load," 2020. [Online]. Available: https://crichard.web.cern.ch/pdf/Manual & Datasheet/Zentro Elektrik EL6000 Electronics Load - Datasheet.pdf. [Accessed: 20-May-2019].

[46] T. Matsuura, J. Chen, J. B. Siegel, and A. G. Stefanopoulou, "Degradation phenomena in PEM fuel cell with dead-ended anode," *Int. J. Hydrogen Energy*, vol. 38, no. 26, pp. 11346–11356, 2013, doi: 10.1016/j.ijhydene.2013.06.096.

[47] S. Abbou *et al.*, "High Potential Excursions during PEM Fuel Cell Operation with Dead-Ended Anode," *J. Electrochem. Soc.*, vol. 162, no. 10, pp. F1212–F1220, 2015, doi: 10.1149/2.0511510jes.

[48] L. Dumercy *et al.*, "PEFC stack operating in anodic dead end mode," *Fuel Cells*, vol. 4, no. 4, pp. 352–357, 2004, doi: 10.1002/fuce.200400053.

[49] M. W. Knobbe, W. He, P. Y. Chong, and T. V. Nguyen, "Active gas management for PEM fuel cell stacks," *J. Power Sources*, vol. 138, no. 1–2, pp. 94–100, 2004, doi: 10.1016/j.jpowsour.2004.06.029.

[50] Q. Jian, L. Luo, B. Huang, J. Zhao, S. Cao, and Z. Huang, "Experimental study on the purge process of a proton exchange membrane fuel cell stack with a dead-end anode," *Appl. Therm. Eng.*, vol. 142, no. March, pp. 203–214, 2018, doi: 10.1016/j.applthermaleng.2018.07.001.

[51] P. Koski, J. Viitakangas, and J. Ihonen, "Determination of fuel utilisation and recirculated gas composition in dead-ended PEMFC systems," *Int. J. Hydrogen Energy*, vol. 45, no. 43, pp. 23201–23226, 2020, doi: 10.1016/j.ijhydene.2020.04.252.

[52] P. Koski, L. C. Pérez, and J. Ihonen, "Comparing Anode Gas Recirculation with Hydrogen Purge and Bleed in a Novel PEMFC Laboratory Test Cell Configuration," *Fuel Cells*, vol. 15, no. 3, pp. 494–504, 2015, doi: 10.1002/fuce.201400102.

[53] L. Xu, C. Fang, J. Li, M. Ouyang, and W. Lehnert, "Nonlinear dynamic mechanism modeling of a polymer electrolyte membrane fuel cell with dead-ended anode considering mass transport and actuator properties," *Appl. Energy*, vol. 230, no. August 2017, pp. 106–121, 2018, doi: 10.1016/j.apenergy.2018.08.099.

[54] S. W. Tsai and Y. S. Chen, "A mathematical model to study the energy efficiency of a proton exchange membrane fuel cell with a dead-ended anode," *Appl. Energy*, vol. 188, pp. 151–159, 2017, doi: 10.1016/j.apenergy.2016.11.128.

[55] J. H. Jang, W. M. Yan, H. C. Chiu, and J. Y. Lui, "Dynamic cell performance of kW-grade proton exchange membrane fuel cell stack with dead-ended anode," *Appl. Energy*, vol. 142, pp. 108–114, 2015, doi: 10.1016/j.apenergy.2014.12.073.

[56] Y. Yang, X. Zhang, L. Guo, and H. Liu, "Overall and local effects of operating conditions in PEM fuel cells with dead-ended anode," *Int. J. Hydrogen Energy*, vol. 42, no. 7, pp. 4690–4698, 2017, doi: 10.1016/j.ijhydene.2016.08.091.

[57] Y. Lee, B. Kim, and Y. Kim, "An experimental study on water transport through the membrane of a PEFC operating in the dead-end mode," *Int. J. Hydrogen Energy*, vol. 34, no. 18, pp. 7768–7779, 2009, doi: 10.1016/j.ijhydene.2009.07.010.

[58] J. Zhao, Q. Jian, Z. Huang, L. Luo, and B. Huang, "Experimental study on water management improvement of proton exchange membrane fuel cells with dead-ended anode by periodically supplying fuel from anode outlet," *J. Power Sources*, vol. 435, no. March, p. 226775, 2019, doi: 10.1016/j.jpowsour.2019.226775.

[59] R. K. Ahluwalia and X. Wang, "Buildup of nitrogen in direct hydrogen polymer-electrolyte fuel cell stacks," *J. power*, vol. 171, pp. 63–71, 2007, doi: 10.1016/j.jpowsour.2007.01.032.

[60] J. B. Siegel, J. E. Soc, J. B. Siegel, S. V Bohac, and A. G. Stefanopoulou, "Nitrogen Front Evolution in Purged Polymer Electrolyte Membrane Fuel Cell with Dead-Ended Anode Nitrogen Front Evolution in Purged Polymer Electrolyte Membrane Fuel Cell with Dead-Ended Anode," *J. Electrochem. Soc.*, vol. 157, no. 7, 2010, doi: 10.1149/1.3425743.

[61] B. Chen, H. Zhou, S. He, K. Meng, Y. Liu, and Y. Cai, "Numerical simulation on purge strategy of proton exchange membrane fuel cell with dead-ended anode," *Energy*, vol. 234, p. 121265, 2021, doi: 10.1016/j.energy.2021.121265.

[62] M. Steinberger, J. Geiling, R. Oechsner, and L. Frey, "Anode recirculation and purge strategies for PEM fuel cell operation with diluted hydrogen feed gas," *Appl. Energy*, vol. 232, no. October, pp. 572–582, 2018, doi: 10.1016/j.apenergy.2018.10.004.

[63] K. Nikiforow, H. Karimäki, T. M. Keränen, and J. Ihonen, "Optimization study of purge cycle in proton exchange membrane fuel cell system," *J. Power Sources*, vol. 238, pp. 336–344, 2013, doi: 10.1016/j.jpowsour.2012.11.153.

[64] Z. Hu *et al.*, "Anode purge strategy optimization of the polymer electrode membrane fuel cell system under the dead-end anode operation," *J. Power Sources*, vol. 320, pp. 68–77, 2016, doi: 10.1016/j.jpowsour.2016.04.023.

[65] H. He, S. Quan, and Y. X. Wang, "Hydrogen circulation system model predictive control for polymer electrolyte membrane fuel cell-based electric vehicle application," *Int. J. Hydrogen Energy*, vol. 45, no. 39, pp. 20382–20390, 2020, doi: 10.1016/j.ijhydene.2019.12.147.

[66] C. Xie, X. Xu, P. Bujlo, D. Shen, H. Zhao, and S. Quan, "Fuel cell and lithium iron phosphate battery hybrid powertrain with an ultracapacitor bank using direct parallel structure," *J. Power Sources*, vol. 279, pp. 487–494, 2015, doi: 10.1016/j.jpowsour.2015.01.029.

[67] B. Wang, H. Deng, and K. Jiao, "Purge strategy optimization of proton exchange membrane fuel cell with anode recirculation," *Appl. Energy*, vol. 225, no. May, pp. 1–13, 2018, doi: 10.1016/j.apenergy.2018.04.058.

[68] H. Karimäki, L. C. Pérez, K. Nikiforow, T. M. Keränen, J. Viitakangas, and J. Ihonen, "The use of on-line hydrogen sensor for studying inert gas effects and nitrogen crossover in PEMFC system," *Int. J. Hydrogen Energy*, vol. 36, no. 16, pp. 10179–10187, 2011, doi: 10.1016/j.ijhydene.2011.04.230.

[69] T. I. Okedi, Q. Meyer, H. M. A. Hunter, P. R. Shearing, and D. J. L. Brett, "Development of a polymer electrolyte fuel cell dead-ended anode purge strategy for use with a nitrogen-containing hydrogen gas supply," *Int. J. Hydrogen Energy*, vol. 42, no. 19, pp. 13850–13859, 2017, doi: 10.1016/j.ijhydene.2016.11.081.

[70] A. Nishizawa, J. Kallo, O. Garrot, and J. Weiss-Ungethüm, "Fuel cell and Li-ion battery direct hybridization system for aircraft applications," *J. Power Sources*, vol. 222, pp. 294–300, 2013, doi: 10.1016/jjpowsour.2012.09.011.

[71] Z. Liu, L. Li, Y. Ding, H. Deng, and W. Chen, "Modeling and control of an air supply system for a heavy duty PEMFC engine," *Int. J. Hydrogen Energy*, vol. 41, no. 36, pp. 16230–16239, 2016, doi: 10.1016/j.ijhydene.2016.04.213.

[72] B. J. Kim and M. S. Kim, "Studies on the cathode humidification by exhaust gas recirculation for PEM fuel cell," *Int. J. Hydrogen Energy*, vol. 37, no. 5, pp. 4290–4299, 2012, doi: 10.1016/j.ijhydene.2011.11.103.

[73] F. Calili, M. S. Ismail, D. B. Ingham, K. J. Hughes, L. Ma, and M. Pourkashanian, "A dynamic model of air-breathing polymer electrolyte fuel cell (PEFC): A parametric study," *Int. J. Hydrogen Energy*, vol. 46, no. 33, pp. 17343–17357, 2021, doi: 10.1016/j.ijhydene.2021.02.133.

[74] D. Yang, R. Pan, Y. Wang, and Z. Chen, "Modeling and control of PEMFC air supply system based on T-S fuzzy theory and predictive control," *Energy*, vol. 188, p. 116078, 2019, doi: 10.1016/j.energy.2019.116078.

[75] H. Y. Lee, H. C. Su, and Y. S. Chen, "A gas management strategy for anode recirculation in a proton exchange membrane fuel cell," *Int. J. Hydrogen Energy*, vol. 43, no. 7, pp. 3803–3808, 2018, doi: 10.1016/j.ijhydene.2018.01.026.

[76] B. Chen, Y. Cai, Y. Yu, J. Wang, Z. Tu, and S. Hwa, "Gas purging effect on the degradation characteristic of a proton exchange membrane fuel cell with dead-ended mode operation II . Under different operation pressures," *Energy*, vol. 131, pp. 50–57, 2017, doi: 10.1016/j.energy.2017.05.035.

[77] K. Shen, S. Park, and Y. Kim, "Hydrogen utilization enhancement of proton exchange membrane fuel cell with anode recirculation system through a purge strategy," *Int. J. Hydrogen Energy*, vol. 45, no. 33, pp. 16773–16786, 2020, doi: 10.1016/j.ijhydene.2020.04.147.

[78] D. A. Brunner, S. Marcks, M. Bajpai, A. K. Prasad, and S. G. Advani, "Design and characterization of an electronically controlled variable flow rate ejector for fuel cell applications," *Int. J. Hydrogen Energy*, vol. 37, no. 5, pp. 4457–4466, 2011, doi: 10.1016/j.ijhydene.2011.11.116.

[79] Q. Zhang, Z. Tong, and S. Tong, "Effect of cathode recirculation on high potential limitation and self-humidification of hydrogen fuel cell system," *J. Power Sources*, vol. 468, no. April, p. 228388, 2020, doi: 10.1016/j.jpowsour.2020.228388.

[80] H. Park, "Effect of the hydrophilic and hydrophobic characteristics of the gas diffusion medium on polymer electrolyte fuel cell performance under non-humidification condition," *Energy Convers. Manag.*, vol. 81, pp. 220–230, 2014, doi: 10.1016/j.enconman.2014.02.029.

[81] X. Chen *et al.*, "Active disturbance rejection control strategy applied to cathode humidity control in PEMFC system," *Energy Convers. Manag.*, vol. 224, no. September, p. 113389, 2020, doi: 10.1016/j.enconman.2020.113389.

[82] W. R. W. Daud, R. E. Rosli, E. H. Majlan, S. A. A. Hamid, R. Mohamed, and T. Husaini, "PEM fuel cell system control: A review," *Renew. Energy*, vol. 113, pp. 620–638, 2017, doi: 10.1016/j.renene.2017.06.027.

[83] W. J. Zou and Y. B. Kim, "Temperature Control for a 5 kW Water-Cooled PEM Fuel Cell System for a Household Application," *IEEE Access*, vol. 7, pp. 144826–144835, 2019, doi: 10.1109/ACCESS.2019.2945986.

[84] H. S. Lee, C. W. Cho, J. H. Seo, and M. Y. Lee, "Cooling performance characteristics of the stack thermal management system for fuel cell electric vehicles under actual driving conditions," *Energies*, vol. 9, no. 5, 2016, doi: 10.3390/en9050320.

[85] N. Steiner *et al.*, "A Review on solid oxide fuel cell models," *Int. J. Hydrogen Energy*, vol. 6, no. 12, pp. 7212–7228, 2011, doi: 10.1016/j.ijhydene.2011.03.051.

[86] R. O'Hayre, S. Cha, W. G. Colella, and F. B. Prinz, *Fuel cell fundamentals*, 3rd ed. New Jersey, USA: Wiley.

[87] P. Pei and H. Chen, “Main factors affecting the lifetime of Proton Exchange Membrane fuel cells in vehicle applications: A review,” *Appl. Energy*, vol. 125, pp. 60–75, 2014, doi: 10.1016/j.apenergy.2014.03.048.

[88] H. Chen, X. Zhao, T. Zhang, and P. Pei, “The reactant starvation of the proton exchange membrane fuel cells for vehicular applications : A review,” *Energy Convers. Manag.*, Paris, France, January, pp. 282–298, 2019, doi: 10.1016/j.enconman.2018.12.049.

[89] Z. Liu, L. Yang, Z. Mao, W. Zhuge, Y. Zhang, and L. Wang, “Behavior of PEMFC in starvation,” *J. Power Sources*, vol. 157, no. 1, pp. 166–176, Jun. 2006, doi: 10.1016/J.JPOWSOUR.2005.08.006.

[90] S. Palani, S. C. Subramanian, and R. Chetty, “Component sizing based on multi-objective optimization for a fuel cell hybrid vehicle,” in *2019 6th International Conference on Control, Decision and Information Technologies, CoDIT*, Paris, France,2019, pp. 434–439, doi: 10.1109/CoDIT.2019.8820544.

[91] C. A. Ramos-Paja, R. Giral, L. Martinez-Salamero, J. Romano, A. Romero and G. Spagnuolo, "A PEM Fuel-Cell Model Featuring Oxygen-Excess-Ratio Estimation and Power-Electronics Interaction," in *IEEE Transactions on Industrial Electronics*, vol. 57, no. 6, pp. 1914-1924, June 2010, doi: 10.1109/TIE.2009.2026363.

[92] E. J. Choi, S. H. Hwang, J. Park, and M. S. Kim, “Parametric analysis of simultaneous humidification and cooling for PEMFCs using direct water injection method,” *Int. J. Hydrogen Energy*, vol. 42, no. 17, pp. 12531–12542, 2017, doi: 10.1016/j.ijhydene.2017.03.201.

[93] Q. Guo, F. Ye, H. Guo, and C. F. Ma, “Gas/Water and Heat Management of PEM-Based Fuel Cell and Electrolyzer Systems for Space Applications,” *Microgravity Sci. Technol.*, vol. 29, no. 1–2, pp. 49–63, 2017, doi: 10.1007/s12217-016-9525-6.

[94] Y. F. Lin and Y. S. Chen, “Experimental study on the optimal purge duration of a proton exchange membrane fuel cell with a dead-ended anode,” *J. Power Sources*, vol. 340, pp. 176–182, 2017, doi: 10.1016/j.jpowsour.2016.11.039.

[95] F. Migliardini, T. M. Di Palma, M. F. Gaele, and P. Corbo, “Hydrogen purge and reactant feeding strategies in self-humidified PEM fuel cell systems,” *Int. J. Hydrogen Energy*, vol. 42, no. 3, pp. 1758–1765, 2017, doi: 10.1016/j.ijhydene.2016.06.196.

[96] G. Guzzella and A. Sciarretta, *Vehicle Propulsion Systems*, 1st ed. Berlin: Springer, 2013.

[97] Y. Guezennec, Ta-Young Choi, G. Paganelli, and G. Rizzoni, “Supervisory control of fuel cell vehicles and its link to overall system efficiency and low-level control requirements,” in *2003 American Control Conference*, Denver, CO, USA, 2003, pp. 2055–2061, doi: 10.1109/acc.2003.1243377.

[98] R. Johri and Z. Filipi, “Self-Learning Neural Controller for Hybrid Power Management Using Neuro-Dynamic Programming,” *SAE Tech. Pap. Ser.*, vol. 1, pp. 1–16, 2011, doi: 10.4271/2011-24-0081.

[99] D. F. Opila, X. Wang, R. McGee, R. B. Gillespie, J. A. Cook, and J. W. Grizzle, "An energy management controller to optimally trade off fuel economy and drivability for hybrid vehicles," *IEEE Trans. Control Syst. Technol.*, vol. 20, no. 6, pp. 1490–1505, 2012, doi: 10.1109/TCST.2011.2168820.

[100] T. Deppen, "Optimal Energy Use in Mobile Applications with Storage," Thesis, University of Illinois, 2013.

[101] J. Bauman and M. Kazerani, "A comparative study of fuel-cell-battery, fuel-cell-ultracapacitor, and fuel-cell-battery-ultracapacitor vehicles," *IEEE Trans. Veh. Technol.*, vol. 57, no. 2, pp. 760–769, 2008, doi: 10.1109/TVT.2007.906379.

[102] R. Steinberger-Wilckens, Z. Kurban, P. E. Dodds, J. Radcliffe, and A. V. Abad, " Extended Summary," in The role of hydrogen and fuel cells in delivering energy security for the UK., R. Steinberger-Wilckens, Z. Kurban, P. E. Dodds, J. Radcliffe, and A. V. Abad, Eds. H2FC SUPERGEN, London, UK, 2017

[103] J. Kurtz, S. Sprik, C. Ainscough, G. Saur, and S. Onorato, "Fuel Cell Electric Vehicle Performance Composite Data Products : Spring 2018," *Analysis Catergories*, 2018. [Online]. Available: https://www.nrel.gov/hydrogen/fuel-cell-electric-vehicle-cdps.html. [Accessed: 01-Jan-2019].

[104] U. Eberle, B. Muller, and R. von Helmolt, "Fuel cell electric vehicles and hydrogen infrastructure : status 2012," *Energy Environ. Sci*, vol. 5, no. 8780, pp. 8780–8798, 2012, doi: 10.1039/c2ee22596d.

[105] Automotive council UK, "Fuel Cell Roadmap 2020 report," London, UK, v 1.0, February 2021.

[106] P. Thounthong, V. Chunkag, P. Sethakul, B. Davat, and M. Hinaje, "Comparative Study of Fuel-Cell Vehicle Hybridization with Battery or Supercapacitor Storage Device," *IEEE Trans. Veh. Technol.*, vol. 58, no. 8, pp. 3892–3904, 2009, doi: 10.1109/TVT.2009.2028571.

[107] J. T. Pukrushpan, H. Peng, and A. G. Stefanopoulou, "Control-Oriented Modeling and Analysis for Automotive Fuel Cell," *J. Dyn. Sys., Meas., Control*, vol. 126, no. 1, pp. 14–25, 2004, doi: 10.1115/1.1648308.

[108] A. Vahidi, A. Stefanopoulou, and H. Peng, "Current management in a hybrid fuel cell power system: A model-predictive control approach," *IEEE Trans. Control Syst. Technol.*, vol. 14, no. 6, pp. 1047–1057, 2006, doi: 10.1109/TCST.2006.880199.

[109] W. Greenwell and A. Vahidi, "Predictive Control of Voltage and Current in a Fuel Cell – Ultracapacitor Hybrid," *IEEE Trans. Ind. Electron.*, vol. 57, no. 6, pp. 1954–1963, 2010, doi: 10.1109/TIE.2009.2031663.

[110] F. G. Harmon, A. A. Frank, and S. S. Joshi, "The control of a parallel hybrid-electric propulsion system for a small unmanned aerial vehicle using a CMAC neural network *," *Neural Networks*, vol. 18, no. 2005, pp. 772–780, 2005, doi: 10.1016/j.neunet.2005.06.030.

[111] C. C. Lin, H. Peng, J. W. Grizzle, and J. M. Kang, "Power management strategy for a parallel hybrid electric truck. IEEE Trans Control Syst Technol," *IEEE Trans. Control Syst. Technol.*, vol. 11, no. 6, pp. 839–849, 2001.

[112] I. V Kolmanovsky, "Game Theory Controller for Hybrid Electric Vehicles," *Trans. Control Syst. Technol.*, vol. 22, no. 2, pp. 652–663, 2014, doi: 10.1109/TCST.2013.2254597.

[113] C.-C. Lin, H. Peng, J. W. Grizzle, J. Liu, and M. Busdiecker, "Control System Development for an Advanced-Technology Medium-Duty Hybrid Electric Truck," *SAE Tech. Pap. Ser.*, vol. 1, no. 3369, 2003, doi: 10.4271/2003-01-3369.

[114] X. Wang, Q. Hua, P. Liu, and L. Sun, "Stochastic dynamic programming based optimal energy scheduling for a hybrid fuel cell/PV/battery system under uncertainty," *Process Saf. Environ. Prot.*, vol. 165, no. May, pp. 380–386, 2022, doi: 10.1016/j.psep.2022.07.025.

[115] W. Xiong, Y. Zhang, and C. Yin, "Configuration design, energy management and experimental validation of a novel series-parallel hybrid electric transit bus," *J. Zhejiang Univ. A*, vol. 10, no. 9, pp. 1269–1276, 2009, doi: 10.1631/jzus.a0820556.

[116] A. Schell, H. Peng, D. Tran, E. Stamos, C. C. Lin, and M. J. Kim, "Modelling and control strategy development for fuel cell electric vehicles," *Annu. Rev. Control*, vol. 29, no. 1, pp. 159–168, 2005, doi: 10.1016/j.arcontrol.2005.02.001.

[117] E. Schaltz, A. Khaligh, and P. O. Rasmussen, "Influence of battery/ultracapacitor energy-storage sizing on battery lifetime in a fuel cell hybrid electric vehicle," *IEEE Trans. Veh. Technol.*, vol. 58, no. 8, pp. 3882–3891, 2009, doi: 10.1109/TVT.2009.2027909.

[118] A. Rousseau, P. Sharer, and R. Ahluwalia, "Energy Storage Requirements for Fuel Cell Vehicles," *SAE Tech. Pap. Ser.*, vol. 1, no. 1302, 2010, doi: 10.4271/2004-01-1302.

[119] J. Schiffer, O. Bohlen, R. W. de Doncker, D. U. Sauer, and Kyun Young Ahn, "Optimized Energy Management for FuelCell-SuperCap Hybrid Electric Vehicles," in *2005 IEEE Vehicle Power and Propulsion Conference*, Chicago, IL, USA, 2005, pp. 716–723, doi: 10.1109/vppc.2005.1554637.

[120] S. N. Motapon, L. Dessaint, and K. Al-haddad, "A Comparative Study of Energy Management Schemes for a Fuel-Cell Hybrid Emergency Power System of More-Electric Aircraft," *IEEE Trans. Ind. Electron.*, vol. 61, no. 3, pp. 1320–1334, 2014, doi: 10.1109/TIE.2013.2257152.

[121] V. H. Johnson, K. B. Wipke, and D. J. Rausen, "Control Strategy for Real-Time Optimization of Fuel Economy and Emissions," *SAE Technical Paper 2000-01-1543*, 2000, https://doi.org/10.4271/2000-01-1543.

[122] C. Yi, B. I. Epureanu, S.-K. Hong, T. Ge, and X. G. Yang, "Modeling, control, and performance of a novel architecture of hybrid electric powertrain system," *Appl. Energy*, vol. 178, pp. 454–467, 2016, doi: 10.1016/j.apenergy.2016.06.068.

[123] C. Raga, A. Barrado, H. Miniguano, A. Lazaro, I. Quesada, and A. Martin-Lozano, "Analysis and Sizing of Power Distribution Architectures Applied to Fuel Cell Based Vehicles," *Energies*, vol. 11, no. 10, 2018, doi: 10.3390/en11102597.

[124] O. Erdinc and M. Uzunoglu, "Recent trends in PEM fuel cell-powered hybrid systems: Investigation of application areas, design architectures and energy management approaches," *Renew. Sustain. Energy Rev.*, vol. 14, no. 9, pp. 2874–2884, 2010, doi: 10.1016/j.rser.2010.07.060.

[125] D. Feroldi, M. Serra, and J. Riera, "Design and analysis of fuel-cell hybrid systems oriented to automotive applications," *IEEE Trans. Veh. Technol.*, vol. 58, no. 9, pp. 4720–4729, 2009, doi: 10.1109/TVT.2009.2027241.

[126] A. A. Kulikovsky, "A Physically–Based Analytical Polarization Curve of a PEM Fuel Cell," *J. Electrochem. Soc.*, vol. 161, no. 3, pp. F263–F270, 2014, doi: 10.1149/2.028403jes.

[127] H. Yumiya, M. Kizaki, and H. Asai, "Toyota Fuel Cell System (TFCS)," *World Electr. Veh. J.*, vol. 7, no. 1, pp. 85–92, 2015, doi: 10.3390/wevj7010085.

[128] A. Szałek, I. Pielecha, and W. Cieslik, "Fuel Cell Electric Vehicle (FCEV) Energy Flow Analysis in Real Driving Conditions (RDC)," *Energies*, vol. 14, no. 16, p. 5018, 2021, doi: 10.3390/en14165018.

[129] Argonne National Laboratory, "2016 Toyota Mirai," 2016. [Online]. Available: https://www.anl.gov/taps/d3-2016-toyota-mirai. [Accessed: 11-Jun-2020].

[130] C.-C. Lin, M.-J. Kim, H. Peng, and J. W. Grizzle, "System-Level Model and Stochastic Optimal Control for a PEM Fuel Cell Hybrid Vehicle," *J. Dyn. Syst. Meas. Control*, vol. 128, no. 4, p. 878, 2006, doi: 10.1115/1.2362785.

[131] I. Kolmanovsky, I. Siverguina, and B. Lygoe, "Optimization of powertrain operating policy for feasibility assessment and calibration: Stochastic dynamic programming approach," *Proc. Am. Control Conf.*, Anchorage, AK, USA, vol. 2, no. i, pp. 1425–1430, 2002, doi: 10.1109/ACC.2002.1023221.

[132] A. Soltis and Xiang Chen, "A new control strategy for hybrid electric vehicles," pp. 1398–1403, *Proc. Of 2004 American Cont Conference*, Boston, Massachusetts, 2004, doi: 10.1109/acc.2003.1239786.

[133] A. Sciarretta and L. Guzzella, "Optimal Energy-management of Electric Vehicles," *IEEE Control Systems Magazine*, no. April, pp. 60–70, 2007.

[134] Z. Song, X. Zhang, J. Li, H. Hofmann, M. Ouyang, and J. Du, "Component sizing optimization of plug-in hybrid electric vehicles with the hybrid energy storage system," *Energy*, vol. 144, pp. 393–403, Feb. 2018, doi: 10.1016/J.ENERGY.2017.12.009.

[135] S. H. Karaki, R. Dinnawi, R. Jabr, R. Chedid, and F. Panik, "Fuel Cell Hybrid Electric Vehicle Sizing using Ordinal Optimization," *SAE Int. J. Passeng. Cars – Electron. Electr. Syst.*, vol. 8, no. 1, pp. 4–13, 2021, doi: 10.4271/2015-01-0155.

[136] U. Sarma and S. Ganguly, "Determination of the component sizing for the PEM fuel cell-battery hybrid energy system for locomotive application using particle swarm optimization," *J. Energy Storage*, vol. 19, no. February, pp. 247–259, 2018, doi: 10.1016/j.est.2018.08.008.

[137] S. Molina, R. Novella, B. Pla, and M. Lopez-Juarez, "Optimization and sizing of a fuel cell range extender vehicle for passenger car applications in driving cycle conditions," *Appl. Energy*, vol. 285, no. December 2020, p. 116469, 2021, doi: 10.1016/j.apenergy.2021.116469.

[138] E. Tazelaar, Y. Shen, P. A. Veenhuizen, T. Hofman, and P. P. J. van den Bosch, "Sizing Stack and Battery of a Fuel Cell Hybrid Distribution Truck," *Oil Gas Sci. Technol. – Rev. d'IFP Energies Nouv.*, vol. 67, no. 4, pp. 563–573, 2012, doi: 10.2516/ogst/2012014.

[139] O. Sundström and A. Stefanopoulou, "Optimum battery size for fuel cell hybrid electric vehicle with transient loading consideration - Part II," *J. Fuel Cell Sci. Technol.*, vol. 4, no. 2, pp. 176–184, 2007, doi: 10.1115/1.2713779.

[140] J. Zhang, L. Xu, Z. Hu, C. Liang, J. Li, and M. Ouyang, "Optimal sizing of fuel cell electric vehicle powertrain considering multiple objectives," in *IECON Proceedings (Industrial Electronics Conference)*, Singapore, 2020, vol. 20, pp. 317–322, doi: 10.1109/IECON43393.2020.9254713.

[141] X. Wu, X. Hu, X. Yin, L. Li, Z. Zeng, and V. Pickert, "Convex programming energy management and components sizing of a plug-in fuel cell urban logistics vehicle," *J. Power Sources*, vol. 423, no. December 2018, pp. 358–366, 2019, doi: 10.1016/j.jpowsour.2019.03.044.

[142] M.-J. Kim and H. Peng, "Power management and design optimization of fuel cell/battery hybrid vehicles," *J. Power Sources*, vol. 165, pp. 819–832, 2007, doi: 10.1016/j.jpowsour.2006.12.038.

[143] O. Sundström and A. Stefanopoulou, "Optimum battery size for fuel cell hybrid electric vehicle - Part I," *J. Fuel Cell Sci. Technol.*, vol. 4, no. 2, pp. 167–175, 2007, doi: 10.1115/1.2713775.

[144] S. Hou, J. Gao, Y. Zhang, M. Chen, J. Shi, and H. Chen, "A comparison study of battery size optimization and an energy management strategy for FCHEVs based on dynamic programming and convex programming," *Int. J. Hydrogen Energy*, vol. 45, no. 41, pp. 21858–21872, 2020, doi: 10.1016/j.ijhydene.2020.05.248.

[145] Y. He *et al.*, "Research on the power distribution method for hybrid power system in the fuel cell vehicle," *Energies*, vol. 14, no. 3, p. 734, 2021, doi: 10.3390/en14030734.

[146] J. Bauman and M. Kazerani, "An analytical optimization method for improved fuel cell-battery - Ultracapacitor powertrain," *IEEE Trans. Veh. Technol.*, vol. 58, no. 7, pp. 3186–3197, 2009, doi: 10.1109/TVT.2009.2014843.

[147] L. Zhang and D. G. Dorrell, “Genetic Algorithm based optimal component sizing for an electric vehicle,” *IECON Proc. (Industrial Electron. Conf.*, Vienna, Austria, pp. 7331–7336, 2013, doi: 10.1109/IECON.2013.6700352.

[148] J. Lopes, J. A. Pomilio, and P. A. V. Ferreira, “Optimal sizing of batteries and ultracapacitors for fuel cell electric vehicles,” in *IECON Proceedings (Industrial Electronics Conference)*, Melbourne, VIC, Australia, 2011, no. 1, pp. 4603–4608, doi: 10.1109/IECON.2011.6120068.

[149] L. Xu, M. Ouyang, J. Li, F. Yang, L. Lu, and J. Hua, “Optimal sizing of plug-in fuel cell electric vehicles using models of vehicle performance and system cost,” in *Applied Energy*, 2013, vol. 103, no. 2013, pp. 477–487, doi: 10.1016/j.apenergy.2012.10.010.

[150] X. Liu, D. Diallo, and C. Marchand, “Design methodology of fuel cell electric vehicle power system,” in *Proceedings of the 2008 International Conference on Electrical Machines, ICEM’08*, Vilamoura, Portugal, 2008, pp. 1–6, doi: 10.1109/ICELMACH.2008.4800034.

[151] M. Jain, C. Desai, N. Kharma, and S. S. Williamson, “Optimal powertrain component sizing of a fuel cell plug-in hybrid electric vehicle using multi-objective genetic algorithm,” *IECON Proc. (Industrial Electron. Conf.*, Porto, Portugal, pp. 3741–3746, 2009, doi: 10.1109/IECON.2009.5415111.

[152] A. Chauvin, A. Hijazi, E. Bideaux, and A. Sari, “Cost Optimization for Plug-In Integration in a Hybrid Electric Mini-Excavator with Mixed-Integer Linear Programming,” in *2015 IEEE Vehicle Power and Propulsion Conference, VPPC 2015 - Proceedings*, 2015, vol. 15, pp. 1–6, doi: 10.1109/VPPC.2015.7352923.

[153] M. J. Kim and H. Peng, “Power management and design optimization of fuel cell/battery hybrid vehicles,” *J. Power Sources*, vol. 165, no. 2, pp. 819–832, 2007, doi: 10.1016/j.jpowsour.2006.12.038.

[154] X. Wu, B. Cao, X. Li, J. Xu, and X. Ren, “Component sizing optimization of plug-in hybrid electric vehicles,” *Appl. Energy*, vol. 88, no. 3, pp. 799–804, 2011, doi: 10.1016/j.apenergy.2010.08.018.

[155] K. Song, L. Liu, F. Li and C. Feng, "Degree of Hybridization Design for a Fuel Cell/Battery Hybrid Electric Vehicle Based on Multi-objective Particle Swarm Optimization," *2019 3rd Conference on Vehicle Control and Intelligence (CVCI)*, Hefei, China, 2019, pp. 1-6, doi: 10.1109/CVCI47823.2019.8951610.

[156] F. Barbir, *PEM Fuel Cells: Theory and Practice*, 2nd ed. San Diego, California: Elsevier, 2012.

[157] Toyota, “2022 Mirai Full Specs,” *Mirai*, 2022. [Online]. Available: https://www.toyota.com/mirai/features/mpg_other_price/3002/3003. [Accessed: 15-Jun-2020].

[158] E. Padgett, and G, Kleen, “Hydrogen and Fuel Cells Program Record,” Department of Energy, record 20005, 2020.

[159] EV West, "Tesla Mode S Lithium Ion Battery 18650," 2022. [Online]. Available: https://www.evwest.com/catalog/product_info.php?cPath=4&products_id=463. [Accessed: 14-Jun-2020].

[160] Panasonic, "Lithium Ion NCR18650B," *Data sheet*, 2012. [Online]. Available: http://industrial.panasonic.com/lecs/www-data/pdf2/ACA4000/ACA4000CE417.pdf. [Accessed: 11-May-2019].

[161] J. Frith, "Battery Price Declines Slow Down in Latest Pricing Survey," *Green Hyperdrive*, 30-Nov-2021. [online]. Available: https://www.bloomberg.com/news/articles/

[162] Advanced Propulsion Centre UK, "Power Electronics Roadmap 2020,", APC, London, UK, Version 1.0, Febraury 2021, Accessed: 11 Jun 2021. [online]. Available: https://www.apcuk.co.uk/technology-roadmaps/

[163] US DoE, "Target Explanation Document: Onboard Hydrogen Storage for Light-Duty Fuel Cell Vehicles," 2017.

[164] G. Morrison, J. Stevens, and F. Joseck, "Relative economic competitiveness of light-duty battery electric and fuel cell electric vehicles," *Transp. Res. Part C Emerg. Technol.*, vol. 87, pp. 183–196, Feb. 2018, doi: 10.1016/j.trc.2018.01.005.

[165] B. D. James, J. M. Moton, and W. G. Colella, "Mass Production Cost Estimation of Direct H2 PEM Fuel Cell Systems for Transportation Applications: 2018 Update," *8th International Conference on Energy Sustainability*, 2018. [Online]. Available: https://www.energy.gov/eere/fuelcells/articles/mass-production-cost-estimation-direct-h2-pem-fuel-cell-systems-7. [Accessed: 11-Jun-2019].

[166] U. S. D. of Transportation, "U.S. Passenger-Miles," 2020. [Online]. Available: https://www.bts.gov/content/us-passenger-miles. [Accessed: 01-Jun-2020].

[167] Department for Transport, "National Travel Survey," 2022. [Online]. Available: https://www.gov.uk/government/collections/national-travel-survey-statistics. [Accessed: 11-Jan-2022].

[168] M. F. Far, M. Pihlatie, M. Paakkinen, M. Antila, and A. Abdulah, "Pre-Normative Charging Technology Roadmap for Heavy-Duty Electric Vehicles in Europe," *Energies*, vol. 15, no. 7, pp. 1–24, 2022, doi: 10.3390/en15072312.

Appendices

I. Developed Hydrogen Fuel Cell and Balance of Plant

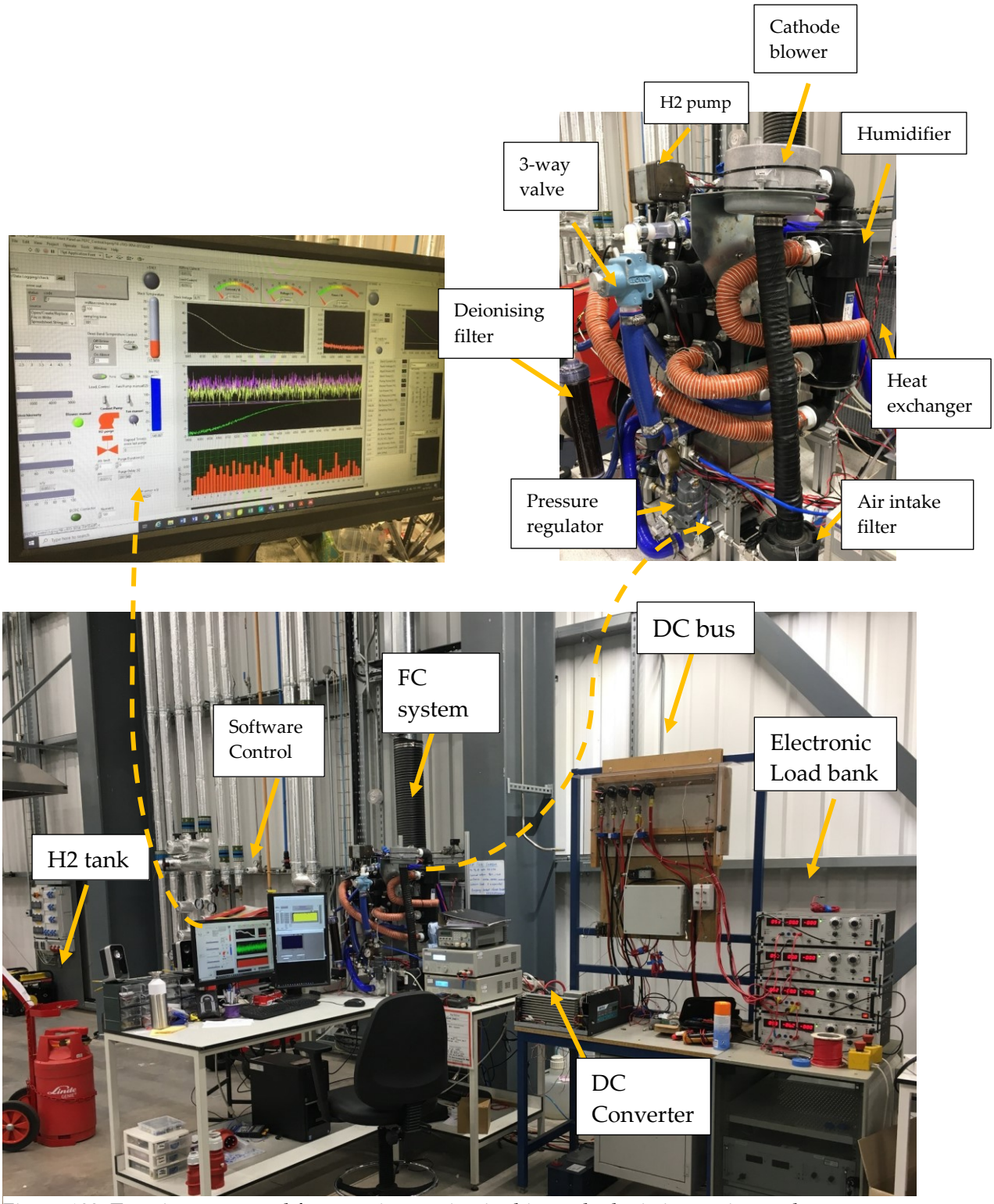


Figure 102: Test rig set up used for experimentation in this work, depicting various sub-systems

II. LabVIEW Front Panel Control and Data Monitoring

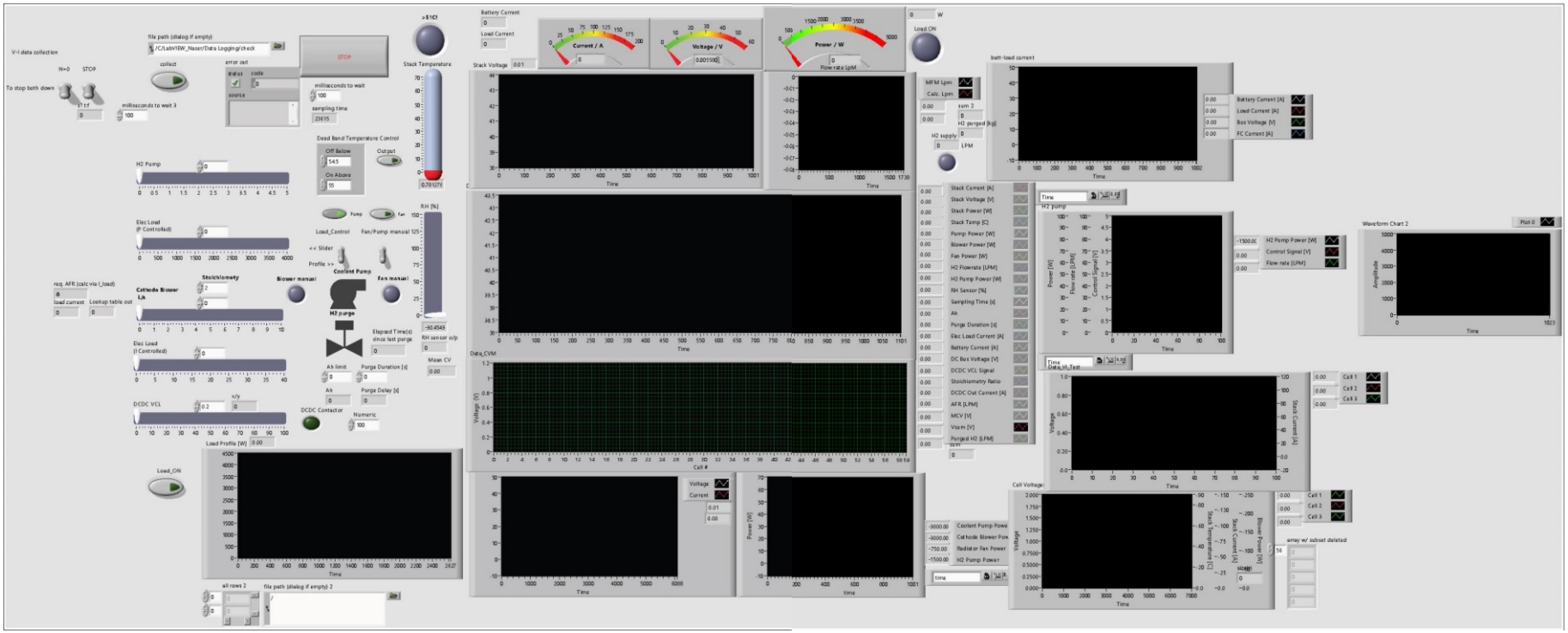


Figure 103: LabVIEW front panel view of the software, for control and data logging.

III. LabVIEW Software Program Code

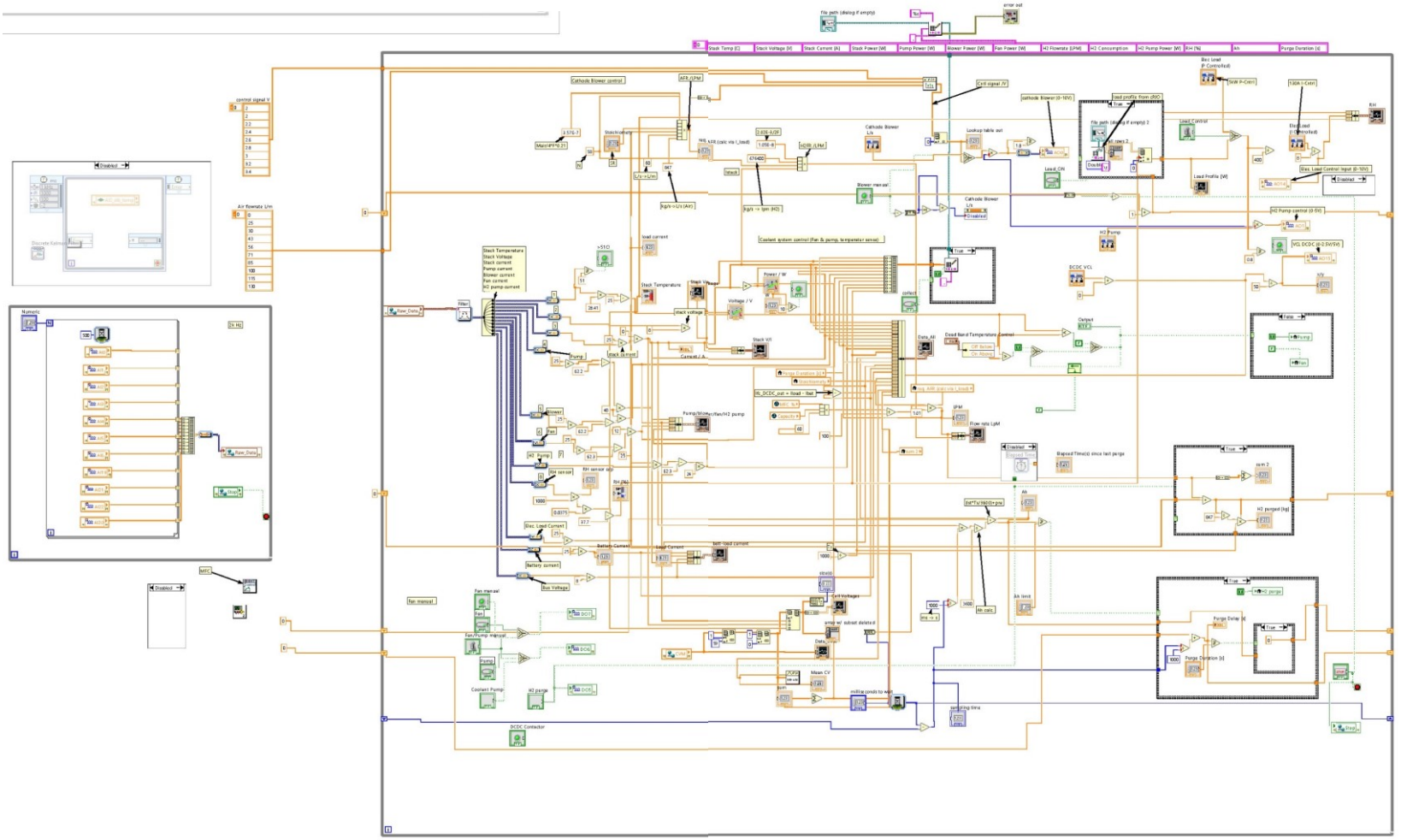


Figure 104: LabVIEW software program with cRIO embedded controller signal and data manipulation.

IV. Toyota Mirai Data

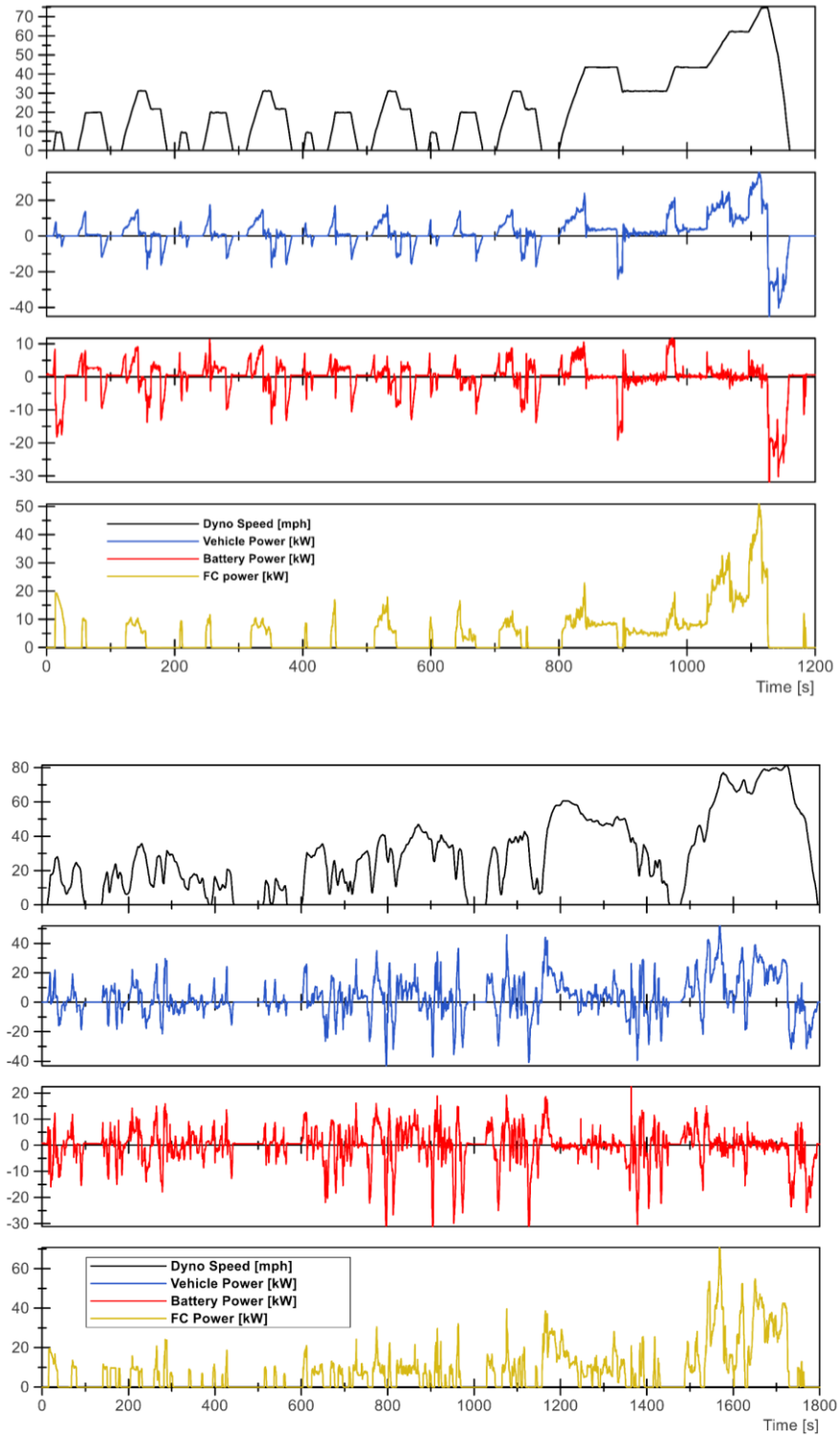


Figure 105: NEDC and WLTP cycle data extracted from Toyota Mirai results available from Argonne National lab.

V. Matlab Design Optimisation Matrices

Constraint (X)	A	b
$0 \leq P_{fc} \leq P_{fc,max}$	$\left[\begin{array}{cccc\|cccc} 1 & 0 & \cdots & 0 & 0 & 0 & \cdots & 0 \\ 0 & 1 & 0 & 0 & 0 & 0 & 0 & 0 \\ \vdots & & \ddots & \vdots & \vdots & & \ddots & \vdots \\ 0 & 0 & \cdots & 1 & 0 & 0 & \cdots & 0 \end{array}\right]_{(N\text{x}2\text{N})}$	$\left[\begin{array}{c} P_{fc,max}\ 0 \\ P_{fc,max}\ 1 \\ \vdots \\ P_{fc,max}\ \text{N} \\ \hline 0 \\ 0 \\ \vdots \\ 0 \end{array}\right]_{(2N\text{x}1)}$
$P_{fc} \leq P_{max}$ $-P_{fc} \leq 0$	$\left[\begin{array}{cccc\|cccc} -1 & 0 & \cdots & 0 & 0 & 0 & \cdots & 0 \\ 0 & -1 & 0 & 0 & 0 & 0 & 0 & 0 \\ \vdots & & \ddots & \vdots & \vdots & & \ddots & \vdots \\ 0 & 0 & \cdots & -1 & 0 & 0 & \cdots & 0 \end{array}\right]_{(N\text{x}2\text{N})}$	$\left[\begin{array}{c} 0 \\ 0 \\ \vdots \\ 0 \\ \hline 0 \\ 0 \\ \vdots \\ 0 \end{array}\right]_{(2N\text{x}1)}$
$P_{bat} \leq P_{bat,max}$	$\left[\begin{array}{cccc\|cccc} 0 & 0 & \cdots & 0 & 1 & 0 & \cdots & 0 \\ 0 & 0 & 0 & 0 & 0 & 1 & 0 & 0 \\ \vdots & & \ddots & \vdots & \vdots & & \ddots & \vdots \\ 0 & 0 & \cdots & 0 & 0 & 0 & \cdots & 1 \end{array}\right]_{(N\text{x}2\text{N})}$	$\left[\begin{array}{c} 0 \\ 0 \\ \vdots \\ 0 \\ \hline P_{bat,max}\ 0 \\ P_{bat,max}\ 1 \\ \vdots \\ P_{bat,max}\ \text{N} \end{array}\right]_{(2N\text{x}1)}$
$-P_{bat} \leq P_{bat,min}$	$\left[\begin{array}{cccc\|cccc} 0 & 0 & \cdots & 0 & -1 & 0 & \cdots & 0 \\ 0 & 0 & 0 & 0 & 0 & -1 & 0 & 0 \\ \vdots & & \ddots & \vdots & \vdots & & \ddots & \vdots \\ 0 & 0 & \cdots & 0 & 0 & 0 & \cdots & -1 \end{array}\right]_{(Nx2N)}$	$\left[\begin{array}{c} 0 \\ 0 \\ \vdots \\ 0 \\ \hline P_{bat,min}\ 0 \\ P_{bat,min}\ 1 \\ \vdots \\ P_{bat,min}\ \text{N} \end{array}\right]_{(2Nx1)}$

$\frac{P_{bat}.T_s}{Q} \leq SoC_0 - SoC_{min}$	$\frac{T_s}{Q}.\left[\begin{array}{cccc\|cccc} 0 & 0 & \cdots & 0 & 1 & 0 & \cdots & 0 \\ 0 & 0 & 0 & 0 & 1 & 1 & 0 & 0 \\ \vdots & & \ddots & \vdots & & \vdots & \ddots & \vdots \\ 0 & 0 & \cdots & 0 & 1 & 1 & \cdots & 1 \end{array}\right]$	$\left[\begin{array}{c} 1 \\ 1 \\ \vdots \\ 1 \\ \hline 1 \\ 1 \\ \vdots \\ 1 \end{array}\right] . SoC_0\text{-}SoC_{min}$
$lb \leq X \leq ub$ $P_{fc} \geq 0$ $P_{bat} \geq P_{bat,min}$	$\left[\begin{array}{cccc\|cccc} 0 & 0 & \cdots & 0 & P_{bat,min} & 0 & \cdots & 0 \\ 0 & 0 & 0 & 0 & 0 & P_{bat,min} & 0 & 0 \\ \vdots & & \ddots & \vdots & & \vdots & \ddots & \vdots \\ 0 & 0 & \cdots & 0 & 0 & 0 & \cdots & P_{bat,min} \end{array}\right]_{(Nx2N)}$	